Soil structure exploration and measurement of its macroscopic behavior for a better understanding of the soil hydropedodynamic functionalities

Smet, Sarah

Publication date:
2018

Citation for pulished version (HARVARD):
Smet, S 2018, 'Soil structure exploration and measurement of its macroscopic behavior for a better understanding of the soil hydropedodynamic functionalities'.

LIÈGE université
Gembloux
Agro-Bio Tech

Soil Structure Exploration and Measurement of its Macroscopic Behavior for a Better Understanding of the Soil Hydropedodynamic Functionalities

Sarah Smet

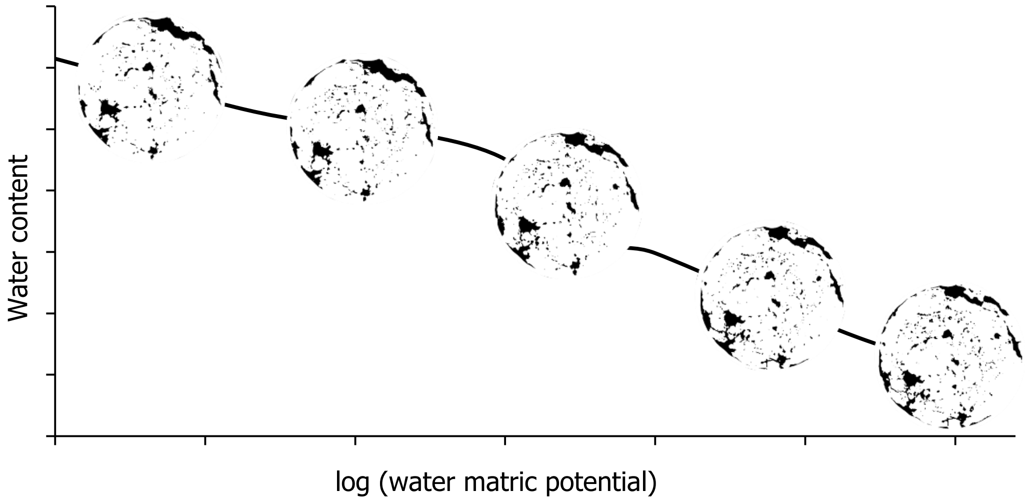

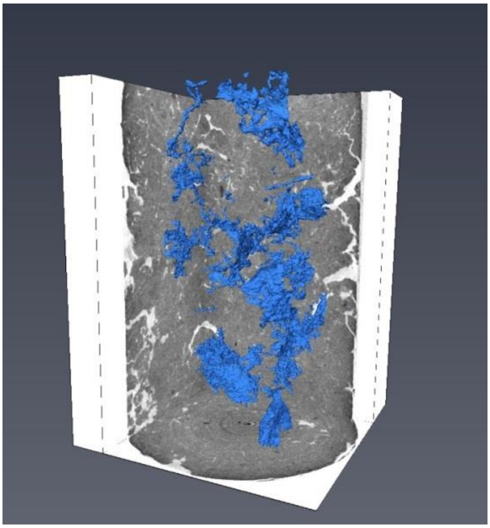

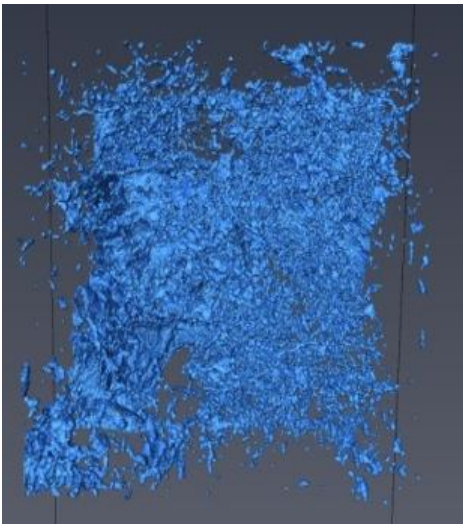

COMMUNAUTÉ FRANÇAISE DE BELGIQUE
UNIVERSITÉ DE LIÈGE – GEMBLOUX AGRO-BIO TECH

SOIL STRUCTURE EXPLORATION AND MEASUREMENT OF ITS MACROSCOPIC BEHAVIOR FOR A BETTER UNDERSTANDING OF THE SOIL HYDROPEDODYNAMIC FUNCTIONNALITIES

Sarah SMET

Dissertation originale présentée en vue de l’obtention du grade de docteur en sciences agronomiques et ingénierie biologique

Promoteurs : Professeur Aurore Degré, Professeur Angélique Léonard

2018

.

Résumé

SMET Sarah (2018). Soil Structure Exploration and Measurement of its Macroscopic Behavior for a Better Understanding of the Soil Hydropedodynamic Functionalities (PhD Thesis). Gembloux Agro-Bio Tech, Université de Liège, Gembloux, Belgium. 136 p., 16 tables, 45 figures.

La perméabilité à l’eau et à l’air du sol sont des propriétés physiques fondamentales dans le rôle d’interface environnementale joué par le sol. À ce jour, les courbes des perméabilités à l’eau $K(\theta)$ et à l’air $k_a(\varepsilon)$ du sol en fonction de sa teneur en eau ne peuvent être connues que de manière discrète et ne sont jamais observées sur toute la gamme de teneur en eau. Pour pallier ce manque d’information, des modèles de prédiction de $K(\theta)$ et $k_a(\varepsilon)$ ont vu le jour, ceux-ci considérant la structure même de l’espace poral du sol comme paramètre d’optimisation alors que nous savons que $K(\theta)$ et $k_a(\varepsilon)$ en dépendent fortement. Cela, ajouté au caractère unique de la relation entre un réseau poral et ses propriétés de transfert, fait que de nouvelles voies d’étude des relations $K(\theta)$ et $k_a(\varepsilon)$ doivent être explorées.

L’observation de la structure de l’espace poral du sol par microtomographie à rayon X (RX) est une option prometteuse qui pourrait permettre de résoudre des questions ouvertes dans la communauté scientifique des physiciens du sol. Cette technique permet l’acquisition d’images 3D d’objets à densités contrastées. Dans le cas d’un milieu poreux naturel tel que le sol, une bonne interprétation des images nécessite un traitement préliminaire de celles-ci, traitement qui doit être choisi de manière éclairée. Une question de recherche transversale de cette thèse, mais néanmoins préliminaire à toute autre manipulation, est dès lors de comparer statistiquement les effets de divers traitements d’images sur les données finales de caractérisation des images RX. En utilisant des images simulées, nous avons pu choisir la meilleure approche pour le traitement de nos images RX de sol.

L’objectif général de la thèse vise à établir des relations entre les caractéristiques structurelles microscopiques du sol (le volume du plus petit pore visible étant de 0,0004 mm^3) et des paramètres de fonctionnalités tels que la perméabilité. Plus spécifiquement, nous avons confirmé que l’utilisation d’images 3D RX permet de mieux appréhender la courbe de rétention du sol proche de la saturation via l’identification des plus gros pores du sol qui sont souvent ignorés, suite à divers artefacts, lors des mesures de rétention par plaques céramiques sous pression. Nous avons aussi identifié des paramètres microscopiques morphologiques du réseau poral du sol expliquant la conductivité hydraulique à saturation du sol, et des paramètres microscopiques de distribution de la porosité expliquant la perméabilité à l’air du sol.

La quantification finale des caractéristiques des images RX dépend du traitement d’images appliqué, mais également de la résolution des images. Nous avons conclu que travailler à une plus haute résolution n’apportait pas assurément un plus haut degré de connaissance du réseau poral observé car la résolution va de pair avec la

taille de l’échantillon étudié. De plus, il est également possible que la distribution des tailles de pores d’un sol étudié soit suffisamment quantifiable à basse résolution. Nous avons néanmoins observé que la connectivité morphologique et topologique du réseau poral d’un sol augmente avec la résolution. Enfin, nous avons souligné les imperfections de la théorie capillaire appliquée aux sols en scannant les mêmes échantillons de sol à diverses teneurs en eau. Tel que supposé, la connectivité du réseau poral du sol joue un rôle important dans l’accessibilité des pores au drainage.

Après avoir exploré les effets de la structure microscopique d’un réseau poral sur les propriétés hydrodynamiques du sol, nous avons évalué les incidences du taux de matière organique et de formes libres de fer (formation d’associations organo-minérales) sur cette même structure microscopique de sol.

Cette dissertation débat donc des avantages et limitations de la technique microtomographique à RX appliquée aux sols pour une compréhension plus réaliste des processus hydropédodynamiques se produisant dans le sol.

Abstract

SMET Sarah (2018). Soil Structure Exploration and Measurement of its Macroscopic Behavior for a Better Understanding of the Soil Hydropedodynamic Functionalities (PhD Thesis). Gembloux Agro-Bio Tech, Université de Liège, Gembloux, Belgium. 136 p., 16 tables, 45 figures.

Air permeability and water conductivity are fundamental physical properties when it comes to the soil functions across the environment. The water conductivity and the air permeability as functions of the soil's degree of saturation ($K(\theta)$ and $k_a(\varepsilon)$, respectively) are only discretely measurable, and the use of models is necessary to obtain continuous expressions of these functions. Most models however consider the soil pore network structure as a fitting parameter although it is public knowledge that $K(\theta)$ and $k_a(\varepsilon)$ depend mostly on the soil microstructure, which is, none the less, unique between samples with homogeneous texture. New ways of studying $K(\theta)$ and $k_a(\varepsilon)$ are needed.

The direct soil pore space visualization is a promising avenue to lead us to objectifying soil physics. The X-ray microtomographic technique (X-ray µCT) is now widely used by soil scientists and delivers 3D grayscale images of objects composed by materials of different densities. When dealing with a porous medium such as the natural soil, the X-ray µCT images need to be cautiously and expertly processed to obtain realistic feature quantification. A parallel, but however perquisite, objective of this dissertation is to statistically compare the effects of various image processing on the final X-ray µCT image features quantification. We simulated grayscale images to be processed to conclude about the image processing methodology we applied in our research.

The overall objective of this dissertation is to explore the relationships between one microscopic soil structure (the volume of the smallest visible pore is 0.0004 mm^3) and its macroscopic functionalities, such as its water conductivity and air permeability. More specifically, we confirmed that the use of 3D X-ray µCT data enables a better estimation of the soil water retention curve near saturation through the identification of the largest soil pores. These are indeed often by-passed with pressure plate's laboratory measurements because of various artefacts. We also identified microscopic pore space morphological parameters that explained the soil saturated hydraulic conductivity, and microscopic porosity distribution measures that explained the soil air permeability.

The final X-ray µCT image features quantification depends on the applied image processing, as stated, but also, clearly, on the image resolution. We concluded that working with a higher resolution would not necessarily lead to a higher degree of knowledge because resolution is sample-size dependent, and one pore size distribution could moreover be sufficiently visible at low resolution. We however observed that the pore network morphological and topological connectivity increases with resolution. Finally, we highlighted the imperfections of the capillary theory applied to soil through scanning the same soil samples at various water contents. As

hypothesized, the pore network connectivity seems to play an important role in the pore accessibility to draining.

After having studied the effects of the soil pore network structure on the soil hydrodynamic properties, we turned the question around and evaluated the effects of the chemical soil composition (organic carbon and free forms of iron) on the very same soil pore network structure.

This dissertation therefore discusses the advantages and limitations of the use of X-ray microtomography to study soils for a more realistic understanding of the soil hydropedodynamic processes.

Acknowledgement

After three years and a half of study, I’m thrilled to submit this dissertation in partial fulfilment of the requirements for the Doctor in Agronomical Sciences and Biological Bioengineering Degree at Gembloux Agro-Bio Tech, University of Liège (Belgium).

This work was funded through a FRIA fellowship (FNRS, Belgium) and my supervisors were Professor Aurore Degré and Professor Angélique Léonard. Professor Jean-Thomas Cornélis, Professor Bernard Bodson, and Professor Benoit Haut were also part of my committee thesis, and I would like to thank them all for their guidance through these years. I especially express my deep gratitude to Professor Aurore Degré who made this all work possible in the beginning. Doctor Eléonore Beckers and Doctor Erwan Plougonven receive my special thanks for their technical, methodological and scientific advices and Professor Yves Brostaux for its statistical support and constant availability. I’m also grateful to the technical, Mr. Daniel Baes and Mr. Stéphane Becquevort, and administrative, Mrs. Katia Berghmans, staff of the department for their availability.

These last years were witnesses of amazing moments in my personal life with my beautiful wedding to Pierre, the birth of my first daughter Hortense, and the approaching arrival of her little sister. These bright instants combined to the excitement of doing research have made of these last years a wonderful time. This preface is also the opportunity to thank my family and friends for their constant presence, empowerment, and beliefs. Thank you.

Sarah

Table of contents

List of figures

List of tables

List of abbreviations and symbols

µCT	Micro-computed tomography
BF	Bayes Factor
CT	Conventional tillage
DVS	Desorption vapor sorption
Fe_DCB	Relative content of soil Fe extracted with dithionite-citrate [MM^{-1}]
Fe_oxalate	Relative content of soil Fe extracted with oxalate [MM^{-1}]
Fe_pyrophosphate	Relative content of soil Fe extracted with pyrophosphate [MM^{-1}]
G	Shape factor [-]
h	Water matric potential [ML^{-1}T^{-2}]
IK	Indicator-kriging
IK/GM	Indicator kriging combined to the gradient masks threshold selection
IK/PBA	Indicator kriging combined to the porosity-based threshold selection
K(θ)	Hydraulic conductivity as a function of water content [LT^{-1}]
ka(ε)	Air permeability as a function of air-filled content [L^{2}]
Ks	Saturated hydraulic conductivity [LT^{-1}]
Lab_FD	Fractal dimension extracted from the laboratory measured soil water retention curve [-]
Lab_PO	Laboratory measured air-filled porosity at a water matric potential of -1 kPa [L^{3}L^{-3}]
ME	Misclassification error [-]
MIL	Mean intercept length
NU	Region non-uniformity [-]
PBA	Porosity-based
PCA	Principal component analysis
POST0	No post-segmentation median filter
POST2	Post-segmentation median filter with a radius of two pixels
PP	Pressure plates
PRE0	No pre-segmentation median filter

PRE1	Pre-segmentation median filter with a radius of one pixel
PRE2	Pre-segmentation median filter with a radius of two pixels
r	Pore radius [L]
RE_g	Relative error on the conductance value [-]
RE_K	Relative error on the global conductance value [-]
RRMSE	Relative root mean square error [-]
RT	Reduced tillage
SOM	Soil organic matter
SWRC	Soil water retention curve
TH	Threshold
TOC	Total organic carbon [MM^{-1}]
θ	Water content [L^3L^{-3}]

Please refer to Table 3 for an extensive review of the microscopic variables.

1

Introduction

It is no surprise the FAO proclaimed 2015 as the year of the soil: this thin continuum layer linking plants and atmosphere plays fundamentals roles in almost all environmental processes. Besides providing the land to food production or the resources for construction or industrial materials, the soil is an invisible and silent machine permanently working in providing the ground for (micro-) organisms, nutrients cycles, water filtration and storage… The numerous functions that the soil holds make it essential in regulating natural events or global climate, and place it at the heart of countless agricultural or industrial applications: the soil functions therefore need to be predictable. Predictability of the soil functions comes through the adequate simulation of the soil processes which, in particular, require a detailed characterization of the soil physical properties. The soil physical properties are traditionally approached by the texture, bulk density, retention curve, and air and water permeability. Soil field descriptions are based on averaging procedure by statistically choosing sampling points across the field, although heterogeneity is the rule at every scale (e.g., Baveye and Laba, 2015). Moreover, it is also cumbersome and delicate to characterize the soil in its unsaturated state, where convective fluxes of air and water are dependent on the degree of saturation. A complete and continuous characterization of the soil physical properties is however needed for the resolution, for example, of physical equations that predict the air and water fluxes across the soil. The use of models producing expression of the hydraulic conductivity as a function of the soil water content [$K(\theta)$], or of the air permeability as a function of the soil air content [$k_a(\varepsilon)$], is therefore unavoidable.

Oldest $k_a(\varepsilon)$ models were based on power-law functions with one discrete measure of $k_a(\varepsilon)$ and an empirical exponent that represented the soil pore space structure (Buckingham, 1904; Millington and Quirk, 1961). These were modified to take into account the soil density (Deepagoda et al., 2011), the pore size distribution (Moldrup et al., 2001, Moldrup et al., 2003), or the particle size distribution (Arthur et al., 2012; Hamamoto et al., 2009). As well, it exists multiple conductivity functions that produce simple analytical expression of $K(\theta)$ from the saturated hydraulic conductivity (Ks) value and a pore size distribution model, where pores are assumed to be capillaries, such as the ones from Burdine (1953) or Mualem (1956). We can cite the model of van Genuchten et al. (1980) which is widely used. Dane et al. (2011) also proposed a model of $K(\theta)$ where the pore size distribution was extracted from discrete measures of $k_a(\varepsilon)$. It is indeed tempting to link air and water permeability measurements (Blackwell et al., 1990; Loll et al., 1999), although no perfect match between water conductivity and air permeability should be expected since water present more affinity to soil particles than air (Loll et al., 1999).

It is the usual norm to use the quoted models, but these have a major drawback: they are not physically interpretable (Hunt et al., 2013). After having considered the pore as capillaries for decades, the trend is now to objectify the fundamentals behind an observed hydrodynamic behavior. The pore space is rather seen as a collection of pore chambers connected to each other by pore throats of smaller section, or as a continuum across the soil that should not be partitioned. The direct visualization of the pore space was an incredible step forward to that purpose. For example, Vogel (1997) postulated that the discrepancy between pore size distributions extracted from soil water retention curve measurements and from serial section images was likely due to the pore space connectivity expressed by the Euler characteristic. Serial sectioning was indeed firstly used by the soil community (e.g. Cousin et al., 1996) but the samples preparation is time-consuming and requires a skilled experimenter. Considering the resolution, X-ray microcomputed tomography (X-ray µCT) is an equivalent technique with the advantage of being non-destructive and less time-consuming because no sample preparation is needed (such as the resin impregnation with serial sectioning). X-ray µCT technique is now widely used in soil science. Landis and Keane (2010) propose a full description of the technology, and Taina et al. (2007) and Wildenschild and Sheppard (2013) discuss the use of X-ray µCT to study the vadose zone. In soil science, the technique has been used at both the core (e.g., Jassogne et al., 2007; Elliot et al., 2010; Luo et al., 2010a.; Larsbo et al., 2014; Katuwal et al., 2015b), and aggregate scale (e.g., Peth et al., 2008; Papadopoulos et al., 2009; Kravchenko et al., 2011) for describing the microscopic pore space morphological and topological structure and studying the impact of land use and agricultural management on soil structure (e.g., Jassogne et al., 2007; Peth et al., 2008; Papadopoulos et al., 2009; Luo et al., 2010a.; Kravchenko et al., 2011) as well as for analyzing the relationships between soil pore space structure and soil physical properties (e.g., Elliot et al., 2010; Larsbo et al., 2014; Katuwal et al., 2015b). As already stated, the heterogeneity is the rule at every scale, and each soil sample presents a unique pore space size distribution and morphological or topological connectivity. Studying the link between the microscopic pore space structure of a sample and its specific fluid transport properties is therefore a step forward in our understanding of how the microscopic soil structure affects the soil functions. On one hand, experimentally visualized infiltration studies shed light on the effective conducting pore space which represents only a small portion of the total pore space (Luo et al., 2008; Koestel and Larsbo, 2014; Sammartino et al., 2015). The procedures developed in these studies are promising, but restricted, as stated in their objectives, to the analysis of large macropores because of the trade-off between resolution and acquisition time. On the other hand, numerical simulations performed on pore space grid are used to predict conductivity. Many studies focus on idealized porous structures (e.g., Vogel et al., 2005; Schaap et al., 2007) and a few deals with actual soil (Elliot et al., 2010; Dal Ferro et al., 2015, Tracy et al., 2015). The latter show encouraging results, but restricted to a defined resolution and/or sample size (Baveye et al., 2017). Indeed, the direct approach of linking one microscopic pore space structure to one soil function is limited by the difficulty in analyzing the structure in a representative way, so that the soil would be adequately characterized (Vogel et al., 2010). The description of soil pore space structure via global characteristics could encompass that challenge and comparisons of one soil sample microscopic structure to its own sample-scale properties have indeed gained attention.

Several studies reported that the global µCT extracted macroporosity explained the sample-scale saturated hydraulic conductivity (Luo et al., 2010b; Paradelo et al., 2016; Mossadeghi-Björklund et al., 2016) or air permeability (Naveed et al., 2012; Katuwal et al., 2015b, Paradelo et al., 2016). Other microscopic measurements calculated on the X-ray µCT images were found to influence the fluid transport, such as the number of independent macropore or macropore hydraulic radius (Luo et al., 2010b), the number of pores (Lamandé et al., 2013, Anderson et al., 2014), and the fractal dimension (Anderson et al., 2014). Naveed et al. (2016) also suggested that biopore-dominated and matrix-dominated flow soil cores should be distinguished before analyzing relationships between microscopic and macroscopic soil properties. These observed relationships between flow parameters and µCT global characteristics are intuitive, but depend on image resolution, water matric potential and soil type. Moreover, the µCT porosity, number of pores, average pore radius, surface area and pore network connectivity and tortuosity all depend on the minimal visible pore size, in other words, on the resolution of the binary X-ray µCT images used to obtain the pore network (Houston et al., 2013b; Peng et al., 2014; Shah et al., 2016). The quoted studies worked with voxel size in average a thousand times larger in volumes than the one we work with, knowing useful information about conducting pores is lost with increased voxel size. For example, Sandin et al. (2017) worked at a smaller voxel size (120^3 μm^3) and observed significant correlations between Ks and a global measure of the pore network connectivity (from the percolation theory) which had, to our knowledge, never been observed. Pore network connectivity and tortuosity are important indicators of flow capacities (Perret et al., 1999; Vogel, 2000), but there is still a lack of information on the links between global pore network connectivity indicators and flow parameters. **The first objective of our dissertation is therefore to unravel the relationships between macroscopic sample-scale soil properties and microscopic soil structure, working with a smaller voxel size ($43^3\mu m^3$) than other studies. Unprecedented, Bayesian statistics are used to explore the relationships between micro- and macroscopic soil data so the uncertainty inherent to the collected and processed µCT data is taken into account. The identification of the key global indicators that induce soil hydrodynamic functions would be of major interest for the generation of phenomenological pore network models.**

An adjacent question although arises: would the observed relationships remain if we had worked with an even higher X-ray µCT resolution? Baveye et al. (2017) recently reviewed the studies that investigated ways to take into account the sub-resolution porosity, such as the use of gray scale images to perform Lattice-Boltzmann water and solutes fluxes simulations, or to consider that the solid phase in binary images is partially permeable. They however pointed out that the X-ray µCT images quality and processing prevent from obtaining meaningful grayscale values, and that we are far to evaluate practically the “penetrability of the voxels”. When reliable estimation of any voxels permeability would be obtained, we would still need to hypothesize about the connectivity of the sub-resolution porosity to the visible pores. To provide reflection areas, and for one soil sample, **we extrapolate**

the X-ray µCT parameters to a lower voxel size on one hand, and we analyze the same X-ray µCT image at its original voxel size (21.5^3µm^3) on the other hand. In the continuity, we also scan a soil aggregate from the same soil sample at a voxel size of 8.99^3 µm^3 and measure its water adsorption-desorption curve to extract a physical pore size distribution. The second objective of this dissertation is therefore to evaluate the evolution of the X-ray µCT extracted parameters with image resolution.

Vogel (1997) or Parvin et al. (2017) postulated that the pore network connectivity influences the soil retention of water. Capillary theory in soil science, although being used for decades, might therefore not be representative of the occurring hydrodynamic processes. Working on the same soil samples for the microscopic pore space and macroscopic hydrodynamic properties characterization, we confirmed these hypothesis and we also reported that the pore network connectivity influences the flow of water and air. **The next objective of this dissertation is therefore to explain, from a microscopic structural point of view, the inadequacy of the capillary law applied to soil. To that purpose, we visualize, quantify, and compare the air-filled pore space of twenty soil samples at five water matric potentials.**

The stated objectives of this dissertation assume that the pore space description generated from the image processing accurately represents the physical reality of the sample microstructure, but the choice of X-ray µCT image processing methodology has a visible impact on the resulting structure. Figure 1 shows an example of the processing steps from sample acquisition to a binary image. Each step involves choosing the appropriate method and parameters, which are numerous and can have a profound effect on the resulting structure. These choices ultimately depend on the experience of the operator, and between soil science research papers, the applied methodology and used software differ profoundly. What is important here is, however, not only the diversity of these choices, but also the fact that they are often inadequately described or justified. Segmentation is the essential step when pixels are assigned to either the solid or porous phase. There are numerous segmentation methods; a review of those used in soil science can be found in Tuller et al. (2013). We here differentiate global and local thresholding methods. The aim of a thresholding method is to select a grayscale value, manually or automatically, that separates the image gray levels into two groups: greater than or equal to the threshold (TH); and less than TH. In soil science, these two groups are often defined as the solid phase (soil matrix) and the void phase (pore space). With global thresholding, a constant TH is chosen for the entire image, whereas with local thresholding the value is computed for every pixel, based on the local neighborhood (Tuller et al., 2013). Segmentation precision depends on the initial quality of the grayscale images. Enhancing the projections before reconstruction and the reconstructed images before segmentation is the typical approach, and an efficient method for improving image quality is to apply noise reduction filters (Kaestner et al., 2008; Wildenschild and Sheppard, 2013). Pre-segmentation processing are more efficient at handling image degradation than post-segmentation ones: a general rule (for more than just image analysis) is that the more upstream a problem is corrected, the easier is it to process the data downstream.

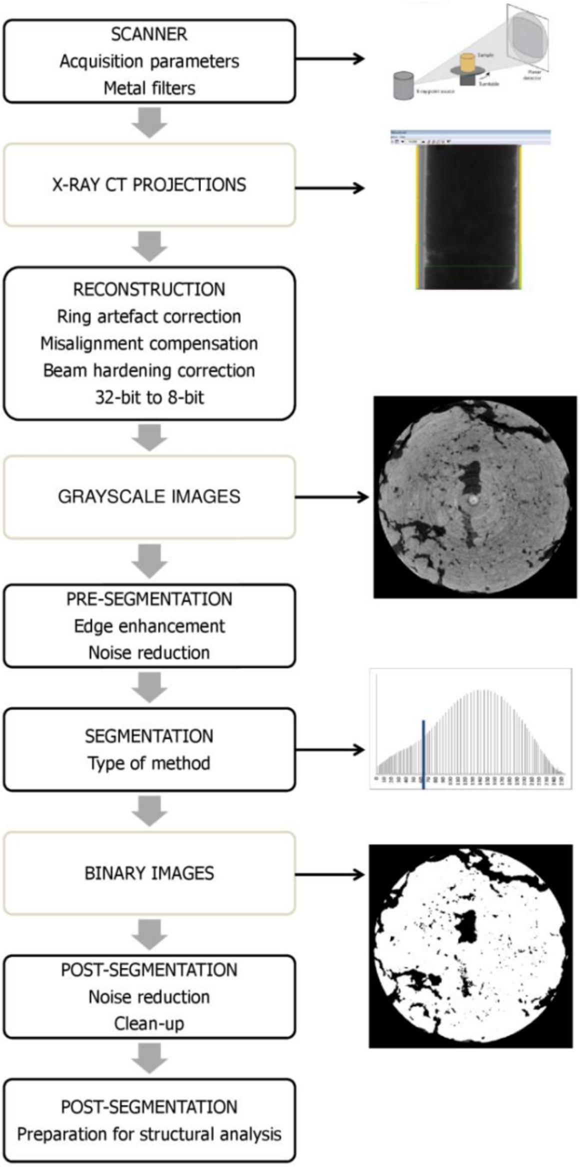

Figure 1. X-ray µCT image processing steps from acquisition to binary image. Some sources of variability are written in lower-case and imaged examples are on the right side.

Some authors have shown (Peth et al., 2008; Tarquis et al., 2009; Lamandé et al., 2013; Beckers et al., 2014b; Peng et al., 2014) that, in most practical cases, the choice of segmentation method plays a crucial role in the resulting pore structure, but no standards have yet been proposed. Several studies sought to classify thresholding techniques based on information available from the resulting binary images (Baveye et al. 2010; Houston et al., 2013b; Iassonov et al., 2009; Schlüter al., 2014). So far as we know, only Wang et al. (2011) have used synthetic soil aggregate images, from which ground-truth information was available, to compare thresholding methods. Even these studies were based on image-by-image analyses and did not provide a tool with which to properly evaluate the processing methodologies. **Within this context, a transversal objective of this dissertation is to provide a statistical analysis of the segmentation processing effects on the resulting data. By evaluating Otsu's global method (Otsu, 1979), the local adaptive-window indicator kriging (IK) method (Houston et al., 2013a) and the porosity-based (PBA) global method (Beckers et al., 2014b) on 2D simulated soil images from which ground-truth information is available, we are able to objectively support existing reviews and be confident with the used image processing methodology.**

2

Materials & Methods: the methodological experiment

2.1. Introduction

We first present a simple example which points out the difficulties in image processing decisions when no ground-truth information is available. For example, a beam hardening correction[1] of 25%, which is a common procedure in X-ray µCT image processing, implies a smaller averaged pore surface area which came from a higher amount of small pores, as a consequence of the extra-noise generated by the beam hardening correction (Fig. 2). However, the gray values histogram shows a slight right-hand shift (pores in black, not shown) in histogram peaks with the 25% beam hardening correction, and this is consistent with the observations of an increasing porosity and a higher visual contrast. This could make the segmentation step more straightforward and could be used in combination to a noise reduction filter to remove the additional small noise. The correction, however, modifies the visible porosity, and therefore the structure, in an unknown way as also demonstrated by Beckers et al. (2014b).

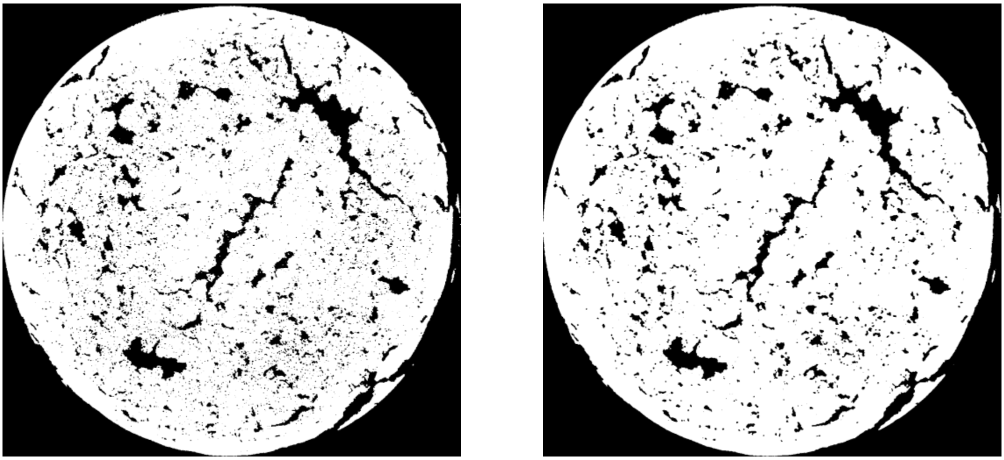

Figure 2. Slice of a binary 3D images of the soil samples. Left-hand: a 25% beam hardening correction was applied during reconstruction. Right-hand: no beam hardening correction was applied.

We also briefly investigated the effects of noise reduction filter on the final resulting binary images. As expected, the number of small pores decreased with the level of pre-segmentation noise reduction, as the visual contrast increased. A higher level of pre-segmentation lead to more uniform phases (Fig. 3) which induces less

---

[1] The beam hardening artefact is due to the polychromatic nature of the X-ray beam implying that the Beer’s Law no longer holds. The images present a radial grayscale intensity variation from the edges to the center.

noisy binary image. Higher the median filtering is, the more information is however lost.

Answering the methodological objective was therefore a perquisite to any real soil image analysis, and we firstly present the developed procedure to that purpose and its ensuing research question which is “what segmentation method and what noise filtering level should we apply?” The methodological experiment was performed on simulated images so ground-truth information would be available for reliable evaluation of the image processing effects on the final binary image features quantification.

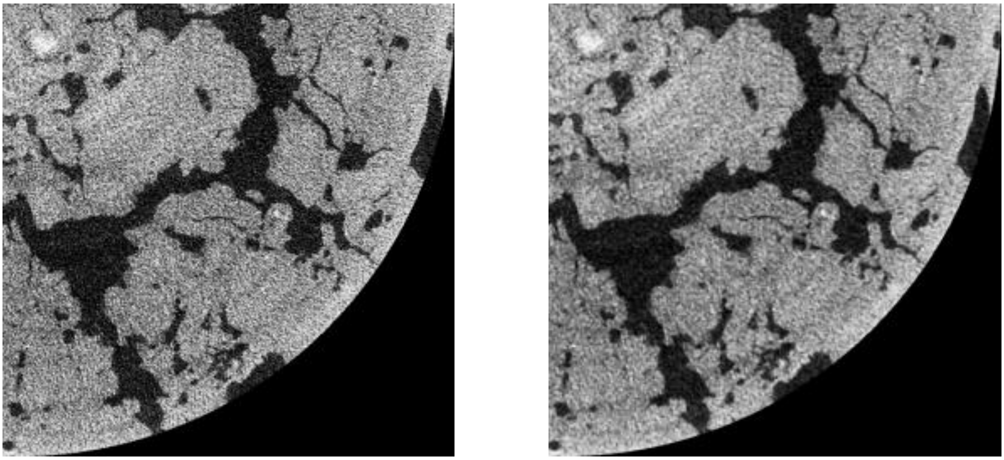

Figure 3. Portion of a slice from a soil sample 3D grayscale image. Left-hand: no pre-segmentation filter was applied. Right-hand: a pre-segmentation median filter with a radius of two pixels was applied.

2.2. Simulated images

Our **Paper I** presents the extensive procedure of the images construction. The general frame was based on the methodology from Wang et al. (2011), which consists in superimposing a realistic binary pore image to an image representing partial volume effects[2] and then adding Gaussian noise (Fig. 4). We have created 15 simulated images from the combination of 15 selected real soil binary images (from Beckers et al., 2014b) to 15 different generated partial volume effect images. The tested thresholding methods should identify the pore region from the original real soil image.

---

[2] Due to a pixel size higher than the smallest pore, the partial volume effect implies that voxels can contain more than one phase which causes the difficulty of the segmentation step.

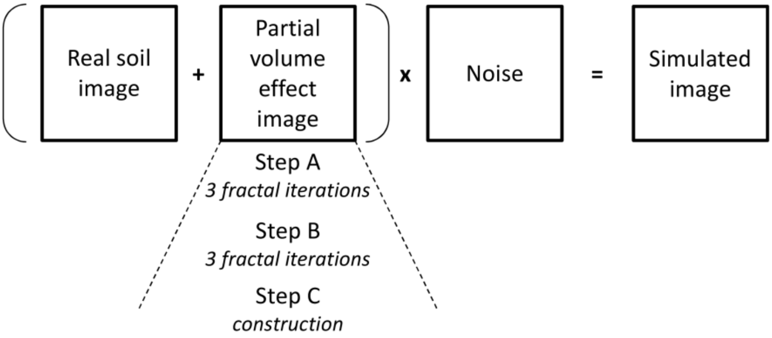

Figure 4. Detailed illustration of the simulated images construction.

The partial volume effect images were generated through the overlaying of decreasing resolution images as proposed by Wang et al. (2011). We did not use real soil images of multiples resolutions as Wang et al. (2011) did, we instead produced fractal images of decreasing resolution with a fractal generator based on the pore-solid fractal approach (Perrier et al., 1999). Many studies reported that the fractal concept provides a good description of the soil microstructure complexity (e.g. Kravchenko et al., 2011). Those images were then combined to form one partial volume effect image; Fig. 5 displays two examples of final simulated images.

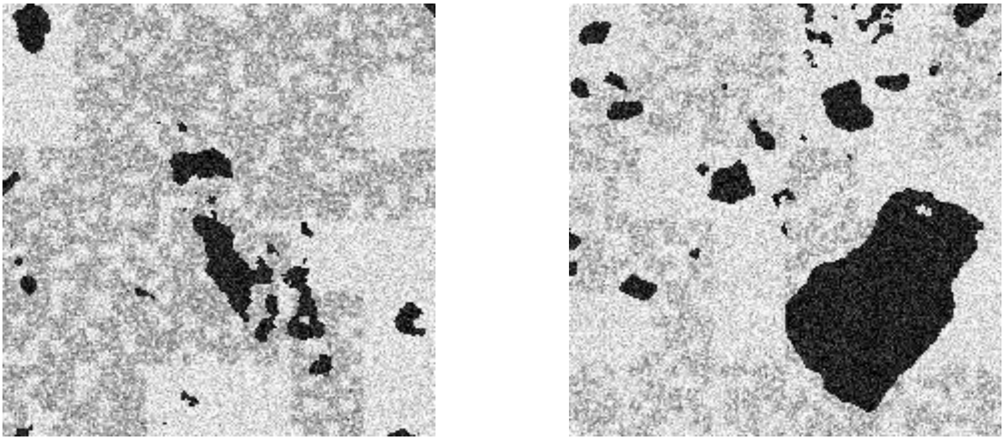

Figure 5. Examples of two simulated images.

2.3. Tested image processing and image features characterization

The complexity of segmentation is tied to the noise, artefacts and partial volume effects found in the grayscale images. Other sources of image degradation include ring artefacts, streak artefacts, high-frequency noise, scattered photons and distortions (Baruchel et al., 2000). We therefore firstly tested the effects of a pre-segmentation median filter on the segmentation quality. Median filters assign the median value of the neighboring pixels to the center pixel. These filters are less sensitive to extreme values and no grayscale value is created near the object boundary implying that the object edges are better preserved (Tuller et al., 2013). The use of a median filter before segmentation seems to be a common step within the field of soil X-ray CT images processing. Three levels were tested: no filter, filter with a radius of one pixel, filter with a radius of two pixels. After enhancing the image quality, choosing the right segmentation method is crucial. We tested three segmentation methods from the literature and adapted one. After all, a post-segmentation median filter was also tested on the simulated images (no filter or filter with a radius of two pixels). A post-processing clean-up was applied by removing the pore strictly smaller than 5 pixels in area, and the pore quantification was performed with the “Analyze Particles” tool available in the public domain image processing ImageJ (Schneider et al., 2012).

2.3.1. Global segmentation methods

The global thresholding method from Otsu (Otsu, 1979) was tested since it provides acceptable results according to Iassonov et al. (2009). Despite its potential non-reliability and the existence of more recent and more efficient methods, it is still a widely used method in the case of soil images, probably for its fast and easy-to-use implementation. This method automatically chooses a threshold based on the minimization of the intra-class variance between two intensity classes of pixels. It was performed with Matlab R2015a (MathWorks, UK).

As we have ground-truth information available, threshold that should be applied can be estimated. Through an iterative loop, the threshold that minimizes the difference between calculated porosity and ground truth porosity is selected and the value will serve as a benchmark. This procedure is based on the method from Beckers et al. (2014b). The Matlab R2015a (MathWorks, UK) code was provided by the authors.

2.3.2. Local segmentation method

The indicator kriging method (Oh and Lindquist, 1999) has provided good results in various studies (Peth et al., 2008; Iassonov et al., 2009; Wang et al., 2011; Houston et al., 2013b). Its variation “window-adaptive indicator kriging method” (Houston et al., 2013a) is however chosen because Houston et al. (2013a) concluded that the adaptive method requires less computational resources than the fixed one while providing very similar results. The indicator kriging concept relies on the selection of a threshold interval, TH1-TH2. All grayscale values below TH1 are set to 0 and all values above TH2 are set to 1. The values between TH1 and TH2 are assigned to a specific color, namely a phase, depending on their grayscale value and their classified neighboring pixels. The adaptive-window indicator kriging method adapts this neighboring area on the information locally available to cut the computational cost when possible. The method was applied with the author's software "AWIK". The choice of TH1 and TH2 was based on the edge detection using gradient masks method (Schlüter et al., 2010), option available within the AWIK software. From now on, we will refer to it as IK/GM.

The PBA method has shown to be satisfactory albeit revealing a lower performance than IK/GM (Beckers et al., 2014b). The weakness in IK/GM is the choice of the interval TH1-TH2. Schlüter et al. (2010) have proposed an improved automatic TH interval selection method, although it remains sensitive to noise. Therefore we wish to combine the physical robustness of the PBA method to the assumed precision of the IK method. The aim is to select a TH interval based on the global PBA threshold and then compute the IK method. This method was tested on the simulated images. We remind that the PBA method was used as a benchmark since we knew the exact porosity of the ground-truth image to be processed. From now on, we will refer to it as IK/PBA.

2.4. Results analysis

2.4.1. Performance indicators

We used the ground-truth information available to compute the misclassification error (ME), whose value is included between 0 and 1. It gives the proportion of pixel wrongly assigned to a phase. The value 0 reflects a perfect segmentation and the value 1 the opposite (Sezgin and Sankur, 2004):

$$ME = 1 - \frac{|P_0 \cap P_T| + |S_0 \cap S_T|}{|P_0| + |S_0|} \qquad \text{[Eq.1]}$$

Where P_0 is the number of pore pixel in the ground-truth image; P_T is the number of pore pixel in the tested image; S_0 is the number of solid pixel in the ground-truth image; S_T is the number of solid pixel in the tested image. We have chosen this simple indicator for its obvious interpretation and for the possibility of comparison with other studies (Wang et al., 2011; Schlüter et al., 2014). Similarly, we used the relative error on the calculated porosity as a performance indicator (RE_P). The calculated porosity is the ratio of black pixels (pores) over the total number of pixels.

Region non-uniformity (NU) is usually calculated to evaluate the segmentation quality without using ground-truth information (Wang et al., 2011). High intra-region uniformity is related to a suitable segmentation method because there is a similarity of property in the region element; the variance of that property is then adequate in expressing the uniformity (Zhang, 1996):

$$NU = \frac{P.\sigma_p^2}{T.\sigma^2} \quad \text{[Eq.2]}$$

Where P is the number of pore pixel; T is the total number of pixel; σ_p^2 is the gray values variance of the pore pixels in the original grayscale simulated image; σ^2 is the total gray values variance in the original grayscale simulated image. NU is a natural choice given the uniformity that the pore space should possess, although shows lower performance compared to ground-truth information based indicator (Zhang, 1996).

For each pore, we computed its shape factor as defined by Mason and Morrow (1990) (Eq. 3) where A is the surface area (pixel²) and P is the perimeter (pixel):

$$G = \frac{A}{P^2} \quad \text{[Eq.3]}$$

Depending on the G value, we calculated the specific dimensionless conductance of each pore (Patzek and Silin, 2001, Table 1). The dimensionless conductance $\tilde{g}$ multiplied by the squared cross-section surface area (A^2) and divided by the fluid viscosity (μ), gives the conductance g (L^5TM^{-1}):

$$g = \frac{\tilde{g}A^2}{\mu} \quad \text{[Eq.4]}$$

The volumetric flow rate through one pore is obtained by multiplying the conductance (g) by the fluid displacement driving force. In analogy with an electric circuit where resistances are summed in series, conductances are summed in parallel. We therefore multiplied each pore dimensionless conductance ($\tilde{g}$) by their squared surface area (A^2) in order to sum all the conductances (g) for each image which resulted in a global conductance. The relative error of the global conductance to the ground truth image was calculated for each image (RE_K). In addition, we calculated the dimensionless conductance ($\tilde{g}$) relative error of each pore (RE_g). RE_K and RE_g indicators were studied in absolute values.

Table 1. Dimensionless conductance (g) calculation depending on shape factor values (G).

G value	$G > 1/16$	$(3^{1/2})/36 < G < 1/16$	$G < (3^{1/2})/36$
Associated shape	Circle	Square	Triangle
Conductance	$\tilde{g} = 3/5.G$	$\tilde{g} = 0.5236.G$	$\tilde{g} = 1/2.G$

2.4.2. The methodological research question

To assess whether the quality of a segmentation method is altered by noise reduction, three-way ANOVA were implemented to test for significant differences in ME, NU, RE_P and RE_K for the various levels of noise reductions and the three different segmentation methods. Randomized complete block design was applied, the simulated images being the random blocks. In case of significant fixed interaction, two-way ANOVA were conducted for each segmentation method to test for significant impact of noise reduction on segmentation results. Tukey's post-hoc test was performed in case of significant effect ($p<0.05$).

Then to determine which combination of segmentation method and noise reduction performs the most accurately and whether IK/PBA brings improvement, four two-way ANOVA were implemented to test for significant difference in ME, NU, RE_P, RE_K between the combinations of segmentation method and noise reduction (10 levels). In case of significance ($p<0.05$), a post-hoc Dunnett test was conducted with IK/PBA as the control.

In each case, similar analyses of RE_g were conducted. However, since each pore has its own shape factor, all the 229 pores (for all 15 images combined) were each considered as a random block.

3

Materials & Methods: the field experiment

3.1. Introduction

The field experiment consisted in the measurements of sample-scale hydrodynamic properties and microscopic X-ray µCT extracted parameters on undisturbed soil samples of 35 cm³. The length ratio between sample size (3 cm in diameter) and scanner voxel size (21.5³ µm³) was around 1400, or 700 when the µCT images were resampled to a voxel size of 43³ µm³. This is a typical ratio value which allows the identification of most of X-ray µCT image characteristics (Vogel et al., 2010). The image characteristics were the soil pore space morphological and topological features, expressed in terms of "microscopic parameters". All of the visible soil porosity (the smallest visible pores were about 0.0004 mm³) was characterized and analyzed without distinction of origins (structural or biological) since hydrodynamic properties measurements were performed on the samples as a whole. The three research questions previously introduced are:

- <u>Research question #1</u>: Which microscopic parameters explain the best the soil hydrodynamic properties measured at the sample scale?
- <u>Research question #2</u>: How do the microscopic parameters evolve with resolution?
- <u>Research question #3</u>: How does the air-filled porosity vary with water matric potential?

Eventually, we also address a fourth research question regarding the likely origins of soil structure:

- <u>Research question #4</u>: How is the soil structure explained by organic carbon and iron content? At the origin of structure.

3.2. Soil sampling

The studied soil samples were taken from an agricultural field in Gembloux (Belgium) classified as a Cutanic Luvisol (WRB soil system, 2006) with the following averaged particle distribution: 14.3 % of clay, 78.3% of silt and 7.4% of sand. Sampling was performed within the summer 2015 (10 samples) and summer 2016 (14 samples) within four plots of a tillage-residue experiment (Fig. 6).

The tillage-residue experiment was conducted by Hiel et al. (2018) and the cultural practices between summer 2013 and summer 2016 are displayed in Table 2. Each sampling year, half of the samples were taken from the "conventional tillage" experiment, the other half from the "reduced-tillage" experiment. The objective was to observe a maximum variability of pore network structure between the samples and not to compare the experiment effects on the pore network. We therefore randomly named the samples according to a logical suite, going from #1 to #24.

After removing the vegetation, we manually drove the ertalon (plastic) cylinders (3 cm in diameter and 5 cm in height) into the soil until the top of the cylinder was at the surface level (Fig. 7) and we also manually excavated the cylinders to minimize the structure disturbance.

Figure 6. Aerial photography of the sampling field (50°56’N, 4°71’E).

Figure 7. Photographs illustrating the sampling. Cylinder dimensions are 3 x 5 cm.

Table 2. Performed cultural practices between 2013 and 2016 on the sampling field.

Date	Operation	Depth [cm]	CT	RT	Date	Operation	Depth [cm]	CT	RT
4/09/2013	harvesting		x	x	**20/04/2015**	nitrogen fertilization		x	x
25/11/2013	ploughing	-25	x		**22/04/2015**	sowing	-10	x	x
25/11/2013	sowing	-7	x	x	**28/05/2015**	weeding		x	x
11/03/2014	nitrogen fertilization		x	x	**27/07/2015**	sampling	-5		x
1/04/2014	weeding		x	x	**25/09/2015**	sampling	-5	x	
15/04/2014	nitrogen fertilization		x	x	**13/11/2015**	harvesting		x	x
15/04/2014	growth regulator		x	x	**7/12/2015**	stubble breaking	-10	x	x
25/04/2014	weeding		x	x	**7/12/2015**	ploughing	-25	x	x
27/04/2014	fungicide		x	x	**7/12/2015**	sowing		x	x
12/05/2014	nitrogen fertilization		x	x	**22/03/2016**	weeding		x	x
16/05/2014	weeding		x	x	**2/04/2016**	nitrogen fertilization		x	x
6/06/2014	fungicide		x	x	**22/04/2016**	nitrogen fertilization		x	x
4/09/2014	harvesting		x	x	**17/05/2016**	fungicide		x	x
12/09/2014	stubble breaking	-10	x	x	**19/05/2016**	nitrogen fertilization		x	x
16/09/2014	cover crop sowing		x	x	**8/06/2016**	fungicide		x	x
6/01/2015	ploughing	-25	x		**26/07/2016**	sampling	-5	x	x
17/03/2015	weeding		x	x					

3.3. Macroscopic measurements

Figure 8 presents the general frame applied to all the soil samples except for four of these which were only scanned at a water matric potential (*h*) of -70 kPa. The saturation was performed with distilled water and the characteristic soil water retention curves (SRWC) were measured using pressure plates (Richards, 1948 and DIN ISO 11274, 2012). After being weighed at the specified *h*, the air permeability of the samples was measured by applying an air flow across the sample and measuring the resulting inner-pressure with an Eijkelkamp air permeameter 08.65 (Eijkelkamp Agrisearch Equipment, Giesbeek, The Netherlands). As recommended by the constructor, each measure was repeated five times and kept as short as possible. Corey’s law was then applied to calculate the air permeability [ka, L^2]

(Corey, 1986 in Olson, 2001). The samples were also scanned at various steps of the SWRC; the X-ray microcomputed tomography procedure is developed in the next section. After reaching -1500 kPa, the soil samples were saturated once again and the saturated hydraulic conductivity (Ks [LT^{-1}]) was measured using a constant head device (Rowell, 1994) and applying Darcy's law. Finally, the soil samples were oven-dried at 105° for five days in order to obtain their dry weight. Porosity [L^3L^{-3}] was calculated as the ratio between the volume of water within the saturated soil sample and its total volume (McKenzie et al., 2002). From McKenzie et al. (2002), the bulk density (BD) [ML^{-3}] was deduced from the porosity value assuming a particle density of 2.65 g/cm³. Soil organic matter content was approached by the measure of the soil organic C content through the Walkley-Black (1934) method, and the mineral constituents of the soil phase were approached by measuring the Fe content because it was shown Fe was one of the most important substrate for the formation of organo-mineral associations (Eusterhues et al., 2005). The different forms of free Fe were extracted with 1) pyrophosphate of Na to provide the quantity of complexed Fe (Bascomb, 1984); 2) Oxalate NH4 to provide the quantity of complex and amorphous Fe (Blackmore et al., 1981); and 3) dithionite-citrate system buffered with bicarbonate (Mehra and Jackson, 1960) to provide the quantity of any free forms of Fe: complex, amorphous and crystalline Fe.

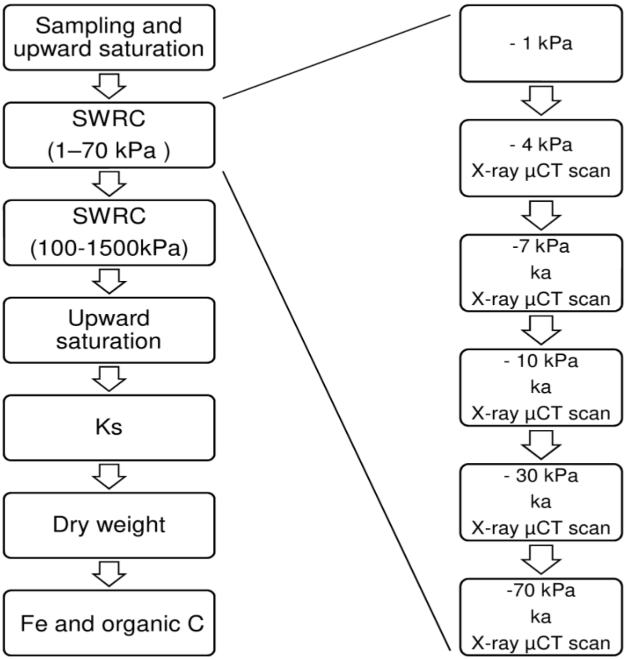

Figure 8. Macroscopic measurements applied to the soil samples.

3.3.1. Fractal dimension from the pore size distribution

The SWRC is usually used to extract the pore size distribution of the studied soil (Nimmo, 2004) by using the capillary theory which is the physical law linking a pore radius to a liquid potential:

$$r = \frac{2.\sigma.\cos(\alpha)}{\rho.g.h} \qquad \text{[Eq. 5]}$$

Where r is the pore radius (L), h is the water matric potential (L), σ is the liquid surface tension (MT^2), α is the contact angle between the liquid and the soil, ρ is the liquid density ($M\ L^{-3}$) and g is the gravitational acceleration ($L\ T^{-2}$). That equation can be simplified when the liquid is water:

$$r = \frac{30}{2.h} \qquad \text{[Eq.6]}$$

Where r is the pore radius (µm), and h is the water matric potential (m).

We then calculated the fractal dimension (Lab_FD) for each pore size distributions to characterize each sample SWRC with one value. The fractal dimension is a single value that is used to characterize the fractal geometry of objects. Fractal geometry states that an object has comparable features at different scales. The fractal dimension (FD) is power-law dependent (Mandelbrot, 1983) and Fig. 9 illustrates the following equation:

$$FD = \frac{\log(N)}{\log(1/r)} \qquad \text{[Eq.7]}$$

Where N is the constant number of transformed element at each iterations (from Eq. 7, N=2 in Fig. 9); r is the ratio between the dimension of the parent-element and the dimension of the transformed element (from Eq. 7, r=1/3 in Fig. 9). Figure 9 is a 1D fractal object (a line) and the FD should be included between 0 and 1 (FD = 0.631 in Fig. 9).

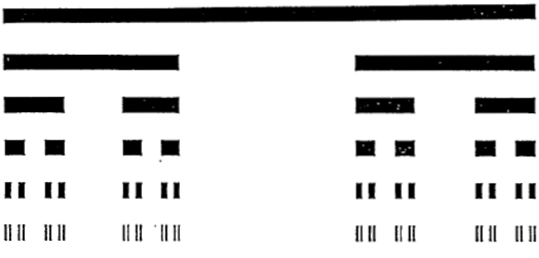

Figure 9. Cantor set (Source: Mandelbrot, 1983).

Since power-law dependencies are observed in soil science, researchers have applied the fractal geometry to study the soil behavior (Pachepsky et al., 2000). For example, Russell and Buzzi (2012) successfully derived a SWRC from the pore-size distribution FD of a silt loam soil. We obtained the Lab_FD from the slope of the linear relationship between the logarithmic radius *r* and the logarithmic cumulative volume of pores having a radius inferior to *r* (Xu, 2004). Because the soil samples are 3D objects, Lab_FD was obtained by subtracting the slope to 3.

3.4. Microscopic measurements: image acquisition, processing, soil features characterization

The soil samples were scanned using a Skyscan-1172 desktop micro-CT system (Bruker microCT, Kontich, Belgium). We refer to our **Paper II** for more information about the scanning parameters and general image processing information, that latter was conducted from the results obtained in our **Paper I**. In the end, the 3D soil X-ray µCT images had a voxel size of 21.5^3 µm^3, however resampled to 43^3 µm^3 for computational savings. From the result of our **Paper I**, we applied the global porosity-based segmentation method developed by Beckers et al. (2014b). The obtained porosity on the X-ray µCT images was compared to the estimated soil sample visible porosity, which was the air-filled porosity at a water matric potential *(h*) of -1 kPa (Lab_PO, equivalent radius of 150 µm according to capillary law) and was calculated from the voxel size information (43^3 µm^3). A visual inspection was performed to evaluate the segmentation quality and, in case the porosity-based segmentation method failed, Otsu's segmentation was used (method previously described). A post-segmentation clean-up was applied by removing any pores smaller than five voxels. To quantify the pore network topology and the pores morphology, we used the Avizo® 9.2 software, where codes developed by Plougonven (2009) are integrated, and the free ImageJ software (Schneider et al., 2012) where the MorphoLib plugin (Legland et al., 2016) was used to perform a five voxels post-segmentation clean-up followed by the BoneJ plugin (Doube et al., 2010) for parameters calculation. Table 3 presents the calculated microscopic parameters that are commonly studied in soil science researches using X-ray µCT, which however often work with voxel sizes a thousand times bigger in volume than the one from this dissertation. We therefore also calculated the large porosity (Large_PO) to be comparable to those results. In addition, we calculated the average pore size of the smallest and biggest pores (Avg_Svol and Avg_Bvol). The limit between the smallest and biggest pores was invariant between samples: 10% of the number of pores accounted for 90% of the total pore volume. These biggest pores were mainly large macropores and fractures that have likely contributed the most to water and air fluxes.

The microscopic parameters presented in Table 3 were calculated for all soil samples scanned at h = -70 kPa, the parameters with a star were calculated for all soil samples scanned at various *h*. For 16 pore size classes distributed between 30 and 1500 µm in radius, we calculated several microscopic parameters for the pores enclosed within the classes (written in italic in Table 3). We therefore had 17 values of those selected microscopic parameters (16 classes + 1 global). Figure 10 displays a 2D schematic view of a pore network to represent the coordination number (Z), the redundant connections concept (Euler number), an isolated pore, and the pore chambers and throats and associated names from ImageJ. In the end, we applied the capillary theory (Eq. 6) to the pore-size distribution extracted from the X-ray µCT images, assuming the pores were elliptic (Beckers et al., 2014a) and calculated the SWRC from X-ray µCT data by adjusting the pore volumes to the total laboratory porosity.

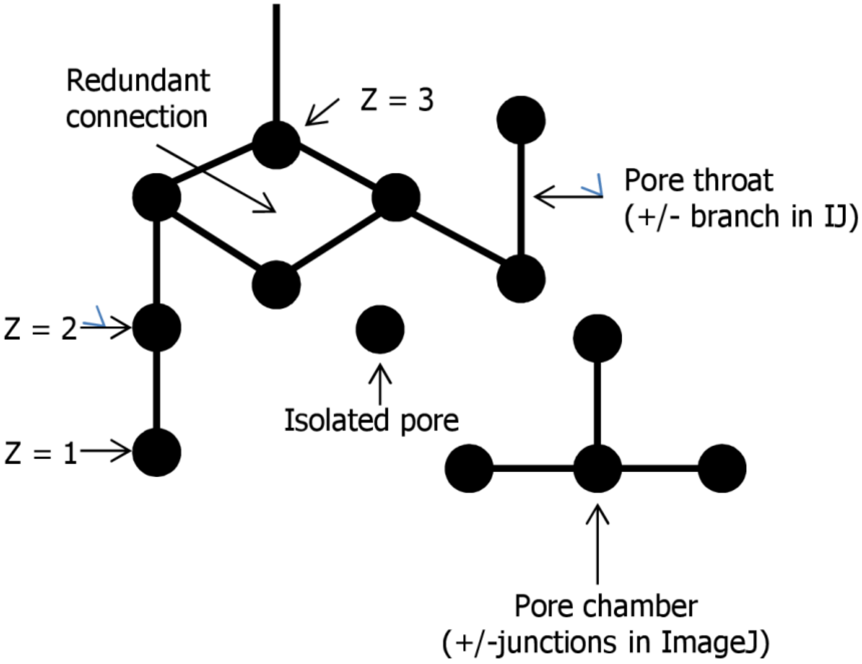

Figure 10. 2D schematic view of a pore network with several microscopic parameters represented.

Table 3. PartI. Calculated microscopic parameters on the X-ray µCT images and their definition. Only the parameters with a star were calculated for all soil samples at various water matric potentials. The parameters with an italic font were calculated by pore size range.

	Microscopic parameter (abbreviation, metric)	**Definition**
Avizo	_Porosity*_ (**µCT_PO**, %)	Ratio of pore voxels over the total amount of voxels
	Large porosity (**Large_PO,** %)	Part of the porosity composed by pores of at least 1000 voxels
	Number of pores (**NP**, -)	Total number of pores
	Averaged pore volume* (**Avg_vol**, mm^3)	Ratio of the total volume of pores over the number of pores
	Averaged pore volume of the biggest pores* (**Avg_Bvol**, mm^3)	The biggest pores are the ones that account for 90% of the pores volumes by only representing 10% of the number of pores
	Averaged pore volume of the smallest pores* (**Avg_Svol**, mm^3)	The smallest pores are the ones that account for 10% of the pores volumes by representing 90% of the number of pores
	Proportion of isolated pores (**IP**, %)	Ratio of the number of pores that have no connection over the total number of pores
	Proportion of isolated porosity* (**IPO**, %)	Ratio of the isolated porosity over the total porosity
	Averaged coordination number* (**Avg_Z**, -)	The average of Z which is the number of connections at one point (Perret et al., 1999)
	Averaged surface connectivity* (**SC**, L^{-1})	The average of sc which is sc = Nc * Ac / Vp, where Nc is the number of connections, Ac the mean surface area of the connections (L^2) and Vp the pore volume (L^3)
	Total connected surface (**Con_surf**, mm^2)	The sum of each pore's connected surface
	Specific surface* (**SS**, m^{-1})	Sum of the specific surface of each pore which is the ratio of the pore surface area over its volume.
Avi. zo+ IJ	Global connectivity * (**Γ**, -)	The sum of each pore's volume squared divided by the total volume of pores. It measures the probability that two pores voxel are part of the same pore (Renard et Allard, 2013).

Table 3. Part II. Calculated microscopic parameters on the X-ray µCT images and their definition Only the parameters with a star were calculated for all soil samples at various water matric potentials. The parameters with an italic font were calculated by pore size range.

	Microscopic parameter (abbreviation, metric)	**Definition**
Image J	Total length of the pore network* (**L**, m)	After skeletonization, it is the sum of all the branches length
	Total number of branches (**B**, -)	After skeletonization
	Total number of junctions (**J**, -)	After skeletonization
	Degree of connectivity (**N/J**, -)	Ratio of the number of branches over the number of junctions. As negative is the ratio, as connected is the medium
	Global tortuosity* (**τ**, mm^{-1})	The geometric tortuosity between two points is the ratio between the effective pore path and the shortest distance between the two extreme points (Perret et al., 1999). We calculated the global tortuosity (τ) of the pore network as the average of the tortuosity of each branch
	Fractal dimension* (**FD**, -)	FD was calculated with a box-counting algorithm (Perret et al., 2003).
	Degree of anisotropy* (**DA**, -)	The value of DA is between 0 and 1, 0 for an isotropic medium. DA was calculated with the mean intercept length method (Harrigan and Mann, 1984)
	Euler number* (**ε**, -)	The Euler number is a quantification of the connectivity. Originaly calculated as ε=N-L+O, where N is the number of isolated objects; L is the number of redundant connections and O the number of cavities or holes (Vogel et al., 2010). As negative is the Euler number, as connected is the medium
	Lowest Euler number (**Min_ε**, -)	The Euler number of the largest connected component of the pore network

3.4.1. Degree of anisotropy

We briefly present the degree of anisotropy (DA) that is a little trickier to apprehend. DA is quantified with the mean intercept length (MIL) method. The point is to calculate the MIL for a large number of vectors of equal length originating from a random point within the studied volume; interceptions were counted when the vector hit a boundary between foreground and background. A cloud of MIL-points is built up; an ellipsoid is fitted to the cloud; the anisotropy tensor is constructed and its subsequent eigendecomposition results in eigenvalues which are characteristics of the orientation of the ellipsoid. The smallest eigenvalue come from the longest MIL which mean that the vectors going in that direction didn’t hit a lot of boundaries between the two phases. Therefore, a long MIL in one direction could be interpreted as a small amount of pores in that direction, or as the direction of the preferential orientation of one large pore. A long MIL could also be understood as the consequence of the pores directions but calculating one principal direction is not straightforward. Figure 11 shows an example of the 3D visualization of MIL vector cloud for one sample, and the 3D representation of the pore space sample aligned to the anisotropy tensor. Instead of being parallel to the Z-axis, the 3D representation of the sample is slightly inclined along the x-axis although, for this sample (#13) the main direction of the smallest eigenvalue was along the z-axis (Results section).

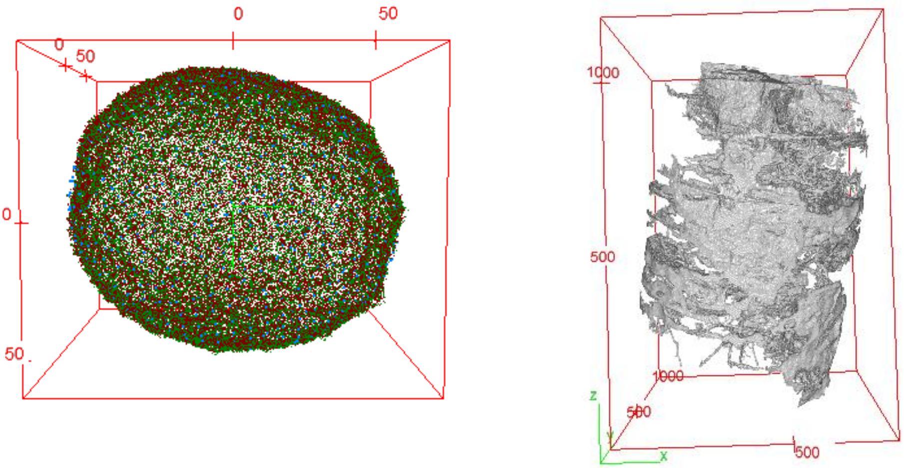

Figure 11. Left-hand: 3D visualization of the mean intercept length vector for one sample. Right-hand: 3D representation of the same sample air-filled pore space aligned to the anisotropy vector.

3.5. Results analyses

For clarity, we divided this section in paragraphs regarding the performed analyses to answer each of the research questions presented in the introduction.

3.5.1. Research question #1

Our first research question deals with the relationships between the microscopic parameters extracted from the X-ray µCT images and the macroscopic laboratory measurements. The microscopic parameters values and their interconnections were also extensively studied. To these purposes, the data set was split into a calibration set (samples #1 to #18) and a validation set (samples #19 to # 24). Basic descriptive statistics were firstly performed on the macroscopic and microscopic data. The correlation coefficients (ρ) between the different microscopic parameters of the calibration data set were then calculated using Bayesian statistics to account for data uncertainty. The advantage of using Bayesian statistics is that the credibility ("significance" in frequentist statistics) of the test is based on the data value and not on the number of observations which implies that a "statistically small" number of observations can be representative of the population. Another advantage of Bayesian statistics is the possibility to quantify the evidence for the null hypothesis whereas a "non-significant" test in frequentist statistics could also come from a noisy data set. The Materials & Methods section of our **Paper II** reports more information about the use of Bayesian statistics. The correlation coefficients were calculated with an associated Bayes factor (BF) which quantifies the credibility of the correlation. Adapted from Jeffreys (1961) in Wetzels and Wagenmakers (2012), BF's larger than 100 are interpreted as decisive evidence for a non-null correlation coefficient; BF's between 30 and 100 as a very strong evidence, BF's between 10 and 30 as a strong evidence, BF's between 3 and 10 as a substantial evidence and BF's below 3 as an anecdotal evidence. The evidences for a null correlation coefficient are quantified through BF's value inferior to one (1/100; 1/30; 1/10; 1/3). In addition, we performed a principal component analysis (PCA) with all the microscopic parameters as *variable*s, and the samples as *individuals*. We then evaluated the relationships between the micro-and macroscopic measurements by calculating Bayesian ρ for the calibration data set. We afterwards established a Bayesian linear regression design to extract relationships between micro- and macroscopic measurements. All combinations between Y and $X_1 + X_2$ were tested and regression models were compared against the same models without the explaining variable (ratio) which resulted in a BF value. In Bayesian statistics, the starting point is not to identify the best regression equation but rather evaluate the unknown values of the equation explaining variables and intercept. We did it through the quantification of the 25 and 75% quantiles. Afterwards, we aimed at predicting the validation data points through the use of the slopes and intercepts posterior 50% quantile.

The relative root mean square errors (RRMSE) were calculated as follows:

$$RRMSE = \sqrt{\frac{1}{n}\sum_{i=1}^{n}\left(\frac{d_i - D_i}{D_i}\right)^2} \quad \text{[Eq. 8]}$$

Where n is the number of data points, d_i is the predicted data point and D_i the observed data point.

3.5.2. Research question #2

As stated in the introduction, the results of the image features characterization ultimately depends on the scanning parameters, the image processing (**Paper I**), the image feature characterization software (**Paper II**), but also on the resolution at which the soil is visualized and studied. We explored different options to characterize the soil with a higher resolution and to compare the resulting extracted microscopic parameters. The obtained results were compared to the main results from our **Paper II**. One sample was concerned, sample #12.

3.5.2.1. Exploration of the pore size dependency

The extrapolation of the microscopic parameters to smaller voxel size than the scanned voxel size is at high computational cost but could provide endless possibilities. The concept relies on the hypothesis that the microscopic parameters would vary similarly if measured with larger or smaller voxel sizes.

To simulate a higher scanning resolution, we calculated several microscopic parameters described in Table 3 for the X-ray µCT image of the sample #12 by gradually not taking into account the smallest pores. Figure 12 displays a schematic pore space view with growing minimal pore size, from a. to d. The next step was to evaluate the relationship between the microscopic parameters values and the minimal pore volume taken into account to, afterwards, use the equation to estimate the microscopic parameters for an infinitely small pore volume. The minimal pore sizes were 10 to 610 voxels by steps of 100. These steps were chosen from a sensitivity analyses. We previously introduced the separation of the pore size distribution into two categories: the small pores and the big pores, and the limit between the categories for sample #12 was a volume of 610 voxels. Only porosity indicators (µCT porosity, the fractal dimension, the pore network length, the number of pores and the average pore volume) were extrapolated from the relationships between microscopic value and minimal voxel size. We did not try to fit a model of the µCT porosity versus the minimal pore volume to reach the total laboratory porosity because we are interested in the structural porosity which is conductive as opposed to the textural porosity (Nimmo, 2004). We did not extrapolate connectivity indicators because the number of connections drastically decreases with small pores. On one hand, the connections are smaller than the pores and are therefore invisible, on the other hand, the larger is a pore, the more connected it is. That would lead us to either fit a model from observed data and ending with an almost null connectivity, or to fit a model from only the largest pores connectivity which is far from the extrapolation region.

The fitted models between minimal volume and parameters were empirically tested and we eventually used a flexible power-law model. The residuals presented a U-shape but their values were between 1% to 0.1% of the fitted values, we therefore considered that extrapolation, from this model and for this specific example, could work. Extrapolation relies on untestable assumptions about the behavior of data and we should keep in mind the stated hypotheses and case study.

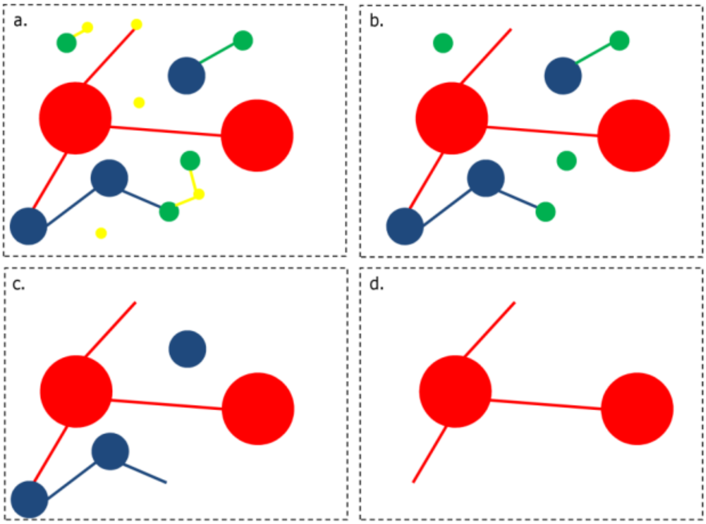

Figure 12. Schematic visible pore network with a growing visible minimal pore size (from a to d).

3.5.2.2. Analysis of X-ray images at 21.5^3 µm^3 voxel size

All the microscopic measurements previously described were performed on the X-ray µCT images scanned at a voxel size of 21.5^3 µm^3 and rescaled to 43^3 µm^3 for computational savings. Microscopic features characterization was therefore also done at the original resolution for the sample #12. The same image processing was applied, besides the resampling and the pre-segmentation median filter. To have similar noise levels on both X-ray µCT images, we applied a 4 pixels radius 3D median filter instead to a 2 pixels radius 3D median filter as for the 43^3 µm^3 voxel sizes X-ray µCT images, Fig. 13 presents a theoretical explanation. Houston et al. (2013b) also observed that using finer resolution images increased the visible noise. Extra attention should be brought to the segmentation step since reliable comparisons of binary images depend on that specific procedure (Houston et al., 2013b; Shah et al., 2016). We applied the same porosity-based segmentation method with the same physically-based porosity (Lab_PO) value to reach. The microscopic parameters as described in Table 3 were calculated except the ones that were concluded irrelevant from the results of our **Paper II.**

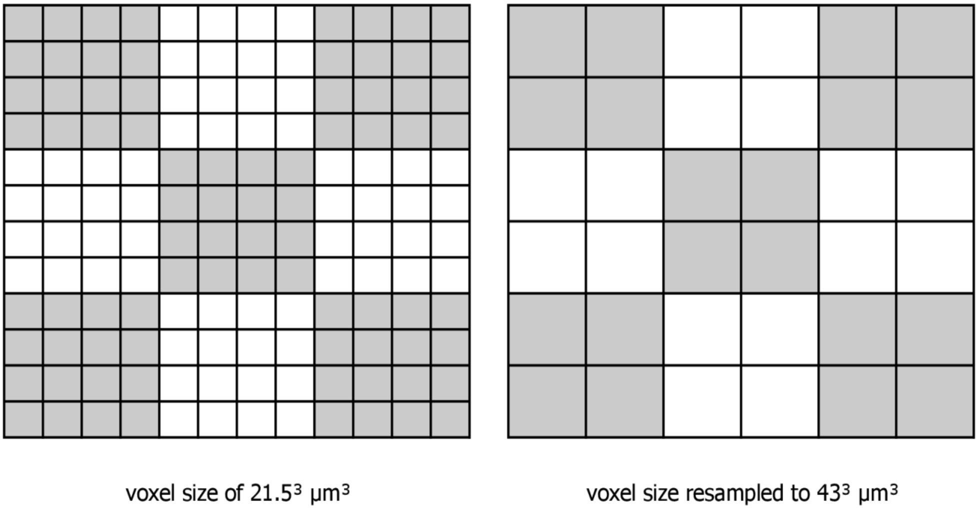

Figure 13. Representation of the pixels distribution of two images with different voxel size.

3.5.2.3. Analysis of an aggregate: X-ray microtomography

We extracted an aggregate from the sample #12 (methodology from Gao et al., 2017) which was scanned at the highest possible resolution; scanning time was not an issue since only one aggregate was scanned for exploratory purpose. The X-ray source was set at 100kV and 100µA and an aluminum-copper filter was used to reduce the beam hardening artefacts in the reconstruction. The rotation step was set at 0.15° over 360° and, to improve the signal-to-noise ratio, the average of 5 projections was recorded at each rotation step. The exposure time was 600 ms. We adjusted the detector configuration (16-bit X-ray camera with 4 × 4 binning, creating 1000 x 666 pixel radiograms) and the distance between the camera and the soil sample to obtain radiographs with a pixel size of 8.99 µm. The image was also reconstructed using the NRecon® software, freely provided by Bruker without the misalignment compensation and with a ring artefact correction of 7. The global Otsu method was applied to binarize the 3D image and the same parameters as presented in Table 3 were calculated.

3.5.2.4. Analysis of an aggregate: Desorption Vapor Sorption

After the X-ray µCT scanning, the desorption-sorption curve of the soil aggregate was measured using a Desorption Vapor Sorption apparatus (DVS). The concept is to place the studied material (the soil aggregate) in an atmosphere-controlled chamber where the relative humidity is gradually increased and afterwards gradually decreased. Temperature can be controlled too and we performed an isotherm experiment. The studied material is weighted at specified time-steps (5 min in our case) to evaluate if the equilibrium between the materials and the atmosphere is reached. The studied soil aggregate initial weight was 69.41 mg and about 5 mm long. The results were mass variations versus atmosphere relative humidity which can be transformed to calculate the material saturation according relative humidity. To extract a pore size distribution, we applied the Kelvin-Laplace's law, which relies on the capillary theory, to link a pore radius to a water potential (relative humidity of the atmosphere):

$$r = -\frac{4\gamma.M}{2R.T.\rho.\ln(RH)} \qquad \text{[Eq.9]}$$

Where R is the perfect gas constant [$IN^{-1}\theta^{-1}$], T the absolute temperature [θ], ρ the volumic mass of water [ML^{-3}], M the molar mass of water [MN^{-1}], Υ the superficial tension [MT^{-2}], RH the relative humidity [MM^{-1}], and r the pore radius [L].

3.5.2.5. Result analyses

On one hand, we compared the pore repartition versus the pore radius for the following data obtained from the sample #12 (Table 4).

Table 4. Enumeration of the available data to evaluate the resolution effects on the calculated microscopic parameters.

Sample scale	**Aggregate scale**
X-ray µCT images at 43^3 µm³	X-ray µCT images at 8.99^3 µm³
X-ray µCT images at 21.5^3 µm³	
Retention curve with pressure plates	Desorption curve with DVS

For comparisons between measurement methods, we calculated the function of the logarithmic desaturated pore radius r^i at the i-th step of desaturation according the following equations, adapted to pore radius from Rougelot et al. (2009):

$$pr\left(r^{i+1}\right) = \frac{S_W(r^i)-S_W(r^{i+1})}{\log(r^i)-\log(r^{i+1})} \qquad \text{[Eq.10]}$$

Where pr is the pore repartition, S_w is the saturation in water at radius r^i. The pore radius at 100% of relative humidity is 371 µm for the desorption curve, and 1534 µm for the retention curve obtained from the X-ray µCT measurements of the soil aggregate and soil sample, respectively.

On the other hand, we compared the resulting microscopic parameters extracted from the sample X-ray µCT images at a voxel size of 43^3 µm³ (previous section), and of 21.5^3 µm³ to the extrapolated microscopic parameters and to the microscopic parameters from the aggregate X-ray µCT image. For non-relative parameters, such as the number of pores or the total network length, we multiplied the value obtained for the aggregate by the ratio of the sample volume over the aggregate volume in order to be comparable. Then, we computed the value of the extrapolated parameters for a minimal volume of 49692 µm^3 (minimum five voxels at a resolution of 21.5 ^{3}µm^3); 3633 µm^3 (minimum five voxels at a resolution of 8.99^3 µm^3); 8000 µm^3 (minimum one voxel at a resolution of 20^3 µm^3); and 1 µm^3. The value of 8000 µm^3 was chosen as the limit defined by Nimmo (2004) to characterize conducting porosity.

3.5.3. Research question #3

For our third research question, we hypothesize that more than the pore volume, is the pore space accessibility relevant for the pore space draining. To that purpose, we scanned the same soil samples at various water matric potentials (*h*, from -4 kPa to -70 kPa). From the voxel size of our images (43^3 µm^3 and minimum 5 voxels for a pore to be taken into account) and the capillary theory (at -4 kPa, pores with radius of 75 µm should have drained), we shouldn't see any differences between these X-ray µCT images. We although analyzed the variations in pore space from a global point of view by comparing global microscopic parameters between the X-ray µCT images of the same samples scanned at various *h*. We also calculated microscopic parameters for pores included between two sizes boundaries. The aim was to identify whether pores of a particular size were more prompt to morphological changes with *h*.

3.5.3.1. Global parameters

The same parameters as Table 3 were calculated (with a star). To answer the question whether the global parameters differ for the same sample at various *h*, we performed two-way ANOVA for each global parameters and post-hoc Tukey tests in cases of significance. Two-way ANCOVA were afterwards performed to evaluate the effects of the hydrodynamics parameters (Ks, ka, and Lab_FD) on the significance of the previously performed ANOVA. The microscopic parameters were then also used as covariates. The ANCOVA relative efficiency (ratio of residual squared means) was calculated in cases where the addition of a covariate adjusted the means in a way that led to non-significant differences between *h*. Afterwards, a PCA was conducted to identify similarities between individuals (one individual is one sample scanned at one *h*), as well as a K-clustering analysis to quantitatively validate the spatial results obtained from the PCA.

3.5.3.2. Local parameters

The local parameters are the several microscopic parameters (in italic in Table 3) calculated for a specified portion of pores, between a minimal and a maximal radius. To assess whether the local microscopic parameters by pore size ranges are different between *h*, we conducted three-way ANOVA followed by two-way ANOVA for each pore size range in case of significance. Post-hoc Tukey tests were afterwards performed.

3.5.4. Research question #4

Shortly, the organo-mineral associations stabilize the soil organic matter by protecting it from decomposition and are the main forming soil structure agents through the formation of soil aggregates (Oades, 1988; Kleber al., 2015). This dissertation aims at unraveling the relationships between soil structure and soil hydrodynamic properties, these sub-section deals with the origin of the soil structure: how the microstructure could be explained by the organic carbon and iron soil content. We therefore firstly investigated the relationships between the soil total organic carbon (TOC) content and the amorphous and crystalline Fe oxyhydroxydes estimated by oxalate and DCB extractions, respectively, with Bayesian correlations. We further compared the TOC and Fe contents to the microscopic parameters measured on the X-ray µCT images (Table 3). The soil organic and mineral phases are spatially and temporally variable; the performed analyses aimed solely at providing first insight within this subject.

4

Results & Discussions: the methodological experiment

The extensive result analysis is presented in our **Paper I**; we here recall the main findings of this experiment which consisted in statistically comparing noise reduction filters and segmentation methods effects on the final resulting binary images. Three pre-segmentation noise reductions were tested through the application, or not (PRE0), of a median filter of radius of one pixel (PRE1) or two pixels (PRE2). Two post-segmentation noise reductions were tested with the application, or not (POST0), of a two pixels radius median filter (POST2).

4.1. Pre-segmentation noise reduction

Figure 14 shows an example of a. a grayscale image to be segmented, and the same image, segmented with b. Otsu method, c. PBA method, and d. IK/GM method. There was no application of median filter (PRE0 and POST0). We observed, not all the images are shown, that Otsu and IK/GM methods, without pre-segmentation filter, performed well for some images but poorly for others, and the PBA method always performed well with misclassification error indicators (ME) below 1% and non-uniformity region indicators (NU) below 5%. In this case, where the exact porosity to reach was known, noise reduction did not improve the PBA method. This is consistent with the working principle of PBA and with our experimental conditions. Figure 15 shows the ME, NU and relative error on porosity (RE_P) averaged for the 15 simulated images. With the Otsu and IK/GM methods, the PRE1 noise reduction filter improved the segmentation accuracy because a decrease in indicator value meant an increase in segmentation accuracy. Compared with the results obtained by Hapca et al. (2011), Wang et al. (2011) and Schlüter et al. (2014), the ME and NU values for PRE1 and PRE2 were satisfactory. Statistical analyses confirmed that the PRE1 filter significantly improved segmentation accuracy with the Otsu and IK/GM methods in terms of ME. With regards to NU, there was a significant difference between the three Otsu method results (PRE0-PRE1-PRE2), but post-Tukey’s test was not able to determine the source of the difference. Similarly, PRE0 to PRE1 and PRE0 to PRE2 were significantly different for IK/GM methods, but, in contrast, RE_P significantly differentiated PRE0 to PRE1 and PRE0 to PRE2 for Otsu method, but not for IK/GM method. These contrasting results illustrate the variability in indicator definitions and reflect the working principles of the global and local methods. Otsu segmentation method results in different porosity values by identifying porosity within the soil matrix where grayscale values are low (porosity is represented by black pixels). This leads to porosity without physical meaning, as noted by Hapca et al. (2011). IK/GM identifies the right pore-region, but the limits might not be accurate. Therefore, despite a high grayscale value, some pixels were taken into account, which increased grayscale value variance and subsequently NU.

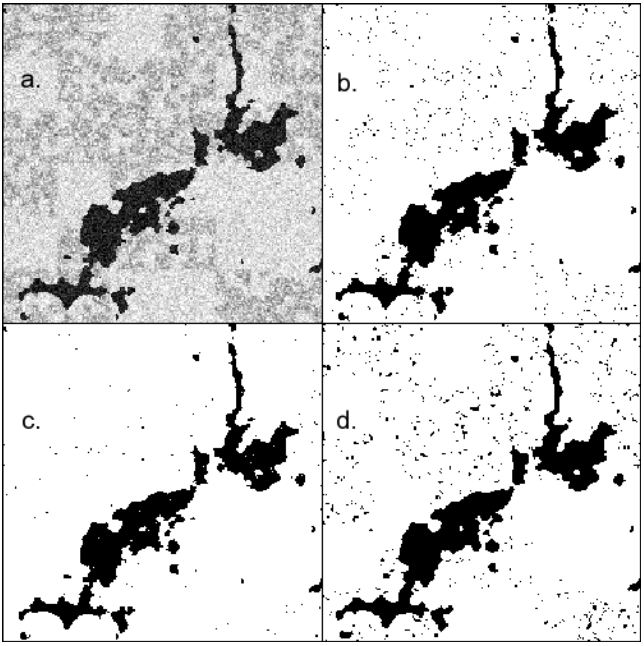

Figure 14. Image #10 at various steps: (a) simulated image 10; (b) Otsu segmentation; (c) PBA segmentation and (d) IK/GM segmentation. There was no application of a pre-segmentation filter.

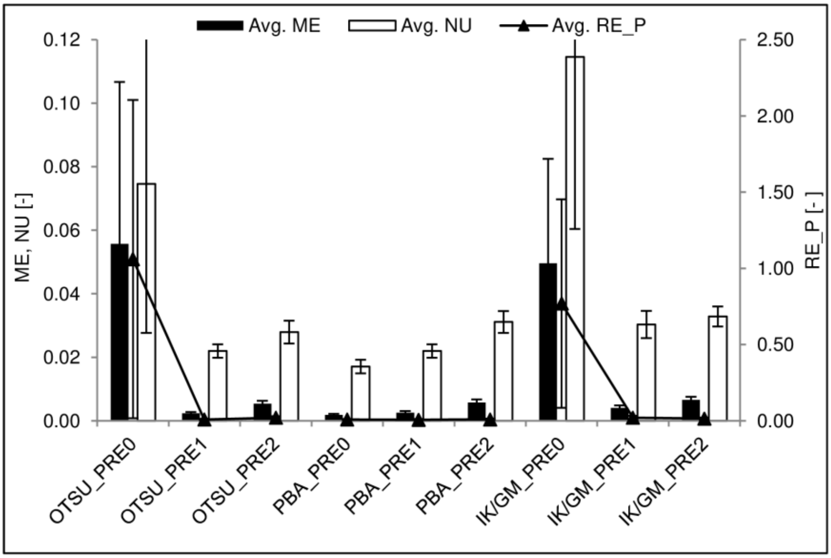

Figure 15. Averaged misclassification error (ME), region non-uniformity (NU) and porosity relative error (RE_P) for all segmentation methods (Otsu, PBA, IK/GM) and for all pre-segmentation noise reductions (PRE0, PRE1, PRE2)

Statistical analyses did not report significant differences between the two levels of pre-segmentation noise reduction filters (PRE1 and PRE2). We however observed that neither Otsu nor IK/GM associated to a PRE2 level of noise reduction provided the best performances. The added noise on our simulated images is uncorrelated and PRE2 noise reduction seemed to be disproportionate and destroyed true information. Figure 16 shows the resulting images after the Otsu and IK/GM segmentation for both noise reductions. Black pixels represent the pores that match the ground-truth information, the blue pixels represent pixels that are allocated to soil matrix but should have been allocated to pore and the red pixels are the one allocated to pore but shouldn't have been. With the Otsu method, from PRE1 to PRE2, small features are removed (blue pixels) and bigger pores have growing edges (red pixels). The differences between PRE1 and PRE2 for IK/GM method are less striking albeit the histogram bimodality is sharpened. This is however consistent with the study reported by Houston et al. (2013b), where they found that Otsu method gave a greater mean difference between two noise reduction levels than IK.

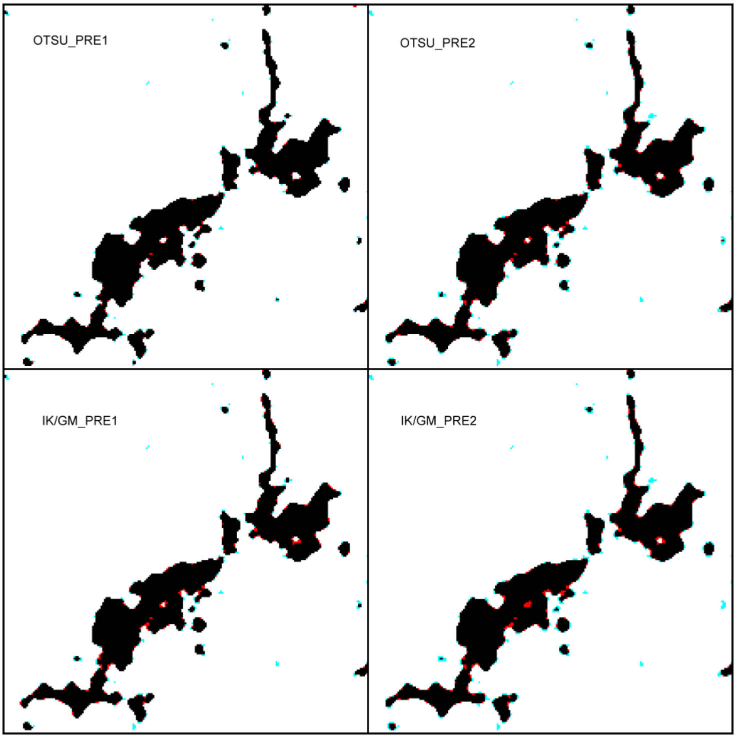

Figure 16. Resulting Image #10 after the OTSU and the IK/GM segmentation methods for two level of pre-segmentation noise reduction (PRE1, PRE2). Black pixels represent the pores that match the ground-truth information, the blue pixels represent pixels that are allocated to soil matrix but should have been allocated to pore and the red pixels are the one allocated to pore but should not have been.

4.2. Post-segmentation noise reduction

Post-segmentation noise reduction always alters the pores edges and we conducted our analyses through the use of performance indicators based on the pores conductance (RE_K) and shapes (RE_g). No matter the pre-segmentation noise reduction applied, RE_K was indeed always higher with a post-segmentation noise reduction than without. Statistical analyses of RE_K confirmed that applying a post-segmentation noise reduction without any pre-segmentation noise reduction (combination PRE0-POST2) lead to a significant higher averaged relative error when compared to any combination of pre-segmentation noise reduction (PRE0-PRE1-PRE2) without post-segmentation noise reduction (POST0). The left plots of Fig. 17 display the main effects plots for RE_K.

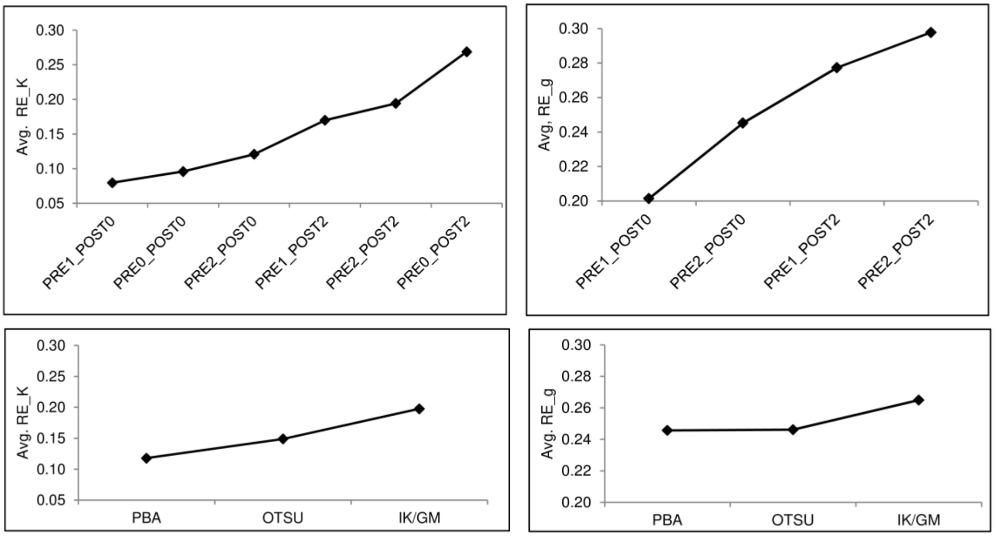

Figure 17. Left-hand: Main effect plots for the conductance relative error (RE_K). Right hand: Main effect plots for the shape factor relative error (RE_g). The upper graphs display the pre-segmentation (PRE0, PRE1, PRE2) and post-segmentation (POST0, POST2) noise reductions combinations as variables. The lower graphs display the segmentation methods as variables (PBA, Otsu, IK/GM).

In contrast to RE_K, there were no significant differences among segmentation methods or the noise reduction levels in RE_g values. The right plots of Fig. 17 display the tendency between noise reduction levels and segmentation methods with regards to RE_g. We did not compute the PRE0 results because some pores had merged with OTSU and IK/GM and relative errors would increase without meaning.

4.3. Segmentation methods

Pre-segmentation noise reduction affects the grayscale histogram shape and therefore the global and interval TH values, as illustrated with Fig. 18. The global TH obtained with Otsu method firstly decreased from PRE0 to PRE1 and then increased from PRE1 to PRE2. There was indeed a right-hand shift in the lower-part of the soil matrix peak (Fig. 18). At noise reduction PRE1, the Otsu and PBA methods even had an identical TH. This could therefore be seen as a satisfactory noise reduction for global methods since these two methods were then equivalent. Figure 14 however previously showed that the PBA segmentation method was not perfect, highlighting the main disadvantage of the selection of one threshold value for an entire 2D (or 3D) image. The lower plots of Fig. 17 also show that the Otsu and PBA methods had almost the same mean because global TH variation would lead to porosity variation within the soil matrix, but less around the pore region edges.

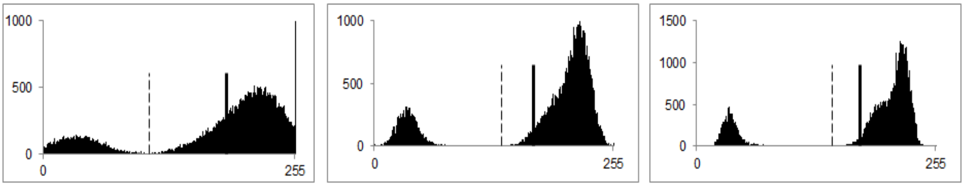

Figure 18. Image #14 grayscale histograms with different pre-segmentation noise reductions. Left to right: PRE0, PRE1, and PRE2. The dotted line represents the global threshold obtained with PBA segmentation method; the plain bold line represents the upper threshold obtained with IK/GM segmentation.

Local segmentation methods have the benefit of usually not identifying pore regions where there is none but the pore boundaries might not be accurately identified, as stated earlier. In terms of RE_K values, IK/GM method was indeed significantly different from the PBA method which was used as a benchmark. Moreover, IK/GM method never performed the best in terms of absolute values of performance indicators. Local segmentation methods are totally dependent on the initial choice of TH interval which in turn, for the gradient mask method, is dependent of the histogram shapes. Figure 18 shows that the TH interval boundaries tended to decrease from PRE0 to PRE1 and PRE2. The IK/GM method performed better with pre-segmentation noise reduction and, in these cases, the TH interval included the global TH from OTSU and PBA. From these observations, we investigated the choice of a TH interval around the global TH computed by PBA (IK/PBA method) to combine the precision of a local method to the robustness of the global PBA method.

4.4. Testing the relevance of IK/PBA

To perform a sensitivity analysis of the TH interval impact on the indicator kriging (IK) method, the TH interval around the global TH selected with PBA ranged from +/-10 to +/-50%. We found that the ME indicator remained unchanged for the intervals +/-10, +/-20 and +/-30%. After that, ME increased constantly, reaching about 25% of the initial ME value at the +/-50% interval. For the following operations, we present only the segmentation results with a +/-10% TH interval. First, the ME, NU, RE_P and RE_K values were all in the same range as those from PBA or OTSU_PRE1. The statistical analyses confirmed this trend by showing only OTSU_PRE0 and IK/GM_PRE0 (which were no good performers) as significantly different from IK/PBA in terms of ME, NU and RE_P. When including post-segmentation noise reduction, RE_K analysis showed that post-segmentation noise reduction did not produce a significantly different result with IK/PBA. According to RE_g, IK/PBA gave the best results and differed significantly from any other combination of method and noise reduction. IK/PBA therefore produced the correct binary images without the use of a noise reduction process (as opposed to OTSU_PRE1) and without knowing the real characteristics of the real soil image used to construct the simulated images (as opposed to PBA). This is consistent with the recommendation made by Iassonov et al. (2009) and Iassonov and Tuller (2010) that a local method could be used as an alternative to pre-segmentation processing. As noted earlier, the choice of the TH interval is of prime importance when using IK. With the two-peak histogram simulated image, the interval around the global PBA TH produced far better results than the interval calculated through the gradient masks method (Schlüter et al., 2010) and this made the original idea of IK/PBA attractive.

4.5. Practical conclusion and discussion

From ME, NU and RE_P analyses and according to the experimental conditions, we showed that the Otsu and IK/GM segmentation methods were more accurate with a PRE1 noise reduction and that OTSU_PRE1 and IK/GM_PRE1 were not statistically different. Post-segmentation noise reduction unnecessarily destroy useful information from the pores edges and its best asset of removing small features wrongly assigned to porosity could equally be performed with a post-segmentation clean-up when features are small enough. The analyses were performed on 2D images although we subsequently work with 3D images. In their image by image study, Wang et al. (2011) reported similar segmentation results between their one 3D image and eight 2D images. Although we cannot statistically confirm our 2D observed results in 3D, we are therefore confident in using our 2D conclusions for our subsequent 3D work. The adopted scheme for our field experiment was therefore the application of a pre-segmentation 3D median filter with 2 pixels radius and the use of the global PBA segmentation method.

The use of multiple performance indicators to assess noise reduction and segmentation methods effects on the final binary images was necessary, which is consistent with Wang et al. (2011) findings. When dealing with real soil images, only the NU indicator could be use because it does not require ground-truth information. That indicator provided comparable results to the other indicators when dealing with pre and post-segmentation noise reduction for the Otsu’s method. Results were a little trickier with the adaptive-window IK method. Comparisons to physical laboratory measurements are possible ways to tackle the ground-truth issue as applied by Beckers et al. (2014a). In the end, we suggest anyway that comparing the binary images to the grayscale images is a subjective necessary first step to evaluate the segmentation quality.

5

Results & Discussions: the field experiment

5.1. Macroscopic measurements

5.1.1. Soil physical properties

The agricultural soil we studied showed large variations between samples with porosity values ranging from 43.09 % to 57.70 % (mean of 49.73% +/-1.57%) and density from 1.12 to 1.51 g/cm³ (mean of 1.33 g/cm³ +/- 0.04 g/cm³). Table 5 presents the maximum, minimum, and average values as well as the associated standard deviations of the logarithmic Ks (cm/d) and ka (µm²). As expected, the range of Ks and ka values is large due to the singular nature of pore network organization and the resulting transfer properties. Figure 19 displays the power-law type relationship between ka and the associated air-filled porosity, measured from the SWRC, as also observed by Ball and Schjønning (2002). There was, however, no linear relationship between log(Ks) and log(ka) as opposed to what has been shown in other studies (e.g. Loll et al., 1999, Mossadeghi-Björklund et al. 2016). The SWRC of four samples were not measured due to equipment failure and Table 6 presents the air-filled porosity of the twenty remaining soil samples. That value is latter use as a target to reach for the segmentation of the grayscale X-ray µCT images. Table 6 also presents the Lab_FD, latter used to characterize each SWRC by one value.

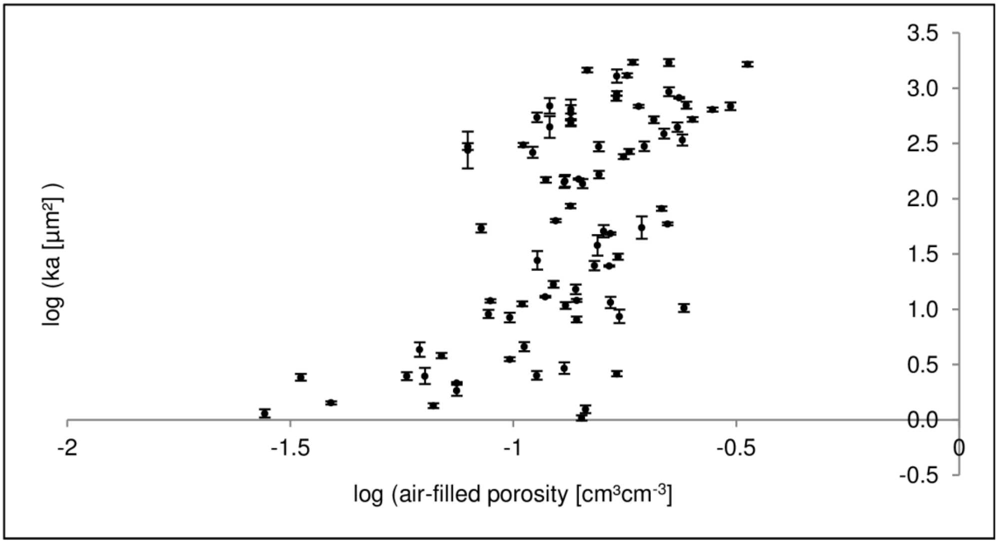

Figure 19. Logarithmic laboratory measured air permeability [ka, µm²] versus logarithmic laboratory measured air-filled porosity for all soil samples at all water matric potentials.

Table 5. Logarithmic saturated hydraulic conductivities (Ks, cm/day) and air permeability (ka, µm^2) measured of -4 kPa, -7 kPa, -10 kPa, -30 kPa and -70 kPa (minimum values [Min], maximum values [Max], mean values [Mean] and standard deviation [St dev])

	[cm/day]	**log [µm^2]**				
	log(Ks)	**ka(-4 kPa)**	**ka(-7 kPa)**	**ka(-10 kPa)**	**ka(- 30 kPa)**	**ka(-70 kPa)**
Calibration data set						
Max	1.591	2.920	3.076	2.992	3.235	3.231
Min	0.443	0.059	0.017	0.095	0.418	0.936
Mean	1.015	1.681	1.735	1.916	2.164	2.318
St dev	0.149	0.505	0.478	0.478	0.603	0.400
Validation data set						
Max	1.709	1.773	2.532	2.718	2.837	3.217
Min	0.352	0.395	-0.051	0.581	1.077	0.402
Mean	1.149	1.132	1.018	1.601	1.852	1.885
St dev	0.400	0.801	1.028	1.013	0.893	0.891
All data						
Max	1.709	2.920	3.076	2.992	3.235	3.231
Min	0.352	0.059	-0.051	0.095	0.418	0.402
Mean	1.049	1.584	1.572	1.853	2.086	2.220
St dev	0.147	0.443	0.445	0.424	0.496	0.376

Table 6. Laboratory measured air-filled porosity at a water matric potential of -1 kPa (Lab_PO) and the fractal dimension extracted from the laboratory measured soil water retention curve (Lab_FD) for all soil samples.

	Lab_PO	Lab_FD		Lab_PO	Lab_FD
#1	7.91	2.873	**#13**	nd	nd
#2	13.51	2.909	**#14**	6.94	2.8547
#3	13.46	2.890	**#15**	11.10	2.8847
#4	10.47	2.901	**#16**	nd	nd
#5	9.81	2.882	**#17**	nd	nd
#6	6.67	2.884	**#18**	5.69	2.7961
#7	13.36	2.896	**#19**	13.80	2.9021
#8	7.94	2.888	**#20**	17.18	2.8733
#9	9.29	2.842	**#21**	4.60	2.8329
#10	nd	nd	**#22**	3.64	2.8578
#11	4.61	2.835	**#23**	4.34	2.8561
#12	4.77	2.855	**#24**	12.63	2.8354

5.1.2. Soil chemical properties

Figure 20 presents the relative content of the total organic carbon (TOC), and of the iron extracted from the three previously quoted techniques. Quick ANOVA confirmed the visual trend that TOC was highly significantly different according cultural practices (CT, conventional tillage; or RT, reduced tillage), as well as was the complex form of Fe (Fe_pyrophosphate). It has often been observed that reduced tillage practices induce an accumulation of soil organic matter (SOM) by decreasing the SOM decomposition (e.g. Six et al., 2000). At the aggregate scale, Gao et al. (2017) also observed significant differences in SOM between the same fields we studied (CT and RT). The Fe forms extracted with DCB and oxalate were highly significantly different according to tillage but also according to the year of sampling. We did not have the objective to compare cultural practices or sampling year but these results should be kept in mind for the following comparisons to microscopic parameters from X-ray µCT images.

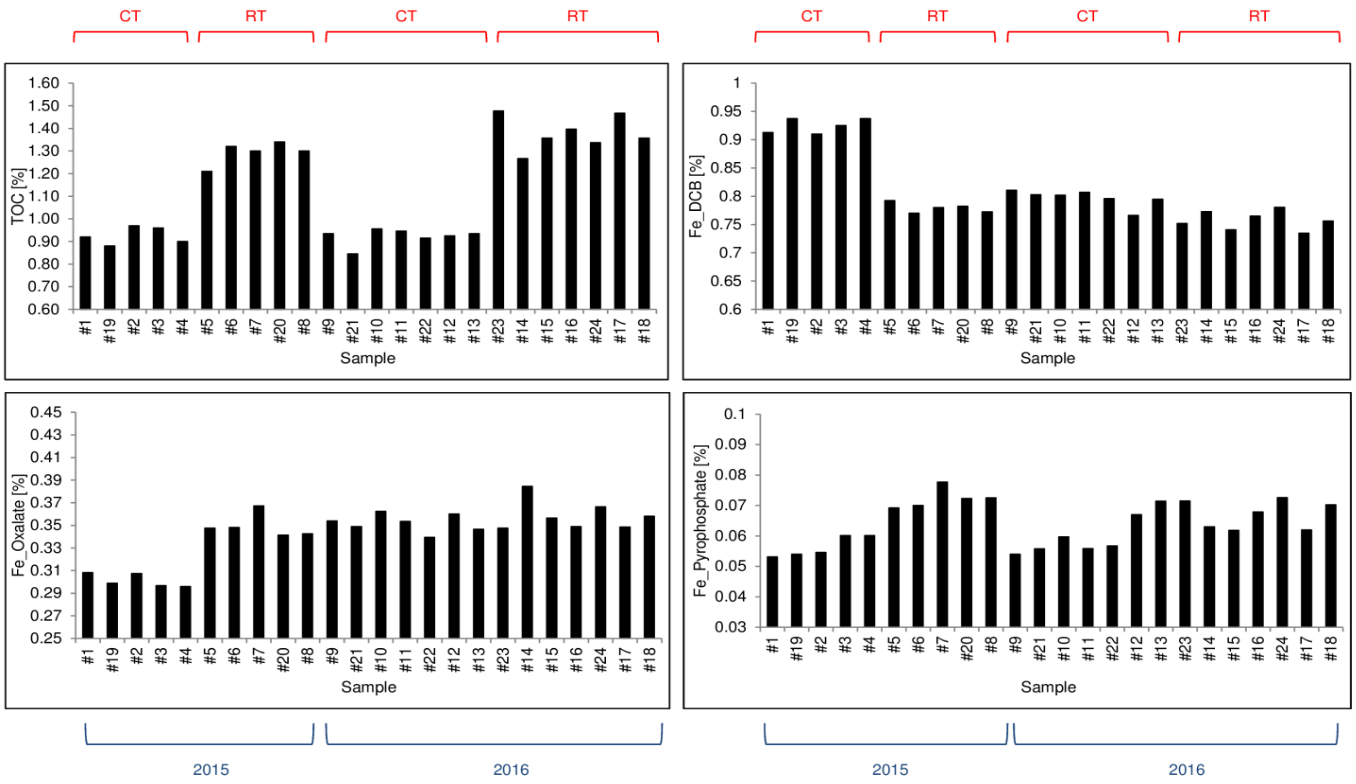

Figure 20. Total organic carbon (TOC) and iron, extracted with three different extractable solutions (pyrophosphate, oxalate, and DCB), contents for all samples. Distinctions of sampling year (2015 or 2016) and cultural practices (CT or RT) are noted in blue and red, respectively.

When all the samples were taken into account, TOC was negatively correlated to all the free forms of iron (Fe_DCB) and positively to the complex form of iron (FE_pyrophosphate). Crytalline Fe oxide (Fe_DCB) was also negatively correlated to amorphous Fe oxide (Fe_oxalate). These correlations were credible because of the presence of two opposite groups (Fig. 21), yet these were logical because, first, the complex forms of iron (Fe_pyrophosphate) play an important role in the stabilization process of the SOM through electrical bridges (e.g. Kleber et al., 2015 ; Oades, 1988; Wagai and Mayer, 2007), and, second, the amorphous forms of iron (Fe_oxalate) that are crystallized become crystal iron (which are identified with a DCB extraction) and as more TOC there is, the less crystallization occurs (Oades, 1988). Any sub-correlations reported within groups of samples (according sampling year or tillage) confirmed these observations (Fig. 22 and 23).

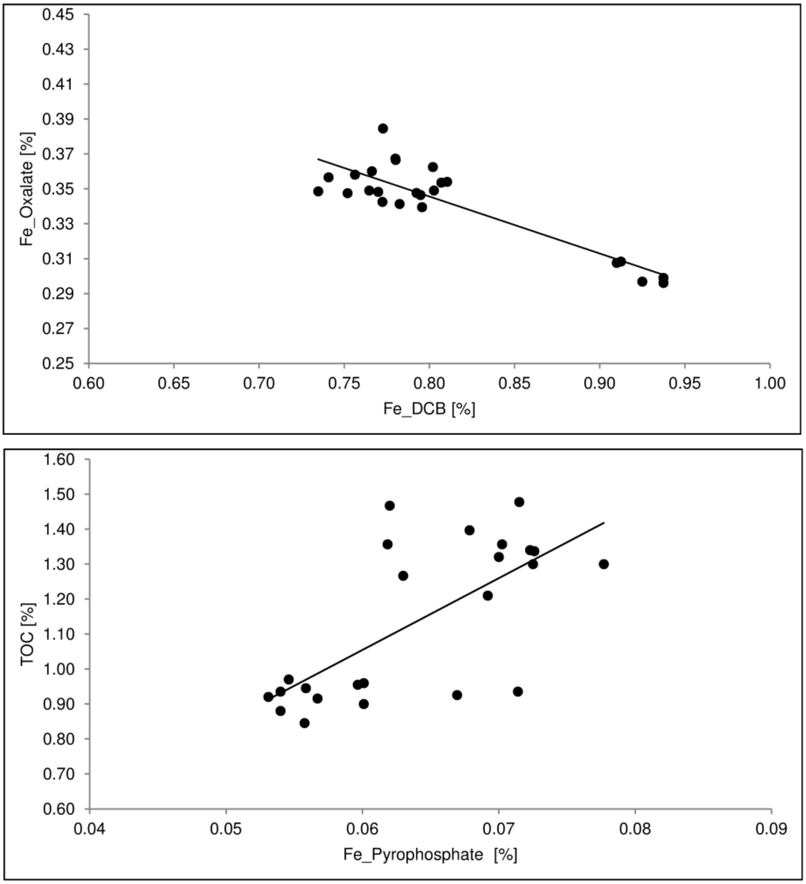

Figure 21. Upper graph: Iron content extracted with oxalate (Fe_Oxalate) versus iron extracted with DCB (Fe_DCB) for all soil samples. Lower graph: Total organic carbon (TOC) versus iron extracted with pyrophosphate (Fe_Pyrophosphate) for all soil samples.

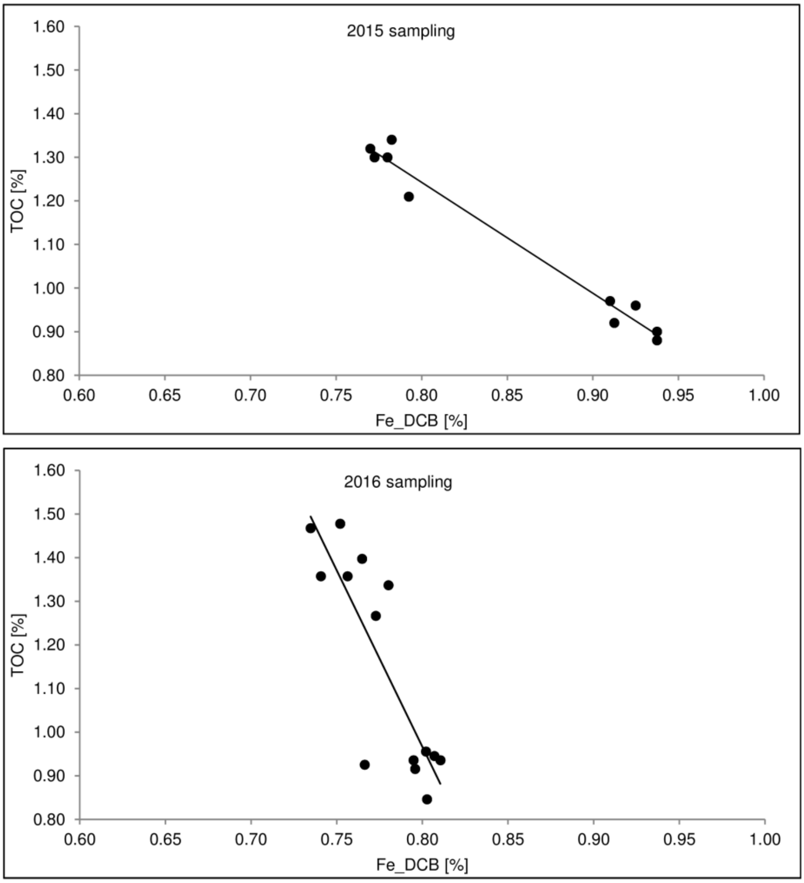

Figure 22. Total organic carbon (TOC) versus iron extracted with DCB (Fe_DCB) for both sampling year.

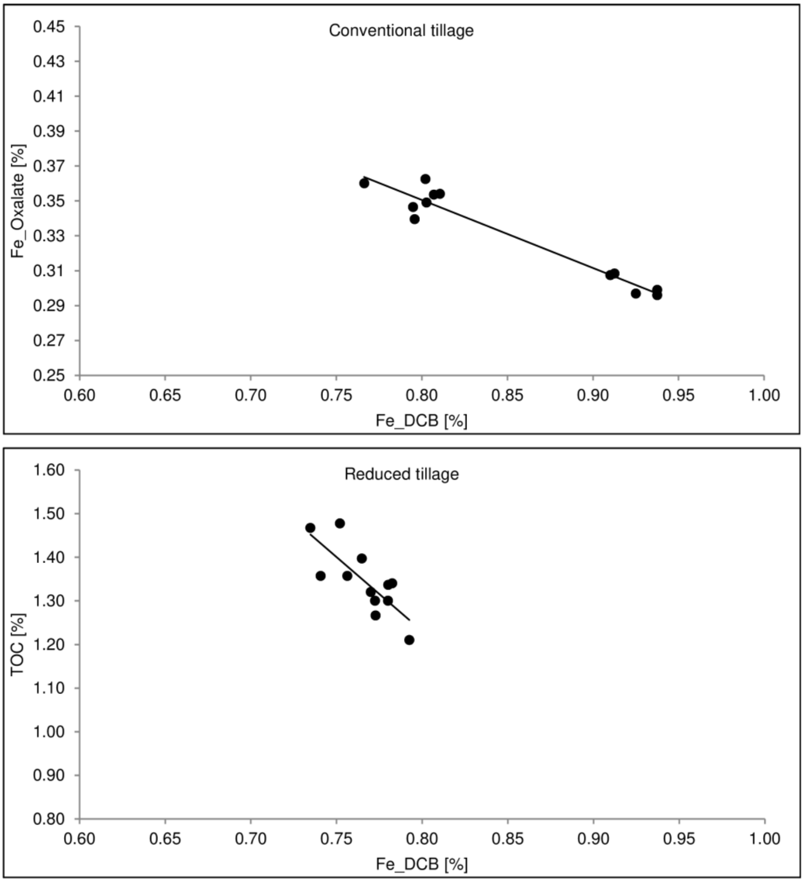

Figure 23. Upper graph: Iron content extracted with oxalate (Fe_Oxalate) versus iron extracted with DCB (Fe_DCB) for the samples from the conventional tillage experiment. Lower graph: Total organic carbon (TOC) versus iron extracted with DCB (Fe_DCB) for the samples from the reduced tillage experiment.

5.2. Microscopic measurements

This section deals with the features (pores) characterization of the X-ray µCT images. In priority, the segmentation quality must be assessed to ensure consistent pore identification. The pores characteristics quantification was then performed on the X-ray µCT images taken at a water matric potential (*h*) of -70 kPa where we assumed all the potential visible porosity was air-filled. A following research question evaluates the changes in microscopic parameters values with resolution and *h*.

5.2.1. Evaluation of the segmentation quality

As demonstrated above, the segmentation has a great impact on the visible porosity calculated on the X-ray µCT image and on the extracted microscopic measurements (Lamandé et al., 2013, **Paper I**). We, therefore, visually verified the accuracy of the global segmentation on each of the 104 X-ray µCT images by superimposing the binary images on the grayscale images. For the 24 samples scanned at *h* = –70 kPa, it appeared that the porosity-based (PBA) global segmentation method did not provide satisfactory results for two soil X-ray µCT images (#2 and #7 from the calibration set and #20 from the validation set). These samples had a large air-filled porosity at *h* =-1 kPa (Lab_PO); the PBA segmentation method therefore increased the TH (increased µCT_PO) to obtain a µCT_PO as close as possible to Lab_PO (resulting threshold of 94 [0-255]). Otsu's method was, therefore, applied to these three samples and the global TH values for samples #2, #7 and #20 were 67, 69 and 69 (0-255), respectively. The comparison to the TH values obtained with the PBA method for the other samples supported this processing choice (Table 7). **Paper II** exposes the plausible physical explanations that lead to use the Otsu's segmentation rather than the PBA method for samples #2, #7, and #20.

Table 7. Global threshold (TH) values for all soil samples scanned at a water matric potential of -70 kPa

Sample	TH (0-255)	Sample	TH (0-255)	Sample	TH (0-255)	Sample	TH (0-255)
#1	70	**#7**	*94*	**#13**	57	**#19**	78
#2	*94*	**#8**	69	**#14**	60	**#20**	*94*
#3	71	**#9**	60	**#15**	61	**#21**	58
#4	68	**#10**	58	**#16**	60	**#22**	60
#5	71	**#11**	58	**#17**	61	**#23**	58
#6	69	**#12**	58	**#18**	61	**#24**	61

Finally, the samples #10, #13, #16 and #17 were segmented using the Otsu's method because their SWRC were not measured. The resulting X-ray µCT images taken at other *h* than - 70 kPa were segmented using the Otsu's method because the Lab_PO used to segment the X-ray µCT images taken at -70 kPa could not rationally be used as a target for the segmentation of the X-ray µCT images taken at other *h*. Moreover, the Otsu's and PBA have provided all along very close threshold values and Otsu's method was proven quite equivalent to PBA when histogram peaks were quite distinct (**Paper I** and Fig. 24); even if the PBA method has the advantage of providing a physical background to the segmentation process.

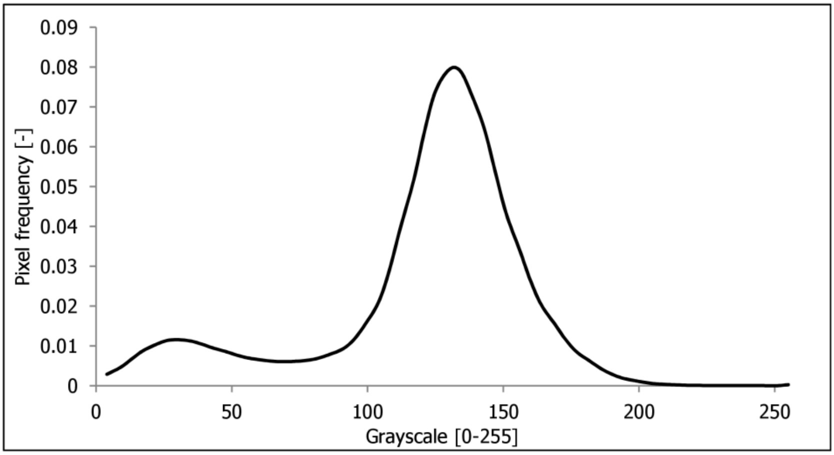

Figure 24. Grayscale histogram of the sample #1 3D image scanned at a water matric potential of -10 kPa.

5.2.2. Microscopic parameters values at full potential visible air-filled porosity

We hypothesize that the X-ray µCT images scanned at *h* = - 70 kPa are the images where all the potential visible porosity is air-filled and we illustrate that latter. The detailed results are presented in **Paper II**. Major findings were that the calculated µCT porosities, taking into account pores of at least five voxels, were only slightly higher than those calculated taking into account pores of at least 1000 voxels. The differences between µCT porosities represented +/- 90% of the number of pores and the pores having a volume between five and 1000 voxels turned out to be the *small pores* as defined in Table 3. The average pore volumes of the small (Avg_Svol) and big (Avg_Bvol) pores were also highly correlated, although these parameters were calculated on strictly different pores. This suggests there is a dependency between pores of different sizes.

As stated earlier, the pore network skeleton, and the resulting pore identification and characterization, is highly sensitive to the scanning equipment and procedure, the image processing, and the skeletonization process. Houston et al. (2017) have recently assessed that the used software for features characterization, and the decomposition method that goes with it, influence the final pore size distribution. Compared to others studies (e.g., Garbout et al., 2013 or Katuwal et al., 2015b), we indeed observed a larger amount of pores that might as well come from the resolution we worked with, or the pore identification method. We therefore calculated a connectivity indicator derived from the percolation theory (the global connectivity parameters, Γ) from the pore size distribution obtained with the algorithm of Plougonven (2009) implemented in Avizo®, and from the cluster size distribution obtained with the BoneJ plugin (Doube et al., 2010) available in ImageJ (Schneider et al., 2012). We observed drastically different Γ values from the two methods of computation. The very low values of Γ from Avizo came from the large amount of pores and the smaller volume (by two orders of magnitude) of the *largest component* than the one identified in BoneJ. In the following, we used the Γ value computed from the BoneJ's cluster size distribution to be comparable to Sandin et al. (2017) who found a link between log(Ks) and Γ. Regarding the others indicators of connectivity, we observed that AvgZ was correlated to the degree of connectivity (B/J) but not to the Euler number (ε) or to the surface connectivity (SC) while B/J was correlated to ε and not to SC, and SC was correlated to ε. These connectivity indicators did not carry the exact same information and should, therefore, be used for their potential explanatory power, as pointed out by Renard and Allard (2013) and Katuwal et al. (2015a).

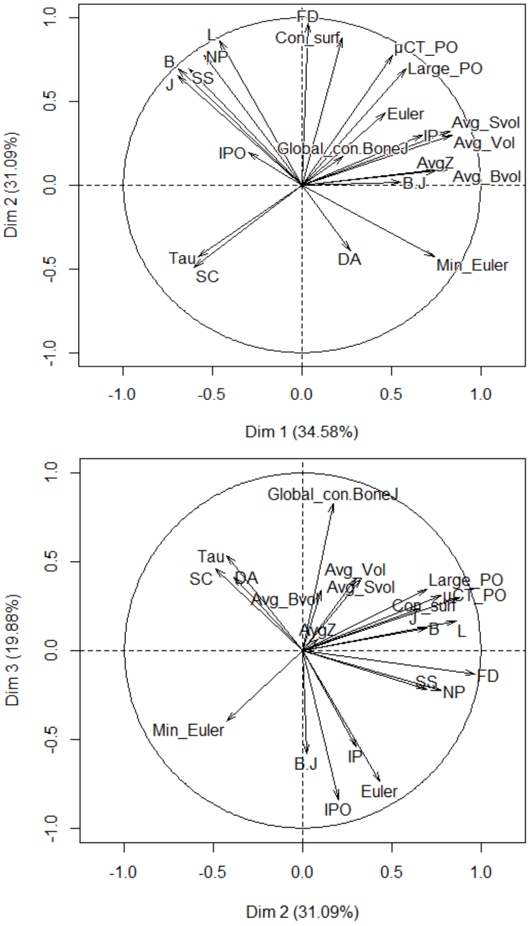

Figure 25. First, second and third dimensions of the variables principal components.

In addition to our **Paper II**, we performed a principal component analysis to validate the observed correlations. Figure 25 represents, on one hand the first and second dimension, and on the other hand the second and third dimension of the performed PCA. The combination of the second and third axis is the best representation of the projected variables (sum of the $\cos^2$). The degree of anisotropy (DA) and the tortuosity (τ) were not well projected on any axis, and indeed, these variables were not correlated to any microscopic parameters (for DA), or correlated without physical meaning (for τ). The average volume of all the pores, the smallest pores and the biggest pores contribute mostly to the construction of the first axis in combination to AvgZ. It indeed appeared that larger pores tended to be more connected. We also observed that the specific surface (SS), the total pore network length (L), the number of branches (B), of junctions (J) and of pores (NP) were all highly correlated as confirmed by the PCA with, however, different contributions to the first and second axis for L and NP compared to B, J, and SS. We although decided to work with all these parameters (instead than with a factorial component) for the subsequent analyses to hold to the physical meaning behind the microscopic parameters.

5.3. Research question #1: Which microscopic parameters explain the best the soil hydrodynamic properties measured at the sample scale?

That research question was extensively presented in our **Paper II** and we here review the main findings.

5.3.1. Measured, calculated and predicted soil water retention curves

As previously stated, samples #10, #13, #16 and #17 were not included in this section because their SWRC were not measured; the calibration data set for these sub-section included 14 samples instead of 18. First, the poor fit between µCT_PO (13.95%) and Lab_PO (7.91%) for sample #1 is likely due an under-evaluation of the saturated sample weight leading to a smaller Lab_PO measurement. Figure 26 indeed shows that a large macropore is connected to the bottom of the sample. Then, all the others samples that were segmented with the PBA segmentation method showed similar values of µCT_PO and Lab_PO since that latter was used as a target during the segmentation process. Elliot et al. (2010) also found congruent air-filled porosity values measured by X-ray µCT (voxel size of 45^3µm^3) and by weight determination. The difference between µCT_PO and Lab_PO increased with Lab_PO but wasn’t correlated to any microscopic parameters. We although presume that the pore network real connectivity would explain the imperfect applicability of the capillary law as Parvin et al. (2017) observed it.

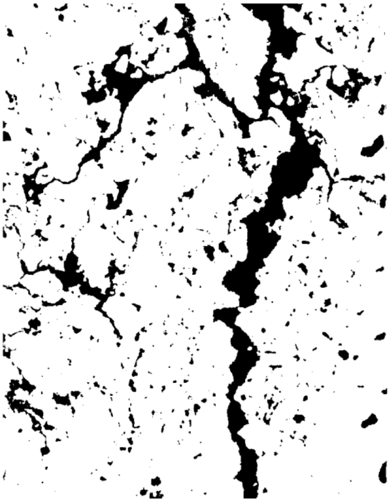

Figure 26. Vertical slice in the middle of sample #1.

Although it is imperfect, the capillary theory was applied to the pore-size distribution extracted from the X-ray µCT images and the resulting calculated air-filled porosities were adjusted to the total laboratory porosity. This lead to the calculation of a SWRC including µCT data and pressure plate's data (µCT+PP), which were afterwards fitted with the bimodal version (Durner et al., 1994) of the van Genuchten (1980) model, and compared to the fitted SWRC measured with pressure plates only (PP). In the end, mainly the fitted parts of the SWRC close to saturation were different between the two methods since only large pores were visible. That procedure was inspired from Beckers et al. (2014a) and successfully applied in Parvin et al. (2017). We obtained similar results than these two studies where volumetric water content (θ) close to saturation was higher when predicted with µCT+PP data than with PP data. RRMSE values were better for SWRC fitted from µCT+PP than only with PP data (except for sample #1 again since the total porosity and the θ are both dependent of the sample saturated weight). Lamandé et al. (2013) also found that X-ray µCT measurements (voxel size of 600^3 μm^3) allowed a more complete description of the pore space than classical laboratory measurements, and Rab et al. (2014) have concluded that X-ray µCT was likely a better method than laboratory SWRC measurements for determining air-filled macroporosity (pores larger than 300 µm in diameter). Although the connectivity of the pore network was not taken into account with the X-ray µCT SWRC calculation, the use of microscopic information improved the prediction of continuous SWRC with the bimodal version (Durner, 1994) of the van Genuchten model (1980). The determination of SWRC through pressure plate measurements are likely more representative of the *in-situ* soil hydrodynamic, but those are not free of artifacts (air entrapment, incomplete saturation), as observed with sample #1.

5.3.1.1. Water content along the soil water retention curve

We analyzed the relationships between θ measured at various h and the microscopic measurements. We found that θ measured at h = -500 kPa and h = -1500 kPa were positively correlated to log(Avg_vol) (ρ = 0.68, BF = 16 and ρ = 0.70, BF = 25), as well as to log(Avg_Bvol) (ρ = 0.72, BF = 34 and ρ = 0.72, BF = 33), and log(Avg_Svol) (ρ = 0.63, BF = 7 and ρ = 0.65, BF = 10). Figure 27 shows the logarithmic relationship between the average volume of the biggest pores and θ. Tested regression models showed that the logarithmic values of the averages pore volumes were the best predicators.

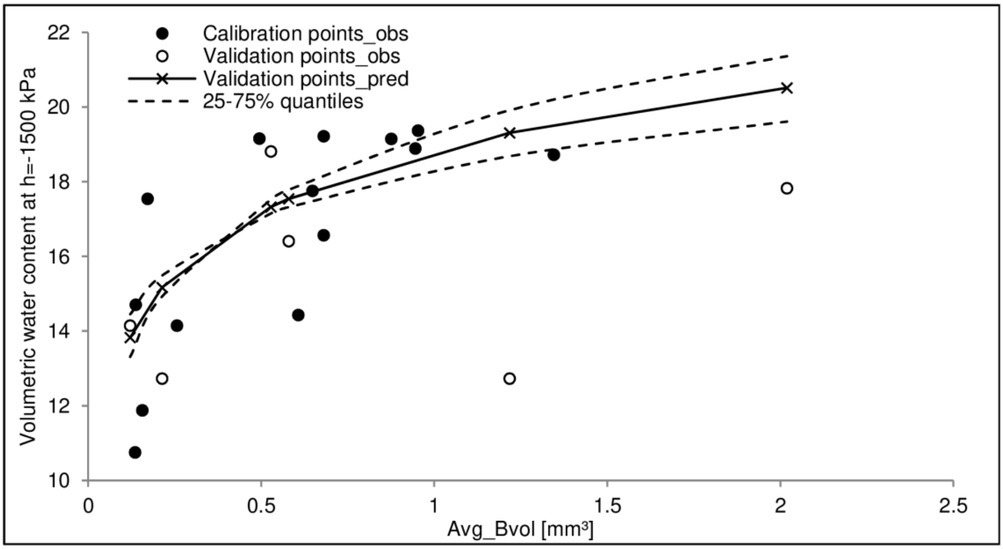

Figure 27. Laboratory measured volumetric water content at a water matric potential of -1500 kPa versus the microscopic average volume of the biggest pores (Avg_Bvol).

The retained soil water at h = -500 kPa and h = -1500 kPa is in the pores that are not visible on the X-ray µCT images because of their small sizes. These regression models therefore suggest that the average volume of the visible pores (i.e. the largest pores) influences the dry end of the retention curve. To our knowledge, this observation was never reported. For example, we recall the often-used van Genuchten formulation of the continuous expression of $\theta(h)$:

$$\theta(h) = \theta_r + \frac{(\theta_s - \theta_r)}{[1+(\alpha h)^n]^m} \qquad \text{[Eq.11]}$$

Where $\theta(r)$ is the residual water content, $\theta(s)$ is the water content at saturation, h is the water matric potential and α, n and m are fitting parameters (van Genuchten, 1980).

Mainly adsorptive forces govern at high negative water matric potentials (Fig. 28 from Daly et al., 2018), another proposition would rather be that pore sizes are connected across scales, as previously seen with the high correlation between the average pore volume of the small and big visible pores.

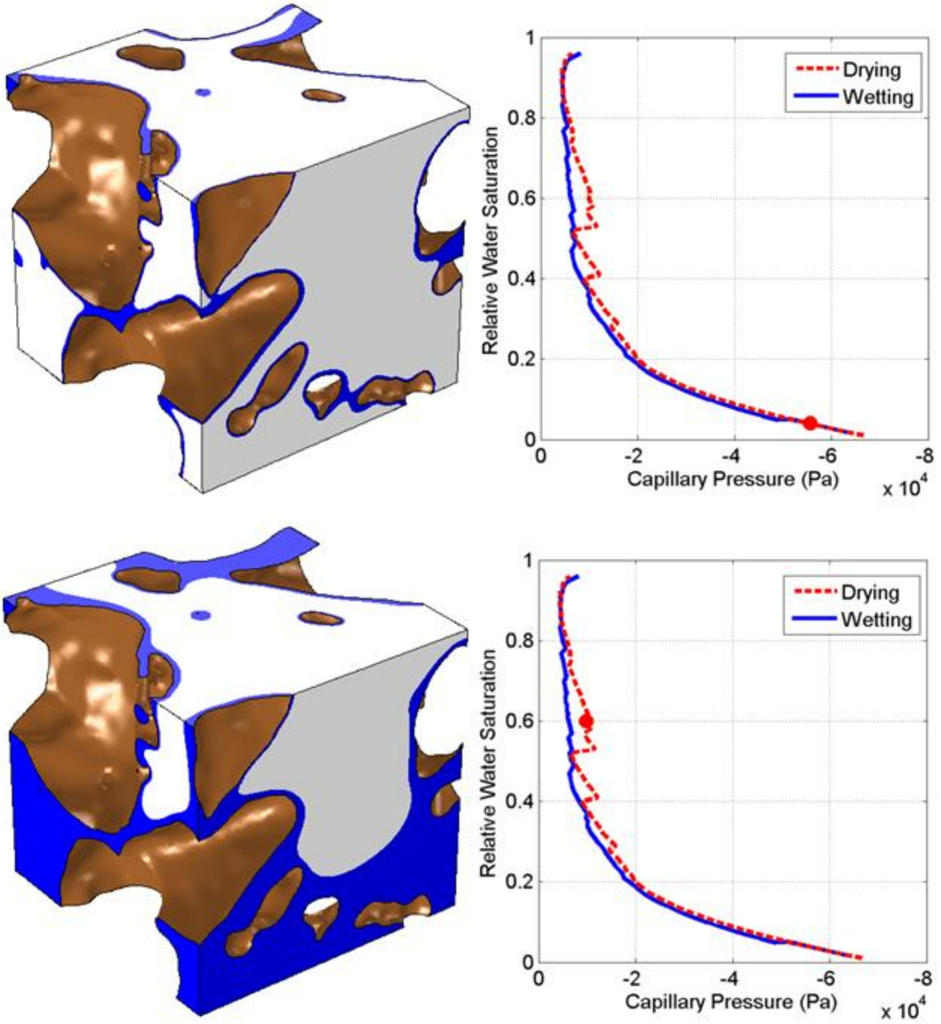

Figure 28. 3D representation of an artificial soil pore network with solid phase in brown, water phase in blue and air phase in white. The red dot on the soil water retention curve indicates the water matrix potentials at which the snapshot was taken (Source: Daly et al., 2018).

5.3.2. Saturated hydraulic conductivity and soil porous structure

Log (Ks) measured on the 24 samples was positively correlated to the global connectivity indicator (Γ) computed from the BoneJ cluster size distribution (ρ=0.59, BF=10) as observed in Sandin et al. (2017). Figure 29 shows the observations of the calibration data (black circles), the observations of the validation data (white circles), the predicted validation points with the 50% quantiles of the regression model (crosses) and the 25% and 75% quantiles of the regression models (dotted lines). The 50% quantiles of the regression models provided a RRMSE of 0.492 for the validation data and the predicted data points were, in most cases, underestimated. The reported regression models that included two explaining variables reported light credible evidence only in the cases where Γ was one of the explaining variables. We did not observe relationships between μCT_PO and log(Ks), despite what the literature reported (Luo et al., 2010b; Kim et al., 2010; Mossadeghi-Björklund et al., 2016 or Naveed et al., 2016). The measured Ks from those studies were, however, higher by several orders of magnitude.

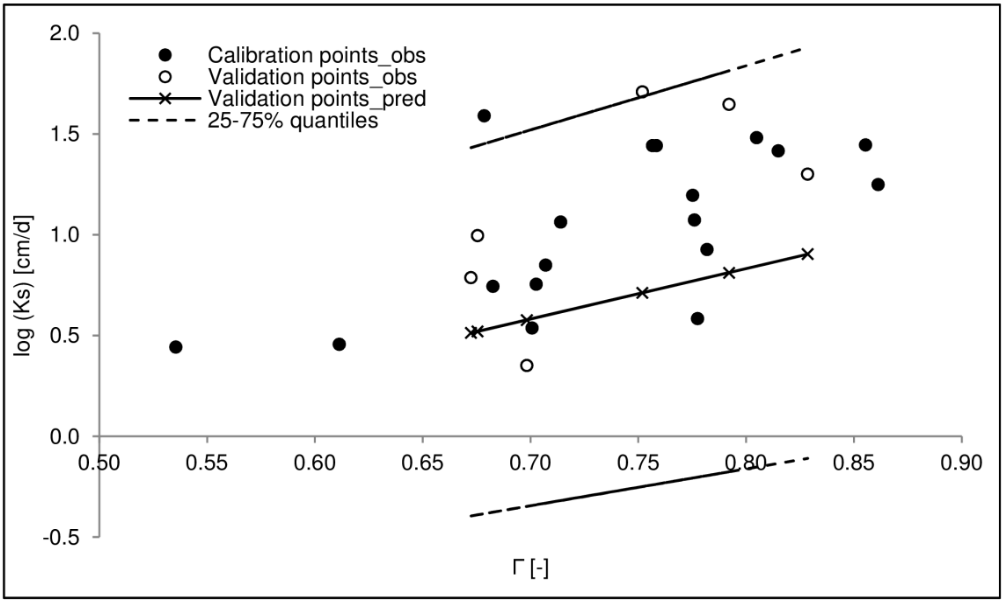

Figure 29. Logarithmic saturated hydraulic conductivity (Ks) versus global connectivity (Γ) calculated from the cluster size distribution extracted from BoneJ.

We did observe a positive correlation between log(Ks) and FD when the calibration samples were separated in two groups according to their Ks values (Fig.30, black circles). By using the Ks value as a boundary, the validation data were visually assigned to a group (Fig. 30, white circles). The global RRMSE calculated on the predicted points was 0.260, which is a rather good performance (Fig. 30, crosses). The 25 and 75% regression model quantiles were highly dispersed (Fig. 30, dotted lines) inducing uncertainty about the regression model.

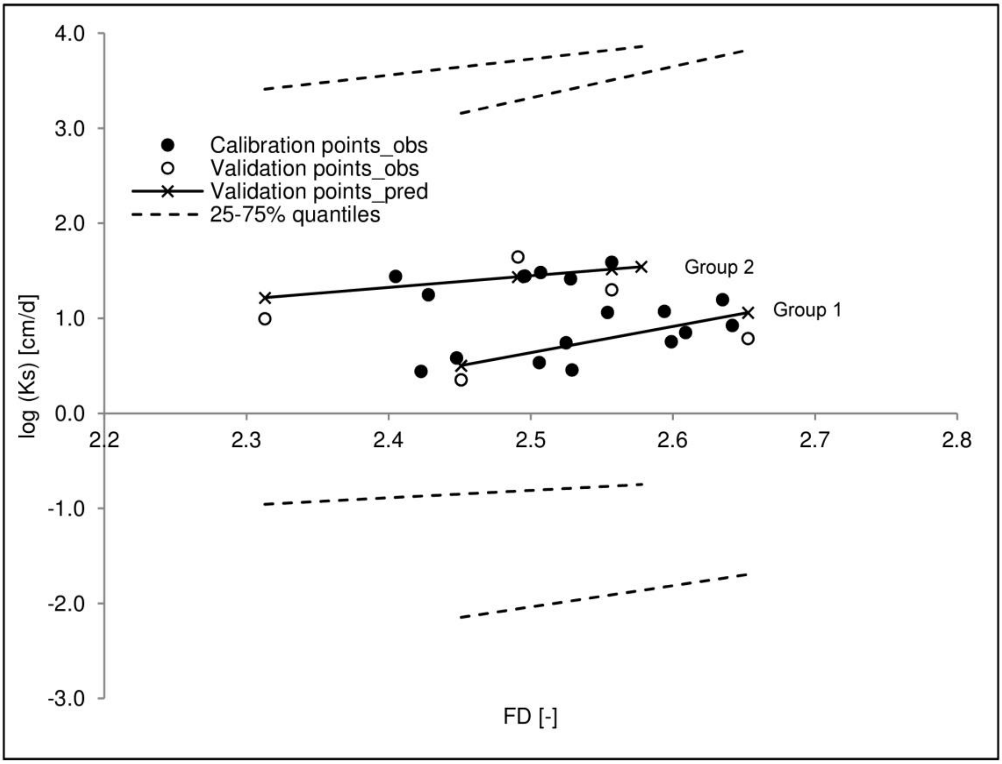

Figure 30. Logarithmic saturated hydraulic conductivity (Ks) versus the fractal dimension measured on X-ray µCT images (FD).

The fractal geometry measures the ability of the studied object to fill the Euclidian space within which it is integrated and, the larger the FD, the closer to a real fractal the object gets, meaning that its shape is similar at different scales. Although Pachepsky et al. (2000) reported that soils are far from being real fractal, Perret et al. (2003) and Kravchenko et al. (2011) pointed out that FD can be used as a global measure of the pore network complexity. For example, FD was found to vary with depth or soil treatment (Rachmann et al., 2005; Udawatta and Anderson, 2008; Kim et al., 2010). Anderson et al. (2014) also observed a positive correlation between log(Ks) and FD. By applying the regression equations, log(Ks) of group 1 equaled log(Ks) of group 2 when FD = 2.935, which was close to the upper limit of the possible FD values of a 3D object (Fig. 31). At FD=3, the object (the porosity) occupies each point of 3D Euclidian space, but that also meant that log(Ks) was limited to 128 cm/day. Would more groups be created with increasing conductivity and would the slopes of the relationships decrease? Would the solutions of the regression equations be identical when the fractal dimension equals three?

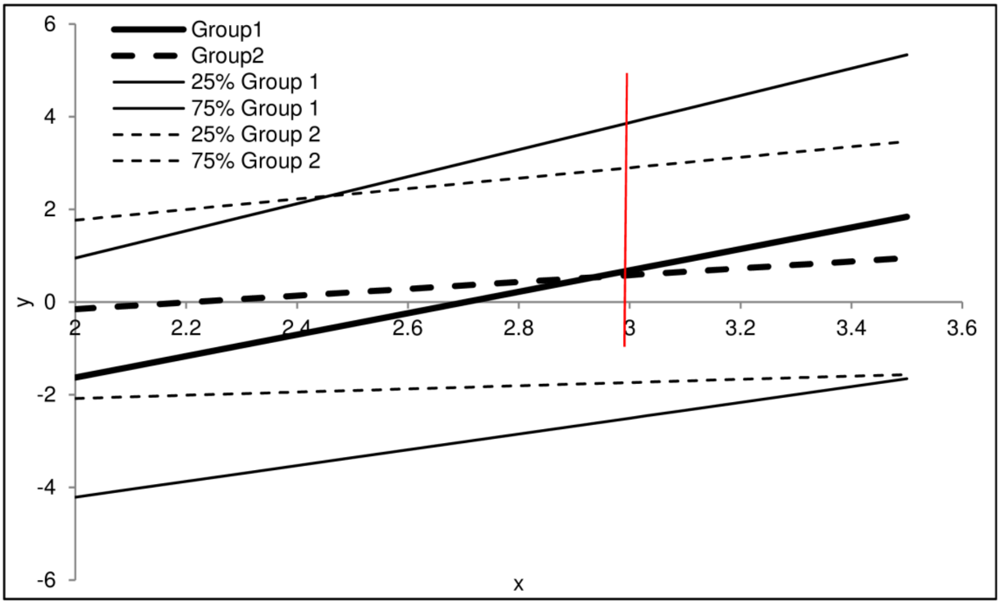

Figure 31. Application of the group 1 and group 2 regression models.

Although no microscopic measurements explained the separation of the samples in two groups, we noticed that some of the less conductive samples presented one or two large macropores (not necessarily vertically oriented nor connected from top to bottom) while some of the more conductive samples had more dispersed pore networks, and we observed a negative trend (not credible) between FD and the degree of anisotropy (DA) for group 2, but not for group 1. This suggested that the porosity arrangement led to the composition of two groups for the relationship between FD and log(Ks).

Anisotropy indeed impacts the soil conductivity (Ursino et al., 2000; Raats et al., 2004; Zhang, 2013). After removing two outliers from the calibration data set (#9 and #10), we obtained a correlation coefficient of 0.74 (BF = 125.3), which presents a convincing link that has, to our knowledge, not been seen before. Figure 32 plots log(Ks) as a function of DA (black circles for the observations of the calibration data). Applying the regression model to the validation data gave variable quality results due to the presence of outliers within the validation data set. It appeared that the relationship between DA and log(Ks) may not be suitable for highly conductive soil sample presenting isotropic-like porosity distribution.

Such a positive correlation could be interpreted as a consequence of preferential flow through large macropores. For example, Dal Ferro et al. (2013) have found that anisotropy was scale-dependent by showing higher average DA in soil cores than in soil aggregate, they hypothesized that as a possible consequence of biological and mechanical macropores. This was later confirmed by a second study where they showed that only the macropores in the range of 250-500 µm were correlated to the global DA (Dal Ferro et al., 2013).

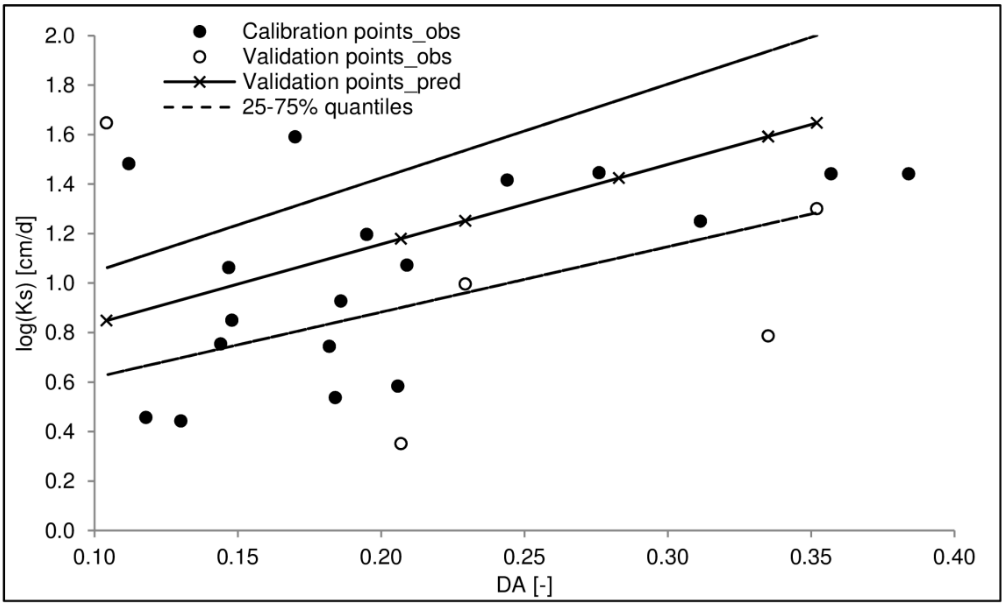

Figure 32. Logarithmic saturated hydraulic conductivity (Ks) versus the soil degree of anisotropy measured on X-ray µCT images (DA).

As explained in the Materials and Methods section, calculating a global direction of anisotropy is not straightforward. Table 8 provides, for each soil sample, the smallest eigenvalue of the ellipsoid and its associated eigenvector, the principal direction is in bold. For four samples, the fitted ellipsoid had equal eigenvalues (due to a display algorithm failure) and the smallest one could not be determined (nd). Ks was measured along the z-axis (vertically) but the main direction of the longest MIL (or smallest eigenvalue) was not systematically in that direction. Therefore, the positive correlation between DA and log(Ks) was not necessarily a result of preferential pore networks paths. Moreover, the directions of the pores connections (Table 8) showed that a majority of the pores junctions were horizontal (x- and y-axis). The repartition was almost always the same between samples, 60% of horizontal and 40% of vertical connections.

Table 8. Logarithmic saturated hydraulic conductivity (Ks), degree of anisotropy calculated on X-ray µCT images (DA), and corresponding characteristics for the calibration data set samples.

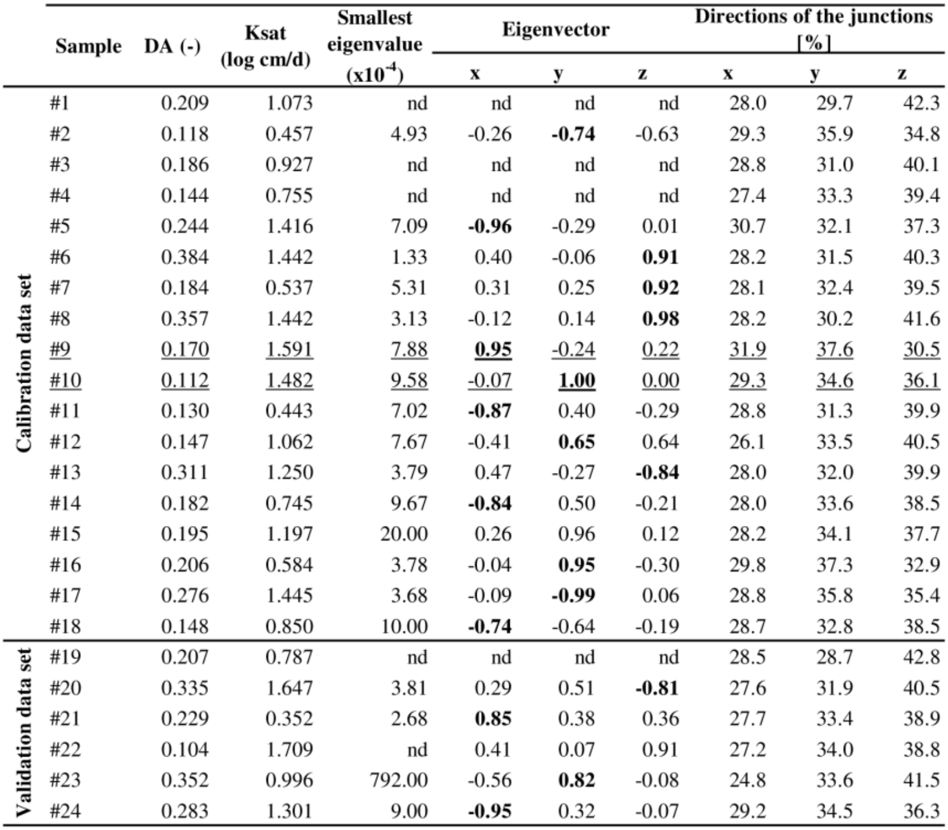

	Sample	DA (-)	Ksat (log cm/d)	Smallest eigenvalue ($x10^{-4}$)	Eigenvector			Directions of the junctions [%]		
					x	y	z	x	y	z
Calibration data set	#1	0.209	1.073	nd	nd	nd	nd	28.0	29.7	42.3
	#2	0.118	0.457	4.93	-0.26	**-0.74**	-0.63	29.3	35.9	34.8
	#3	0.186	0.927	nd	nd	nd	nd	28.8	31.0	40.1
	#4	0.144	0.755	nd	nd	nd	nd	27.4	33.3	39.4
	#5	0.244	1.416	7.09	**-0.96**	-0.29	0.01	30.7	32.1	37.3
	#6	0.384	1.442	1.33	0.40	-0.06	**0.91**	28.2	31.5	40.3
	#7	0.184	0.537	5.31	0.31	0.25	**0.92**	28.1	32.4	39.5
	#8	0.357	1.442	3.13	-0.12	0.14	**0.98**	28.2	30.2	41.6
	#9	0.170	1.591	7.88	**0.95**	-0.24	0.22	31.9	37.6	30.5
	#10	0.112	1.482	9.58	-0.07	**1.00**	0.00	29.3	34.6	36.1
	#11	0.130	0.443	7.02	**-0.87**	0.40	-0.29	28.8	31.3	39.9
	#12	0.147	1.062	7.67	-0.41	**0.65**	0.64	26.1	33.5	40.5
	#13	0.311	1.250	3.79	0.47	-0.27	**-0.84**	28.0	32.0	39.9
	#14	0.182	0.745	9.67	**-0.84**	0.50	-0.21	28.0	33.6	38.5
	#15	0.195	1.197	20.00	0.26	0.96	0.12	28.2	34.1	37.7
	#16	0.206	0.584	3.78	-0.04	**0.95**	-0.30	29.8	37.3	32.9
	#17	0.276	1.445	3.68	-0.09	**-0.99**	0.06	28.8	35.8	35.4
	#18	0.148	0.850	10.00	**-0.74**	-0.64	-0.19	28.7	32.8	38.5
Validation data set	#19	0.207	0.787	nd	nd	nd	nd	28.5	28.7	42.8
	#20	0.335	1.647	3.81	0.29	0.51	**-0.81**	27.6	31.9	40.5
	#21	0.229	0.352	2.68	**0.85**	0.38	0.36	27.7	33.4	38.9
	#22	0.104	1.709	nd	0.41	0.07	0.91	27.2	34.0	38.8
	#23	0.352	0.996	792.00	-0.56	**0.82**	-0.08	24.8	33.6	41.5
	#24	0.283	1.301	9.00	**-0.95**	0.32	-0.07	29.2	34.5	36.3

We reported here that the porosity arrangement described by the global connectivity, the fractal dimension and degree of anisotropy had an impact on the soil conductivity, the combination of those indicators provides information that could be used across scales and to eventually better estimate Ks. No other relationships between log(Ks) or Ks and the other microscopic measurements were reported.

5.3.3. Air permeability variations explained by microscopic structure

Macroscopic measurements showed, as expected, that the air permeability increased with air-filled porosity. We also observed positive credible Bayesian ρ between log(ka) measured at various *h* and microscopic indicators of the porosity, although only log(ka,-70 kPa) was positively correlated to µCT_PO. Given the X-ray µCT image resolution, µCT_PO should be representative of the air-filled PO measured at h = -1 kPa although the soil samples were scanned at h = -70 kPa. The choice to scan soil samples at h = -70 kPa was a compromise between the fact that all the potential visible porosity should be air-filled and avoiding cracks due to drying, and this particular correlation suggests that all the potential visible porosity was indeed air-filled. In their study, Katuwal et al. (2015b) and Naveed et al. (2016) both observed a power-law function between, respectively, ka(-2 kPa) or ka(-3 kPa) and µCT_PO. The µCT_PO calculated on their images is equivalent to the Large_PO on our images as previously stated, and we also reported positive correlations between Large_PO and log(ka). Therefore, the difference between µCT_PO and Large_PO might be the part of the PO that should have drained at low negative potential (from the capillary law), but was actually drained at higher negative potential (due to unusable pathways). We refer to Hunt et al. (2013) to name that part of porosity, the *inaccessible porosity*. This assumption was confirmed by the credible correlations between the inaccessible PO and several microscopic parameters that express a notion of pore network complexity. We previously pointed out that drawback when calculating SWRC from the X-ray µCT data: the connectivity was not taken into account. We here confirmed that the pore network connectivity play a role in the desorption process.

The best regression models calculated on the calibration data (BF) and applied on the validation data reported that the best explaining variable for all measures of log(ka) (RRMSE) was the average pore volume of the smallest pores (Avg_Svol). That parameter might be seen as a limiting factor, and this suggests that ka was more related to pores size distribution than porosity. Figure 33 displays log(ka, -70kPa) as a function of Avg_Svol and the distribution of the 25 and 75% regression model quantiles are rather narrow. The RRMSE equaled 1.256; or 0.0649 when the two worst predicted validation data points were not taken into account. The RRMSE for log(ka, -30kPa) and log(ka, -10kPa) were around 0.800 with one bad validation data point, and the RRMSE for log(ka, -7kPa) was very high (8.154) with three badly predicted data points out of five. The combination of Avg_Svol and average pore volume of all pores (Avg_Vol) performed slightly better in some cases, and slightly worse in others. Figure 33 shows the predicted log(ka) from Avg_Svol and Avg_Vol versus the observed log(ka) values. Although the RRMSE were acceptable, the regression model distributions (the error bars represent the 75% regression models quantiles) were high which inducing large uncertainty. That combination of two explaining variables was, in all cases, the best regression model of two explaining variables models. Other important explaining variables were the average coordination number (Avg_Z), the proportion of isolated porosity (IPO), the average pore volume of the biggest pores (Avg_Bvol) and the combination of µCT_PO and Large_PO.

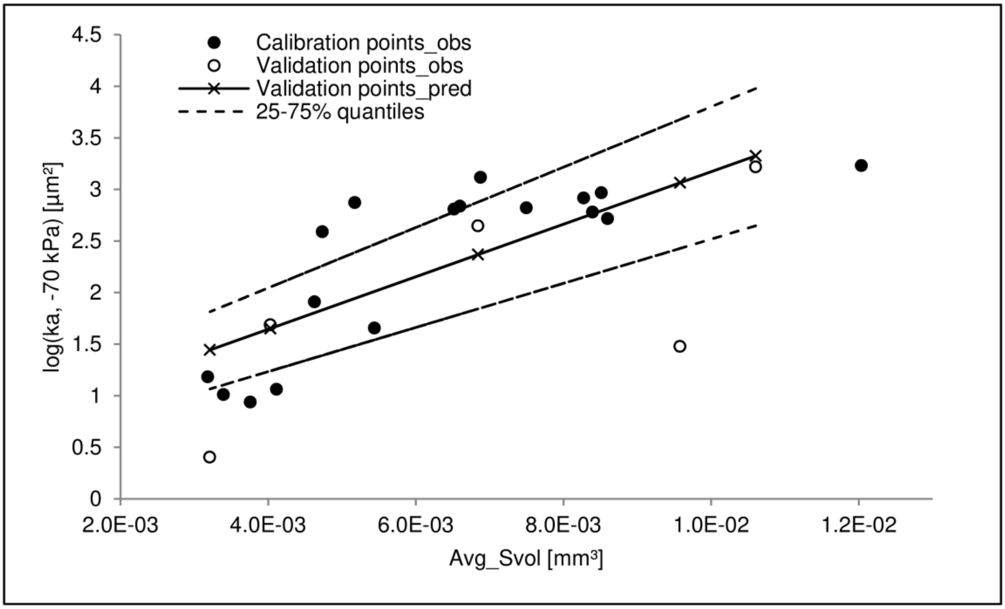

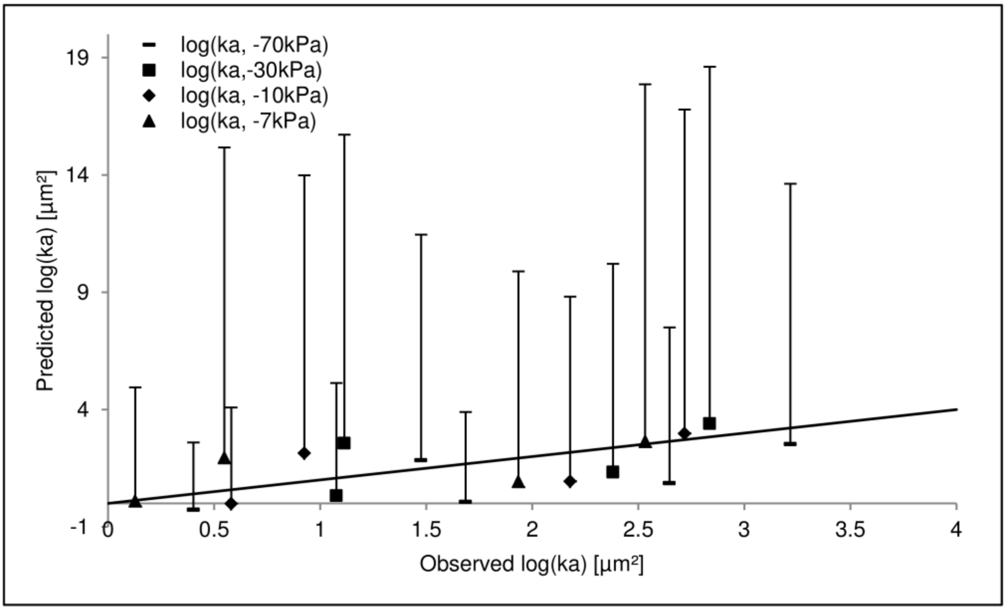

Figure 33. Upper graph: logarithmic air permeability measured at a water matric potential of -70kPa (ka) versus the average pore volume of the smallest pores (Avg_Svol). Lower graph: the predicted logarithmic air permeability (ka) from the average pore volume of the smallest pores (Avg_Svol) and all pores (Avg_Vol) versus the observed logarithmic air permeability. Error bars represent the 75% regression model quantiles.

5.3.4. Practical conclusion and discussion

Studying the soil with X-ray µCT is widespread, but studying it with a small voxel size (43^3 µm^3) is not. First, a pertinent observed link was the positive relationship between the average volume of the biggest pores and that of the smallest ones, suggesting dependence between pores of different volumes.

Then, on one hand, we confirmed previously observed results, such as the better prediction of SWRC near saturation from X-ray µCT derived pore size distribution, although the pore network connectivity was not taken into account. The determination of SWRC through pressure plate measurements are likely more representative of the *in-situ* soil hydrodynamic, but these are not free of artefacts; for example, air entrapment might result in uncomplete saturation leading to inaccurate estimation of the air-filled macroporosity. We also confirmed that the microscopic global connectivity explained the saturated hydraulic conductivity. On the other hand, we observed unprecedented relationships, such as the degree of anisotropy and fractal dimension also explaining the saturated hydraulic conductivity (with some limitations). It is therefore tempting to combine these three indicators to generate information that could be used across scales and to eventually better estimate Ks. That value is indeed important when it comes to the prediction of the hydraulic conductivity curve (Vogel and Roth, 1998). We also observed that the average volume of the smallest pores (between 4×10^5 and +/- 8×10^7 µm^3) best explained the air permeability; we eventually suggested that parameter works as a limiting factor.

Identifying global parameters that convey the complexity of the pore network is a motivating goal to reach. For example, these parameters could be used for the generation of phenomenological pore network models (e.g. Vogel and Roth, 1998; Köhne et al., 2011), which in turn could be used for the simulation of fresh equations linking physics and biology to explain water and air fluxes within the soil (Hunt et al., 2013). The accurate characterization of the SWRC is important for the study of life in soil (e.g. microbial development being water content-dependent in Davidson and Janssens, 2006; soil fungal growth in Falconer et al., 2012), as well is the accurate characterization of the soil air permeability (e.g. plant growth in Ben-Noah and Friedman, 2018). Conversely, soil life affects the soil hydrodynamic properties. For example, besides physically modifying the soil structure or the water dynamic by uptake, the root system influences the soil water retention capacities and transport properties by modifying the spatial liquid phase configuration through the physical properties of mucilage (Daly et al., 2017; Pascal et al., 2018). Or as well, microbial biofilms could affect the pores sections and the resulting soil fluid velocities (Kerboas et al., 2018). Soil structure and functions form a single whole, and a comprehensive understanding of the soil water and air dynamic could be achieved when physical and biochemical processes will be coupled and simulated together.

5.4. Research question #2: How do the microscopic parameters evolve with resolution?

5.4.1. Pore repartition

Figure 34 presents the pore repartitions as a function of the pore radius for the µCT measurements on the soil sample and aggregate, as well as retention curve measured with pressure plates (PP), and desorption curve measured with DVS. As mentioned previously, the X-ray µCT image of the sample at *h* = -70 kPa identifies a greater number of large pores than the macroscopic measurement of the sample retention curve. As well, the DVS measurement did not identify the large pores constituting the largest part of the aggregate porosity. This is likely due to the fact that the largest pores were connected with the atmosphere and could not retain water. Figure 36 presents a 3D view of the aggregate. DVS measurements although identifies pores smaller than the X-ray µCT resolution as reported by Dal Ferro et al. (2012) who compared results from µCT and mercury intrusion porosimetry.

Figure 35 presents pore repartition of others soil samples scanned at *h* = -70 kPa which confirms that curves are different between samples scanned at the same resolution. Interestingly, the µCT pore repartitions of the aggregate and sample show similar curve shapes with a scaling factor of six. The scaling factor between the X-ray µCT voxel sizes was 4.78 and the scaling factors between the scanned volumes was 5.38. This suggests that the pore repartition between scales could be similar. We previously observed that the average pore volume of the small pores (volume between 5 and +/- 1000 voxels) was highly correlated to the average pore volume of the biggest pore (volume between +/- 1000 voxels and the largest pore), implying a possible relationship between pore of different sizes. The sample analyzed at 21.5^3 µm³ does not however present the concavity between the two picks, as observed for the coarsened resolution or for the µCT image of the aggregate. Comparing the sample scanned at 21.5^3 µm³ and coarsened to 43^3 µm³, it appeared that the former present a pore repartition with more large pores then medium size pores. The highest resolution made visible the connections that were invisible at 43^3 µm³. These likely connected the medium size pores together to form larger pores. Then, the pore repartition of the sample at 21.5^3µm³ and the soil aggregate are shifted in different directions. The large pores observed within the sample are likely inter-aggregate pores. The pick around a radius of 100 µm for the X-ray µCT soil aggregate image is about pores that were likely not visible at the sample scale since we counted at least 5 voxels in volume for a pore to be considered. The combination of the aggregate and sample scans could therefore provide a more complete description of the soil pore size distribution.

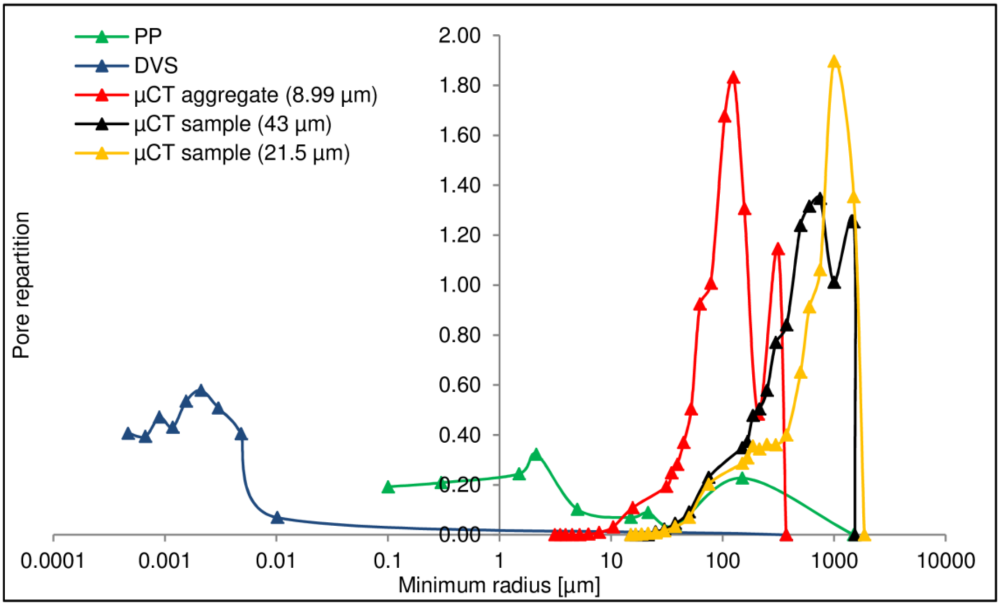

Figure 34. Pore repartition measured by pressure plates (green line), desorption-sorption vapor (blue line), on X-ray µCT images of the soil aggregate (red line), and on X-ray µCT image of the soil sample at a voxel size of 43^3 µm³ (black line) and 21.5^3µm³ (yellow line).

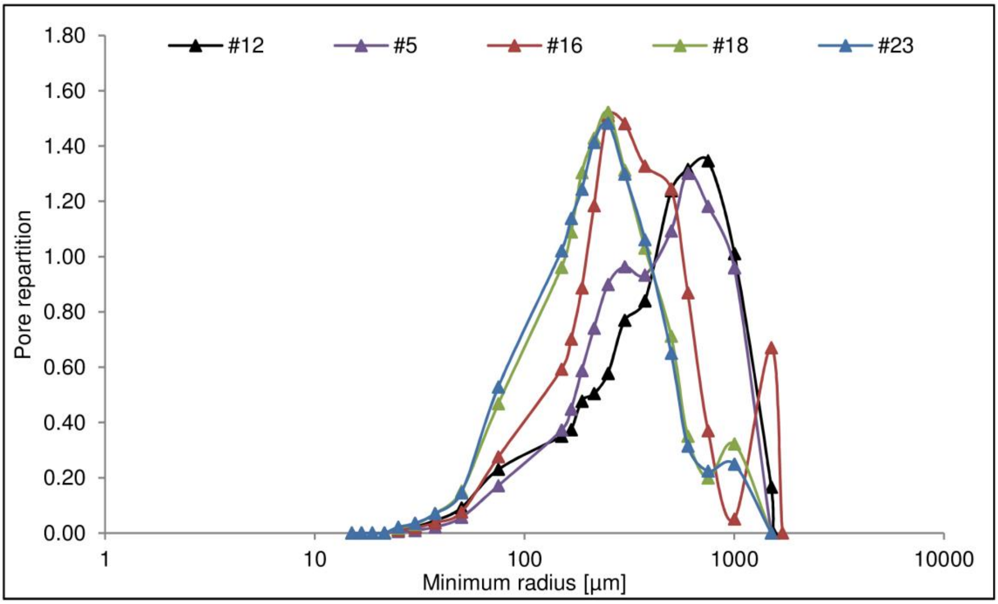

Figure 35. Pore repartition measured on X-ray µCT images (43^3 µm³) of several soil samples.

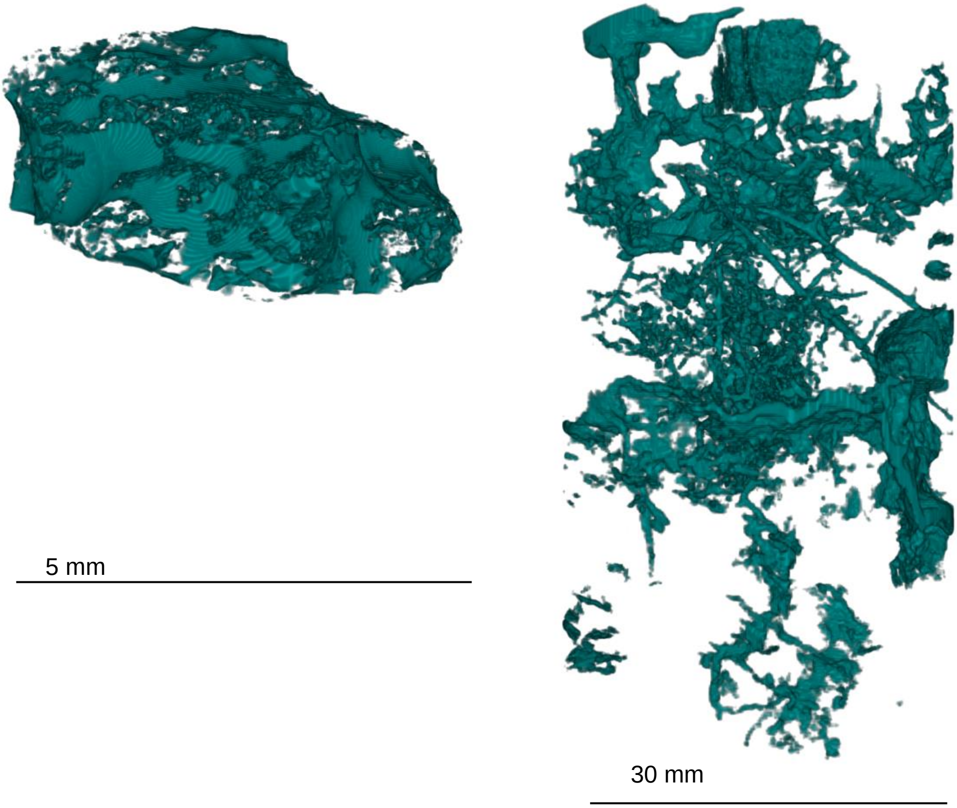

Figure 36. 3D representation of the soil aggregate (left) and the soil sample #12 (right).

5.4.2. Microscopic parameters

5.4.2.1. Porosity indicators

The aggregate porosity (µCT_PO) was larger than any of the other measures although its fractal dimension (FD), total pore network length (L) and number of pores (NP) were smaller (Table 9). This should come from pores larger relatively to its total size (Fig. 36). The comparison of the aggregate porosity indicators to the extrapolated ones (8.99^3 μm^3) for the same voxel size was not conclusive. It is likely that the hypothesis about the regular and continuous changes in µCT porosity and pore geometries across scales was not valid. As well, the comparison between the sample µCT porosity indicators and the extrapolated ones (21.5^3 μm^3) was not conclusive. The extrapolated µCT_PO is 150% higher while the number of pores (NP) is overestimated by 400%, the smaller average pore volume counteracts that effects. The hypothesis was that the µCT_PO would increase with resolution, however, the µCT_PO, NP (and therefore L and FD) decreased from the coarsened resolution (43^3 μm^3) to the original resolution (21.5^3 μm^3). The pores were likely not distributed in the range made visible by the higher resolution (as shown in Fig. 34). Peng et al. (2014) and Shah et al. (2016) observed higher porosity and number of pores with higher resolution but also noticed that the resolution effects on X-ray µCT images were certainly dependent on the soil type. In our case, the skeletonization process could have altered the pore decomposition leading to less identified porosity. The comparison of the images from the two resolutions is therefore uncertain. Houston et al. (2013b) also observed that an increase in resolution would increase the amount of noise, and Shah et al. (2016) reported that the partial volume effect artefact increases with resolution. Extra attention should therefore be brought to the image processing. Figure 37 presents the grayscale images with the identified pore space superimposed in white color. The segmentation process with the porosity-based method clearly identified less porosity on the X-ray µCT images at 21.5^3 µm³, but we also see that some pores merged as previously (red circle, lower row of Fig. 37).

Table 9. Porosity indicators of the scanned sample (43^3 and 21.5^3 µm³) and aggregate (8.99^3µm³), and from the extrapolation equations.

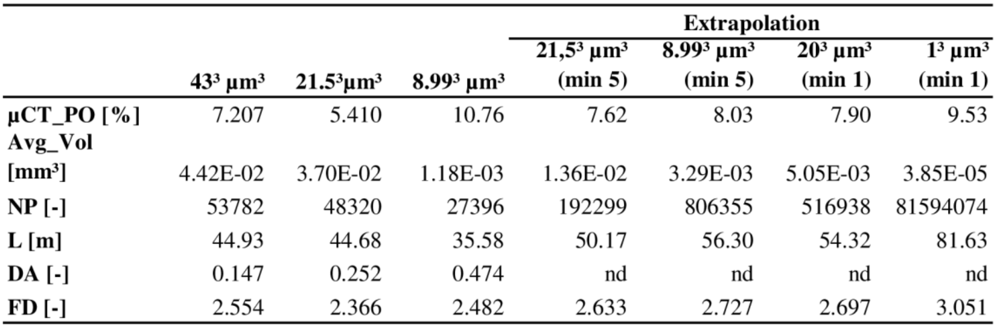

				Extrapolation			
	43³ µm³	**21.5³µm³**	**8.99³ µm³**	**21,5³ µm³ (min 5)**	**8.99³ µm³ (min 5)**	**20³ µm³ (min 1)**	**1³ µm³ (min 1)**
µCT_PO [%]	7.207	5.410	10.76	7.62	8.03	7.90	9.53
Avg_Vol [mm³]	4.42E-02	3.70E-02	1.18E-03	1.36E-02	3.29E-03	5.05E-03	3.85E-05
NP [-]	53782	48320	27396	192299	806355	516938	81594074
L [m]	44.93	44.68	35.58	50.17	56.30	54.32	81.63
DA [-]	0.147	0.252	0.474	nd	nd	nd	nd
FD [-]	2.554	2.366	2.482	2.633	2.727	2.697	3.051

The degree of anisotropy (DA) increased between resolutions, as FD decreased. We also observed in our **Paper II** a negative trend between DA and FD. This is inconsistent with Dal Ferro et al. (2013) who observed higher DA in soil cores than in soil aggregates. The extrapolated FD however increased with resolution due to the larger extrapolated porosity and number of pores. Regarding the sample with a 21.5^3 µm³ voxel size, the porosity and number of pores decreased, so did FD. Regarding the aggregate, porosity increased but NP decreased as well as FD. The calculation of FD is dependent on the porosity but also on the number of boxes of the smallest size (Halley et al. 2004).

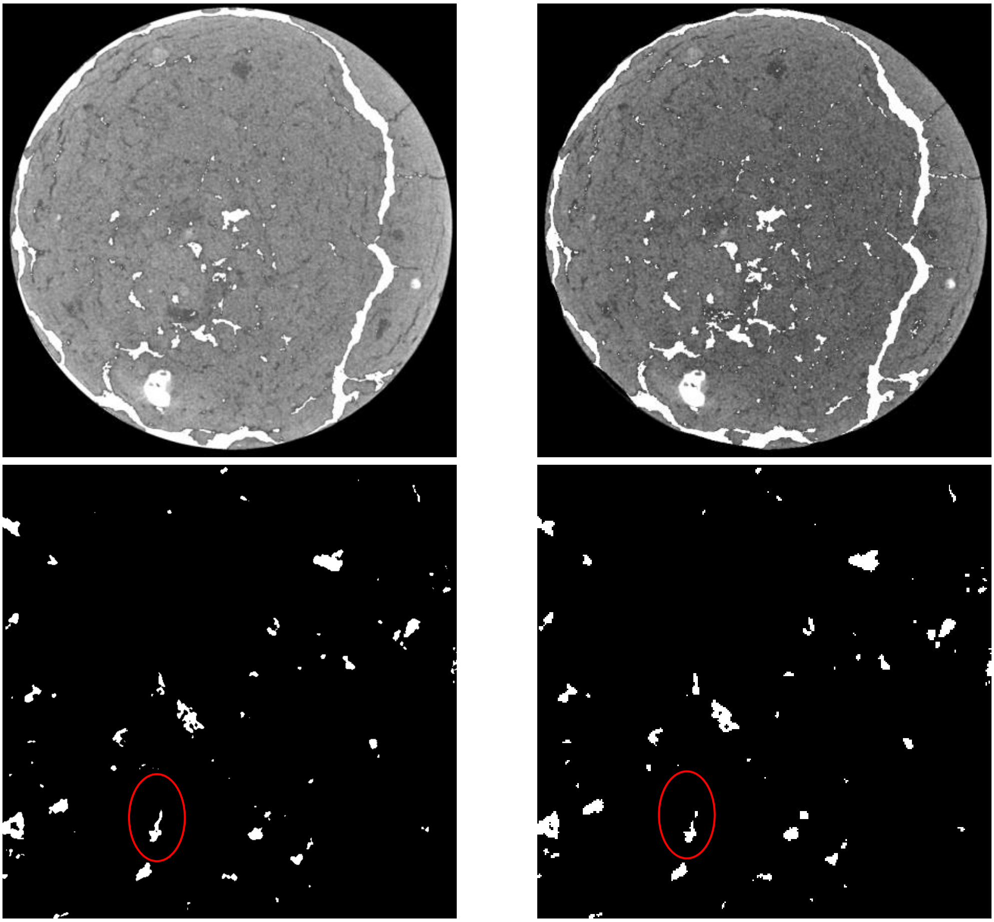

Figure 37. Upper row: Grayscale X-ray µCT images with the identified pore space in white. Lower row: Zoom-in of the binary X-ray µCT images. The original resolution (21.5^3 µm^3) is on the left-hand side and the coarsened resolution (43^3 µm^3) on the right-hand side.

5.4.2.2. Connectivity indicators

From the coarsened resolution (43^3 µm^3) to the original one (21.5^3 µm^3), the proportion of isolated porosity (IPO) and the Euler number (ε) decreased, the number of coordination (Avg_Z) increased as well as the global connectivity (Γ) and the total surface of connections (Con_Surf), see Table 10. This is consistent with our previous observations (Fig. 34) where we hypothesized that medium sizes pore probably merged to form larger pores. The value of Γ reflects that almost all pores were connected to each other. Houston et al. (2013b), comparing soils at 26 and 54^3 µm^3, did not observe a clear pattern of ε's evolution. Shah et al. (2016) observed that Avg_Z remained identical for some of their studied rock samples. Again, resolution effects are highly soil-type dependent. The smaller tortuosity with resolution is also consistent with the observed increased pore network connectivity and the fairly constant L (Table 9). Regarding the soil aggregate, IPO also decreased, and Avg_Z and Γ also increased with resolution, although not proportionally to the resolution. Again, inter-aggregate pores were contributors to the high connectivity observed at the sample scale and voxel size of 21.5^3 µm³. Con_Surf and ε did not however increase (or decrease for ε) with resolution. This is likely due to the proportionally smaller number of pores (Table 9). The decrease in tortuosity is however consistent.

Table 10. Connectivity indicators of the scanned sample (43^3 and 21.5^3 µm³) and aggregate (8.99^3 µm³).

	43^3 µm³	**21.5^3µm³**	**8.99^3 µm³**
IPO [%]	8.491	4.939	7.609
Avg_Z [-]	3.742	5.607	4.906
SC [voxel^{-1}]	0.283	0.209	0.172
Con_surf [mm²]	4420	93141	4377
Γ/IJ [-]	0.714	0.998	0.828
ε [-]	7226	6018	7559
τ [-]	1.280	1.253	1.205

5.4.2.3. Hydrodynamic predicators

Using the microscopic values from the X-ray µCT images at the original resolution (21.5^3 µm³) to predict log(Ks) and log(ka) led to reasonable results between the 25- 50% quantiles of the regression models, in comparison to the 50-75% for the X-ray µCT images at the coarsened results (43^3 µm³), see Table 11. As well, Shah et al. (2016) and Peng et al. (2014) concluded that coarsening the µCT images was sufficient to resolve Lattice-Boltzmann or Kozeny-Carman equations to evaluate sample permeability.

Table 11. Observed and predicted logarithmic values of the saturated hydraulic conductivity (Ks) and air permeability measured at a water matric potential of -70 kPa (ka) for sample #12. Predictions performed from the microscopic parameters extracted from the original resolution X–ray µCT images (21.5^3 µm^3) and coarsened resolution (43^3 µm^3) X-ray µCT images.

			log(Ks) [cm/d]		**log(ka) -70kPa [µm^2]**
Laboratory measurements			1.062		1.802
Predicted from		**Γ [-]**	**DA [-]**	**FD [-]**	**Avg_Svol [mm^3]**
43^3 µm^3	**25%**	-0.319	0.743	-3.265	1.391
	50%	0.617	0.986	-0.347	1.8320
	75%	1.564	1.224	2.418	2.260
21.5^3 µm^3	**25%**	0.201	1.020	-3.585	1.115
	50%	1.329	1.325	-0.782	1.504
	75%	2.470	1.622	1.878	1.883

5.4.3. Practical conclusion and discussion

Studying X-ray µCT images at various resolutions leads to various identified pore spaces and various microscopic parameters values. Comparisons between resolutions are highly dependent on the image processing and the pore network decomposition, and the working resolution should ultimately depend on the final research purpose. As also observed by other researchers (for their case studies), it appeared that scanning at the highest possible resolution and then coarsening the X-ray µCT image provide good results for our case study: due to the use of Bayesian statistics, which take into account the uncertainty inherent to the data, the microscopic parameters from the original, or the coarsened, resolution X-ray µCT images were both reasonable predicators of the sample-scale hydrodynamic properties.

Increasing the resolution led to the apparition of yet invisible connections, the soil pore network is indeed a continuum across space. We however observed that the pore distribution of the studied soil is not necessarily better approached with a smaller minimal pore volume. Moreover, the visible minimal volume is limited by the sample size, and finer details about the pore network would therefore come with a loss of information due to the required smaller sample size (Vogel et al., 2010). After all, we hypothesize that rather than pore volume continuous scale-dependency (as initially proposed); the pore volumes distributions between specified pore sizes could be similar across scales. That statement is similar to theories that postulate about the multifractal behavior of the SWRC (e.g. De Bartolo et al., 2018).

5.5. Research question #3: How does the air-filled porosity vary with water matric potential?

We first present a 3D visualization of identified pore space superimposed on the grayscale image of sample #20 scanned at -30 kPa. The volume in green is the identified pore space at -30 kPa that was not identified at -4 kPa. Some pores appeared and others got bigger with the increasing negative water matric potential (*h*).

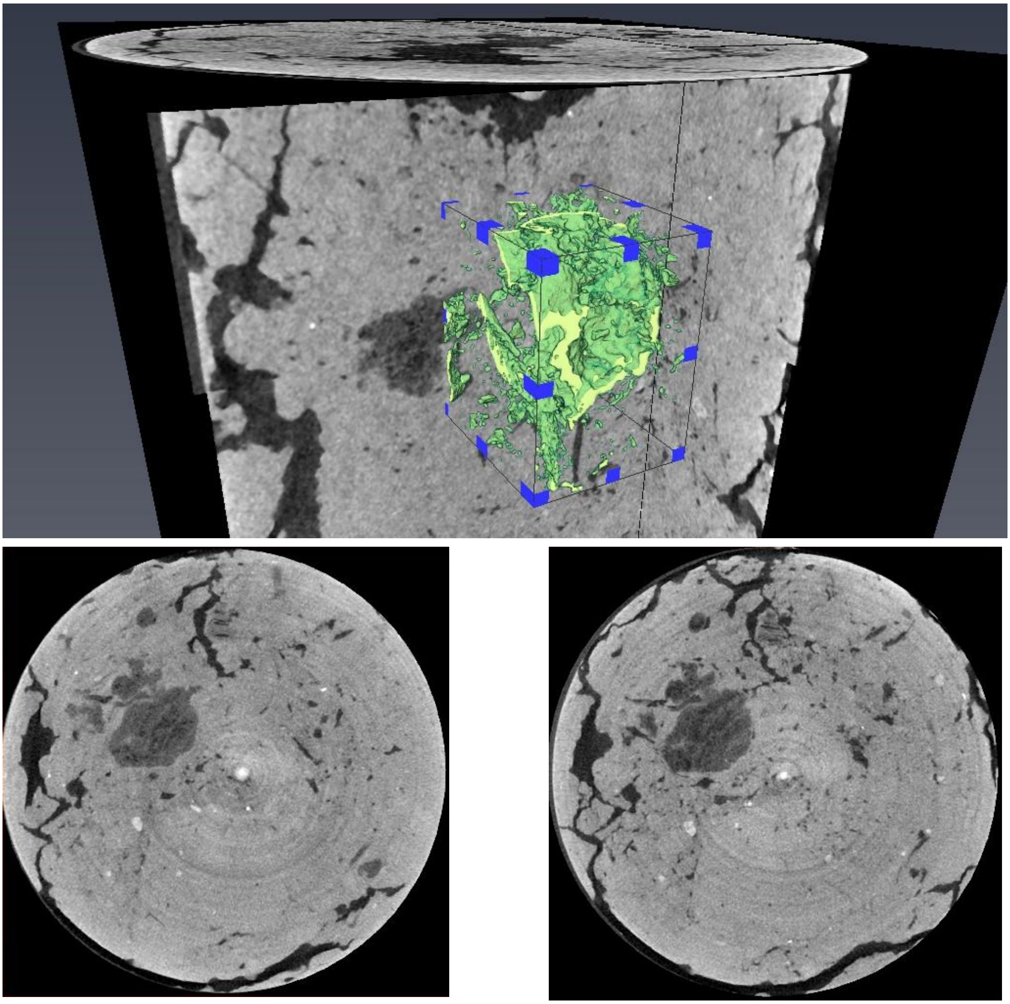

Figure 38. Upper row: X-ray µCT grayscale image of sample #20 scanned at -30 kPa with the green volume of the difference in identified pore space between -30 kPa and -4 kPa. Lower row: One slice of the X-ray µCT grayscale image of sample #20 scanned at -4 kPa (left-hand) and at -30 kPa (right-hand).

5.5.1. Global parameters

Table 12 presents the significant differences of the global parameters on the 3D images from the same soil samples scanned at various *h*. As a reminder, the visible pore space on the 3D images is the air-filled pore space and we expect the pore space to grow with a higher negative *h*. Many global parameters evolutions were logical:

- µCT porosity (µCT_PO) increased with increasing negative *h*, as did the fractal dimension (FD).
- Euler number (ε) was smaller at smaller negative *h* coming from the smaller amount of isolated pores, although the ratio of isolated porosity (IPO) was not different between -4 kPa and -10, -30, or -70 kPa. IPO was just larger at -10 kPa than at the other *h*. Figure 39 present the IPO values according *h* and samples.
- Tortuosity (τ) decreased with increasing negative *h*, more pore pathways should be available, indeed, total pore network length (L) increased with *h*.
- The averaged coordination (AvgZ) increased with increasing negative *h* except between -4 and -7 kPa where AvgZ decreased (from 3.81 to 3.68) but not significantly. Differences between -4 and -7 kPa are likely due to image processing and not from the soil sample drainage.
- The average volume of the small pores (Avg_Svol) decreased between -4 and -10 kPa, likely due to the apparition of smaller pores.
- The global connectivity (Γ) increased with increasing negative *h*.

The degree of anisotropy varied erratically between *h* (Figure 40) which is understandable since a growing pore space shouldn't make the pore space more isotropic or anisotropic. Some pores appeared and others grew dependent on their volume but also mostly on their accessibility.

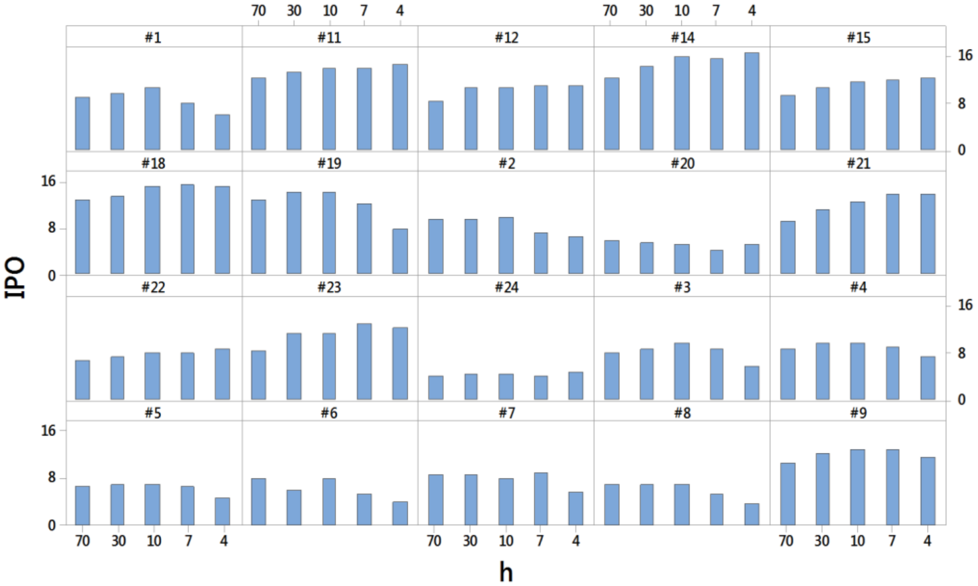

Figure 39. Proportion of isolated porosity (IPO, %) values by samples and water matric potential (*h*).

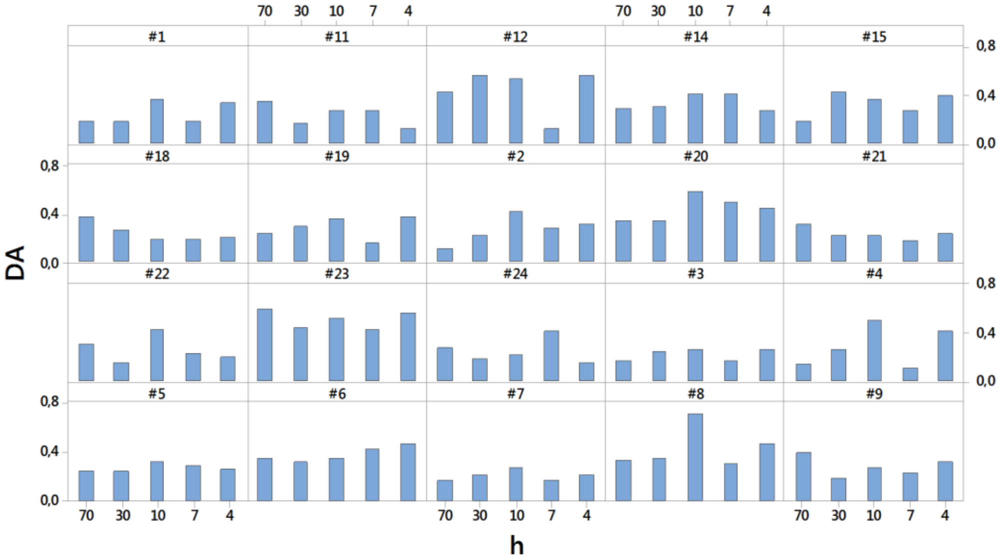

Figure 40. Degree of anisotropy (DA, -) values by samples and water matric potential (*h*).

Table 12. ANOVA results for the global parameters between water matric potentials (expressed in absolute values). Refer to Table 3 for the definitions of the microscopic parameters.

	comparison between scans at water matric potential [kPa] of									
	4-7	**4-10**	**4-30**	**4-70**	**7-10**	**7-30**	**7-70**	**10-30**	**10-70**	**30-70**
µCT_PO	*	*	*	*			*	*	*	
ε			*	*						
FD		*	*	*			*			
DA					*			*	*	
τ	*	*	*	*						
L			*	*			*			
Avg_Z			*	*	*	*	*			
SC										
IPO		*							*	
Avg_vol										
Avg_Bvol										
Avg_Svol		*								
SS		*	**	**						
Γ/IJ			*	*			*		*	

** 0.05 or ** 0.01 probability levels*

When including a covariate within the ANOVA model (ANCOVA analysis), it appeared that the hydrodynamic properties of the soil (Ks, ka measured at the specified *h*, and Lab_FD) influenced the significance of many tested global parameters. This means that the observed significant differences came from the particular hydrodynamic properties of the soil samples and not from purely processing variations of the X-ray µCT images quantification. In other words, we can be confident that the observed differences between 3D images of one soil sample scanned at various *h*, came from the inner hydrodynamic properties of the soil sample: how it drained in reaction to a specified negative *h*. Table 13 presents the relative efficiency of the ANCOVA over the ANOVA in cases where the covariate (left column) significantly changed the ANOVA outcome. Mainly the Ks and Lab_FD changed the ANOVA results to a higher test power.

Table 13. Relative efficiency of the ANCOVA over the ANOVA performed on the global parameters (columns) with associated covariates (rows). Refer to Table 3 for the definitions of the microscopic parameters.

	Global parameters													
Covariates	**μCT_PO**	**ε**	**FD**	**DA**	**τ**	**L**	**Avg_Z**	**SC**	**IPO**	**Avg_vol**	**Avg_Bvol**	**Avg_Svol**	**SS**	**Γ/IJ**
log(Ks)	17.08	1.92	5.41			5.59	4.20		4.86			9.74	9.893	
log(ka)		1.92	0.83			0.95						0.61		0.96
Lab_FD	18.27	1.92	5.37			4.81			5.35			8.99	8.265	3.12
μCT_PO		0.69	0.79			0.86						1.00	0.653	
ε												0.82		
FD		1.92				0.41						0.82	0.75	
DA														
τ		0.55										1.01		
L		0.98										0.94		
AvgZ														
SC												1.01		
IPO												0.69		
Avg_vol		0.83												
Avg_Bvol		0.96										0.43		
Avg_Svol		0.82												
SS														
Γ/IJ														

We also performed ANCOVA analyses with the other microscopic parameters used as the covariate. On one hand, only ε and Avg_Svol ANOVA significance were changed but without a higher power (relative efficiencies between 0 and 1, except for the ε by FD), and on the other hand, results might be trickier to interpret since measurements were performed on the same data: these were not *a priori* or *a posteriori* bias. The soil connectivity expressed by the Euler number is not significantly different between images of the same soil samples scanned at various h when other microscopic parameters are taken into account.

A principal component analysis between the samples scanned at various *h* as the individuals and the microscopic parameters as the variables, revealed that, although presenting varying global parameters with *h*, the combination of all the morphological and topological characteristics of the samples remained similar between *h*, in other words, the coordinates of the first four dimensions of the PCA remained similar between *h* (Fig. 41 and Fig. 42 for the first two dimensions). We quantitatively confirmed this with a K-clustering analysis which revealed various cases (Table 14):

- case1: all samples from various *h* were included in the same cluster of coordinates (for samples #5, #9, #18, #20, #23);
- case 2: all samples from various *h* were included in the same cluster but different than the initial one (for sample #24);
- case 3: all samples from various *h* were included in the same cluster except the sample scanned at -70 kPa which was the initial (for samples #11, #22);
- case 4: the samples scanned at -4 kPa had different coordinate than the samples scanned at the others *h* (for samples #1, #2, #6, #7, #8);
- case 5: all the samples scanned at various *h* were close to the others samples scanned at various h (for samples #3, #4, #12, #14, #15, #19, #21).

In cases where a sample at various *h* (individuals) was part of different clusters (case 3-5), the main differences between individuals came from the second dimension coordinates which was mostly constructed by the following well-projected variables ($\cos^2 > 0.5$): the Euler number, the fractal dimension, and the tortuosity.

Table 14. K-clustering analysis from the fourth principal component analysis dimensions. The cluster numbers are identical to the sample numbers.

	Water matric potential [kPa]						**Water matric potential [kPa]**				
Sample	**-70**	**-30**	**-10**	**-7**	**-4**	**Sample**	**-70**	**-30**	**-10**	**-7**	**-4**
#1	1	1	1	1	24	**#12**	12	12	12	9	12
#2	2	2	2	2	12	**#14**	14	14	11	11	18
#3	3	3	4	4	24	**#15**	15	11	2	2	2
#4	4	4	8	2	11	**#18**	18	18	18	18	18
#5	5	5	5	5	5	**#19**	19	7	2	2	11
#6	6	6	6	6	23	**#20**	20	20	20	20	20
#7	7	7	7	7	20	**#21**	21	21	9	9	9
#8	8	8	6	8	20	**#22**	22	21	21	21	21
#9	9	9	9	9	9	**#23**	23	23	23	23	23
#11	11	18	18	18	18	**#24**	22	22	22	22	22

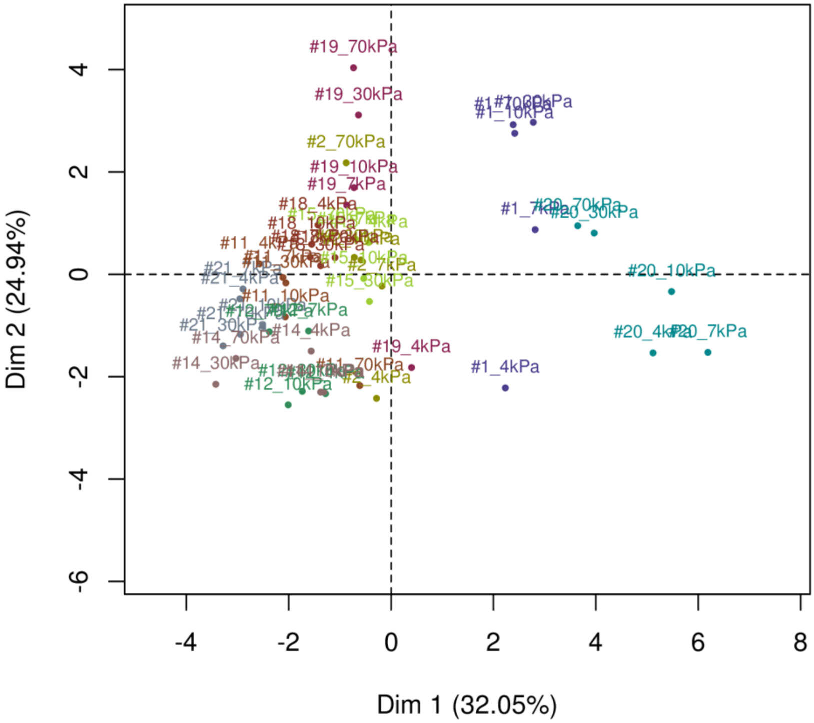

Figure 41. First and second dimensions of the individuals principal components for ten samples. One color per sample.

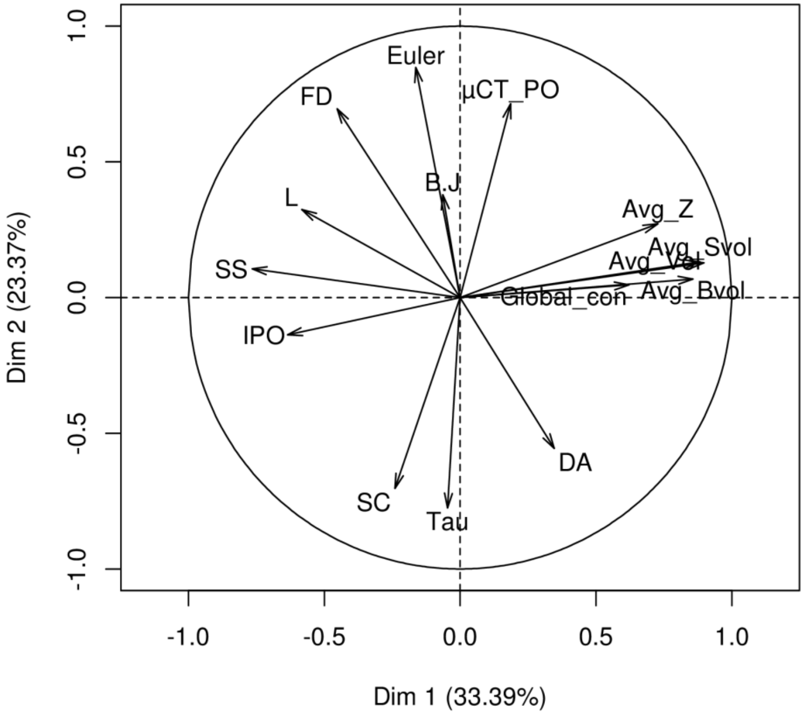

Figure 42. First and second dimensions of the variables principal components. The variables are the X-ray µCT global parameters. Refer to Table 3 for the definitions of the microscopic parameters.

5.5.2. Local parameters

The parameters evolutions between pore size ranges were logical with increasing connectivity and decreasing isolated porosity and averaged specific surface with growing pore size ranges. The conducted three-way ANOVA firstly revealed differences between several parameters calculated on specified pore size ranges (Table 15), but the performed post-hoc Tukey's test did not identify the significant differences between *h*. The mean squares of the following two-way ANOVA for the fixed parameters were indeed lower than the mean squares of the random interaction from the three-way ANOVA (higher sum of square). Neither Avg_Z nor the pore size distributions (f(r)) were different between *h* at any pore size ranges although Avg_Z was different between the lowest and highest negative *h* from a global point of view. The pore size distributions did not show any pattern between *h*, as illustrated by Fig. 43 for few samples. It then appeared that only the averaged specific surfaces (Avg_SS) of the smallest and biggest pores were affected by *h*. It is an opposite scheme for the surface connectivity (SC), the ratio of isolated porosity (IPO) and the average pore volume (Avg_Vol).

Table 15. Significant differences in local parameters between all water matric potentials. Refer to Table 3 for the definitions of the microscopic parameters.

Min radius (µm)	f(r)	SS	SC	Avg_Z	IPO	Avg_Vol
30		*				
37,5			*			
50		***				
75		***	**			
150		***	**			
167			***		**	
187			***		***	
215			***		**	**
250			**		**	**
300		*	***		*	
375		***	**			
500		***	**		**	
600		*	**			
750						*
1000		*				
1500			*			

** 0.05, ** 0.01, or ***0.001 probability levels*

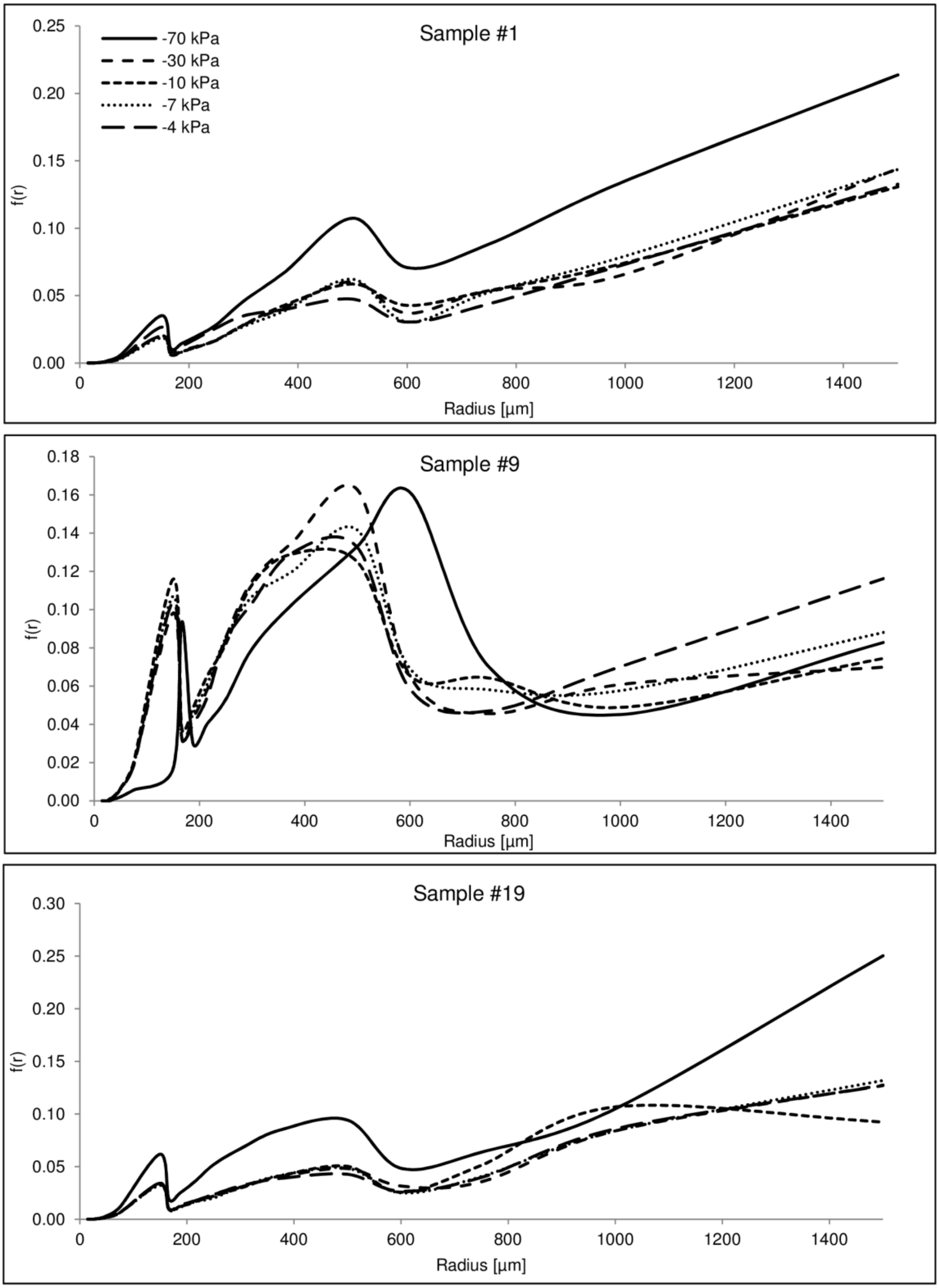

Figure 43. Pore size distribution at various water matric potential for three samples.

5.5.3. Practical conclusion and discussion

From the capillary theory, the X-ray µCT images voxel size (43^3 µm^3), and the water matric potentials at which the samples were scanned, no visible (quantifiable) differences between X-ray µCT images of the same sample should have appeared. We although observed significant differences in global microscopic parameters between the lowest and highest *h* at which the samples were scanned and significant differences in pores specific surfaces, connectivity and average pore volumes calculated on specific pore size ranges. We therefore quantitatively confirmed that the capillary theory applied to soil fluxes is an approximation. Retention curve data are usually converted into an available volume of pore with a specific size characterized in terms of radius from the capillary law. It is likely that retention curves data should rather be approached in term of accessible volume of pores, volume that should be characterized with microscopic parameters representing the connectivity and arrangement of the pore space.

5.6. Research question #4: How is the soil structure explained by organic carbon and iron content? At the origin of structure

Table 16 presents the credible observed correlations between the contents of organic carbon and iron within the studied soil samples and the microscopic parameters measured on the X-ray µCT images from Table 3. Only the forms of iron extracted with DCB (Fe_DCB) and oxalate (Fe_oxalate) were correlated to either the soil porosity, either measures of connectivity, highlighting the ability of crystalline and amorphous Fe oxides to affect these microscopic parameters values (Fig. 44 for an example). Their correlations to microscopic measurements were in opposite direction as suggested by the previously reported negative correlation between Fe_DCB and Fe_oxalate. When only considering the soil samples from the CT experiment, the same correlations as in Table 9 were observed, with however a higher degree of credibility (Fig. 45, lower graph) due to the contrasted values of Fe_DCB and Fe_oxalate. TOC was however not correlated to any microscopic parameters due to its high dependence on tillage practices, neither were the complex forms of Fe (Fe_pyrophosphate). Figure 45 (upper graph) displays the Euler number versus the TOC content for all samples with a visual distinction of CT (black circles) or RT experiment (white circles). When only considering the soil samples from the RT experiment, TOC was positively correlated to the pore network tortuosity (τ, $\rho=0.61$, BF=3.91) and surface connectivity (SC, $\rho=0.60$, BF=3.28), and negatively correlated to the Euler number (ε, $\rho=-0.65$, BF=6.36). Six et al. (2000) showed that the macroaggregate turnover is twice as fast in CT than in RT and the formation of microaggregate within macroaggregate is reduced by a factor 2 in CT than in RT, in other words, there is more sequestration of organic carbon in RT than in CT. However, the same value of ε was observed in RT or CT experiment, and from a microscopic characterization point of view, we did not observe any differences between the tillage experiments. We therefore turn the question around: would the accumulation of organic carbon and resulting associations to free forms of Fe have shaped the pore network and increased the connectivity and tortuosity? The monitoring of soil sample microscopic structure after incubation of Fe and organic matter could be an interesting option to evaluate the effects of organo-mineral associations on the evolution of the pre network complexity. For example, Schlüter and Vogel (2016) proposed an approach to track changes in soil structure with small incorporated garnet particles.

Table 16. Correlations between Fe_DCB, or Fe_oxalate, and several microscopic parameters. Refer to Table 3 for the definitions of the microscopic parameters.

	Fe_DCB	**Fe_Oxalate**
µCT_PO	0.48	-0.47
Large_PO	0.48	-0.47
Avg_Z		-0.53
ε	0.56	
τ	-0.61	0.52
Con_Surf		-0.51
SC	-0.57	0.48

3>BF<10 in green; 10<BF<30 in yellow

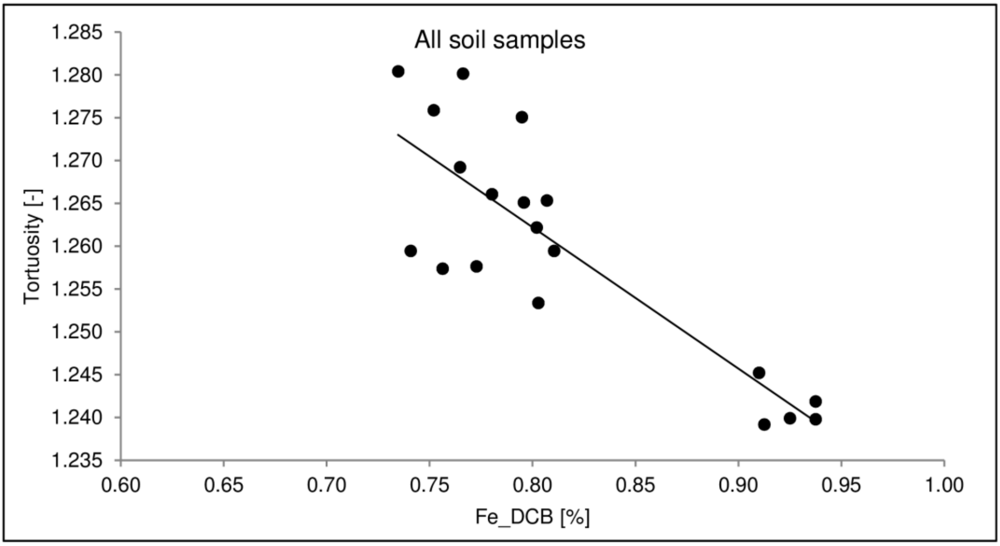

Figure 44. Tortuosity measured on the X-ray µCT images (τ) versus Fe extracted with DCB (Fe_DCB) for all soil samples.

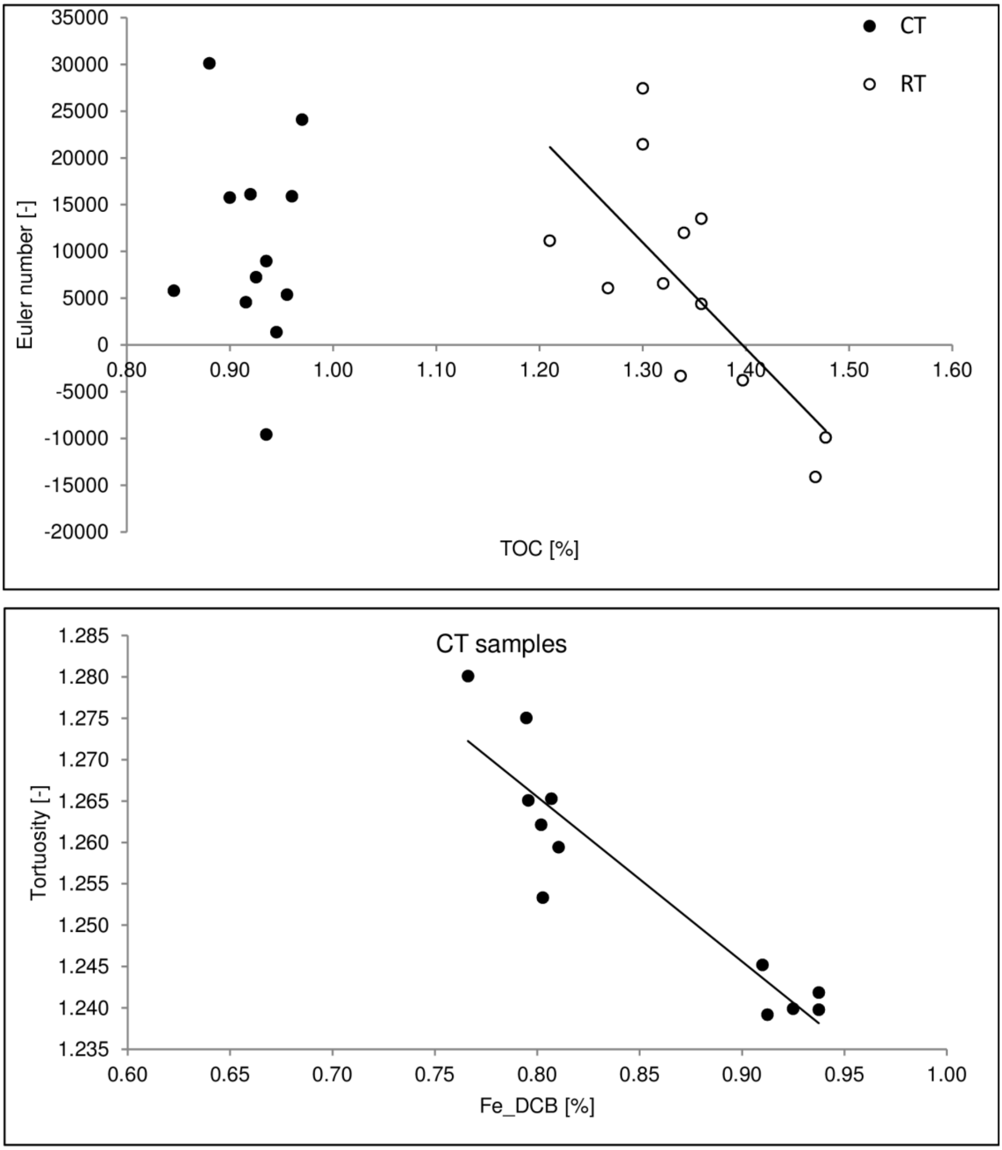

Figure 45. Upper-graph: The Euler number calculated on the X-ray µCT images (ε) versus the total organic carbon content (TOC) for all samples. Lower-graph: Tortuosity calculated on the X-ray µCT images (τ) versus the Fe extracted with DCB (Fe_DCB) for the samples from the CT experiment.

6

Perspectives

The use of soil X-ray µCT images goes hand in hand with an appropriate image processing scheme. To be confident with the applied image processing methodology, a transversal objective of this dissertation was the evaluation of several segmentation methods and pre- and post-segmentation median filtering effects on the extracted data of the resulting binary images. To that purpose, we generated artificial 2D grayscale "simulated images" to be processed. We hypothesized the statistical outcomes would be transposable to 3D real soil grayscale X-ray µCT images. 3D processing should indeed be promoted instead of the 2D processing of 3D stacks, otherwise unrealistic pore space geometry could be generated (Kaestner et al., 2008; Tuller et al., 2013). We admit the generated grayscale histograms presented more distinct peaks than the ones from the real soil X-ray µCT images, we were however confident in the transposability of our research conclusions because the real soil X-ray µCT images histograms also showed two peaks (representing the air and "solid+liquid" phases), which is required for the proper use of the selected global segmentation method. Possible ways to improve the generation of grayscale simulated images are to evaluate the effects on the grayscale histogram of 1) the ratio of the pores sizes over the image size, and 2) the applied noise to the original binary phase. A critical analysis would also point out that local segmentation is more appropriate for 3D processing because scanner source inhomogeneity could occur and alter the phase's identification across the sample height. In our case study, however, the X-ray microtomograph was equipped with a stabilized electron source and no density variations were observed. Moreover, local thresholding is more computationally demanding and the algorithms are usually not even written for large data set (e.g., greater than 8 Go). After all, beside the median filter, which is widely used, there are other edge-preserving filters in the literature that should/could also worth a test. The image processing methodologies applied in research papers are often not enough substantiated, and the generation of artificial images from which ground-truth information (the original binary phases) is available is the option we have chosen to justify the image processing methodology we applied.

Because the multiple image processing steps can all have a profound impact on the binary images, it is less straightforward to compare studies and data. The open access to grayscale data would be an opportunity for more scientific outcomes and encouraging scientific collaboration and networking. We don't argue in favor of image processing standardization because it is highly dependent on the raw grayscale image quality and subjective controls of the applied process should be performed. Standardization of pore decomposition methods could although be homogenized. A recent initiative by Koestel (2018) was the uploading of a user-friendly ImageJ plugin specifically designed for the quantification of soil X-ray µCT images features. We have not tested it and we do not favor one method more than other, yet, more assessments of quantification algorithms, such as the review recently published by Houston et al. (2017), are necessary.

Last but not least, quantifying and weighing the uncertainty of the processed X-ray µCT images could as well bring improvement into the appropriate use of X-ray µCT information. We did it within this dissertation through the use of Bayesian statistics when we analyzed the relationships of our X-ray µCT images to our laboratory measurements. Uncertainty could also be taken into account immediately from the segmentation step, for example, Kulkarni et al. (2011) proposed a Bayesian Markov random field framework to segment multiphase grayscale images. Another option would be to "classically" segment grayscale images and associate the resulting 3D binary images to a 3D uncertainty propagation map that would be associated to any quantification performed on the binary image.

The experimental decisions we needed to take also concerned the samples preparation and the hydrodynamic measurements. For example, we scanned the samples at a water matric potential of -70 kPa so most of the potential visible porosity would be air-filled. This led to the apparition of drying cracks, which was not, after all, a major issue since the hydrodynamic measurements were performed on the very same samples. This is also the reason why we measured the saturated hydraulic conductivity (Ks) at the end of the retention curve, so the X-ray µCT visible cracks would affect the measured conductivities, although bearing in mind that the sample re-saturation could also have modified the structure and affect the measured conductivities. In their study, Elliot et al. (2010) observed different Ks values when measured before or after scanning (and therefore draining) and emphasized the fact that there is no way to determine the "real" Ks value. They mentioned a "real" Ks value because they predicted Ks directly from the X-ray µCT visible observed pore size distribution through the use of physical equations. Within that context, it is indeed impossible to argue in favor of one or another Ks measurement time. From these considerations, we argue in favor of unified measurements techniques and "time of measures" that would rather lead us to define soil X-ray µCT global characteristics that could afterwards be used for the generation of phenomenological models, for example.

Still regarding the experimental choices, it is worth noticing that we calculated the soil samples density from the standard quartz density value although is it possible to measure the real soil density with a pycnometer or to adjust that value according the organic matter content (Rawls, 1983). Within this research project, these last values were however available only after our second paper was published. In terms of density (and therefore porosity), we also observed large variations between samples that were, in the end, taken from an area of 1 m². Soil structure is indeed unique and we emphasize on the importance of analyzing the same soil samples at the micro- and macroscopic scales.

As just stated, the structure was different between samples, as well was the origins of the observed pore network structure: biological, structural, with or without drying cracks (as mentioned above). Methodologies exist to distinguish biopores from non-biopores, for example by visual identification (Naveed et al., 2016), or under successive geometrical hypotheses (Zhang et al., 2018). We did not consider the structural or biological origins of pores within this research project because on one hand, both types of pore could contribute to air and water fluxes and on the other hand, distinguishing the type of pores is still subjective. Again, we aimed at describing the soil pore network from a global perspective. The simpler it is, the more reproducible would it be. In the end, we indeed succeeded at explaining the soil saturated hydraulic conductivity by three global pore network characteristics and the soil air permeability by the average volume of the smallest pore. Moreover, we highlighted the drawbacks of using the capillary law to extract pore size distribution from soil water retention curve measurements, and showed several times that there was likely a scaling relationship between groups of pores of similar volumes. From these findings, we propose that the available volume of porosity for water or air transport as a function of water matric potential could be converted into an *accessible* (word borrowed from Hunt et al., 2013) volume of porosity that should be characterized, not by a minimal and maximal circular section, but by a global microscopic attribute. When scaling relationships between groups of pores will be well identified, the pores only accessible at high negative potential (and invisible even with the highest X-ray µCT resolution) could also be characterized by global structural microscopic characteristics derived from the ones of the visible pores. To reach these goals, we encourage experiments and analyses in a way where massive substantiated data resources could be shared.

Multiplying data would also enable the generation of pore network representation grid from microscopic global characteristics. This type of representation would be useful for the simulation of water of air fluxes from equations that would couple biochemical processes to fluid mechanics, for example. We indeed previously pointed out that soil physics and soil biochemistry are inextricably linked and interdependent. Moreover, the biochemical processes occurring within the soil affect, or control, the exchange of gases with the atmosphere and the storing of organic carbon through its stabilization or decomposition, both are of major importance when it comes to the prediction of global climate. Chenu et al. (2018) recently reviewed several studies showing that the localizations of microorganisms or chemical elements is not random and depend on pore size or undecomposed organic matter proximity, for example, and that the biochemical processes occurring at nano- or micro-scale affect the soil functions at the field scale. For example, Cornelis et al. (2018) recently confirmed the occurrence of micro-spots where the physico-chemical conditions promote, or not, the formation of organo-mineral associations. We also showed, within this dissertation, that several global microscopic structural parameters were correlated to the soil organic matter and iron contents. More experiments are needed to draw firm relationships, as proposed in the conclusion of that chapter. It either way points out the potential of using of X-ray microtomography to study the soil biochemistry.

We believe there are two stages to that end. It is first essential to understand how the pore network geometry (and the resulting physico-chemical conditions, or micro-organisms distributions) influences the soil biochemical processes. Afterwards, the use of simplified pore network representation grids becomes most important to evaluate the equations that would resolve physico-biochemical interactions. To understand processes, combining X-ray microtomography to other visualization technique is an interesting option. X-ray microtomography is the most efficient technique when it comes to the identification of physical phases at high resolution. Regarding the chemical composition of samples, there are visualization techniques that identify the chemicals distributions on, however, smaller two-dimensional samples. The technique choice ultimately depends on the desired resolution and final information (bulk, interfaces, surfaces, sub-surfaces, buried layers, atomic scale information). The sample nature and its stability, its preparation and destructive possibilities are points to evaluate before selecting a measurement technique. Moreover, it is not straightforward to combine visualization outcomes from two techniques (Hapca et al., 2015). After all, precious care should be brought to the visualization representation potential risks (T. Morineau, personal communication). User could consider a representation as valid although the study area and/ or the technical measure are inappropriate. An appropriate representation should be connected to a well-understood study area and performed with a technique that enables that representation. Otherwise, there are many risks of performing induction rather than abductive reasoning, but that statement is valuable in any scientific field.

The use of X-ray microtomography in soil science has the potential to bring the study of the soil hydrodynamic to an upper level; it must however come with an appropriate use of the technique and a well-defined experimental environment.

References

Anderson, S.H. (2014). Tomography-measured macropore parameters to estimate hydraulic properties of porous media. *Procedia Comput. Sci.* 36, 649-654. doi:10.1016/j.procs.2014.09.069

Arthur, E., Modlrup, P., Schjonning, P., and de Jonge, L. W. (2012). Linking particle and pore size distribution parameters to soil gas transport properties. *Soil Sci. Soc. Am. J*. 76(1), 18-27

Ball, B. C., and Schjønning, P. (2002). "Air permeability" in *Methods of Soil Analysis, Part 1,* ed. J.H. Dane, G.C Topp. (Soil Science Society of America), 1141-1158

Baruchel, J., Buffière J-Y., Maire, E., Merle, P., and Peix, G. (2000). *X-ray tomography in material science*. Paris:Hermes Science Publications

Bascomb, C. L. (1984). Distribution of pyrophosphate extractable iron and organic carbon in soils of various groups. *J. Soil Sci.* 19, 251-268.

Baveye, P. C., and Laba, M. (2015). Moving away from the geostatistical lamppost: Why, where, and how does the spatial heterogeneity of soils matter? *Ecol. Modell.* 298, 24-38.

Baveye, P. C., Laba, M., Otten, W., Bouckaert, L., Dello Sterpaio, P., Goswami, R. R., et al. (2010). Observer-dependent variability of the thresholding step in the quantitative analysis of soil images and X-ray microtomography data. *Geoderma*. 157, 51-63.

Baveye, P. C., Pot, V., and Garnier, P. (2017). Accounting for sub-resolution pores in models of water and solute transport in soils based on computed tomography images: Are we there yet? *J. Hydrology*. 555, 253-256

Beckers, E., Plougonven, E., Gigot, N., Léonard, A., Roisin, C., Brostaux, Y. et al. (2014a). Coupling X-ray microtomography and macroscopic soil measurements: a method to enhance near saturation functions *? Hydrol. Earth Syst. Sci.* 18, 1805-1817.

Beckers, E., Plougonven, E., Roisin, C., Hapca, S., Léonard, A., and Degré, A. (2014b). X-ray microtomography: A porosity-based thresholding method to improve soil pore network characteristization? *Geoderma.* 219-220, 145-154.

Ben-Noah, I., and Friedman, S. P. (2018). Review and evaluation of root respiration and of natural and agricultural processes of soil aeration. *Vadose Zone J.* 17 (1). doi: 10.2139/vzj2017.06.0119

Blackmore, L. C., Searler, P. L., and Daly, B. K. (1981). *Methods for chemical analysis of soils.* New Zealand: Soil Bureau Scientific, Report 10A. 19B1-2nd revision.

Blackwell, P. S., Ringrose-Voase, A. J., Jayawardane, N. S., Olsson, K. A., McKenzie, D. C., and Mason, W. K. (1990). The use of air-filled porosity and intrinsic permeability to air to characterize structure of macropore space and unsaturated hydraulic conductivity of clay soils. *J Soil Sci.* 41, 215-28.

Buckingham, E. (1904). *Contributions to our knowledge of the aeration of soils*. Washigton, DC: U.S. Gov. Print. Office.

Burdine, N.T. (1953). Relative permeability calculations from pore size distribution data. *J. of Petroleum Technology*, 5(3), 71-78.

Calvet, R. (2005). *Les pesticides dans le sol: conséquences agronomiques et environnementales*. Paris : France Agricole Editions.

Chenu, C., Nunan, N., Vieublé, L., Garnier, P., Pot, V., and Recous, S. (2018). “Localisation des matières organiques et des activités microbiennes : conséquences pour le fonctionnement du sol” in *Les sols et la vie souterraine,* ed. Quae, 26-36.

Corey, A.T. (1986). “Air permeability”, in *Methods of Soil Analysis, Part 1,* ed. J.H. Dane, G.C Topp. (Soil Science Society of America), 1121-1136.

Cornelis, J.-T., Delvaux, B., Van Ranst, E., and Rouxhet, P.G. (2018). Sub-micrometer distribution of Fe oxides and organic matter in Podzol horizons. *Geoderma.* 323, 126-135.

Cousin, I., Levitz, P., and Bruand, A. (1996). Three-dimensional analysis of a loamy-clay soil using pore and solid chord distributions. *Eur. J. of Soil Sci.* 47, 439-452.

Dal Ferro, N., Delmas, P., Duwig, C., Simonetti, G., and Morari, F. (2012). Coupling X-ray microtomography and mercury intrusion porosimetry to quantify aggregate structures of cambisol under different fertilization treatments. *Soil & Tillage Res.* 119, 13-21.

Dal Ferro, N., Charrier, P., and Morari, F. (2013). Dual-scale micro-CT assessment of soil structure in a long-term fertilization experiment. *Geoderma.* 204-205, 84-93.

Dal Ferro, N., Strozzi, A. G., Duwig, C., Delmas, P., Charrier, P., and Morari, F. (2015). Application of smoothed particle hydrodynamics (SPH) and pore morphologic model to predict saturated water conductivity from X-ray CT imaging in a silty loam Cambisol. *Geoderma.* 255-256, 27-34.

Daly, K. R., Cooper, L. J., Koebernick, N., Evaristo, J., Keyes, S. D., van Veelen, A., et al. (2017). Modelling water dynamics in the rhizosphere. *Rhizosphere.* 4, 139-151.

Daly, K. R., Cooper, L. J., Koebernick, N., van Veelen, A., Mayon, R. Fletcher, D. M., et al. (2018). Using image based modelling to predict soil water dynamics. GRA, 20, EGU2018-744. Abstract retrieved from the Geophysical Research Abstracts database.

Dane, J. H., Vrugt, J. A., and Unsal, E. (2011). Soil hydraulic functions determined from measurements of air permeability, capillary modeling, and high-dimensional parameter estimation. *Vadose Zone J.* 10, 459-65.

Davidson, E. A., and Janssens, I. A. (2006). Temperature sensitivity of soil carbon decomposition and feedbacks to climate change. Nature. 440, 165-173. doi:10.1038/nature04514.

De Bartolo, S., Fallico, C., and Severino, G. (2018). A fractal analysis of the water retention curve. *Hydrol. Proc.* 32, 1401-1405. doi: 10.1002/hyp.11498.

Deepagoda, T. K. K. C., Moldrup, P., Schjonning, P., de Jonge, L. W., and Komatsu, T. (2011). Density-corrected models for gas diffusivity and air permeability in unsaturated soil. *Vadose Zone J.* 10, 226-38.

DIN ISO 11274 (2012). Soil quality – Determination of the water retention characteristics – Laboratory methods (ISO 11274:1998 + Cor. 1:2009) English translation of DIN ISO 11274, 2012-04. Deutsches Institut für Normung, Berlin, Germany.

Doube, M., Klosowski, M. M., and Arganda-Carreras, I. et al. (2010). Bone-J: Free and extensible bone image analysis in ImageJ. *Bone.* 47(6), 1076-1079.

Durner, W. (1994). Hydraulic conductivity estimation for soils with heterogeneous pore structure. *Water Resour. Res.* 30, 211–223. doi:10.1029/93WR02676

Elliot, T.R., Reynolds, W.D., and Heck, R.J. (2010). Use of existing pore models and X-ray computed tomography to predict saturated soil hydraulic conductivity. *Geoderma* 156, 133-142.

Eusterhues, K., Rumpel, C., and Kögel-Knabner, I. (2005). Organo-mineral associations in sandy acid forest soils: importance of specific surface area, ironoxides and micropores. *Eur. J. of Soil Sci.* 56, 753-763.

Falconer, E. R., Houston, A. N., Otten, W., and Baveye, P. C. (2012). Emergent behavior of soil fungal dynamics: Influence of soil architecture and water distribution. *Soil Sci.* 177(2), 111-119.

Gao, L., Beckers, E. Liang, G., Houssou, A. A., Wu, H., Wu, X. et al. (2017). Effect of different tillage systems on aggregate structure and inner distribution of organic carbon. *Geoderma.* 288, 97-104.

Garbout, A., Munkholm, L.J., and Hansen, S.B. (2013). Tillage effects on topsoil structural quality assessed using X-ray CT, soil cores and visual soil evaluation. *Soil Tillage Res.* 128, 104-109.

Hamamoto, S., Moldrup, P., Kawamoto, K., and Komatsu, T. (2009). Effect of particle size and soil compaction on gas transport parameters in variably saturated, sandy soils. *Vadose Zone J.* 8(4), 986-95.

Hapca, S. M., Houston, A. N., Otten, W., and Baveye, P. C. (2013). New local thresholding method for soil images by minimizing grayscale intra-class variance. *Vadose Zone J.* 12(3). doi:10.2136/vzj2012.0172.

Hapca, S. M., Baveye, P. C., Wilson, C., Lark, R. M., and Otten, W. (2015). Three-dimensional mapping of soil chemical characteristics at micrometri scale by combining 2D SEM-EDX data and 3D X-ray CT images. *PLos ONE*. 10(9). doi: 10.1371/journal.pone.0137205.

Harrigan, T. P., and Mann, R. W. (1984). Characterization of microstructural anisotropy in orthotropic materials using a 2nd rank tensor. *J. Mater. Sci.* 19(3), 761–767.

Hiel, M. P., Barbieux, S., Pierreux, J., Olivier, C., Lobet, G., Roisin, C., Garré, S., Colinet, G., Bodson, B., and Dumont, B. (2018). Impact of crop residue management on crop production and soil chemistry after seven years of crop rotation in temperate climate, loamy soils. *PeerJ.* 6, e4836. doi: https://doi.org/10.7717/peerj.4836

Houston, A. N., Otten, W., Baveye, P. C., and Hapca, S. M. (2013a). Adaptive-window indicator kriging: A thresholding method for computed tomography images of porous media. *Comput. Geosci.* 54, 239-248.

Houston, A. N., Schmidt, S., Tarquis, A. M., Otten, W., Baveye, P. C., and Hapca, S. M. (2013b). Effect of scanning and image reconstruction settings in X-ray computed microtomography on quality and segmentation of 3D soil images. *Geoderma.* 207-208, 154-165.

Houston, A. N., Otten, W., Falconer, R., Monga, O., Baveye, P. C., and Hapca, S. M. (2017). Quantification of the pore size distribution of soils: Assessment of existing software using tomographic and synthetic 3D images. *Geoderma* 299, 73-82.

Hunt, A. G., Ewing, R. P., and Horton, R. (2013). What’s wrong with soil physics? *Soil Sci. Soc. Am. J.* 77, 1877-1887.

Iassonov, P., Gebrenegus, T. and Tuller, M. (2009). Segmentation of X-ray computed tomography images of porous materials: A crucial step for characterization and quantitative analysis of pore structures. *Water Resour. Res.* 45(9). doi:10.1029/2009WR008087.

Iassonov, P., and Tuller, M. (2010). Application of segmentation for correction of intensity bias in X-ray computed tomography images. *Vadose Zone J.* 9(1), 187-191.

Jassogne, L., McNeill, A., and Chittleborough, D. (2007). 3D-visualization and analysis of macro- and meso-porosity of the upper horizons of a sodic, texture-contrast soil. *Eur. J. of Soil Sci.* 58, 589-598.

Jeffreys, H. (1961). Theory of probability. Oxford: UK Oxford University Press.

Kaestner, A., Lehmann, E., and Stampanoni, M. (2008). Imaging and image processing in porous media research. *Adv. Water Resour.* 31, 1174-1187.

Katuwal, S., Moldrup, P., Lamandé, M.,Tuller, M., and de Jonge, L. W. (2015a). Effect of CT number derived matrix density on preferential flow and transport in a macroporous agricultural soil. *Vadose Zone J.* 14, 1-13 pages. doi: 10.2136/vzj2015.01.0002.

Katuwal, S. Norgaard, T., Moldrup, P., Lamandé, M., Wildenschild, D., and de Jonge, L. W. (2015b). Linking air and water transport in intact soils to macropore characteristics inferred from X-ray computed tomography. *Geoderma.* 237-238, 9-20. doi: 10.1016/geoderma.2014.08.006.

Kerboas, C., Hamada, M., Mahe, S., and de Anna, P. (2018). Flows through confined micro-structures in presence of microbial growth. GRA, 20, EGU2018-17598. Abstract retrieved from the Geophysical Research Abstracts database.

Kim, H., Anderson, S. H., Motavalli, P. P., and Gantzer, C. J. (2010). Compaction effects on soil macropore geometry and related parameters for an arable field. *Geoderma.* 160, 244-251.

Kleber, M., Eusterhues, K., Keiluweit, M., Mikutta, C., Mikutta, R., and Nico, P.S. (2015). Mineral-organic associations: formation, properties, and relevance in soil environments. *Adv. Agron.* 130 (chapter one).

Koestel, J., and Larsbo, M. (2014). Imaging and quantification of preferential solute transport in soil macropores. *Water Resour. Res.* 50(5), 4357-4378. doi:10.1002/2014WR015351

Koestel, J. (2018). SoilJ: an ImageJ plugin for the semiautomatic processing of three-dimensional X-ray images of soils. *Vadose Zone J.* 17. doi: 10.2136/vzj.03.0062

Köhne, J.M., Schlüter, S., and Vogel, H-J. (2011). Predicting solute transport in structured soil using pore network models. *Vadose Zone J.* 10, 1082-1096.

Kravchenko, A. N., Wang, A. N. W., Smucker, A. J. M., and Rivers, M. L. (2011). Long-term differences in tillage and land use affect intra-aggregate pore heterogeneity. *Soil Sci. Soc. Am. J.* 75(5),1658-1666.

Kulkarni, R., Tuller, M., Fink, W., and Wildenschild, D. (2012). Three-dimensional multiphase segmentation of X-rat CT data of porous materials using a Bayesian Markov random field framework. Vadose Zone J. 11(1) doi: 10.2136/vzj2011.0082.

Lamandé, M., Wildenschild, D., Berisso, F.E., Garbout, A., Marsh, M., Moldrup, P., et al. (2013). X-ray CT and laboratory measurements on glacial till subsoil cores: assessment of inherent and compaction-affected soil structure characteristics. *Soil Sci.* 178(7), 359-368.

Landis, E.N. and Keane, D.T. (2010). X-ray microtomography. *Mater. Charact.* 61, 1305-1316.

Larsbo, M., Koestel, J., and Jarvis, N. (2014). Relations between macropore network characteristics and the degree of preferential solute transport. *Hydrol. Earth Syst. Sci.* 18,5255-5269.

Legland, D., Arganda-Carreras, I., and Andrey, P. (2016). MorphoLibJ: Integrated library and plugins for mathematical morpholofy with ImageJ. *Bioinformatics.* 32(22), 3532-3534. doi: 10.1093/bioinformatics/btw413.

Loll, P., Moldrup, P., Schjønning, P., and Riley, H. (1999). Predicting saturated hydraulic conductivity from air permeability: Application in stochastic water infiltration modeling. *Water Resour. Res.* 35 (8), 2387-2400.

Luo, L., Lin, H., and Halleck, P. (2008). Quantifying soil structure and preferential flow in intact soil using X-ray computed tomography. *Soil Sci. Soc. Am. J.* 72(4), 1058-1069.

Luo, L., Lin, H., and Li, S. (2010a). Quantification of 3-D soil macropore networks in different soil types and land uses using computed tomography. *J. Hydrol.* 393, 53-64.

Luo, L., Lin, H., and Schmidt, J. (2010b). Quantitative relationships between soil macropore characteristics and preferential flow and transport. *Soil Sci. Soc. Am. J.* 74(6), 1929-1937.

Mandelbrot, B.B. (1983). *The fractal geometry of nature.* San Francisco: W.H. Freelan.

Mason, G., and Morrow, N.R. (1991). Capillary behavior of perfectly wetting liquid in irregular triangular tubes. *J. Colloid Interface Sci.* 141(3), 262-274.

McKenzie, N., Coughlan, K., and Cresswell, H. (2002). Soil physical measurement and interpretation for land evaluation. Collingwood, Australia: Csiro Publishing.

Mehra, O. P., and Jackson, M. L. (1960). “Iron acid removal from soils and clays by a dithionite-citrate system buffered with sodium bicarbonate” In: *Clays and Clay Minerals: proceesings of the Seventh National Conference*, Ana Swineford (New-York: Pegramon press), 317-327.

Millington, R. J., and Quirk, J. M. (1961). Permeability of porous solids. *Trans. Faraday Soc.* 57, 1200-1207.

Moldrup, P., Olesen, T., Komatsu, T., Schjonning, P., and Rolston, D.,E. (2001). Tortuosity, diffusivity, and permeability in the soil liquid and gaseous phases. *Soil Sci. Soc. Am. J.* 65, 613-23.

Moldrup, P., Yoshikawa, S., Olesen, T., Komatsu, T., and Rolston, D. E. (2003). Air permeability in undisturbed volcanic ash soils: predictive model test and soil structure fingerprint. *Soil Sci. Soc. Am. J.* 67(1), 32-40.

Mossadeghi-Björklund, M., Arvidsson, J., Keller, T., Koestel, J., Lamandé, M., Larsbo, M., et al. (2016). Effects of subsoil compaction on hydraulic properties and preferential flow in a Swedish clay soil. *Soil Til. Res.*, 156, 91-98. doi: 10.1016/j.still.2015.09.013.

Mualem, Y. (1976). A new model for predicting the hydraulic conductivity of unsaturated porous media. *Water Resour. Res.* 12, 513-22.

Naveed, M., Moldrup, P., Arthur, E., Wildenschild, D., Eden, M., Lamandé, M., et al. (2012). Revealing soil structure and functional macroporosity along a clay gradient using X-ray computed tomography. *Soil Sci. Soc. Am. J.* 77, 403-411. doi: 10.2136/sssaj2012.0134

Naveed, M., Moldrup, P., Schaap, M. G., Tuller, M., Kulkarni,R., Vogel, H-J., et al. (2016). Prediction of biopore- and matrix-dominated flow from X-ray CT-derived macropore networkds characteristics. *Hydrol. Earth. Syst. Sci.* 20, 4017-4030.

Nimmo, J. R. (2004). "Porosity and pore size distribution". In: *Encyclopedia of Soils in the Environment*, ed. Hillel, D. (London: Elsevier), 295-303.

Oades, J. M. (1988). The retention of organic matter in soils. *Biogeochemistry*. 5, 35-70.

Oh, W., and Lindquist, W.B. (1999). Image thresholding by indicator kriging. *IEEE Trans. Pattern Anal. Mach. Intell.* 21, 590-602.

Olson, M. S., Tillman Jr., F. D., Choi, J-W., and Smith, J. A. (2001). Comparison of three techniques to measure unsaturated-zone air permeability at Picatinny Arsenal, NJ. *J. Contam. Hydrol.* 53, 1-19.

Otsu, N. (1979). A threshold selection method from gray-level histograms. *IEEE Trans. Syst. Man Cybern.* 9, 62-66.

Pachepsky, Y.A., Giménez, D., Crawford, J.W., and Rawls, W.J. (2000). "Conventional and fractal geometry in soil science." In: *Fractals in Soil Science.* Pachepsky, Y.A., Crawford, J.W., and Rawls, W.J. (Elsevier Science B.V.) 7-18.

Papadopoulos, A. Bird, N. R. A. Whitmore, A. P., and Mooney, S. J. (2009). Investigating the effects of organic and conventional management on soil aggregate stability using X-ray computed tomography. *Eur. J. of Soil Sci.* 60, 360-368.

Paradelo, M., Katuwal, S. Moldrup, P., Norgaard, T., Herath, L., and de Jonge, L. W. (2016). X-ray CT-derived characteristics explain varying air, water, and solute transport properties across a loamy field. *Vadose Zone J.* 192, 194-202. doi: 10.2136/vzj2015.07.0104.

Parvin, N., Beckers, E., Plougonven, E.,Léonard, A., and Degré A. (2017). Dynamic of soil drying close to saturation: What can we learn from a comparison between X-ray computed microtomography and the evaporation method? *Geoderma.* 302, 66-75.

Pascal, B., Zarebanadkouki, M., and Carminati, A. (2018). The rhizosphere physical network. GRA, 20, EGU2018-6296. Abstract retrieved from the Geophysical Research Abstracts database.

Patzek, T. W., and Silin, D. B. (2001). Shape factor and hydraulic conductance in noncircular capillaries. I. One-phase creeping flow. *J. Colloid and Interface Sci.* 236, 295-304.

Peng, S. Marone, F., and Dultz, S. (2014). Resolution effect in X-ray microcomputed tomography imaging and small pore's contribution to permeability for a Berea sandstone. *J. Hydrol.* 510, 403-411.

Perret, J. S., Prasher, S. O., Kantzas, A., and Langford, C. (1999). Three-Dimensional Quantification of Macropore Networks in Undisturbed Soil Cores. *Soil Sci. Soc. Am. J.* 63, 1530-1543. doi:10.2136/sssaj1999.6361530x

Perret, J. S., Prasher, S. O., and Kacimov, A. R. (2003). Mass fractal dimension of soil macropores using computed tomography: from the box-counting to the cube-counting algorithm. *Eur. J. Soil Sci.* 54, 569-579.

Perrier, E., Bird, N., and Rieu, M. (1999). Generalizing the fractal model of soil structure: the pore-solid fractal approach. *Geoderma.* 88 (3), 137-164.

Peth, S., Horn, R., Beckmann, F., Donath, T. Fischer, J., and Smucker, A. J. M. (2008). Three-dimensional quantification of intra-aggregate pore-space features using synchrotron-radiation-based microtomography. *Soil Sci. Soc. Am. J.* 72(4), 897-908.

Plougonven, E. (2009). Link between the microstructure of porous materials and their permeability. [PhD thesis]. [Bordeaux, France]: Université Sciences et Technologies - Bordeaux I.

R Core Team (2015). R: A language and environment for statistical computing. R Foundation for Statistical Computing, Vienna, Austria. URL http://www.R-project.org/.

Raats, P. A. C., Zhang, Z. F., Ward, A. L., and Gee, G. W. (2004). The relative connectivity-tortuosity tensor for conduction of water in anisotropic unsaturated soils. *Vadose Zone J.* 3, 1471-1478.

Rab, M.A., Haling, R.E., Aarons, S.R., Hannah, M., Young, I.M., and Gibson, D. (2014). Evaluation of X-ray computed tomography for quantifying macroporosity of loamy pasture soils. *Geoderma*. 213, 460-470

Rachman, A., Anderson, S. H., and Gantzer, C. J. (2005). Computed-Tomographic measurement of soil macroporosity parameters as affected by stiff-stemmed grass hedges. *Soil Sci. Soc. Am. J.* 69(5), 1609-1616.

Renard, P., and Allard, D. (2013). Connectivity metrics for subsurface flow and transport. *Adv. Wat. Res.* 51, 168-196. doi: 10.1016/j.advwatres.2011.12.001.

Richards, L.A. (1948). Porous plate apparatus for measuring moisture retention and transmission by soils. *Soil Sci.* 66, 105–110.

Rougelot, T., Skoczylas, F., and Burlion, N. (2016). Water desorption and shrinkage in mortars and cement pastes: experimental study and poromechanical model. *Cement and Concrete Res*. 39, 36-44.

Rowell, D. L. (1994). Soil Science: methods and application. Department of Soil Science, University of Reading : Longman Scientific & Technical.

Russell, A. R., and Buzzi, O. (2012). A fractal basis for soil-water characteristics curves with hydraulic hysteresis. *Geotechnique*. 62(3), 269-274.

Sammartino, S., Lissy, A-S., Bogner, C., Van Den Bogeart, R., Capowiez, Y., et al. (2015). Identifying the functional macropore network related to preferential flow in structured soils. *Vadose Zone J.* 14(10) doi:10.2136/vzj2015.05.0070.

Sandin, M., Koestel, J., Jarvis, N., and Larsbo, M. (2017). Post-tillage evolution of structural pore space and saturated and near-saturated hydraulic conductivity in a clay loam soil. *Soil Til. Res.*165, 161-168. doi: 10.1016/j.still.2016.08.004.

Schaap, M. G., Porter, M. L., Christensen, B. S. B., and Wildenschild, D. (2007). Comparison of pressure-saturation characteristics derived from computed tomography and lattice Boltzmann simulations. *Water Resour. Res.* 43. doi:10.1029/2006WR005730.

Schlüter, S. Weller, U., and Vogel, H. J. (2010). Segmentation of X-ray microtomography images of soil using gradient masks. *Comput. Geosci.* 36, 1246-1251.

Schlüter, S., Sheppard, A., Brown, K., and Wildenschild, D. (2014). Image processing of multiphase images obtained via X-ray microtomography: a review. *Water Resour. Res.* 50, 3615-3639.

Schlüter, S., and Vogel, H-J. (2016). Analysis of soil structure turnover with garnet particles and X-ray microtomography. *PLoS ONE.* 11(7), e0159948. doi: 10.1371/journal.pone.0159948.

Schneider, C.A., Rasband, W. S., and Eliceiri, K. W. (2012). NIH Image to ImageJ: 25 years of image analysis. *Nature methods.* 9(7), 671-675.

Sezgin, M., and Sankur, B. (2004). Survey over image thresholding techniques and quantitative performance evaluation. *J. Electron. Imaging.* 13(1), 146-165.

Shah, S. M., Gray, F., Crawshaw, J.P., and Boek, E.S. (2016). Micro-computed tomography pore-scale study of flow in porous media: Effect of voxel resolution. *Adv. Wat. Res.* 95, 276-287. doi: 10.1016/j.advwatres.2015.07.012.

Six, J., Elliot, E. T., and Paustian, K. (2000). Soil macroaggregate turnover and microaggregate formation: a mechanism for C sequestration under no-tillage agriculture. *Soil Biology & Biochemistry.* 32, 2099-2103.

Taina, I.A., Heck, R.J., and Elliot, T.R. (2008). Application of X-ray computed tomography to soil science: a literature review. *Can. J. Soil Sci.* 88(1), 1-20.

Tarquis, A. M., Heck, R. J., Andina, D., Alvarez, A., and Antón, J. M. (2009). Pore network complexity and thresholding of 3D soil images. *Ecol. Complex.* 6, 230-239.

Tracy, S. R., Daly, K. R., Sturrock, C.J., Crout, N. M. J., Mooney, S. J., and Roose, T. (2015). Three-dimensional quantification of soil hydraulic properties using X-ray computed tomography and image-based modeling. *Water Resour. Res.* 51, 1006-1022. doi: 10.1002/2014WR016020.

Tuller, M., Kulkarni, R. and Fink, W. (2013). Segmentation of X-ray CT data of porous materials: a review of global and locally adaptive algorithms. *Soil Sci. Soc. Am. J.* 61(SP), 157-182.

Udawatta, R. P., and Anderson, S. H. (2008). CT-measured pore characteristics of surface and subsurface soils influenced by agroforestry and grass buffers. *Geoderma.* 145, 381-389.

Ursino, N., Roth, K., Gimmi, T., and Flühler, H. (2000). Upscaling of anisotropy in unsaturated Miller-similar porous media. *Water Resour. Res.* 36(2), 421-430.

van Genuchten, M. T. (1980). A closed-form equation for prediction the hydraulic conductivity of unsaturated soils. *Soil Sci. Soc. Am. J.* 44(5), 892-898.

Vogel, H-J. (1997). Morphological determination of pore connectivity as a function of pore size using serial sections. *Eur. J. of Soil. Sci.* 48, 365-377.

Vogel, H-J., and Roth, K. (1998). A new approach for determining effective soil hydraulic functions. *Eur. J. Soil Sci.* 49, 547-556.

Vogel, H-J. (2000). A numerical experiment on pore size, pore connectivity, water retention, permeability, and solute transport using network models. *Eur. J. of Soil Sci.* 51, 99-105.

Vogel, H-J., Tölke, J., Schulz, V.P., Krafczyk, M., and Roth K. (2005). Comparison of a Lattice-Boltzmann model, a full-morphology model and a pore network model for determining capillary pressure-saturation relationship. *Vadose Zone J.* 4, 380-388.

Vogel, H-J., Weller, U., and Schlüter, S. (2010). Quantification of soil structure based on Minkowski functions. *Comput. Geosci.* 36, 1236-1245.

Wagai, R., and Mayer, L. M. (2007). Sorptive stabilization of organic matter in soils by hydrous iron oxides. *Geochimica et Cosmochimica Acta.* 71, 25-35.

Walkley, A., and Black, I. A. (1934). An examination of the Degtjareff method for determining soil organic matter, and a proposed modification of the chromic acid titration method. *Soil Sci.* 37(1), 29-38.

Wang, W., Kravchenko, A. N., Smucker, A. J. M., and Rivers, M. L. (2011). Comparison of image segmentation methods in simulated 2D and 3D microtomographic images of soil aggregates. *Geoderma.* 162, 231-241.

Wetzels, R., and Wagenmakers, E-J. (2012). A default Bayesian hypothesis test for correlations and partial correlations. *Psychon. Bull. Rev.* 19, 1057-1064.

Wildenschild, D., and Sheppard, A.P. (2013). X-ray imaging and analysis techniques for quantifying pore-scale structure and processes in subsurface porous medium systems. *Adv. Water. Resour.* 51, 217-246.

Xu, Y. (2004). Calculation of unsaturated hydraulic conductivity using a fractal model for the pore-size distribution. *Computers and Geotechnics.* 31, 549-557.

Zhang, Y.J. (1996). A survey on evaluation methods for image segmentation. *Pattern Recognit.* 29(8), 1335-1346.

Zhang, Z. F. (2013). Relationship between anisotropy in soil hydraulic conductivity and saturation. *Vadose Zone J.* 13(6). doi: 10.2136/vzj2013.09.0172.

Zhang, Z., Liu, K., Zhou, H., Lin, H., Li, D., and Peng, X. (2018). Three dimensional characteristics of biopores and non-biopores in the subsoil respond differently to land use and fertilization. *Plant Soil.* doi:10.1007/s11104-018-3689-3

Supporting papers

Smet, S., Plougonven E., Léonard, A., Degré, A., and Beckers E. (2017). X-ray Micro-CT: How soil pore space description can be altered by image processing. *Vadose Zone J.* in press. doi:2136/vzj2016.06.0049

Smet, S., Beckers, E., Plougonven, E., Léonard, A., and Degré, A. (2018). Can the pore scale topology geometry explain soils sample scale hydrodynamic? *Frontiers in Env. Sci.* 6(20). doi: 10.3389/fenvs.2018.00020

Special Section: Noninvasive Imaging of Processes in Natural Porous Media

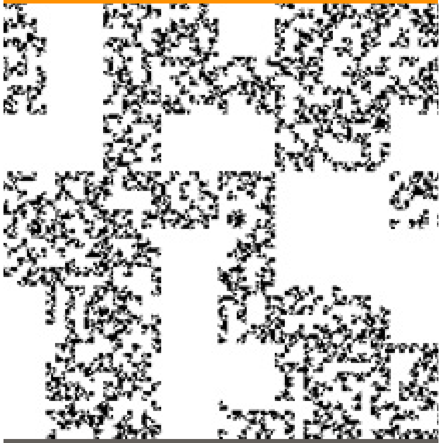

X-ray Micro-CT: How Soil Pore Space Description Can Be Altered by Image Processing

Sarah Smet,* Erwan Plougonven, Angélique Leonard, Aurore Degré, and Eléonore Beckers

A physically accurate conversion of the X-ray tomographic reconstructions of soil into pore networks requires a certain number of image processing steps. An important and much discussed issue in this field relates to segmentation, or distinguishing the pores from the solid, but pre- and post-segmentation noise reduction also affects the pore networks that are extracted. We used 15 two-dimensional simulated grayscale images to quantify the performance of three segmentation algorithms. These simulated images made ground-truth information available and a quantitative study feasible. The analyses were based on five performance indicators: misclassification error, non-region uniformity, and relative errors in porosity, conductance, and pore shape. Three levels of pre-segmentation noise reduction were tested, as well as two levels of post-segmentation noise reduction. Three segmentation methods were tested (two global and one local). For the local method, the threshold intervals were selected from two concepts: one based on the histogram shape and the other on the image visible-porosity value. The results indicate that pre-segmentation noise reduction significantly ($p < 0.05$) improves segmentation quality, but post-segmentation noise reduction is detrimental. The results also suggest that global and local methods perform in a similar way when noise reduction is applied. The local method, however, depends on the choice of threshold interval.

Abbreviations: CT, computed tomography; GM, gradient masks; IK, indicator kriging; ME, misclassification error; NU, non-uniformity; PBA, porosity-based; RE_g, relative error in the pore shape; RE_K, relative error in conductance; RE_P, relative error in calculated porosity; RS, real soil; TH, threshold.

Core Ideas

- Thresholding X-ray soil images influences the resulting images.
- Prior noise reduction improves the thresholding accuracy.
- Local and global thresholding perform similarly when prior noise reduction is applied.
- The local threshold interval choice determines the local segmentation quality.

S. Smet, A. Degré, and E. Beckers, Univ. of Liège, Gembloux Agro-Bio Tech, BIOSE, Soil–Water–Plant Exchanges, 2 Passage des Déportés, 5030, Gembloux, Belgium; E. Plougonven and A. Léonard, Univ. of Liège, Products, Environment, Processes (PEPs), Chemical Engineering, Sart Tilman, 4000, Liège, Belgium. *Corresponding author (sarah.smet@ulg.ac.be).

Received 8 June 2016.
Accepted 2 Jan. 2017.

Citation: Smet, S., E. Plougonven, A. Leonard, A. Degré, and E. Beckers. 2018. X-ray micro-CT: How soil pore space description can be altered by image processing. Vadose Zone J. 17:160049. doi:10.2136/vzj2016.06.0049

Characterizing the soil's physical properties and understanding the resulting functions of the soil is of major importance for many agricultural and environmental issues. The soil is at the interface of most physical, chemical, and biological processes. In this regard, there is increasing interest in the use of noninvasive X-ray microtomography to obtain a microscopic three-dimensional view of the inner soil pore space (for a full description of the technology, see Landis and Keane, 2010).

Several reviews (Taina et al., 2008; Helliwell et al., 2013; Wildenschild and Sheppard, 2013) have discussed the use of X-ray microtomography in soil and hydrological sciences. In these fields, the technique has been used at both the core scale (e.g., Gantzer and Anderson, 2002; Jassogne et al., 2007; Elliot et al., 2010; Luo et al., 2010; Piñuela et al., 2010; Capowiez et al., 2011; Köhne et al., 2011; Garbout et al., 2013; Larsbo et al., 2014; Katuwal et al., 2015) and the aggregate scale (e.g., Nunan et al., 2006; Peth et al., 2008; Papadopoulos et al., 2009; Kravchenko et al., 2011; Zhou et al., 2013) for describing the pore space and studying the impact of land use and agricultural management on soil structure (Gantzer and Anderson, 2002; Nunan et al., 2006; Jassogne et al., 2007; Peth et al., 2008; Papadopoulos et al., 2009; Luo et al., 2010; Capowiez et al., 2011; Kravchenko et al., 2011; Garbout et al., 2013; Zhou et al., 2013), as well as for analyzing the relationships between soil pore networks and soil physical properties (Elliot et al., 2010; Köhne et al., 2011; Larsbo et al., 2014; Katuwal et al., 2015). Flow simulations in observed pore networks (Dal Ferro et al., 2015) or a similar constructed pore network (Vogel et al., 2005) have also been conducted. These analyses assumed that the pore space description generated from the image processing accurately represents the physical reality of the sample microstructure, but the choice of X-ray computed tomography (CT) image processing methodology has a visible impact on the resulting structure. Figure 1 shows an example of the processing steps from sample acquisition to binary image. Each step involves choosing the appropriate method and parameters, which are numerous and can have a profound effect on the resulting structure. These choices ultimately depend on the experience of the operator.

What is important here is not only the diversity of these choices but also the fact that they are often inadequately described or justified. Table 1 shows an example of the diversity of methodologies used in a selection of soil science research papers (selection based on number of citations and diversity of research teams). Within Table 1, the pre-segmentation and post-segmentation steps are differentiated. Pre-segmentation steps are varied and are more efficient at handling image degradation than post-segmentation processing; a general rule (for more than just image analysis) is that the more upstream a problem is corrected, the easier is it to process the data downstream. Segmentation is the essential step when pixels are assigned to either the solid or porous phase. There are numerous segmentation methods; a review of those used in soil science was provided by Tuller et al. (2013). In this study, we differentiated global and local thresholding methods. The aim of a thresholding method is to select a grayscale value, manually or automatically, that separates the image gray levels into two groups: greater than or equal to the threshold (TH) and less than the TH. In soil science, these two groups are often defined as the solid phase (soil matrix) and the void phase (pore space). With global thresholding, a constant TH is chosen for the entire image, whereas with local thresholding, the value is computed for every pixel based on the local neighborhood (Tuller et al., 2013). Segmentation precision depends on the initial quality of the grayscale images. Enhancing the projections before reconstruction and the reconstructed images before segmentation is the typical approach, but each research team has its own procedures (see Table 1). An efficient method for enhancing image quality is to apply noise reduction filters (Kaestner et al., 2008; Wildenschild and Sheppard, 2013) as mentioned in six of the 15 studies listed in Table 1.

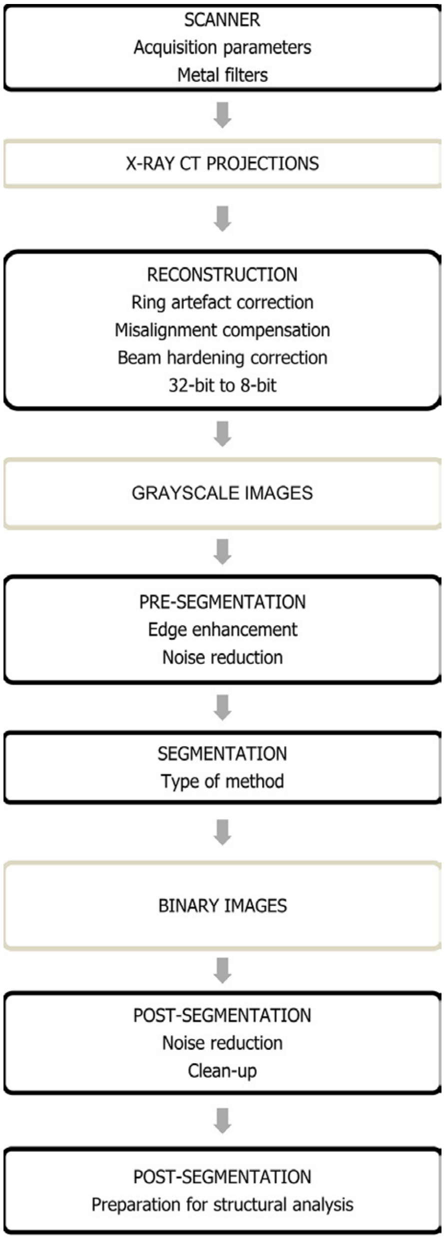

Fig. 1. Processing steps from sample to binary image. Some sources of variability are written in lowercase.

Some researchers have shown (Beckers et al., 2014b; Lamandé et al., 2013; Peth et al., 2008; Peng et al., 2014; Tarquis et al., 2009) that, in most practical cases, the choice of segmentation method plays a crucial role in the resulting pore structure, but no standards have yet been proposed. Several studies have sought to classify thresholding techniques based on information available from the resulting binary images (Baveye et al., 2010; Houston et al., 2013b; Iassonov et al., 2009; Schlüter al., 2014). So far as we know, only Wang et al. (2011) have used synthetic soil aggregate images, from which ground-truth information was available, to compare thresholding methods. Even these studies were based on image-by-image analyses and did not provide a tool with which to properly evaluate the processing methodologies.

Within this context, our study sought to provide a statistical analysis of the segmentation processing effects on the resulting data. By evaluating Otsu's global method (Otsu, 1979), the local adaptive-window indicator kriging (IK) method (Houston et al., 2013a), and the porosity-based (PBA) global method (Beckers et al., 2014b) on two-dimensional simulated soil images from which ground-truth information was available, we could also objectively support existing reviews. The first objective of our study was to quantify the effects of pre-segmentation noise reduction on the accuracy of the thresholding method based on the performance indicators. The second objective was to evaluate the impact of post-segmentation processing on pore functionalities. The third objective was to propose an

Table 1. Summary of selected studies in which x-ray computed tomography (CT) was used to study soil, sorted by number of citations within each section.

Study	Objective	Scanner†	Sample or aggregate size	Voxel size	Preprocessing	Segmentation	Post-processing	Additional notes
			———— mm	————				
	Pore space description at the core scale							
Gantzer and Anderson (2002)	quantification of tillage effects on macropore characteristics	MCT UHCT	75 by 75	0.19^2 by 1 0.148^2 by 0.097	reduction of BH‡ with a 70-mm circular region of interest	calibration procedure	no mention	necessary to improve segmentation
Luo et al. (2010)	implementation of a protocol to quantify macropore characteristics; comparison of macropore characteristics between cultural practices	MCT	102 by 350	0.234^2 by 2	median filter	global: max. entropy	removal of pores with ECD§ <0.75 mm	validation of segmentation through visual inspection
Jassogne et al. (2007)	characterization of the porosity relevant to root growth	MCT µCT	150 by 500 15 by 40	$\pm 0.6^2$ by 0.8 $\pm 0.038^3$	no mention	global: max. entropy	median filter, radius = 2	test with local segmentation necessary
Capowiez et al. (2011)	computation of quantitative estimates of bioturbation by earthworms	MCT	160 by 350	0.4^2 by 3	no mention	local: tracing algorithm adaptive to local changes in density in an object	selection of macropore with area >100 voxels	description of voids, not bioturbated zones
Garbout et al. (2013)	quantification of tillage effects on pore network characteristics: correlation of the pore network characteristics with visual evaluation and laboratory analysis	X-ray CT	200 by 200	0.39^2 by 0.6	no mention	global: Otsu (1979)	no mention	
	Pore-space description at the aggregate scale							
Peth et al. (2008)	comparison of intra-aggregate pore-space network between management systems	SR-µCT	3.3 4.6	0.0032^3 0.0054^3	no mention	global: manual local: IK¶	removal of disconnect grain and void voxel clusters and dead ends (under certain conditions)	
Nunan et al. (2006)	comparison of aggregate characteristics between treatments and quantification for mathematical modeling	SR-CT	1–3	0.0044^3	reducing the grayscale range; sigma filtering	adaptive grayscale segmentation	3-step noise reduction algorithm; removal of pores <5 pixels; reclassification of cracks by valley detection	monochromatic beam
Papadopoulos et al. (2009)	comparison of aggregate characteristics among farming systems	µCT	5	0.008^3	no physical filter within scanner	global: manual	test of morphological filters but not adopted	automated global thresholding tested but not adopted
Zhou et al. (2013)	comparison of aggregate characteristics among fertilization practices	SR-µCT	5	0.009^3	removal of ring artifact by Fourier transform	local: IK	no mention	choice of threshold interval is subjective
Kravchenko et al. (2011)	comparison of aggregate characteristics between tillage use and land use	SR-CT	4–6	0.0146^3	removal of ring artifact	local: IK	no mention	monochromatic beam

continued on next page

Table 1. continued.

Study	Objective	Scanner†	Sample or aggregate size	Voxel size	Preprocessing	Segmentation	Post-processing	Additional notes
	Link between pore space and physical properties							
Elliot et al. (2010)	calculation of saturated hydraulic conductivity from 3D pore network characteristics	MμCT	65 by 76	0.02^3	removal of radial and signal noise with local-region Gaussian noise filter	1. sharpening histogram with local low-variance region criteria (5 by 5 by 5) 2. global thresholding: equiprobability point between two normal Gaussian distributions	1. post-classification with 3D mean filter (3 by 3 by 3) 2. local voxel reassignment	validation of segmentation through histogram comparison with original CT histograms
Köhne et al. (2011)	prediction of conservative tracer and adsorbed solute transport by transforming observed pore structure into a set of descriptors	μCT	75 by 80 46 by 50 10 by 10	0.075^3 0.05^3 0.01^3	reduction of BH with 0.25-mm Cu filter	local: bilevel segmentation with automated threshold detection using gradient masks	no mention	
Piñuela et al. (2010)	quantification of soil pore distribution through wavelet-based approach in the context of multi-scaling structure analysis	μCT	64 by –	0.0451^3	reduction of noise and BH with 3D Gaussian filter	1. sharpening histogram with a 3D filter 2. smoothing histogram 3. global thresholding: equiprobability point between two normal Gaussian distributions		
Katuwal et al. (2015)	characterization of relationship between macropore features and air and chemical transport parameters	MCT	190 by 200	0.43^2 by 0.6	reduction of noise with Gaussian filter	global: minimum point of a fitted parabola between histogram peak of air and peak of soil matrix	removal of pores with Ferret's diameter <1.2 mm	
Larsbo et al. (2014)	characterization of influence of macropore network across degree of preferential flow of a nonreactive tracer under near-saturated conditions	X-ray CT	200 by 200	0.2422^3	reduction of BH with 60th and 80th percentile correction and noise with 3D median filter, radius = 2	global: Otsu (1979)	definition of macropore of at least two pore voxels	

† MCT, medical CT scanner; UHCT, ultra-high-resolution CT scanner; SR-CT, synchrotron CT.

‡ BH, beam hardening.

§ ECD, equivalent circular diameter.

¶ IK, indicator kriging.

approach for calculating the initial TH interval necessary using the local IK method based on the global TH calculated using the PBA method (Beckers et al., 2014b), considering that IK is sensitive to the initial choice of TH interval (Iassonov et al., 2009; Schlüter et al., 2010; Wang et al., 2011; Houston et al., 2013a).

Materials and Methods

Here we focus initially on the construction of our simulated images. The general framework was based on the methodology described by Wang et al. (2011). It involved superimposing a realistic binary pore image (real soil [RS] images) on an image representing partial volume effects and then adding Gaussian noise (see Fig. 2 for a detailed illustration). We created 15 simulated images from the combination of 15 selected RS binary images and 15 generated partial volume effect images using a method based on fractals and the method of Wang et al. (2011). The thresholding methods tested should identify the pore region from the original RS image.

Real Soil Images

The RS images were derived from the Beckers et al. (2014a) study. We selected 15 two-dimensional images from silt loam soil. Details about the materials, sampling, and X-ray acquisition parameters can be found in Beckers et al. (2014a). Reconstructions were performed using NRecon software provided free of charge by Brucker micro-CT. This software provides tomographic artifact correction methods, which were not tested in this study. Automatic misalignment compensation was used, along with a Level 7 (out of 20) ring artifact correction. The RS images were not subjected to a beam hardening correction. In X-ray microtomography, the most commonly cited artifact is beam hardening due to the polychromatic nature of the X-ray beam, implying a deviation from the Beer Lambert law. For cylindrical objects, it results in a radial grayscale intensity variation from the edges to the center. The beam hardening effect is barely distinguishable from the circular compaction that occurs when sampling soil, and removing beam hardening effects might create noise. Finally, an intensity rescaling was applied to increase contrast (Tuller et al., 2013).

Partial Volume Effect Images

The partial volume effect images were generated through the overlaying of decreasing resolution images, as proposed by Wang et al. (2011). Our addition to Wang's method was to produce decreasing resolution fractal images with a fractal dimension calculated from the RS images' fractal dimension (Steps A and B). Those images were then combined to form one partial volume effect image (Step C).

Fractal Geometry

Fractal geometry states that a fractal object has comparable features at different scales and can be described by a so-called fractal dimension, D, which is power-law dependent (Mandelbrot, 1983):

$$D=\frac{\log(N)}{\log(1/r)} \qquad [1]$$

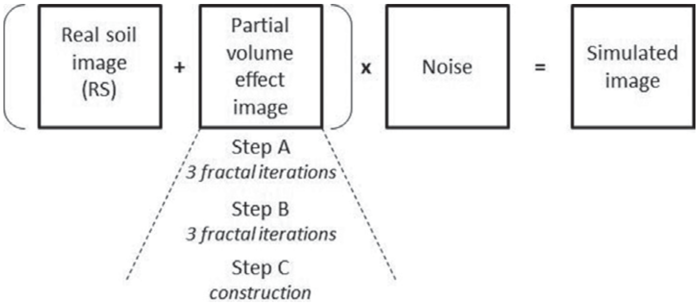

Fig. 2. Detailed illustration of the simulated image construction.

where N is the constant number of transformed elements at each iteration and r is the ratio between the dimension of the parent element and the dimension of the transformed element.

Because power-law dependencies have been observed in soil science, researchers have applied fractal geometry to the study of soil behavior (Pachepsky et al., 2000). For example, Russell and Buzzi (2012) successfully derived a soil-water retention curve from the pore-size distribution fractal dimension of a silt loam soil. Many studies have reported that this concept provides a good description of the complexity of soil microstructure (e.g., Kravchenko et al., 2011).

The Fractal Generator: Steps A and B

We generated two-dimensional fractal images with a fractal generator using the pore–solid fractal approach (Perrier et al., 1999), which works as follows. The first action is the division of an initiator into n^2 elements. Within these elements, a proportion of x/n^2 is allocated to pore pixels and a proportion of y/n^2 is allocated to solid pixels. The remaining pixels (z/n^2) are available for the next iteration, which involves their division by n. This is a recursive process. Equation [1] then becomes

$$D=d+\frac{\log(z)}{\log(n)} \qquad [2]$$

where d is the Euclidian dimension.

To construct partial volume effect images, we first generated decreasing resolution fractal images. This process was based on two main steps (A and B), each consisting of three fractal iterations. Step A involved generating fractal images to be used as the background of the final constructed partial volume effect image and represented by white pixels in Fig. 3c. These pixels could not be further modified during the rest of the process. Step B involved allocating smaller pixels to the solid and pore phases; the black pixels of Fig. 3c were the pixels subjected to further fractal divisions.

The fractal dimension in the Step A iterations was set as follows:

1. The fractal dimension of the associated RS image (D_{obs} in Table 2) was calculated using the Fractal Box Counting tool available in the public domain image processing ImageJ (Version 1.47c, National

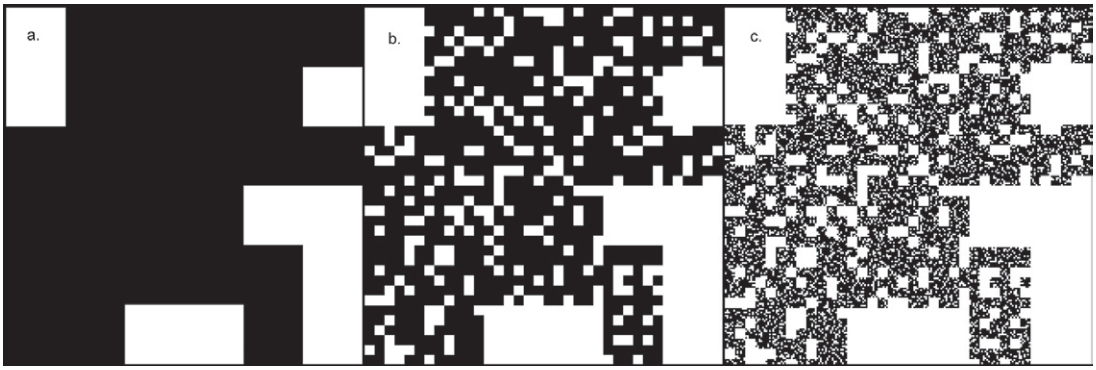

Fig. 3. Step A in the generation of decreasing resolution fractal images for Image no. 1, sorted by iteration from left to right: construction of the partial volume effect background. The white pixels represent the soil matrix.

Institutes of Health, http://rsb.info.nih.gov/ij). The number of diminishing size boxes containing pore pixels was counted.

2. The variable z of the RS image was calculated using Eq. [2] (z_{obs} in Table 2), considering that $n = 6$.
3. The variable z of the simulated image (z_{sim} in Table 2) was calculated to represent the complement of z_{obs}. It was calculated based on the fractal generator theory (see above), and therefore

$$z_{obs} = n^2 - z_{sim} = x_{sim} + y_{sim} \qquad [3]$$

4. The fractal dimension of the simulated image (D_{sim} in Table 2) was then calculated from z_{sim} and $n = 6$ (Eq. [2]).

As noted above, Step B involved allocating smaller pixels to the solid and pore phases, and the black pixels in Fig. 3c are the pixels subjected to further fractal divisions. The three iterations of Step B (see Fig. 4) were produced with $z = 2$, $n = 2$, and $D = 1$:

- $n = 2$ because those images were used to construct the partial volume effect within a 2 by 2 pixels averaging process (see below).
- $z = 2$ because this was the only way of having at least one pore pixel and one solid pixel with at least two elements remaining for the next step.

Table 2. Calculation of the fractal dimension (D_{sim}) for the simulated images, using the fractal dimension observed on the real soil image (D_{obs}), the observed number of fractals (z_{obs}), and the simulated number of fractals (z_{sim}).

Image	D_{obs}	z_{obs}	z_{sim}	D_{sim}
1	1.20	9	27	1.85
2	1.43	13	23	1.75
3	1.53	15	21	1.69
4	1.52	15	21	1.70
5	1.21	9	27	1.84
6	1.30	10	26	1.81
7	1.14	8	28	1.86
8	1.72	22	14	1.48
9	1.31	10	26	1.81
10	1.38	12	24	1.78
11	1.61	18	18	1.62
12	1.58	17	19	1.65
13	1.61	18	18	1.61
14	1.48	14	22	1.72
15	1.45	13	23	1.74

Partial Volume Effect Image Construction: Step C

The partial volume effect construction following the method of Wang et al. (2011) was applied to the generated fractal images (from Step B), and Fig. 4c shows the first image to be processed. From a size of 1728 by 1728, the image was scaled down into an 864 by 864 image by calculating the average of 2 by 2 squares. The down-scaled image (Fig. 4c) was then overlaid on Fig. 4b, which had also been down-scaled from 1728 by 1728 to 864 by 864, by adding the corresponding pixel color to fully represent the effect of all sizes of pores. This newly created image (not shown) was scaled down to 432 by 432 using the same averaging process, overlaid on Fig. 4a, and the resulting image was then scaled down to 216 by 216 by averaging. The result is shown in Fig. 5. Figure 6 illustrates the impact of the averaging process between Fig. 4c and Fig. 5.

Simulated Image Construction

The next step involved the overlaying of Fig. 5 on the corresponding RS image derived from Beckers et al. (2014a). We then added random normal noise to the pure white and pure black pixels, and variance and means were calculated from our scanner noise by scanning the empty chamber (within [0; 255]: mean = 222 and variance = 15.9). The final step was to add Gaussian noise (mean = 0; variance = 0.01) to the whole image to represent high-frequency noise (Fig. 7).

Pre-Segmentation Processing

Adhering to an algebraic comparison in its strictest sense, the effect of a pre-segmentation median filter (PRE0, none; PRE1, radius one pixel; PRE2, radius two pixels) was tested on the segmentation quality of the simulated images. Median filters assign the median value of the neighboring pixels to the center pixel. These filters are less sensitive to extreme values and no grayscale value is created near the object boundary, resulting in the object edges being better preserved (Tuller

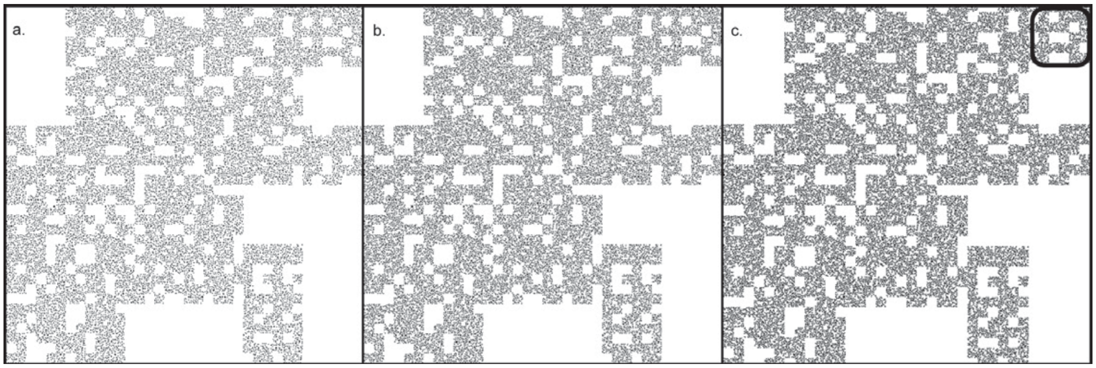

Fig. 4. Step B in the generation of decreasing resolution fractal images for Image no. 1, sorted by iteration from left to right. The black pixels represent pores.

et al., 2013). The use of a median filter before segmentation seems to be a common step in the field of soil X-ray CT image processing.

Tested Segmentation Methods

The complexity of segmentation is linked to the noise, artifacts, and partial volume effects in the grayscale images. Other sources of image degradation include ring artifacts, streak artifacts, high-frequency noise, scattered photons, and distortions (Baruchel et al., 2000). Therefore, besides enhancing image quality, choosing the right segmentation method is crucial.

Global Methods

The global thresholding method described by Otsu (Otsu, 1979) was tested because it provides acceptable results (Iassonov et al., 2009) and can be used in preference to the IK method where there are poorly distinguishable histogram peaks (Wang et al., 2011). Despite its non-reliability and the existence of more recent and more efficient methods, it is still a widely used method for soil images, probably because it is rapid and easy to use. It automatically chooses a TH based on the minimization of the intraclass variance between two intensity classes of pixels. In our study, it was performed with MATLAB R2015a (The MathWorks).

As we had ground-truth information available, the TH that should be applied could be estimated. Through an iterative loop, the TH that minimized the difference between calculated porosity and ground-truth porosity was selected, and this value served as a benchmark. This procedure was based on the method described by Beckers et al. (2014b). The MATLAB R2015a code was provided by the authors. Hereafter, we refer to the method as the PBA method.

Local Method

The IK method (Oh and Lindquist, 1999) has provided good results in various studies (Houston et al., 2013a, 2013b; Peth et al., 2008; Iassonov et al., 2009; Wang et al., 2011). Its variation, the adaptive-window indicator kriging method (Houston et al., 2013a), was chosen because Houston et al. (2013a) concluded that the adaptive method required fewer computational resources than the fixed one while providing very similar results. The IK concept relies on the selection of a TH interval, T1 to T2. All grayscale values below T1 are set at 0 and all values above T2 are set at 1. The values between T1 and T2 are assigned to a specific color, namely a phase, depending on their grayscale value and their already classified neighboring pixels. The adaptive-window IK method modifies this neighboring area based on locally available information to reduce the computational costs when possible. The method was applied using the authors' software, AWIK. The choice of T1 and T2 was based on edge detection using the gradient masks (GM) method (Schlüter et al., 2010), an option available within AWIK software. Hereafter, we refer to the method as IK/GM.

Fig. 5. Final partial volume effect constructed by the fractal generator for Image no. 1.

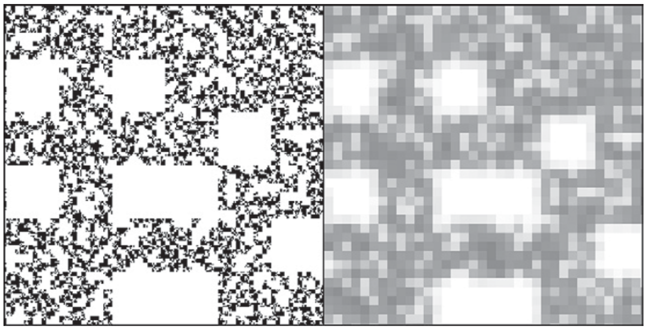

Fig. 6. The left-hand image is an enlargement of Fig. 4c (black rounded square in the upper right corner). The right-hand image is an enlargement of a portion of Fig. 5 (black rounded square in the upper right corner).

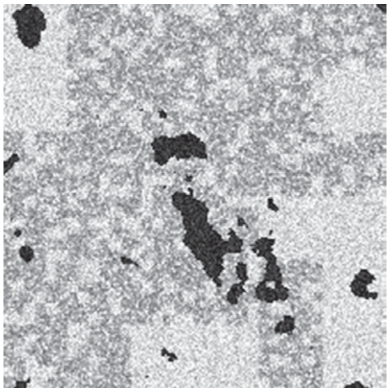

Fig. 7. Final simulated grayscale image for Image no. 1.

Hybrid Method

The PBA method was shown to be satisfactory, although its performance was poorer than that of IK/GM (Beckers et al., 2014b). The weakness in IK is the choice of the T1 to T2 interval. Schlüter et al. (2010) proposed an improved automatic TH interval selection method, although it remained sensitive to noise. We therefore sought to combine the physical robustness of the PBA method with the edge-preserving IK method. The aim was to select a TH interval based on the global PBA threshold and then compute the IK method. The TH intervals tested were ±10, ±20, ±30, ±40, and ±50% of the global TH value. For example, if the PBA TH was 94 (on a 0–255 grayscale), the ±10% IK–PBA interval would be 85 to 103, the ±20% interval would be 75 to 113, and so on. Commonly, histogram percentiles would have been tested. We have, however, chosen this approach because the final objective would be to apply the IK–PBA to real soil images from which the porosity would be estimated with laboratory measurements. Because this porosity value would be uncertain, the global TH obtained with the original PBA method would also be uncertain. Therefore, the priority was that the interval include the supposedly "true" global TH value, corresponding to the "true" soil sample porosity. Hereafter, we will refer to the method as IK–PBA.

Post-Segmentation Processing

For a functional comparison, a post-segmentation median filter (POST0, none; POST2, radius two pixels) was also tested on the simulated images. A post-processing cleanup was also applied by removing the pores smaller than five pixels in area. The pore characterization was performed using the Analyze Particles tool that is available in the public domain image processing ImageJ (Version 1.47c, National Institutes of Health, http://rsb.info.nih.gov/ij).

Results Analysis

Performance Indicators

We used the ground-truth information available to compute the misclassification error (ME), whose value is between 0 and 1. It gives the proportion of pixels wrongly assigned to a phase. The value 0 reflects perfect segmentation and the value 1 the opposite (Sezgin and Sankur, 2004):

$$\mathrm{ME} = 1 - \frac{|P_0 \cap P_\mathrm{T}| + |S_0 \cap S_\mathrm{T}|}{|P_0| + |S_0|} \qquad [4]$$

where P_0 is the number of pore pixels in the ground-truth image, P_T is the number of pore pixels in the tested image, S_0 is the number of solid pixels in the ground-truth image, and S_T is the number of solid pixels in the tested image. We chose this simple indicator for its clear interpretation and because it offered the possibility of comparison with other studies (Wang et al., 2011; Schlüter et al., 2014).

Similarly, we used the relative error in the calculated porosity (RE_P) as a performance indicator. Calculated porosity is the ratio of black pixels (pores) to the total number of pixels.

Region non-uniformity (NU) was calculated to evaluate segmentation quality without using ground-truth information (Wang et al., 2011). High intra-region uniformity is achieved with a suitable segmentation method because there is a similarity of property in the region element; the variance in that property is then adequate for expressing the uniformity (Zhang, 1996):

$$\mathrm{NU} = \frac{P\sigma_\mathrm{p}^2}{T\sigma^2} \qquad [5]$$

where P is the number of pore pixels, T is the total number of pixels, $\sigma_\mathrm{p}{}^2$ is the grayscale value variance in the pore pixels in the original grayscale simulated image, and σ^2 is the total grayscale value variance in the original grayscale simulated image. Non-uniformity is a natural choice given the uniformity that a pore space should have, although it gives a poorer performance than the ground-truth information based indicator (Zhang, 1996).

Physical Performance

The physical evaluation of the segmentation methods was based on the pore network modeling concept, which is effective, for example, in computing soil-water retention curves (Vogel et al., 2005). Because we were dealing with two-dimensional images, we could focus only on the effects of segmentation on the two-dimensional pore network characteristics, such as pore geometry. More specifically, we focused on the irregular pore shapes, which, despite their name, tend to be the norm rather than the exception in real soils. In addition to the empty–filled dynamic within pores, the wetting film plays an important role in fluid displacement (Celia et al., 1995). Irregular pore shapes have corners where there might be an accumulation of wetting fluid.

For each pore, we computed its shape factor as defined by Mason and Morrow (1991):

$$G = \frac{A}{P^2} \qquad [6]$$

where A is the surface area (pixel^2) and P is the perimeter (pixel). Depending on the G value, we calculated the specific dimensionless conductance of each pore (Patzek and Silin (2001) (see Table 3). The dimensionless conductance $\tilde{g}$ multiplied by the squared cross-section surface area (A^2) and divided by the fluid viscosity (μ), gives the conductance g ($L^5 T M^{-1}$):

$$g = \frac{\tilde{g}A^2}{\mu} \quad [7]$$

The volumetric flow rate through one pore was obtained by multiplying the conductance (g) by the fluid displacement driving force. As in an electric circuit, where resistances are summed in series, conductance values were summed in parallel. We therefore multiplied each pore's dimensionless conductance ($\tilde{g}$) by its squared surface area (A^2) to sum all the conductance values (g) for each image, which resulted in a global conductance value. The relative error in conductance (RE_K) was calculated for each image. We also calculated the dimensionless conductance ($\tilde{g}$) relative error of each pore (RE_g).

For the physical analysis, we then had two types of parameters: RE_K, reflecting the global conductance of the image, and RE_g, describing the pore shape accuracy. The RE_K and RE_g indicators were studied as absolute values.

Statistical Analysis

To assess whether or not the quality of the segmentation methods was altered by noise reduction, a three-way ANOVA was conducted to test for significant differences in the ME, NU, RE_P, and RE_K indicators for the various levels of noise reduction and the three segmentation methods. A randomized complete block design was applied, the simulated images being the random blocks. For the significant fixed interaction, three two-way ANOVAs were conducted (one per segmentation method) to test for a significant impact of noise reduction on the segmentation results. Tukey's post-hoc test was performed in cases of a significant effect ($p < 0.05$).

To determine which segmentation method and noise reduction combination performed most accurately and to see if the IK–PBA method brought improvement, four two-way ANOVAs were conducted to test for significant differences in the ME, NU, RE_P, and RE_K values between the segmentation method and noise reduction combinations (10 levels). In cases of significance ($p < 0.05$), a post-hoc Dunnett test was conducted, with IK–PBA as the control.

Table 3. Dimensionless conductance ($\tilde{g}$) calculation depending on shape factor values (G) (Patzek and Silin, 2001).

G value	Associated shape	Conductance
$G > 1/16$	circle	$\tilde{g} \approx (3/5)G$
$(3^{1/2})/36 < G < 1/16$	square	$\tilde{g} \approx 0.5236G$
$G < (3^{1/2})/36$	triangle	$\tilde{g} \approx (1/2)G$

In each case, similar analyses of RE_g were conducted. Because each pore had its own shape factor, each one of the 229 pores (for all 15 images combined) was considered as a random block.

Results and Discussion

From a Structural Analysis

Figure 8 shows the ME, NU, and RE_P averaged for the 15 simulated images. With OTSU and IK/GM, PRE1 noise reduction filtering improved the segmentation accuracy because a decrease in indicator value meant an increase in segmentation accuracy. Compared with the results obtained by Hapca et al. (2013), Wang et al. (2011), and Schlüter et al. (2014), the ME and NU values for PRE1 and PRE2 were satisfactory. Without noise reduction (PRE0), the ME value for OTSU was 60% lower than that obtained by Schlüter et al. (2014) but 34% higher for IK/GM. These high differences probably arose because we considered averaged ME values with high standard errors. The OTSU_PRE0 and IK/GM_PRE0 performed very well for some images but poorly for others, with some porosity relative error values about 315% for OTSU and 500% for IK/GM. The PBA method performed well, with ME indicators below 0.01 and NU indicators below 0.05. In this case, where the exact porosity to reach was known, noise reduction did not improve the PBA method. This is consistent with the working principle of PBA and with our experimental conditions. The segmentation was not perfect, however, highlighting the main disadvantage of the selection of one threshold value for an entire two- (or three-) dimensional image.

Table 4 presents the relative variations in performance indicator values between two noise reduction levels for each segmentation method. First, the variations among the indicators were not comparable. Therefore, to characterize the effect of one noise reduction,

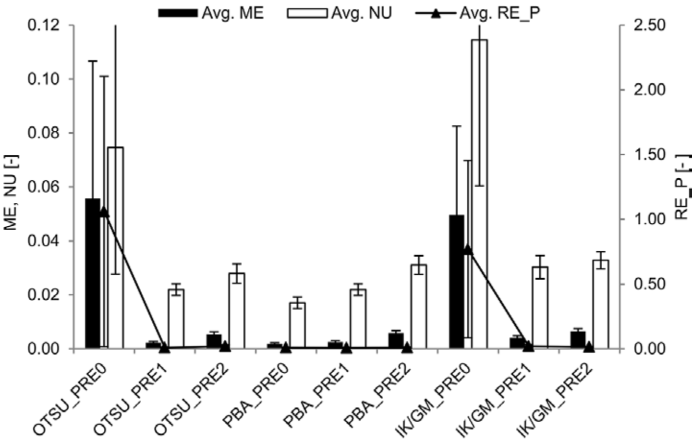

Fig. 8. Averaged misclassification error (ME), region non-uniformity (NU), and porosity relative error (RE_P) for all segmentation methods (OTSU, porosity-based [PBA], and adaptive indicator kriging + gradient masks [IK/GM]) and for all pre-segmentation noise reductions (PRE0, PRE1, and PRE2).

it is advisable to use multiple and various performance indicators. Then, the variations from a PRE1 to a PRE2 noise reduction were greater for the global segmentation methods (OTSU and PBA) than for the local IK/GM method albeit the histogram bimodality was sharpened. This is, however, consistent with the study of Houston et al. (2013b), who found that OTSU gave a greater mean difference between two noise reduction levels than IK. Figure 9 shows the resulting images after OTSU and IK/GM segmentation for both noise reduction levels. Black pixels represent the pores that match the ground-truth information, the blue pixels represent pixels that are allocated to the soil matrix but should have been allocated to pores, and the red pixels are those allocated to pores but shouldn't have been. With OTSU, from PRE1 to PRE2, small features are removed (blue pixels) and bigger pores have growing edges (red pixels). The differences between PRE1 and PRE2 for IK/GM are less striking.

With regard to the occurrence of the lowest ME, PBA_PRE0 provided the lowest indicator 12 times; together, PBA_PRE1 and OTSU_PRE1 provided the lowest one three times and almost always had the same ME value (13 times out of 15). In terms of NU, PBA_PRE0 always provided the lowest indicator value and, if its performance had not been taken into account, OTSU_PRE1 would always have provided the lowest ME and NU values. With regard to RE_P, OTSU_PRE1 and PBA_PRE1 provided the identical closest value to real porosity for 13 images. The IK/GM_PRE1 twice provided the lowest RE_P. This is not consistent with the findings reported by Wang et al. (2011), who concluded that IK performed better than OTSU in the case of clear bimodal histograms, which was the case with the simulated images. The difference between the two studies was probably due to the TH interval choice when using IK. The gradient masks method (Schlüter et al., 2010) for calculating the TH interval was developed for unimodal images. We discuss this point further below. At no point did OTSU_PRE2 or IK/GM_PRE2 give the best performance. Because the added noise on our simulated images is uncorrelated, PRE2 noise reduction seems to be disproportionate and destroys true information.

Statistical analyses confirmed that the PRE1 filter significantly improved segmentation accuracy with OTSU and IK/GM in terms of ME. With regard to NU, there was a significant difference between the three OTSU values (PRE0–PRE1–PRE2), but post-Tukey's test was not able to determine the source of the difference. Similarly, PRE0 to PRE1 and PRE0 to PRE2 were significantly different for IK/GM, but in contrast RE_P significantly differentiated PRE0 to PRE1 and PRE0 to PRE2 for OTSU but not for IK/GM. These contrasting results illustrate the variability in indicator definitions and reflect the working principles of the global and local methods. The OTSU method gives different porosities by identifying porosity within the soil matrix where grayscale values are low (porosity is represented by black pixels). This leads to porosity without physical meaning, as noted by Hapca et al. (2013). The IK/GM method identifies the right pore region, but the limits might not be accurate. Therefore, despite a high grayscale value, some pixels were taken into account, which increased the grayscale value variance and subsequently the NU. Wang et al. (2011) concluded that the use of NU is not enough for characterizing segmentation quality but provided acceptable results in the absence of ground-truth information. They observed that selecting the best segmentation method based on both ME and NU agreed for most images. Again, the use of multiple indicators allowed us to better characterize the accuracy of the segmentation methods. From ME, NU, and RE_P analyses and according to the experimental conditions, we showed that OTSU and IK/GM were more accurate with a PRE1 noise reduction and that OTSU_PRE1 and IK/GM_PRE1 were not statistically different.

Table 4. Misclassification error (ME), region non-uniformity (NU), porosity relative error (RE_P), and conductance relative error (RE_K) relative variations among the noise reductions (PRE0, PRE1, and PRE2) for the segmentation methods (Otsu, 1979 [OTSU], porosity-based [PBA], and adaptive indicator kriging + gradient masks [IK/GM]).

Processing		**Relative variations**			
Noise reduction	Segmentation	ME	NU	RE_P	RE_K
		%			
From PRE0 to PRE1	OTSU	−96	−71	−99	−49
	PBA	39	29	−14	152
	IK/GM	−92	−74	−97	−20
From PRE1 to PRE2	OTSU	131	27	132	66
	PBA	129	42	28	80
	IK/GM	62	8	−29	28

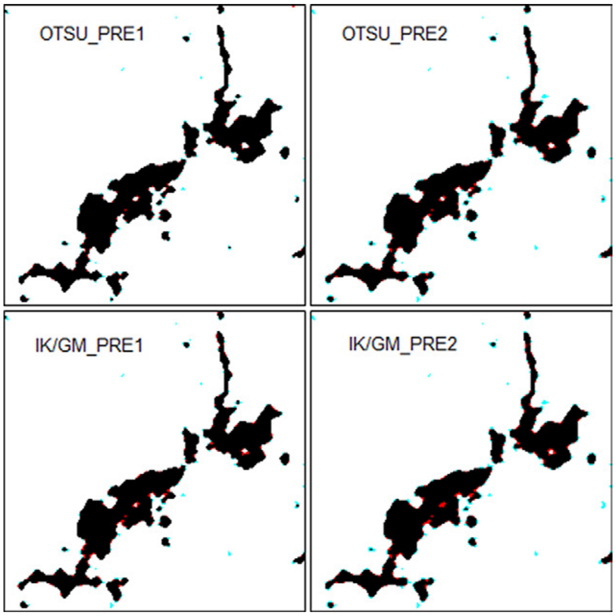

Fig. 9. Resulting Image no. 10 after the OTSU and the adaptive indicator kriging + gradient masks (IK/GM) segmentation methods for two level of pre-segmentation noise reduction (PRE1, PRE2). Black pixels represent the pores that match the ground-truth information, the blue pixels represent pixels that are allocated to soil matrix but should have been allocated to pore and the red pixels are the one allocated to pore but shouldn't have been.

From a Functional Analysis

With regard to the global conductance results (RE_K), Fig. 10 depicts the averaged relative error for RE_K for all 15 images. Post-segmentation noise reduction always provided higher averaged RE_K with high standard errors. Indeed, post-segmentation noise reduction alters the pores edges and has influenced the pore conductance values (Fig. 11). However, post-segmentation has the advantage of removing small features wrongly assigned to porosity, albeit a post-segmentation cleanup could also do the job if those features are small enough.

Table 5 presents the variations in RE_K between OTSU or IK/GM and PBA. As noted above, PBA is here based on the images' ground-truth information and should therefore perform well. The two global methods performed in a similar way when a PRE1 noise reduction was applied (low relative variations), which is consistent with previously discussed results. In this case, where we compared one segmentation method to a supposedly accurate segmentation method (PBA), the relative variations of RE_K were fairly similar to NU values. This is an interesting point because the NU indicator is calculated without ground-truth information, while RE_K is.

The statistical analyses concluded that the segmentation method and combination of noise reduction factors separately had a significant impact on RE_K. Figure 12 shows the main factor effect plot for these factors. It shows that applying a post-segmentation noise reduction without any pre-segmentation noise reduction (combination PRE0–POST2) led to a significantly higher averaged relative error when compared with any combination of pre-segmentation noise reduction (PRE0–PRE1–PRE2) without post-segmentation noise reduction (POST0). In particular, a Tukey post-hoc test concluded that the comparison of PRE0–POST0 (or PRE1–POST0) and PRE0–POST2 was highly significant ($p < 0.01$), and the comparison between PRE2–POST0 and PRE0–POST2 was significant ($p < 0.05$). Post-hoc tests also concluded that there was a significant difference between the PBA and IK/GM methods but none between OTSU and IK/GM or between OTSU and PBA, as also illustrated in Fig. 13.

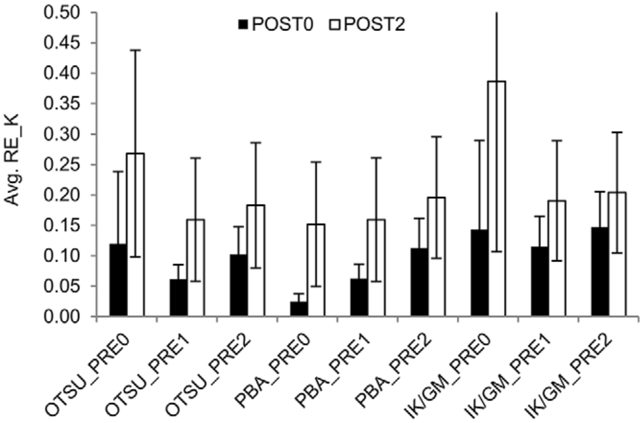

Fig. 10. Averaged conductance relative error (RE_K) for all segmentation methods (Otsu, 1979 [OTSU], porosity-based [PBA], and adaptive indicator kriging + gradient masks [IK/GM]), for all pre-segmentation noise reductions (PRE0, PRE1, and PRE2), and for both post-segmentation noise reductions (POST0 and POST2).

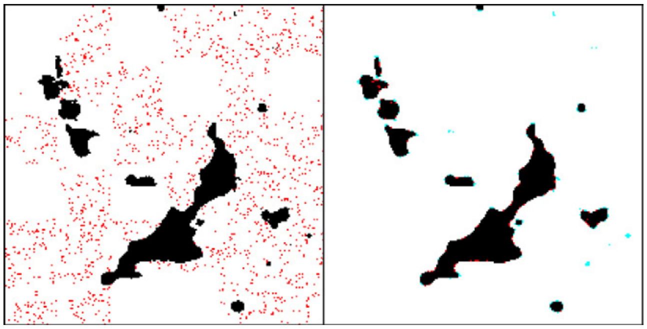

Fig. 11. Resulting Image no. 6 after the OTSU (Otsu, 1979) segmentation method. The left-hand image was obtained without a pre- or post-segmentation noise reduction. The right-hand image was obtained without a pre-segmentation noise reduction and with a two-level post-segmentation noise reduction. Black pixels represent the pores that match the ground-truth information, the blue pixels represent pixels that are allocated to the soil matrix but should have been allocated to pores, and the red pixels are those allocated to pores but shouldn't have been.

Figure 14 shows the tendency between noise reduction levels and segmentation methods with regard to RE_g (the relative error across the shape factor). We did not compute the PRE0 results because some pores had merged with OTSU and IK/GM and relative errors would increase without meaning. The OTSU and PBA methods had almost the same mean. This is consistent with the fact that global TH variation would lead to porosity variation within the soil matrix but less so around the pore region edges (also illustrated in Fig. 13). Post-segmentation noise reduction led to higher relative errors, which was consistent with the RE_K results. Some small pores were removed and pore edges were smoothed when POST2 was applied. There was no significant difference, however, among segmentation methods or the noise reduction levels, which was in contrast with the statistical results of RE_K.

Table 5. Misclassification error (ME), non-region uniformity (NU), porosity relative error (RE_P), and conductance relative error (RE_K) variations among the segmentation methods (Otsu, 1979 [OTSU], porosity-based [PBA], and adaptive indicator kriging + gradient masks [IK/GM]) for an identical pre-segmentation noise reduction (PRE0, PRE1, or PRE2).

Processing		Relative variations			
Segmentation	Noise reduction	ME	NU	RE_P	RE_K
		%			
From OTSU to PBA	PRE0	−97	−77	−99	−79
	PRE1	8	0	−16	2
	PRE2	7	11	−54	11
From IK/GM to PBA	PRE0	−96	−85	−99	−83
	PRE1	−38	−28	−64	−45
	PRE2	−12	−5	−35	−23

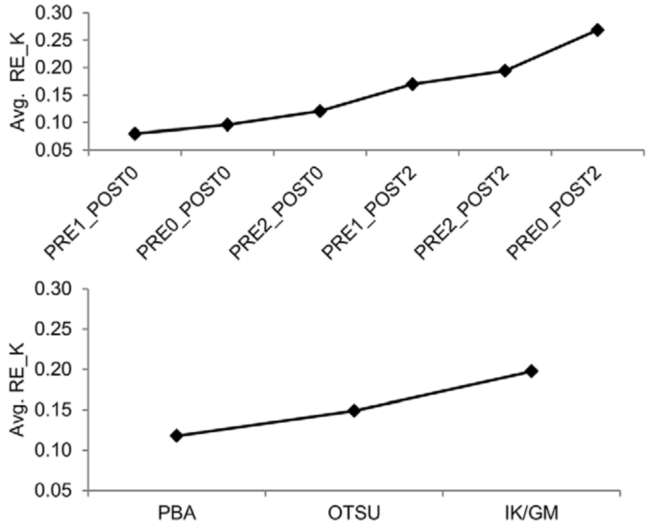

Fig. 12. Main effect plots for the conductance relative error (RE_K). The upper graph displays the pre-segmentation (PRE0, PRE1, and PRE2) and post-segmentation (POST0 and POST2) noise reduction combinations as variables. The lower graph displays the segmentation methods (porosity-based [PBA]; Otsu, 1979 [OTSU]; and adaptive indicator kriging + gradient masks [IK/GM]) as variables.

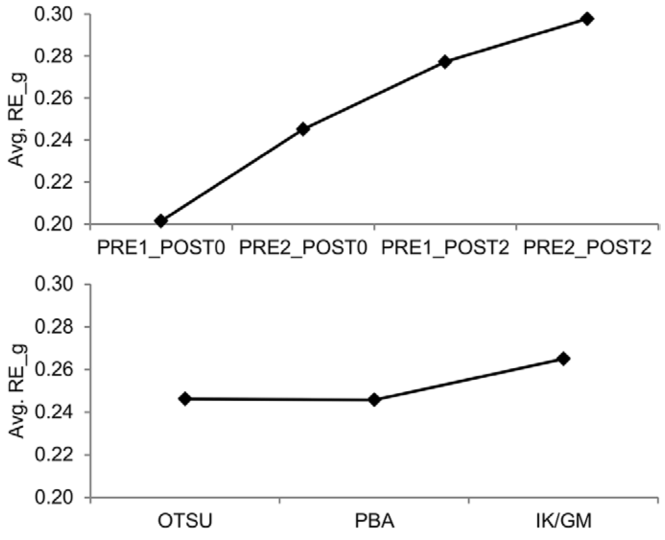

Fig. 14. Main effect plots for the shape factor relative error (RE_g). The upper graph displays the pre-segmentation (PRE0, PRE1, and PRE2) and post-segmentation (POST0 and POST2) noise reduction combinations as variables. The lower graph displays the segmentation methods (porosity-based [PBA]; Otsu, 1979 [OTSU]; and adaptive indicator kriging + gradient masks [IK/GM]) as variables.

From a Threshold Analysis

Table 6 shows the TH median values for the segmentation methods and associated noise reduction. For IK/GM, the TH interval boundaries tended to decrease from PRE0 to PRE1 and PRE2. For OTSU, this was also the case from PRE0 to PRE1. The TH then increased, however, from PRE1 to PRE2. There was indeed a right-hand shift in the lower part of the soil matrix peak (see Fig. 15). At noise reduction PRE1, OTSU and PBA even had an identical TH. This could therefore be seen as a satisfactory noise reduction for the global method. As noted above, IK/GM performed better with pre-segmentation noise reduction. In those cases, the TH interval included the global TH from OTSU and PBA. With increasing noise reduction, the IK/GM TH interval increased. The TH2 was selected as the pore–solid boundary intensity level, and this one moved to a lower value with noise reduction (see Fig. 15). The TH1 selection was based on the TH2 value and the mode value. On the basis of these findings, we investigated the choice of a TH interval around the global TH computed by PBA.

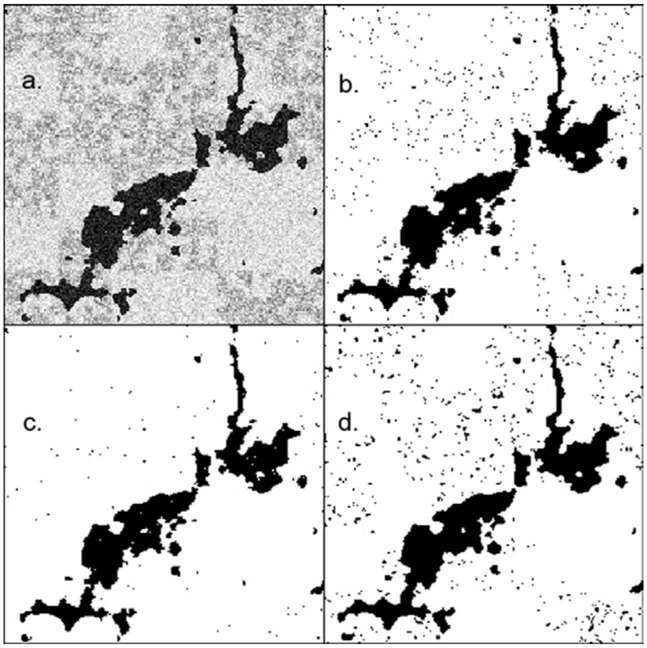

Fig. 13. Image no. 10 at various steps: (a) simulated image; (b) image after a PRE0 pre-segmentation noise reduction and OTSU segmentation (Otsu, 1979); (c) image after a PRE0 pre-segmentation noise reduction and the porosity-based segmentation (PBA); and (d) image after a PRE0 pre-segmentation noise reduction and the adaptive indicator kriging + gradient masks segmentation (IK/GM).

Testing the Relevance of the IK–PBA Method

The IK–PBA method tended to combine the precision of the local IK method with the robustness of the global PBA method by selecting the initial local TH interval around the global TH calculated by PBA. To perform a sensitivity analysis of the TH interval impact on the IK method, the TH interval around the global TH selected with

Table 6. Median threshold values according to segmentation methods (Otsu, 1979 [OTSU], porosity-based [PBA], and adaptive indicator kriging + gradient masks [IK/GM]) and pre-segmentation noise reductions (PRE0, PRE1, and PRE2); TH1 and TH2 represent the threshold interval for the local method.

	Segmentation method			
Noise reduction	OTSU	PBA	IK/GM TH1	IK/GM TH2
PRE0	125	102	147	180
PRE1	121	121	114	162
PRE2	123	135	96	151

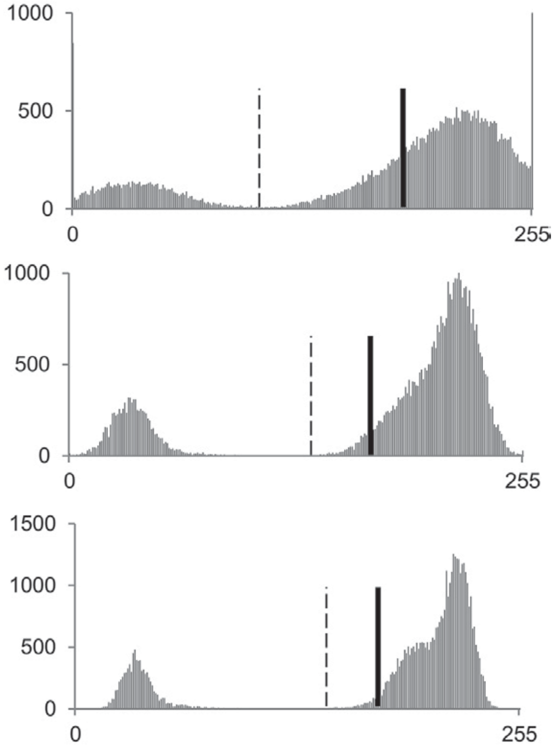

Fig. 15. Image no. 14 histograms with different pre-segmentation noise reductions. Top to bottom: PRE0, PRE1, and PRE2. The dotted line represents the global threshold obtained with the porosity-based (PBA) segmentation method; the plain bold line represents the upper threshold obtained with adaptive indicator kriging + gradient masks (IK/GM) segmentation.

PBA ranged from ±10 to ±50%. We found that the ME indicator remained unchanged for the intervals ±10, ±20, and ±30%. After that, ME increased constantly, reaching about 25% of the initial ME value at the ±50% interval. For the following operations, we present only the segmentation results with a ±10% TH interval. First, the averaged ME (0.0023), NU (0.0217), RE_P (0.0096), and RE_K (0.064) values for IK–PBA were all in the same range as those from PBA or OTSU_PRE1. For ME, IK–PBA had the best performance twice, but for NU, RE_P, or RE_K it never had the best performance. The statistical analyses confirmed this trend by showing only OTSU_PRE0 and IK/GM_PRE0 as significantly different from IK–PBA in terms of ME, NU, and RE_P. When including post-segmentation noise reduction, RE_K analyses showed that post-segmentation noise reduction did not produce a significantly different result with IK–PBA. The IK–PBA method provided a significant improvement, however, compared with IK/GM_PRE0_POST2, which was consistent with previous findings. The RE_g again gave contrasting results. According to this indicator, IK–PBA gave the best results and differed significantly from any other combination of method and noise reduction. The IK–PBA method therefore produced the correct binary images without the use of a noise reduction process (as opposed to OTSU_PRE1) and without knowing the real characteristics of the RS image used to construct the simulated images (as opposed to PBA). This is consistent with the recommendation made by Iassonov et al. (2009) and Iassonov and Tuller (2010) that a local method could be used as an alternative to pre-segmentation processing. As noted above, the choice of the TH interval is of prime importance when using IK. With the two-peak histogram simulated image, the interval around the global PBA TH produced far better results than the interval calculated by the gradient masks method (Schlüter et al., 2010), and this made the original idea of IK–PBA attractive.

Conclusion

X-ray computed tomography is widely used in soil and hydrological sciences. To be able to apply it to many situations, the prior concern is to have an accurate and correct pore space description. This comes with suitable choices of image processing that will modify the information initially available on grayscale images. The conscious and relevant processing decisions are therefore of great importance. Within this context, various noise reduction and segmentation method combinations were tested on multiple simulated grayscale images to perform statistical analyses on five types of indicators.

It was shown that pre-segmentation noise reduction through a median filter led to a significant improvement in segmentation accuracy for the global segmentation method introduced by Otsu (1979) and for the local adaptive-window indicator kriging (Houston et al., 2013a) segmentation method whose threshold interval was calculated with the gradient masks method (Schlüter et al., 2010). Moreover, the statistical analyses did not significantly differentiate those two methods when a pre-segmentation median filter was applied.

The PBA method calculated the global threshold value that should be applied; however, the global segmentation wasn't perfect. Therefore, a pre-segmentation noise reduction filter seems to be a necessity with global thresholding. Post-segmentation noise reduction was shown to be detrimental to segmentation quality by altering the pore shapes.

The threshold interval choice with the IK method is of major importance. Adapting the calculating method to the type of image histogram is advised. Our approach (IK–PBA) based on the global threshold value calculated with the PBA method performed well by providing indicator values that were similar to those generated by PBA, but IK–PBA had the advantage of using neither ground-truth information nor noise reduction filters.

Acknowledgments

We acknowledge the support of the National Fund for Scientific Research (Brussels, Belgium). We also thank Dr. Alasdair Houston for providing the AWIK software and Professor Yves Brostaux for advising us on the statistical analyses. We thank the AgriGES project, its coordinator Professor Bernard Heinesh, and Donat Regaert for supplying the fractal generator code. Finally, we wish to thank the anonymous reviewers and the editor for improving the quality of this paper.

References

Baruchel, J., J.-Y. Buffière, E. Maire, P. Merle, and G. Peix. 2000. X-ray tomography in material science. Hermes Science Publ., Paris.

Baveye, P.C., M. Laba, W. Otten, L. Bouckaert, P. Dello Sterpaio, R.R. Goswami, et al. 2010. Observer-dependent variability of the thresholding step in the quantitative analysis of soil images and X-ray microtomography data. Geoderma 157:51–63. doi:10.1016/j.geoderma.2010.03.015

Beckers, E., E. Plougonven, N. Gigot, A. Léonard, C. Roisin, Y. Brostaux, and A. Degré. 2014a. Coupling X-ray microtomography and macroscopic soil measurements: A method to enhance near saturation functions? Hydrol. Earth Syst. Sci. 18:1805–1817. doi:10.5194/hess-18-1805-2014

Beckers, E., E. Plougonven, C. Roisin, S. Hapca, A. Léonard, and A. Degré. 2014b. X-ray microtomography: A porosity-based thresholding method to improve soil pore network characterization? Geoderma 219–220:145–154. doi:10.1016/j.geoderma.2014.01.004

Capowiez, Y., S. Sammartino, and E. Michel. 2011. Using X-ray tomography to quantify earthworm bioturbation non-destructively in repacked soil cores. Geoderma 162:124–131. doi:10.1016/j.geoderma.2011.01.011

Celia, M.A., P.C. Reeves, and L.A. Ferrand. 1995. Recent advances in pore scale models for multiphase flow in porous media. Rev. Geophys. 33:1049–1057. doi:10.1029/95RG00248

Dal Ferro, N., A.G. Strozzi, C. Duwig, P. Delmas, P. Charrier, and F. Morari. 2015. Application of smoothed particle hydrodynamics (SPH) and pore morphologic model to predict saturated water conductivity from X-ray CT imaging in a silty loam Cambisol. Geoderma 255-256:27–34. doi:10.1016/j.geoderma.2015.04.019

Elliot, T.R., W.D. Reynolds, and R.J. Heck. 2010. Use of existing pore models and X-ray computed tomography to predict saturated soil hydraulic conductivity. Geoderma 156:133–142. doi:10.1016/j.geoderma.2010.02.010

Gantzer, C.J., and S.H. Anderson. 2002. Computed tomographic measurement of macroporosity in chisel-disk and no-tillage seedbeds. Soil Tillage Res. 64:101–111. doi:10.1016/S0167-1987(01)00248-3

Garbout, A., L.J. Munkholm, and S.B. Hansen. 2013. Tillage effects on topsoil structural quality assessed using X-ray CT, soil cores and visual soil evaluation. Soil Tillage Res. 128:104–109. doi:10.1016/j.still.2012.11.003

Hapca, S.M., A.N. Houston, W. Otten, and P.C. Baveye. 2013. New local thresholding method for soil images by minimizing grayscale intra-class variance. Vadose Zone J. 12(3). doi:10.2136/vzj2012.0172

Helliwell, J.R., C.J. Sturrock, K.M. Grayling, S.R. Tracy, R.J. Flavel, I.M. Young, et al. 2013. Applications of X-ray computed tomography for examining biophysical interactions and structural development in soil systems: A review. Eur. J. Soil Sci. 64:279–297. doi:10.1111/ejss.12028

Houston, A.N., W. Otten, P.C. Baveye, and S. Hapca. 2013a. Adaptive-window indicator kriging: A thresholding method for computed tomography images of porous media. Comput. Geosci. 54:239–248. doi:10.1016/j.cageo.2012.11.016

Houston, A.N., S. Schmidt, A.M. Tarquis, W. Otten, P.C. Baveye, and S. Hapca. 2013b. Effect of scanning and image reconstruction settings in X-ray computed microtomography on quality and segmentation of 3D soil images. Geoderma 207-208:154–165. doi:10.1016/j.geoderma.2013.05.017

Iassonov, P., T. Gebrenegus, and M. Tuller. 2009. Segmentation of X-ray computed tomography images of porous materials: A crucial step for characterization and quantitative analysis of pore structures. Water Resour. Res. 45:W09415. doi:10.1029/2009WR008087

Iassonov, P., and M. Tuller. 2010. Application of segmentation for correction of intensity bias in X-ray computed tomography images. Vadose Zone J. 9:187–191. doi:10.2136/vzj2009.0042

Jassogne, L., A. McNeill, and D. Chittleborough. 2007. 3D-visualization and analysis of macro- and meso-porosity of the upper horizons of a sodic, texture-contrast soil. Eur. J. Soil Sci. 58:589–598. doi:10.1111/j.1365-2389.2006.00849.x

Kaestner, A., E. Lehmann, and M. Stampanoni. 2008. Imaging and image processing in porous media research. Adv. Water Resour. 31:1174–1187. doi:10.1016/j.advwatres.2008.01.022

Katuwal, S., T. Norgaard, P. Moldrup, M. Lamandé, D. Wildenschild, and L. de Jonge. 2015. Linking air and water transport in intact soils to macropore characteristics inferred from X-ray computed tomography. Geoderma 237–238:9–20. doi:10.1016/j.geoderma.2014.08.006

Köhne, J.M., S. Schlüter, and H.-J. Vogel. 2011. Predicting solute transport in structured soil using pore network models. Vadose Zone J. 10:1082–1096. doi:10.2136/vzj2010.0158

Kravchenko, A.N., A.N.W. Wang, A.J.M. Smucker, and M.L. Rivers. 2011. Long-term differences in tillage and land use affect intra-aggregate pore heterogeneity. Soil Sci. Soc. Am. J. 75:1658–1666. doi:10.2136/sssaj2011.0096

Lamandé, M., D. Wildenschild, F.E. Berisso, A. Garbout, M. Marsh, P. Moldrup, et al. 2013. X-ray CT and laboratory measurements on glacial till subsoil cores: Assessment of inherent and compaction-affected soil structure characteristics. Soil Sci. 178:359–368. doi:10.1097/SS.0b013e3182a79e1a

Landis, E.N., and D.T. Keane. 2010. X-ray microtomography. Mater. Charact. 61:1305–1316. doi:10.1016/j.matchar.2010.09.012

Larsbo, M., J. Koestel, and N. Jarvis. 2014. Relations between macropore network characteristics and the degree of preferential solute transport. Hydrol. Earth Syst. Sci. 18:5255–5269. doi:10.5194/hess-18-5255-2014

Luo, L., H. Lin, and S. Li. 2010. Quantification of 3-D soil macropore networks in different soil types and land uses using computed tomography. J. Hydrol. 393:53–64. doi:10.1016/j.jhydrol.2010.03.031

Mandelbrot, B.B. 1983. The fractal geometry of nature. W.H. Freeman and Co., San Francisco.

Mason, G., and N.R. Morrow. 1991. Capillary behavior of perfectly wetting liquid in irregular triangular tubes. J. Colloid Interface Sci. 141:262–274. doi:10.1016/0021-9797(91)90321-X

Nunan, N., K. Ritz, M. Rivers, D.S. Feeney, and I.M. Young. 2006. Investigating microbial micro-habitat structure using X-ray computed tomography. Geoderma 133:398–407. doi:10.1016/j.geoderma.2005.08.004

Oh, W., and W.B. Lindquist. 1999. Image thresholding by indicator kriging. IEEE Trans. Pattern Anal. Mach. Intell. 21:590–602. doi:10.1109/34.777370

Otsu, N. 1979. A threshold selection method from gray-level histograms. IEEE Trans. Syst. Man Cybern. 9:62–66. doi:10.1109/TSMC.1979.4310076

Pachepsky, Y.A., D. Giménez, J.W. Crawford, and W.J. Rawls. 2000. Conventional and fractal geometry in soil science. In: Y.A. Pachepsky et al, editors, Fractals in soil science. Elsevier Science, Amsterdam. p. 7–18. doi:10.1016/S0166-2481(00)80003-3

Papadopoulos, A., N.R.A. Bird, A.P. Whitmore, and S.J. Mooney. 2009. Investigating the effects of organic and conventional management on soil aggregate stability using X-ray computed tomography. Eur. J. Soil Sci. 60:360–368. doi:10.1111/j.1365-2389.2009.01126.x

Patzek, T.W., and D.B. Silin. 2001. Shape factor and hydraulic conductance in noncircular capillaries: I. One-phase creeping flow. J. Colloid Interface Sci. 236:295–304. doi:10.1006/jcis.2000.7413

Peng, S., F. Marone, and S. Dultz. 2014. Resolution effect in X-ray microcomputed tomography imaging and small pore's contribution to permeability for a Berea sandstone. J. Hydrol. 510:403–411. doi:10.1016/j.jhydrol.2013.12.028

Perrier, E., N. Bird, and M. Rieu. 1999. Generalizing the fractal model of soil structure: The pore–solid fractal approach. Geoderma 88:137–164. doi:10.1016/S0016-7061(98)00102-5

Peth, S., R. Horn, F. Beckmann, T. Donath, J. Fischer, and A.J.M. Smucker. 2008. Three-dimensional quantification of intra-aggregate pore-space features using synchrotron-radiation-based microtomography. Soil Sci. Soc. Am. J. 72:897–908. doi:10.2136/sssaj2007.0130

Piñuela, J., A. Alvarez, D. Andina, R.J. Heck, and A.M. Tarquis. 2010. Quantifying a soil pore distribution from 3D images: Multifractal spectrum through wavelet approach. Geoderma 155:203–210. doi:10.1016/j.geoderma.2009.07.007

Russell, A.R., and O. Buzzi. 2012. A fractal basis for soil-water characteristics curves with hydraulic hysteresis. Geotechnique 62:269–274. doi:10.1680/geot.10.P.119

Schlüter, S., A. Sheppard, K. Brown, and D. Wildenschild. 2014. Image processing of multiphase images obtained via X-ray microtomography: A review. Water Resour. Res. 50:3615–3639. doi:10.1002/2014WR015256

Schlüter, S., U. Weller, and H.-J. Vogel. 2010. Segmentation of X-ray microtomography images of soil using gradient masks. Comput. Geosci. 36:1246–1251. doi:10.1016/j.cageo.2010.02.007

Sezgin, M., and B. Sankur. 2004. Survey over image thresholding techniques and quantitative performance evaluation. J. Electron. Imaging 13:146–165. doi:10.1117/1.1631315

Taina, I.A., R.J. Heck, and T.R. Elliot. 2008. Application of X-ray computed tomography to soil science: A literature review. Can. J. Soil Sci. 88:1–19. doi:10.4141/CJSS06027

Tarquis, A.M., R.J. Heck, D. Andina, A. Alvarez, and J.M. Antón. 2009. Pore network complexity and thresholding of 3D soil images. Ecol. Complex. 6:230–239. doi:10.1016/j.ecocom.2009.05.010

Tuller, M., R. Kulkarni, and W. Fink. 2013. Segmentation of X-ray CT data of porous materials: A review of global and locally adaptive algorithms. In: S.H. Anderson and J.W. Hopmans, editors, Soil–water–root processes: Advances in tomography and imaging. SSSA Spec. Publ. 61. SSSA, Madison, WI. p. 157–182. doi:10.2136/sssaspecpub61.c8

Vogel, H.-J., J. Tölke, V.P. Schulz, M. Krafczyk, and K. Roth. 2005. Comparison of a lattice–Boltzmann model, a full-morphology model, and a pore network model for determining capillary pressure–saturation relationship. Vadose Zone J. 4:380–388. doi:10.2136/vzj2004.0114

Wang, W., A.N. Kravchenko, A.J.M. Smucker, and M.L. Rivers. 2011. Comparison of image segmentation methods in simulated 2D and 3D microtomographic images of soil aggregates. Geoderma 162:231–241. doi:10.1016/j.geoderma.2011.01.006

Wildenschild, D., and A.P. Sheppard. 2013. X-ray imaging and analysis techniques for quantifying pore-scale structure and processes in subsurface porous medium systems. Adv. Water Resour. 51:217–246. doi:10.1016/j.advwatres.2012.07.018

Zhang, Y.J. 1996. A survey on evaluation methods for image segmentation. Pattern Recognit. 29:1335–1346. doi:10.1016/0031-3203(95)00169-7

Zhou, H., X. Peng, E. Perfect, T. Xiao, and G. Peng. 2013. Effects of organic and inorganic fertilization on soil aggregation in an Ultisol as characterized by synchrotron based X-ray micro-computed tomography. Geoderma 195–196:23–30. doi:10.1016/j.geoderma.2012.11.003

frontiers in Environmental Science

ORIGINAL RESEARCH
published: 23 April 2018
doi: 10.3389/fenvs.2018.00020

Can The Pore Scale Geometry Explain Soil Sample Scale Hydrodynamic Properties?

Sarah Smet[1]*, Eléonore Beckers[1], Erwan Plougonven[2], Angélique Léonard[2] and Aurore Degré[1]

[1] Soil Water Plant Exchanges, BIOSE, Gembloux Agro-Bio Tech, University of Liège, Gembloux, Belgium, [2] Chemical Engineering, University of Liège, Liège, Belgium

For decades, the development of new visualization techniques has brought incredible insights into our understanding of how soil structure affects soil function. X-ray microtomography is a technique often used by soil scientists but challenges remain with the implementation of the procedure, including how well the samples represent the uniqueness of the pore network and structure and the systemic compromise between sample size and resolution. We, therefore, chose to study soil samples from two perspectives: a macroscopic scale with hydrodynamic characterization and a microscopic scale with structural characterization through the use of X-ray microtomography (X-ray μCT) at a voxel size of 21.5^3 μm^3 (resampled at 43^3 μm^3). The objective of this paper is to unravel the relationships between macroscopic soil properties and microscopic soil structure. The 24 samples came from an agricultural field (*Cutanic Luvisol*) and the macroscopic hydrodynamic properties were determined using laboratory measurements of the saturated hydraulic conductivity (Ks), air permeability (ka), and retention curves (SWRC). The X-ray μCT images were segmented using a global method and multiple microscopic measurements were calculated. We used Bayesian statistics to report the credible correlation coefficients and linear regressions models between macro- and microscopic measurements. Due to the small voxel size, we observed unprecedented relationships, such as positive correlations between log(Ks) and a μCT global connectivity indicator, the fractal dimension of the μCT images or the μCT degree of anisotropy. The air permeability measured at a water matric potential of −70 kPa was correlated to the average coordination number and the X-ray μCT porosity, but was best explained by the average pore volume of the smallest pores. Continuous SWRC were better predicted near saturation when the pore-size distributions calculated on the X-ray μCT images were used as model input. We also showed a link between pores of different sizes. Identifying the key geometrical indicators that induce soil hydrodynamic behavior is of major interest for the generation of phenomenological pore network models. These models are useful to test physical equations of fluid transport that ultimately depend on a multitude of processes, and induce numerous biological processes.

Keywords: soil, X-ray micro-computed tomography, saturated hydraulic conductivity, soil water retention curve, air permeability, Bayesian statistics

Edited by:
Philippe C. Baveye,
AgroParisTech Institut des Sciences et Industries du Vivant et de L'environnement, France

Reviewed by:
Steffen Schlüter,
Helmholtz-Zentrum für Umweltforschung (UFZ), Germany
Nicholas Jarvis,
Swedish University of Agricultural Sciences, Sweden

***Correspondence:**
Sarah Smet
sarah.smet@uliege.be

Specialty section:
This article was submitted to Soil Processes, a section of the journal Frontiers in Environmental Science

Received: *30 January 2018*
Accepted: *05 April 2018*
Published: *23 April 2018*

Citation:
Smet S, Beckers E, Plougonven E, Léonard A and Degré A (2018) Can The Pore Scale Geometry Explain Soil Sample Scale Hydrodynamic Properties? Front. Environ. Sci. 6:20. doi: 10.3389/fenvs.2018.00020

INTRODUCTION

The development of visualization techniques has played a major role in fully describing soil functions. Serial sectioning, a well-established method (Cousin et al., 1996), has been replaced by replaced by 3D non-destructive visualization techniques are becoming more easily available, with added benefit of less time-consuming procedures that provide higher resolution images (Grevers et al., 1989). However, Roose et al. (2016) have wisely said, "Technological advances alone are not sufficient. Real advances in our understanding will only be achieved if these data can be integrated, correlated, and used to parameterize and validate image based and mechanistic models." X-ray micro-computed tomography (X-ray μCT) has been widely used in soil science making comparisons between studies possible. (Taina et al., 2008) and Wildenschild and Sheppard (2013) discuss the use of X-ray μCT to study the vadose zone. We also will mention the visual analysis of the air and water distributions within pore spaces, which are both important physical variables for activity of soil biota (e.g., Young et al., 1998; Or et al., 2007; Falconer et al., 2012; Monga et al., 2014; Vogel et al., 2015). One approach is to visualize the soil at high resolution to identify hot-spots of microbial activity (e.g., Gutiérrez Castorena et al., 2016), simulate air-water interfaces within the pore network (e.g., Pot et al., 2015) or quantify the impact of the pore network architecture on the microorganism's activity (e.g., Kravchenko and Guber, 2017). Another approach is to provide a more specific description of the fluid transport capacities (Vogel et al., 2015) which could ultimately improve field-scale models of microbial activity and biochemical processes (Blagodatsky and Smith, 2012). De facto, when dealing with agricultural and environmental properties of the soil, an accurate description and prediction of its transport capacities in the unsaturated state is the overarching goal.

It is well-known that, due to natural or anthropogenic actions, there is quite a range in the variability in fluid transport parameters [e.g., saturated hydraulic conductivity (Ks) or air permeability (ka)] between samples with homogenous textures (Baveye and Laba, 2015; Naveed et al., 2016), due to the uniqueness of the porosity distribution and the connectivity within a sample. Studies have, therefore, focused on the link between the inner pore space structure of a sample and its specific fluid transport properties. On one hand, experimentally visualized infiltration studies shed light on the effective conducting pore network which represents only a small portion of the total network (Luo et al., 2008; Koestel and Larsbo, 2014; Sammartino et al., 2015). The procedures developed in these studies are promising, but restricted to the analysis of large macropores because of the trade-off between resolution and acquisition time. On the other hand, numerical simulations based on pore space are used to predict conductivity. Many studies focused on idealized porous structures (e.g., Vogel et al., 2005; Schaap et al., 2007) and a few deal with actual soil (Elliot et al., 2010; Dal Ferro et al., 2015; Tracy et al., 2015). The latter show encouraging results, but are restricted to a defined resolution and/or sample size (Baveye et al., 2017). Indeed, the direct approach of linking one structure to one function is limited by the difficulty in analyzing the structure in a representative way, so that the soil is adequately characterized (Vogel et al., 2010). The description of soil microscopic structure via global characteristics could encompass that challenge and comparisons of one soil microscopic structure to its own macroscopic properties have indeed gained attention.

Luo et al. (2010) were among the first to measure Ks and the break through curve characteristics on soil samples that were also scanned with X-ray μCT and analyzed in 3D (16 soil cores of 5 × 6 cm and 10.2 × 35 cm and voxel sizes ranging from $250^2 \times 1{,}000\ \mu m^3$ to $1^2 \times 10\ mm^3$). They found that μCT macroporosity, the number of independent macropore, macropore hydraulic radius and angle were identified as the most important microscopic characteristics to explain fluid transport. From 18 soils cores (10 × 9 cm) scanned at a voxel size of $186^3\ \mu m^3$ and 17 soil cores (19 × 20 cm) scanned at $430^2 \times 600\ \mu m^3$, respectively, Naveed et al. (2012) and Katuwal et al. (2015b) found that the lowest μCT macroporosity value for any quarter length of sample height adequately explained air permeability (ka) measured at a water matric potential (h) of -3 or -2 kPa, respectively. Paradelo et al. (2016) showed that the minimum value of macroporosity along a sample depth was most correlated to Ks and ka (45 soil cores of 20 × 20 cm and voxel size of $430^2 \times 600\ \mu m^3$). Mossadeghi-Björklund et al. (2016) also demonstrated that Ks was significantly correlated to μCT macroporosity within a compaction experiment (32 soils cores of 20 × 20 cm and voxels size of $430^2 \times 600\ \mu m$). Eventually, Naveed et al. (2016) suggested that biopore-dominated and matrix-dominated flow soil cores should be distinguished before analyzing relationships between microscopic and macroscopic soil properties. They indeed found distinct significant power regressions between Ks or ka (measured at $h = -3$ and -0 kPa) and μCT macroporosity for the two categories of the 65 soil cores (6 × 3.5 cm and voxel size of $129^3\ \mu m^3$). These observed relationships between flow parameters and μCT porosity are actually intuitive, but they depend on image resolution, water matric potential and soil type. For example, Lamandé et al. (2013) did not find the expected relationship between μCT porosity and ka measured at $h = -10$ kPa, but rather a linear positive relationship between the number of pores and ka (32 soil cores of 19 × 20 cm and voxel size of $600^3\ \mu m^3$). Finally, Anderson (2014) found that Ks could reasonably be estimated from the μCT number of pores and the μCT macroporosity fractal dimension (336 soil cores of 7.62 × 7.62 cm and voxel size of $0.19^2 \times 0.5\ \mu m^3$).

The μCT porosity, number of pores, average pore radius, surface area, and pore network connectivity and tortuosity all depend on the minimal visible pore size, in other words, on the resolution of the binary X-ray μCT images used to obtain the pore network (Houston et al., 2013; Peng et al., 2014; Shah et al., 2016), additionnaly, useful information about conducting pores is lost with increased voxel size. One strategy to minimize this limitation is to use grayscale information. Crestana et al. (1985) demonstrated a linear dependence between the gray value of the

---

Abbreviations: h, water matric potential; θ, water content; SWRC, soil water retention curve; Ks, saturated hydraulic conductivity; ka, air permeability; LabPO, laboratory measured air-filled porosity at a water matrix potential of 1 kPa; BF, Bayes factor. The rest of the uncommon abbreviations are defined in **Table 1.**

soil matrix in Hounsfield unit (HU) and the soil water content. More recently, Katuwal et al. (2015a) found the CT number of the soil matrix (average grayscale value in HU) as a useful descriptor for determining the magnitude of preferential flow, and Paradelo et al. (2016) showed that global macroporosity values combined with the CT-matrix number best explained the variation in air and water transport parameters. Another strategy would be to scan soil samples at higher resolutions. For example, Sandin et al. (2017) worked at a voxel size of 120^3 μm^3 and observed significant correlations between Ks and a global measure of the pore network connectivity (from the percolation theory) which had, to our knowledge, never been observed (20 soil samples of 6.8 × 10 cm). Pore network connectivity and tortuosity are important indicators of flow capacities (Perret et al., 1999; Vogel, 2000). There is still a lack of information on the links between global pore network complexity indicators and flow parameters. It is indeed challenging to identify and describe the part of the conducting pore network that dominates flow. We, however, hypothesize that it might come from the resolution at which previous studies were performed.

Within that context, the objectives of this study are to: (i) characterize the microscopic structure of twenty-four soil samples at a resolution of 21.5 μm resampled to 43 μm; and (ii) explore the relationships between soil microscopic characteristics and its saturated hydraulic conductivity, air permeability and retention capacities using Bayesian statistics.

MATERIALS AND METHODS

Soil Sampling

Twenty-four vertical undisturbed soil samples (3 cm in diameter and 5 cm in height) were taken at the surface of an agricultural soil in Gembloux, Belgium (50°33′N, 4°42′E). According to the WRB soil system (2006), this soil is classified as a *Cutanic Luvisol* with an average of 14.3% of clay, 78.3% of silt and 7.4% of sand. This type of soil is representative of the intensive central agricultural area in Belgium. Sampling was performed 24 to 48 h after a rain. In order to minimize sampling disturbance, the plastic cylinders were manually driven into the soil until the top of the cylinder was at the surface level and then manually excavated.

Macroscopic Measurements

Soil samples were first upward saturated with distilled water. Their characteristic soil water retention curve (SRWC) was then measured using pressure plates (Richards, 1948; DIN ISO 11274, 2012). After being weighed at a water matric potential of −7, −10, −30 and −70 kPa, the air permeability of the samples was measured by applying an air flow across the sample and measuring the resulting inner-pressure with an Eijkelkamp air permeameter 08.65 (Eijkelkamp Agrisearch Equipment, Giesbeek, The Netherlands). As recommended by the constructor, each measure was repeated five times and kept as short as possible. Corey's law was then applied to calculate the air permeability [L^2] (Corey, 1986 in Olson et al., 2001). At −70 kPa, the soil samples were scanned using an X-ray microtomograph (see next section) before the end of their SWRC was measured (water matric potential of −100, −500, and −1500 kPa). After reaching −1,500 kPa, the soil samples were saturated once again and the saturated hydraulic conductivity (Ks [LT^{-1}]) was measured using a constant head device (Rowell, 1994) and applying Darcy's law. Finally, the soil samples were oven-dried at 105° for 7 days to obtain their dry weight. Porosity [L^3L^{-3}] was calculated as the ratio between the volume of water within the saturated soil sample and its total volume (McKenzie et al., 2002). From McKenzie et al. (2002), the bulk density (BD) [ML^{-3}] was deduced from the porosity value (PO) assuming a particle density of 2.65 g/cm^3.

Microscopic Measurements

Image Acquisition

After reaching a water matric potential of −70 kPa, the soil samples were scanned using a Skyscan-1172 desktop micro-CT system (Bruker microCT, Kontich, Belgium). The choice of scanning parameters (filters, number of projections, 180 or 360°, projection averaging) was made by evaluating reconstruction quality over acquisition time. The X-ray source was set at 100 kV and 100 μA and an aluminum-copper filter was used to reduce the beam hardening artifacts in the reconstruction. The rotation step was set at 0.3° over 180° and, to improve the signal-to-noise ratio, the average of 2 projections was recorded at each rotation step. The exposure time was 600 ms. The field of view was 21 × 14 mm and, to cover the entire sample, a 2 × 4 grid of sub-regions were scanned (in the Skyscan software this corresponds to using both the "wide image" mode and "oversize scan" mode). Given these parameters, the total acquisition time was ∼4 h. We adjusted the detector configuration (16-bit X-ray camera with 4 × 4 binning, creating 1000 × 666 pixel radiograms) and the distance between the camera and the soil sample in order to obtain radiographs with a pixel size of 21.5 μm.

Image Processing

Tomographic reconstruction was performed with the NRecon® software, freely provided by Brüker. Automatic misalignment compensation was used along with a level 7 (out of 20) ring artifact correction. No beam hardening post-corrections were applied. The lower limit for the histogram grayscale range was set at zero, as recommended by Tarplee and Corps (2008). The upper limit, the same for all samples, was the maximum value between the automatically generated upper limit for each sample. After reconstructions, the 3D images were cropped to only select the volume within the sampling cylinders (radius of 700 pixels) and the image's contrast was improved in Matlab (MathWorks, UK).

Prior to segmentation, a 3D median filter with a radius of 2 pixels was applied to the images to decrease noise (Smet et al., 2017). Because of computational cost, sub-sampling was performed and the final voxel size was 43 μm in all directions. This process follows recommendation from Houston et al. (2013) and Shah et al. (2016), which is to scan a sample at the highest possible resolution even if a post-scan coarsening is necessary. We then applied the global porosity-based segmentation method developed by Beckers et al. (2014b). To that purpose, we firstly calculated the potential maximal visible pore size from capillary law and voxel size information ($43^3 \mu m^3$). Then, from the laboratory SWRC data, the potential visible porosity for each soil samples was obtained; it was the air-filled porosity at $h = -1$ kPa (equivalent radius of 150 μm). The porosity-based segmentation method selects an initial global threshold with Otsu's method (Otsu, 1979), and then compares the porosity of the resulting binary image (ratio of pore voxels over the total amount of voxels) to the estimated soil sample visible porosity. Through an iterative loop, the threshold is then adjusted to minimize the difference between this calculated porosity and the estimated soil sample visible-porosity. This method has been proven satisfactory (Beckers et al., 2014b; Smet et al., 2017) and the Matlab R2015a (MathWorks, UK) code was provided by the authors. Finally, a visual inspection was performed to evaluate the segmentation quality and, in case the porosity-based segmentation method failed, Otsu's segmentation was used. A post-segmentation cleanup was applied to remove any pores smaller than five voxels.

Quantification of Soil Microscopic Features

After segmentation, the images were imported into Avizo where codes developed by Plougonven (2009) were used. Those codes provide a 3D morphological quantification of the pores based on the skeleton where a pore is defined as "part of the pore space, homotopic to a ball, bounded by the solid, and connected to other pores by throats of minimal surface area" (Plougonven, 2009), the pore boundaries are demarcated by the local geometry. The resulting 3D quantification information regarding pores chambers connected by pores throats included pore localization, volumes, specific surface, connected surfaces, number of connections, deformation and inertia tensor. From those data, we calculated several microscopic parameters (**Table 1**) as well as the pore-size distribution with radius calculated from the assumption that pores were elliptic cylinders (Beckers et al., 2014a). After morphological processing in Avizo, we imported the binary images in ImageJ (Schneider et al., 2012) where the BoneJ plugin (Doube et al., 2010) functionalities were used; all the measurements into ImageJ were performed in 3D. The skeletonisation tool was used to find the pore's centerline and extract a skeleton made of branches that are connected by junctions. It was achieved by external erosion with a 3D medial axis thinning algorithm. All the calculated microscopic parameters presented in **Table 1** are commonly used in studies regarding the use of X-ray in soil science. We calculated the large porosity (Large_PO) in order to be comparable to the results discussed in the introduction of this paper where the voxel size was ∼10 times larger.

3D Visualization

In order to obtain clear 3D representations, all 24 soil X-ray μCT images were subjected to the following process: any pore that was not part of the largest connected component was removed using the MorphoLib plugin (Legland et al., 2016) in ImageJ (Schneider et al., 2012), a cylindrical region of interest of 295 pixels in radius was then used to remove the edge effects caused by sampling with the initial height going unchanged. Visualization was performed using the 3DViewer plugin (Schmid et al., 2010) in ImageJ (Schneider et al., 2012).

Results Analysis

Basic descriptive statistics were performed on the macroscopic and microscopic data. The correlation coefficients (ρ) between the different microscopic parameters were then calculated using Bayesian statistics (see next section) to account for data uncertainty. Then, Bayesian correlation coefficients were calculated between relevant microscopic and macroscopic measurements as well as Bayesian linear regression models. Before implementation, the data were randomly split into calibration (18 soil samples) and validation (6 soil samples) sets. To that purpose, a number was assigned to each of the 24 soil samples and six numbers were randomly picked. Therefore, the soil samples have a sequential numbering. The calibration set includes samples from #1 to #18 and the validation set from #19 to #24.

Bayesian Statistics for Correlation and Linear Regression

When a linear relationship was visually assumed between two variables, the correlation coefficient between those two variables was calculated using Bayesian statistics. In Bayesian statistics a probability is assigned to a model [P(observations|model)] rather than to an observation, as in frequentist statistics. From the observations, the models (the *prior*) are updated to *posterior* distributions [P(model|observations)] and the uncertainty of the statistic description is expressed in a probabilistic way through the posterior distributions parameters. We refer to Marin and Robert (2007) for more information about Bayesian statistics. In this study, we used the package "BayesMed" (Nuijten et al., 2015) in R (R Core Team, 2015), which computes a Bayesian correlation test, the null hypothesis (H_0) being that the correlation coefficient is null. The correlation test is based on a linear regression between two variables with a Jeffreys-Zellner-Siow (JZS) prior as a mixture of g-priors (Liang et al., 2008; Wetzels and Wagenmakers, 2012). The correlation coefficient is extracted from the posterior variance matrix. We computed the test without expectation about the direction of the correlation effect (Wagenmakers et al., 2016). The credibility of the test is assumed by comparing the marginal likelihoods of the regression model to the same regression model without the explaining variable (Bayes Factor, BF), which quantify the evidence for one or the other hypothesis. Another advantage of using the Bayesian approach is the possibility of quantifying the evidence for the null hypothesis (Wetzels and Wagenmakers, 2012). Non-significant tests in frequentist statistics are interpreted in favor of the null hypothesis although the result could be induced by a noisy data set. Therefore, because the posterior distributions are updated from the observations, the conclusion of the test will not depend on the number of observations and it is possible to recalculate BF as the observations are logged-in and stop the collect when the evidence is compelling. Adapted from Jeffreys (1961) in Wetzels and Wagenmakers (2012), BF's larger than 100 were interpreted as decisive evidence for $H_{1;}$ BF's between 30 and 100 as a very strong evidence for H_1, BF's between 10 and 30 as a strong

TABLE 1 | Calculated microscopic parameters on the X-ray μCT images and their definition.

	Microscopic parameter (abbreviation, metric)	Definition
Avizo	Porosity (μCT_PO, %)	Ratio of pore voxels over the total amount of voxels
	Large porosity (Macro_PO,%)	Part of the porosity composed by pores of at least 1,000 voxels
	Number of pores (NP, –)	Total number of pores
	Averaged pore volume (Avg_vol, mm^3)	Ratio of the total volume of pores over the number of pores
	Averaged pore volume of the biggest pores (Avg_Bvol, mm^3)	The biggest pores are the ones that account for 90% of the pores volumes by only representing 10% of the number of pores
	Averaged pore volume of the smallest pores (Avg_Svol, mm^3)	The smallest pores are the ones that account for 10% of the pores volumes by representing 90% of the number of pores
	Proportion of isolated pores (IP, %)	Ratio of the number of pores that have no connection over the total number of pores
	Proportion of isolated porosity (IPO, %)	Ratio of the isolated porosity over the total porosity
	Averaged coordination number(Avg_Z, –)	The average of Z, which is the number of connections at one point (Perret et al., 1999), of the connected pores
	Averaged surface connectivity (SC, L^{-1})	The average of sc which is sc = Nc * Ac / Vp, where Nc is the number of connections, Ac the mean surface area of the connections (L^2) and Vp the pore volume (L^3)
	Total surface connected (Con_surf, mm^2)	The sum of each pore's connected surface
	Specific surface (SS, m^{-1})	Sum of the specific surface of each pore which is the ratio of the pore surface area over its volume
Av. + IJ	Global connectivity (Γ, –)	The sum of each pore's volume squared divided by the total volume of pores. It measures the probability that two pores voxel are part of the same pore (Renard and Allard, 2013).
Image J	Total length of the pore network (L, m)	After skeletonization, it is the sum of all the branches length
	Total nomber of branches (B, –)	After skeletonization
	Total number of junctions (J, –)	After skeletonization
	Degree of connectivity (B/J, –)	Ratio of the number of branches over the number of junctions. As negative is the ratio, as connected should be the medium
	Global tortuosity (τ, m^{-1})	The geometric tortuosity between two points is the ratio between the effective pore path and the shortest distance between the two extreme points (Perret et al., 1999). We calculated the global tortuosity (τ) of the pore network as the average of the tortuosity of each branch
	Fractal dimension (FD, –)	FD was calculated with a box-counting algorithm (Perret et al., 2003)
	Degree of anisotropy (DA, –)	The value of DA is between 0 and 1, 0 for an isotropic medium. DA was calculated with the mean intercept length method (Harrigan and Mann, 1984)
	Euler number (ε, –)	The Euler number is a quantification of the connectivity. Originaly calculated as ε =N-L+O, where N is the number of isolated objects; L is the number of redundant connections and O the number of cavities or holes (Vogel et al., 2010). As negative is the Euler number, as connected is the medium
	Lowest Euler number (Min_ε, –)	The Euler number of the largest connected component of the pore network

evidence for H_1, BF's between 3 and 10 as a substantial evidence for H_1 and BF's below 3 as an anecdotal evidence for H_1. The values of BF's that were inferior to one (1/100; 1/30; 1/10; 1/3) were interpreted in the same way as the BF values superior to one, the evidence going for H_0.

We also established a Bayesian linear regression design to extract relationships between micro- and macroscopic measurements. All combinations between Y and $X_1 + X_2$ were tested and regression models were compared against the same models without the explaining variable (BF). The variables priors were JZS prior as a mixture of g-priors (Liang et al., 2008). We used the "BayesFactor" package (Morey and Rouder, 2015) in R (R Core Team, 2015), the autocorrelation and the convergence were verified. In Bayesian statistics, the starting point is not to identify the best regression equation but rather evaluate the unknown values of the equation explaining variables and intercept. We did it through the quantification of the 2.5 and 97.5% quantiles. The regression equations are reported in the Supplementary Materials section. Afterwards, we aimed at predicting the validation data points through the use of the slopes and intercepts posterior mean. The relative root mean square errors (RRMSE) were calculated as follows:

$$RRMSE = \sqrt{\frac{1}{n}\sum_{i=1}^{n}\left(\frac{d_i - D_i}{D_i}\right)^2} \tag{1}$$

Where n is the number of data points, d_i is the predicted data point and D_i the observed data point.

RESULTS AND DISCUSSIONS

Macroscopic Measurements

The agricultural soil we studied showed large variations between samples with porosity values ranging from 43.09 to 57.70% and density from 1.12 to 1.51 g/cm^3. **Table 2** presents the maximum, minimum, and average values as well as the associated standard deviations of the logarithmic saturated hydraulic conductivities

TABLE 2 | Logarithmic saturated hydraulic conductivities (Ks, cm/day) and air permeability (ka, μm²) measured after applying a draining pressure of −4, −7, −10, −30, and −70 kPa for the calibration and validation data sets [minimum values (Min), maximum values (Max), mean values (Mean), and standard deviation (St dev)].

	[cm/d]	log [μm²]				
	log(Ks)	**ka(−4 kPa)**	**ka(−7 kPa)**	**ka(−10 kPa)**	**ka(− 30 kPa)**	**ka(−70 kPa)**
CALIBRATION DATA SET						
Max	1.591	2.920	3.076	2.992	3.235	3.231
Min	0.443	0.059	0.017	0.095	0.418	0.936
Mean	1.015	1.681	1.735	1.916	2.164	2.318
St error	0.149	0.505	0.478	0.478	0.603	0.400
VALIDATION DATA SET						
Max	1.709	1.773	2.532	2.718	2.837	3.217
Min	0.352	0.395	−0.051	0.581	1.077	0.402
Mean	1.149	1.132	1.018	1.601	1.852	1.885
St error	0.400	0.801	1.028	1.013	0.893	0.891
ALL DATA						
Max	1.709	2.920	3.076	2.992	3.235	3.231
Min	0.352	0.059	−0.051	0.095	0.418	0.402
Mean	1.049	1.584	1.572	1.853	2.086	2.220
St error	0.147	0.443	0.445	0.424	0.496	0.376

[Ks (cm/day)] and air permeabilitys [ka (μm²)]. As expected, the range of Ks and ka values is large due to the singular nature of pore network organization and the resulting transfer properties. For all studied soil samples, we observed a power-law type relationship between ka and the associated air-filled porosity measured from the SWRC (e.g., Ball and Schjønning, 2002). There was, however, no linear relationship between log(Ks) and log(ka) as opposed to what has been shown in other studies (e.g., Loll et al., 1999; Mossadeghi-Björklund et al., 2016). Those transport properties, as well as the water content at various matric potentials, were compared to the microscopic measurements made on the X-ray images.

X-ray μCT Images Analysis

The segmentation step, within the image processing scheme, has a great impact on the visible porosity calculated on the X-ray μCT image and on the extracted microscopic measurements (Lamandé et al., 2013; Smet et al., 2017). We, therefore, visually verified the accuracy of the global segmentation on each of the 24 X-ray μCT images by superimposing the grayscale images on the binary images. It appears that the porosity-based global segmentation method did not provide satisfactory results for two soil X-ray μCT images (#6 from the calibration set and #20 from the validation set). Those samples had a large air-filled porosity at $h = -1$ kPa (Lab_PO); the porosity-based segmentation method increased the threshold (increased μCT_PO) in order to obtain a μCT_PO as close as possible to Lab_PO [resulting threshold of 94 (0–255)]. In addition, the algorithm did not converge for one soil sample (#2), which had a large Lab_PO. Otsu's method was, therefore, applied to those three samples and the global threshold values for samples #2, #6, and #20 were 67, 69, and 69 (0–255), respectively. The threshold values comparisons obtained with the porosity-based method for the other samples supported this processing choice; the averaged threshold value was 63 (± 0.75). Finally, the samples #10, #13, #16 and #17 were segmented using the Otsu's method because their soil water retention curves (SWRC) were not measured. **Figure 1** presents a 3D visualization of each soil sample (calibration and validation sets) followed by a 2D vertical slice from the middle of the soil sample. We will refer to this figure within the Results section.

Microscopic Measurements

Table 3 presents the data ranges, averages and associated standard deviations for all the previously introduced microscopic measurements made on the X-ray μCT soil images (**Table 1**). The calculated μCT porosities, taking into account pores of at least five voxels, were only slightly higher than those calculated taking into account pores of at least 1,000 voxels. The differences represented ± 90% of the number of pores (the pores having a volume between five and 1,000 voxels happened to be the "small pores" as defined in **Table 1**). There was no surprise that we observed longer pore networks (L), higher numbers of pore branches (B) and junctions (J) than Katuwal et al. (2015b) or Garbout et al. (2013) who both worked with larger voxel sizes. Consequently to the high number of pores (NP), the observed Euler numbers (ε) were frequently highly positive and the differences between the percentage of isolated pore (IP) and isolated porosity (IPO) was large. Comparisons to others studies are however tricky because the pore network skeleton is highly sensitive to the scanning equipment and procedure, the image processing, the skeletonisation process and the pore identification.

Table 4 provides the credible (BF > 3) Bayesian correlation coefficients between each of the microscopic measurements. The coefficients were initially calculated for the calibration data and then the validation data were included. In Bayesian statistics, the number of observations does not count for the credibility of a hypothesis, so when a BF was improved with the addition of the validation data, it meant that the correlation was more credible thanks to the observation *values*. The BF were highlighted with colors according to the classes described in the Materials and Methods section. We did not compute the Bayesian regression equations between microscopic measurements since it was not in the scope of this paper. We did not observe any substantial evidence for the null hypothesis between any of the microscopic measurements.

As Perret et al. (1999) observed, μCT_PO and NP were not correlated; NP cannot be a measure of porosity, but rather expresses a notion of pore density and distribution through the soil sample. The positive correlation between μCT_PO and the fractal dimension (FD) has often been observed in the literature (Rachman et al., 2005; Larsbo et al., 2014) and its dependence on μCT_PO is actually the main drawback of being used as an indicator of pore network heterogeneity and complexity. FD was also correlated to the specific surface area (SS), L, B, J, and NP, which is consistent with studies from Kravchenko et al. (2011)

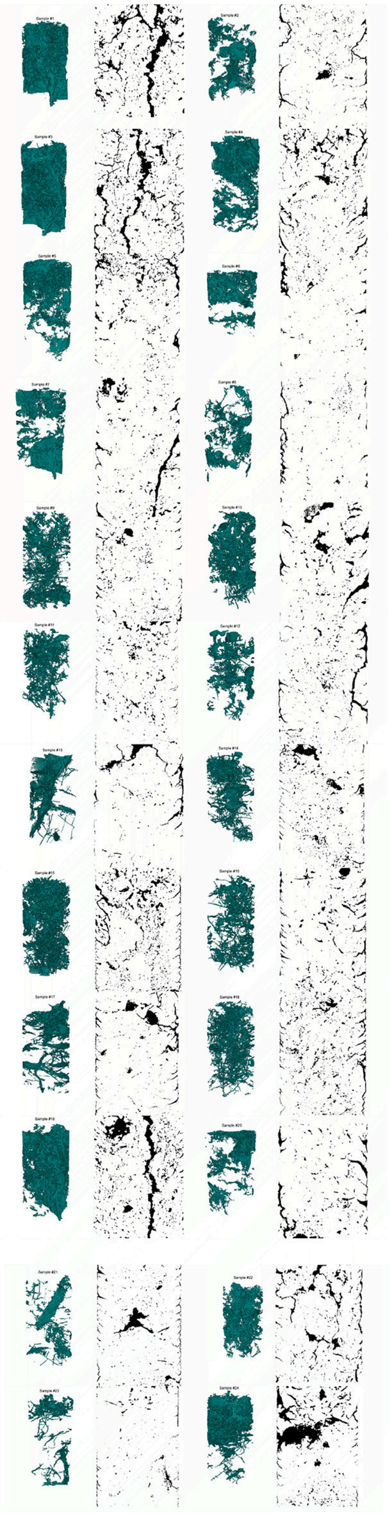

FIGURE 1 | 3D and 2D representations of the 24 studied soil samples.

and Anderson (2014). Those five parameters were all highly correlated to each other but selecting one to represent the other could distort the analysis.

The correlation between μCT_PO and average pore volumes (Avg_vol, Avg_Bvol, and Avg_Svol) also made sense since the average pore volumes were not negatively correlated to NP. The average pore volumes were all slightly correlated to Avg_Z; we observed that larger pores tended to be more connected; Avg_Z and Large_PO were also correlated. This is consistent with the results from Luo et al. (2010); Larsbo et al. (2014); Katuwal et al. (2015a,b). Regarding the other connectivity indicators [degree of connectivity (B/J), the Euler number [ε], and the average surface connectivity (SC)], we observed that AvgZ was correlated to B/J but not to ε or to SC while B/J was correlated to ε and not to SC, and SC was correlated to ε. Those connectivity indicators did not carry the exact same information and should, therefore, be used for their potential explanatory power, as pointed out by Renard and Allard (2013) and Katuwal et al. (2015a), Jarvis et al. (2017), and Sandin et al. (2017) have focused on connectivity indicators based on the percolation theory, and they found that four indicators of connectivity were interchangeable and dependent on soil porosity. We calculated the global connectivity (Γ) indicator from the pore size distribution extracted from Avizo and, from the cluster distribution extracted from BoneJ to be comparable to Jarvis et al. (2017) and Sandin et al. (2017). We observed drastically different Γ values from the two methods of computation. As Houston et al. (2017) assessed it, the software, and the decomposition method that goes with it, influence the final pore size distribution. The very low values of Γ from Avizo came from the decomposition of the pore space into a large amount of connected (or not) pores and the resulting smaller (by two orders of magnitude) largest component than the one identified in BoneJ, where cluster of connected pores are quantified. In the following, to be comparable to Sandin et al. (2017), we used the Γ value computed from the BoneJ's cluster size distribution.

Relationships Between the Microscopic and Macroscopic Measurements

Measured, Calculated, and Predicted Soil Water Retention Curves

In the following section, samples #10, #13, #16, and #17 were not included because SWRC were not measured; the calibration data set included 14 samples instead of 18.

Air-filled porosity at $h = -1$ kPa

In the calibration data set, the relationship between μCT_PO and Lab_PO was neither linear nor credible because of three outliers (#1, #2, #7, **Figure 2**). As discussed above, samples #2 and #7 were segmented with Otsu's method. In the case of sample #7, Lab_PO was too large for the porosity-based method, introducing unrealistic porosity that would explain the deviations. Lab_PO was calculated by weighing the soil samples after draining. If the pore surfaces were rough or loose, water films could have covered up the pores surface by adsorption and pores could appear smaller than they are. Difference between adsorption and desorption curves, also known as the hysteresis effect, can indeed be substantial close to saturation (McKenzie et al., 2002). A physical explanation for sample #1 could be that it had large pores which drained just before being weighed at

TABLE 3 | Microscopic measurements on μCT X-ray images for the calibration and validation data set [minimum values (Min), maximum values (Max), mean values (Mean), and standard deviation (St dev)].

Microscopic measurements	Calibration data set				Validation data set			
	Min	Max	Mean	St dev	Min	Max	Mean	St dev
μCT_PO [%]	3.71	14.23	7.66	2.69	2.76	12.77	8.55	4.06
Macro_PO [%]	2.87	13.22	6.69	2.68	1.97	11.86	7.54	3.93
NP [–]	31,770	79,749	46,649	12,957	32,197	66,192	44,478	12,346
Avg_vol [mm^3]	0.0260	0.1110	0.0567	0.0223	0.0260	0.1010	0.0620	0.0294
Avg_Bvol [mm^3]	0.1350	1.3450	0.5958	0.3656	0.1210	2.0190	0.7795	0.7191
Avg_Svol [mm^3]	3.000E-03	1.200E-02	6.278E-03	2.372E-03	3.000E-03	1.100E-02	7.000E-03	3.162E-03
IP [%]	66.29	87.32	76.58	5.97	64.28	83.76	75.51	7.31
IPO [%]	3.10	12.76	8.44	2.62	4.16	12.88	7.93	3.02
Avg_Z [–]	3.07	5.40	4.29	0.83	3.58	5.24	4.36	0.59
SC [$voxel^{-1}$]	0.206	0.304	0.250	0.029	0.209	0.315	0.258	0.036
Con_surf [mm²]	2553	7921	4722	1321	2696	5984	4703	1282
SS [m^{-1}]	2.040E-03	5.078E-03	2.991E-03	8.484E-04	2.027E-03	4.008E-03	2.843E-03	7.034E-04
Γ [–] / Avizo	9.200E-04	4.817E-02	5.152E-03	1.080E-02	1.400E-03	4.100E-02	1.307E-02	1.601E-02
Γ [–] / BoneJ	0.8613	0.5356	0.7386	0.0820	0.8286	0.6724	0.7365	0.0649
L [m]	28.22	71.58	43.83	10.95	30.97	57.57	43.63	12.17
B[–]	77,776	22,3143	126,510	36,757	81,850	158,219	124,115	30,407
J [–]	28,480	94,542	51,812	16,524	32,605	65,150	51,595	13,053
B/J [–]	2.230	2.930	2.529	0.183	2.280	2.740	2.443	0.166
Tortuosity [mm^{-1}]	1.240	1.280	1.257	0.014	1.240	1.276	1.258	0.013
FD [–]	2.405	2.642	2.527	0.072	2.313	2.653	2.507	0.118
DA [–]	0.112	0.384	0.206	0.080	0.104	0.352	0.252	0.092
ε [–]	−14,125	27,434	8,761	10,969	−9,897	30,112	6,534	13,836
Min_ε [–]	−39,624	−7,196	−20,034	9,141	−2,7461	−9,747	−19,667	6410

The abbreviations of the microscopic measurements are listed in ***Table 1****.*

saturation. Therefore, the volume of water used to calculate the total laboratory porosity could have been under-evaluated. This is most likely since one gram of water can change the Lab_PO from 8.02 to 14.21%. The 3D visualization of sample #1 shows that a large part of its porosity was connected from top to bottom (**Figure 1**). The validation data were in agreement with the calibration data except for sample #20, which was segmented with Otsu for the same reasons as sample #7, and sample #22, which showed a behavior similar to sample #1.

Eventually, the samples that were segmented with the porosity-based method displayed similar Lab_PO and μCT_PO values. Lab_PO was used as a target during the segmentation process. Elliot et al. (2010) also found congruent air-filled porosity values measured by X-ray μCT (voxel size of $45^3 \mu m^3$) and by weight determination. The slope of the relationship between Lab_PO and μCT_PO was higher than one and Lab_PO was indeed positively correlated to the difference between Lab_PO and μCT_PO. The applied capillary theory to calculate Lab_PO and μCT_PO simplifies the pore network to capillaries. We, therefore, suggest that the difference between Lab_PO and μCT_PO reflected the systematic error produced by considering pores as capillaries, and increasing the volume of data to which the theory was applied (PO) had increased the *error* (the difference). The difference between Lab_PO and μCT_PO, whether in absolute value or not, could, however, not be correlated to any microscopic measurements. We presumed that the pore network real connectivity would explain the imperfect applicability of the capillary law. For example, Parvin et al. (2017) reported that the percentage of isolated pores explained the difference in volumetric water content (between laboratory evaporation measurements and X-ray μCT calculation) at a water matric potential ranging from −0.35 to −0.4 kPa by only considering pores larger than 350 μm (pores that should drain at a matric potential of −0.42 kPa from capillary law). The isolated pores were actually connected to others by throats smaller than the voxel size and may not have drained at the required potential calculated from capillary law.

From discrete to continuous data

Beckers et al. (2014a) and Parvin et al. (2017) applied nearly the same methodology to compare predicted SWRC with the bimodal version (Durner, 1994) of the van Genuchten (1980) model. On one hand, they only used macroscopic input data [from pressure plates weighting procedure for Beckers et al. (2014a) and from the evaporation method for Parvin et al. (2017)], and on the other hand, they used those macroscopic data in combination with microscopic data (pore-size distribution extracted from X-ray μCT images) as input. They both found that using the X-ray μCT data allows a better prediction of SWRC close to saturation in terms of RRMSE. We noted, however,

TABLE 4 | Significant Bayesian correlation coefficients between the microscopic measurements for the calibration data set (Cal. data) or the complete data set (All data).

		Large_PO	**NP**	**Avg_vol**	**Avg_Bvol**	**Avg_Svol**	**IP**	**IPO**	**Avg_Z**	**SC**	**Con_surf**	**SS**	**Γ /Avizo**	**Γ/BoneJ**	**L**	**B**	**J**	**B/J**	**τ**	**FD**	**DA**	**ε**	**Min_ε**
µCT_PO	Cal. data	0.98		0.78	0.58	0.80					0.87									0.59			
	All data	0.98		0.77	0.56	0.80				−0.49	0.87									0.69			
Large_PO	Cal. data			0.86	0.68	0.87		0.70	0.53		0.79												
	All data			0.83	0.63	0.85				−0.48	0.82									0.61			
NP	Cal. data											0.98			0.87	0.90	0.84			0.70			
	All data							0.49				0.98			0.87	0.89	0.82			0.71			
Avg_vol	Cal. data				0.87	0.98			0.62			0.52		0.50									
	All data				0.88	0.99		−0.47	0.57		0.52												
Avg_Bvol	Cal. data					0.83			0.55			0.54				−0.54	−0.54						
	All data					0.86	0.50	−0.47	0.51														
Avg_Svol	Cal. data								0.62		0.52												
	All data									−0.49	0.55												
IP	Cal. data									−0.68								0.80	−0.60			0.86	0.68
	All data									−0.73								0.78	−0.67			0.87	
IPO	Cal. data													−0.78									
	All data											0.46	0.56	−0.76								0.49	
Avg_Z	Cal. data																	0.52					
	All data																	0.51	−0.56				
SC	Cal. data																		0.79			−0.78	−0.66
	All data																		0.80	−0.55		−0.80	
Con_surf	Cal. data														0.59					0.73			
	All data														0.67					0.77			
SS	Cal. data														0.83	0.90	0.83			0.61			
	All data														0.83	0.90	0.83			0.63			
Γ/Avizo	Cal. data																						
	All data																						

(Continued)

TABLE 4 | Continued

		Large_PO	**NP**	**Avg_vol**	**Avg_Bvol**	**Avg_Svol**	**IP**	**IPO**	**Avg_Z**	**SC**	**Con_surf**	**SS**	**Γ /Avizo**	**Γ/BoneJ**	**L**	**B**	**J**	**B/J**	**τ**	**FD**	**DA**	**ε**	**Min_ε**
Γ/BoneJ	Cal. data																						
	All data																						
L	Cal. data															0.95	0.95			0.72			−0.70
	All data															0.94	0.93			0.75			−0.74
B	Cal. data																0.95	−0.51		0.57			−0.83
	All data																0.99			0.58			−0.85
J	Cal. data																	−0.60		0.53			−0.84
	All data																	−0.49		0.53			−0.86
B/J	Cal. data																					0.64	0.63
	All data																		−0.52			0.71	
τ	Cal. data																						0.60
	All data																					−.84	−.49
FD	Cal. data																						
	All data																						
DA	Cal. data																						
	All data																						
ε	Cal. data																						.62
	All data																						

The abbreviations of the microscopic measurements are listed in ***Table 1****. Red BF > 100, orange 30 < BF < 100, yellow 10 < BF < 30 and green 3 < BF < 10.*

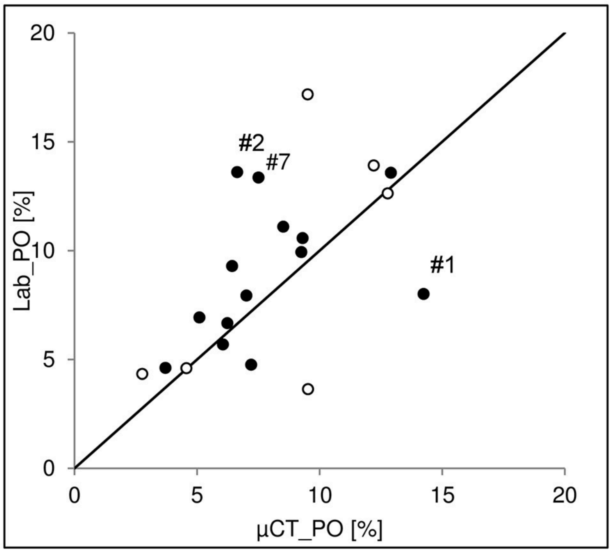

FIGURE 2 | Air-filled porosity measured in the laboratory at a water matric potential of −1 kPa (Lab_PO) vs. the visible porosity measured on X-ray images (μCT_PO) for the calibration data set (black circles) and the validation data set (white circles).

that those studies used macroscopic data from one set of soil samples and microscopic data from another set of soil samples. We aimed at validating the results by using the same samples for both types of measurements. To that purpose, capillary theory was applied to the pore-size distribution extracted from the X-ray μCT images and the calculated SWRC were adjusted to the total laboratory porosity. **Figure 3** illustrates the SWRC for three samples and shows that for all samples, except #1, the volumetric water content (θ) close to saturation was higher when predicted with the combination of X-ray μCT data and pressure plates data (μCT+PP) than with only the pressure plates data (PP), confirming previous results from Beckers et al. (2014a) to Parvin et al. (2017). We also observed that according to the RRMSE values, prediction with μCT+PP data were better than with only the PP data (**Table 5**), except for sample #1. Lamandé et al. (2013) also found that X-ray μCT measurements (voxel size of 600^3 μm^3) allowed a more complete description of the pore space than classical laboratory measurements, and Rab et al. (2014) have concluded that X-ray μCT was likely a better method than laboratory SWRC measurements for determining air-filled macroporosity (pores larger than 300 μm in diameter). The poor performance from sample #1 came from the fact that Lab_PO was lower than μCT_PO, as discussed in **Figure 2**. Apart from sample #1, the use of microscopic information undeniably improved the prediction of continuous SWRC with the bimodal version (Durner, 1994) of the van Genuchten model (1980).

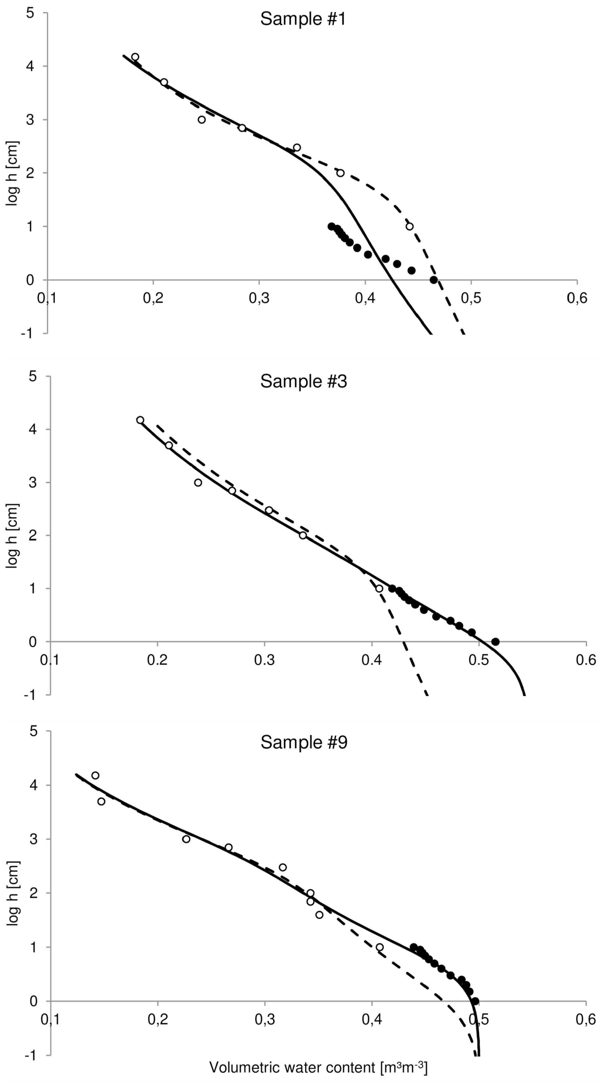

FIGURE 3 | Measured and predicted soil-water retention curves for three samples. Unlike the samples, the SWRC for #1 predicted with the pressure plates data alone (plain line, Pred_PP_DP) performed better than with X-ray μCT data (dotted line, Pred_PP+μCT_DP). Black circles represent the X-ray μCT data and white circles the pressure plate measurements.

Altogether

The determination of SWRC through pressure plate measurements are likely more representative of the *in-situ* soil hydrodynamic, but those are not free of artifacts; for example, air entrapment might result in incomplete saturation leading to inaccurate estimation of the air-filled macroporosity. And, although the connectivity of the pore network was not taken into account with the X-ray μCT SWRC calculation, we still observed that the combination of laboratory measurements and X-ray μCT data improved the SRWC prediction close to saturation. The accurate characterization of the air-filled macroporosity is important for the study of microorganism development (e.g., soil fungal growth in Falconer et al., 2012).

Saturated Hydraulic Conductivity and Soil Porous Structure

The saturated hydraulic conductivity was positively correlated to the global connectivity indicator (Γ) computed from the

TABLE 5 | Relative root mean squared error (RRMSE, %) for the predicted soil water retention curves with the pressure plates data (PP) or the μCT data plus the pressure plates data (μCT + PP) for the calibration data set samples.

Sample	RRMSE	
	PP	μCT+PP
#1	3.445	0.0538
#2	1.816	0.0157
#3	2.867	0.0201
#4	3.617	0.0254
#5	3.711	0.0300
#6	2.311	0.0165
#7	1.727	0.0134
#8	2.906	0.0216
#9	6.526	0.0474
#11	2.427	0.0232
#12	6.135	0.0556
#14	2.734	0.0223
#15	3.840	0.0275
#18	4.781	0.0385

BoneJ cluster size distribution (**Figure 4A**, $\rho = 0.593$, BF = 9.5) as observed in Sandin et al. (2017), unlike that study, we did not observe a credible correlation, but a positive trend between μCT_PO and Γ/BoneJ. It is worth noticing again that Sandin et al. (2017) worked with a resolution close to our but with a different textural soil. Pöhlitz et al. (2018) also reported similar trend of Ks and connectivity values (and μCT_PO) between cultural practices. They worked with a voxel size of $60^3 \mu m^3$ on different samples for the Ks and microscopic measurements, with although a large number of repetitions. **Figure 4A** shows the observations of the calibration data (black circles), the observations of the validation data (white circles), the predicted validation points with the 50% quantiles of the regression model (crosses) and the 25 and 75% quantiles of the regression models (dotted lines). The 50% quantiles of the regression models provided a RRMSE of 0.492 for the validation data and the predicted data points were, in most cases, underestimated. The reported regression models that included two explaining variables reported light credible evidence in the cases where Γ was one of the explaining variables. We did not observe relationships between μCT_PO and log(Ks), despite what the literature reported (Kim et al., 2010; Luo et al., 2010; Mossadeghi-Björklund et al., 2016; Naveed et al., 2016). The measured Ks from those studies were, however, higher by several orders of magnitude. We did observe a positive correlation between log(Ks) and FD when the calibration samples were visually separated in two groups according to their Ks value (**Figure 4B**, black circles). Samples #1, #2, #3, #4, #7, #11, #12, #14, #15, #16, #18 were part of group 1 and samples #5, #6, #8, #9, #10, #13, #17 were part of group 2. No microscopic measurements explained that separation and it was difficult to visually distinguish a pore distribution trend within the pore space (**Figure 1**). We noticed that some of the less conductive samples presented one or two large macropores (not necessarily vertically oriented nor connected from top to bottom) while some of the more conductive samples had more dispersed pore networks, and we observed a negative trend (not credible) between FD and the degree of anisotropy (DA) for group 2, but not for group 1. This suggested that the porosity arrangement led to the composition of two groups for the relationship between FD and log(Ks). By using the Ks value as a boundary, the validation data were assigned to a group (**Figure 4B**, white circles). FD measures the

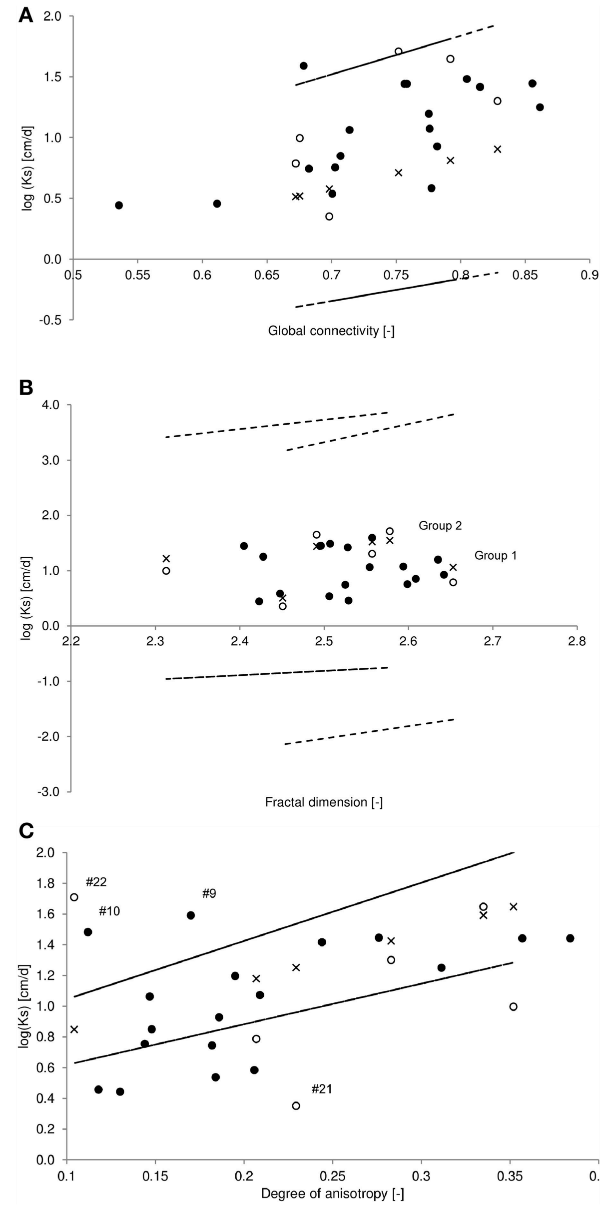

FIGURE 4 | Logarithmic saturated hydraulic conductivity (Ks) vs. **(A)** global connectivity calculated from the pore size distribution extracted from BoneJ, **(B)** the fractal dimension measured on X-ray μCT images, and **(C)** the soil degree of anisotropy measured on X-ray μCT images. Black and white circles represent the observations from the calibration and validation data sets, respectively. Crosses represent predicted validation data points and dotted lines represent the 25 and 75% regression model quantiles.

ability of the studied object to fill the Euclidian space within which it is integrated and, the larger the FD, the closer to a real fractal the object gets, meaning that its shape is similar at different scales. Although Pachepsky et al. (2000) reported that soils are far from being real fractal, Perret et al. (2003) and Kravchenko et al. (2011) pointed out that FD can be used as a global measure of the pore network complexity. For example, FD was found to vary with depth or soil treatment (Rachman et al., 2005; Udawatta and Anderson, 2008; Kim et al., 2010). Anderson (2014) also observed a positive correlation between log(Ks) and FD. By applying the regression equations, log(Ks) of group 1 equal to log(Ks) of group 2, when FD = 3.03, which was close to the upper limit of the possible FD values of a 3D object. At FD = 3, the object (the porosity) occupies each point of 3D Euclidian space, but that also meant that log(Ks) was limited to 128 cm/day. It is reasonable to ask if more groups would be created with increasing conductivity and if the slopes of the relationships would decrease, or if the solutions of the regression equations would be identical when the fractal dimension equals three, which is the fractal dimension upper limit for an Euclidian 3D object. The global RRMSE was 0.260, which is a rather good performance (**Figure 4B**, crosses). The 25 and 75% regression model quantiles were highly dispersed (**Figure 4B**, dotted lines) inducing uncertainty about the regression model.

Anisotropy has been shown to impact soil conductivity (Ursino et al., 2000; Raats et al., 2004; Zhang, 2014). **Figure 4C** plots log(Ks) as a function of DA (black circles for the observations of the calibration data) and by removing two outliers from the calibration data set (#9 and #10), we obtained a correlation coefficient of 0.74 (BF = 125.3), which presents a convincing link that has, to our knowledge, not been seen before. Such a positive correlation could be interpreted as a consequence of preferential flow through large macropores. For example, Dal Ferro et al. (2013) have found that anisotropy was scale-dependent by showing higher average DA in soil cores (DA of 0.32 and voxel size of 40 μm) than in soil aggregates (DA of 0.14 and voxel size of 6.25 μm), they hypothesized that as a possible consequence of biological and mechanical macropores. This was later confirmed by a second study where they showed that only the macropores in the range of 250–500 μm were correlated to the global DA (Dal Ferro et al., 2014). From the DA calculation decomposition (in the Supplementary Materials section), it was possible, but not straightforwardly, to evaluate the main direction of the anisotropy which could be represented by a small amount of pores in that direction, or as the direction of the preferential orientation of one large pore. Ks was measured along the z-axis (vertically) but the main direction of anisotropy was not systematically in that direction. Therefore, the positive correlation between DA and log(Ks) was not necessarily a result of preferential pore networks paths. Moreover, the directions of the pore connections showed that a majority of the pores junction were horizontal (x- and y-axis). The repartition was practically the same between samples, 60% horizontal and 40% vertical connections. Applying the regression model to the validation data gave consistent results for four samples with a RRMSE for those of 0.414 (**Figure 4C**, crosses). Sample #21 gave poor results with a predicted log(Ks) of 1.03 cm/day instead of an observed log(Ks) of 0.35 cm/day and a resulting RSE of 3.742. As well, sample #22 gave a RSE of 0.433, its low DA and large log(Ks) made it similar to the two outliers of the calibration data (#9 and #10). The relationship between DA and log(Ks) may not be suitable for highly conductive soil sample presenting isotropic-like porosity distribution (Samples #9, #10, #22, **Figure 1**). Subjective comparisons between 3D representations and DA need to be made cautiously. We observed that, compared to samples #9, #10, #22, samples #15 and #18 had similar visually homogenous porosity (and equivalent low DA) but with a lower Ks. Samples from group 2 in **Figure 4** (#5, #6, #8, #13, #17 and #20, #23, #24) had higher log(Ks) with a more heterogeneous porosity (and higher DA). The narrower distribution of the 25 and 75% regression model quantiles came from the exclusion of two outliers in the model computation.

The prediction of the hydraulic conductivity curve is frequently extracted from the SWRC shape and absolute values of K(h) can be obtained by matching both curves with a specific point, which is often Ks (Vogel and Roth, 1998). Ks is however cumbersome and time-consuming to measure *in-situ*. We reported here that the porosity arrangement described by the global connectivity, the fractal dimension, and degree of anisotropy had an impact on the soil conductivity, the combination of those indicators provided information that could be used across scales and to eventually better estimate Ks. No other relationships between log(Ks) or Ks and the other microscopic measurements were reported.

Air Permeability Variations Explained by Microscopic Structure

Macroscopic measurements showed, as expected, that the air permeability increased with air-filled porosity. We also observed positive credible Bayesian correlation coefficients between log(ka) measured at various h and microscopic indicators of the porosity (μCT_PO, Large_PO, Avg_vol, Avg_Bvol, and Avg_Svol), although only log(ka,−70 kPa) was positively correlated to μCT_PO (**Table 6**). Given the X-ray μCT image resolution, μCT_PO should be representative of the air-filled PO measured at $h = -1$ kPa although th e soil samples were scanned at $h = -70$ kPa. The choice to scan soil samples at $h = -70$ kPa was a compromise between the fact that all the potential visible porosity should be air-filled and without cracks due to drying, and this particular correlation suggests that all the potential visible porosity was indeed air-filled. In their study, Katuwal et al. (2015b.) and Naveed et al. (2016) both observed a power-law function between, respectively, ka(−2 kPa) or ka(−3 kPa) and μCT_PO. The μCT_PO calculated on their images is equivalent to the Large_PO on our images as previously stated, and we also reported a correlation between Large_PO and log(ka) (**Table 6**). Therefore, the difference between μCT_PO and Large_PO might be the part of the PO that should have drained at low negative potential (from the capillary law), but was actually drained at higher negative potential (due to unusable pathways). We refer to Hunt et al. (2013) to name that part of porosity, the *inaccessible porosity*. This assumption was confirmed by the credible correlations between the inaccessible PO and microscopic parameters which expresses a notion of pore network complexity (B, J, L, NP, SS, IPO, FD). We previously pointed out the drawback that, when calculating SWRC from the X-ray µCT data (namely from the visual pore size distribution), the connectivity was not taken into account. We here confirmed that the pore network connectivity play a role in the desorption process.

Lamandé et al. (2013) found a positive correlation between log(ka,−10 kPa) and NP. We observed negatives correlations (as well as with B, J, and SS). Many pores of our samples were connected to others with connections smaller than the voxel size and were considered isolated (high IP and ε, **Table 3**). It would make sense, that an increasing volume of small (invisible) connections reduces the airflow through the pore network. The air permeability is also largely dependent on the tortuosity and connectivity of the pore network (Ball and Schjønning, 2002; Moldrup et al., 2003), but to our knowledge, no study has reported these links from µCT measurements. From **Table 6**, it appears that the air permeability increased with a growing average number of connections (Avg_Z) as well with a growing global connectivity (Γ/BoneJ), but also with Min_ε and B/J. The last two parameters indicate a decreasing connectivity with an increasing value. First, from **Table 4**, it was observed that B/J increased with decreasing B or decreasing J. That purely algebraic relationship might explain why the air permeability would decrease with decreasing B/J (increasing connectivity). Then, Min_ε was calculated over the largest connected pore component, and, because there are no cavities in real soil pore space (Vogel and Roth, 1998), Min_ε decreased as the number of redundant connections increased. When calculating Avg_Z by class of pore according to their volumes, it appeared that the values of Avg_Z we observed came from a large number of small pores having few connections; the biggest pores had ten times more connections. Avg_Z was correlated to Avg_Z calculated on the pores having a radius between 250 and 375 µm. Therefore, air permeability was correlated to the fact that "medium" size pores had more connections. Moreover, there was a negative trend between log(ka) and Avg_Z calculated on the largest pores which corroborated the positive correlation between ka and Min_ε.

The best regression models calculated on the calibration data (Bayes factor) and applied on the validation data reported that the best explaining variable for all measures of log(ka) (RRMSE) was the average pore volume of the smallest pores (Avg_Svol). That parameter might be seen as a limiting factor, and this suggested that ka was more related to pore size distribution than porosity. **Figure 5A** displays log(ka, −70 kPa) as a function of Avg_Svol and the distribution of the 25 and 75% regression model quantiles are rather narrow. The RRMSE was 1.256 or 0.0649 when the two worst predicted validation data points were not taken into account. The RRMSE for log(ka, −30 kPa) and log(ka, −10 kPa) were around 0.800 with one bad validation data point, and the RRMSE for log(ka, −7 kPa) was very high (8.154) with three

TABLE 6 | Credible Bayesian correlation coefficients between microscopic measurements and logarithmic air permeability (ka) measured at water matric potentials of −70, −30, −10, and −7 kPa for the calibration data set.

	log			
	ka (−7 kPa)	**ka (−10 kPa)**	**ka (−30 kPa)**	**ka (−70 kPa)**
µCT_PO				0.53
Large_PO	0.54	0.60		0.64
Avg_Vol	0.72	0.76	0.72	0.79
Avg_Svol	0.75	0.85	0.75	0.84
Avg_Bvol	0.69	0.76	0.69	0.77
NP		−0.70	−0.76	
Avg_Z	0.55	0.78	0.85	0.69
SS	−0.64	−0.73	−0.80	−0.54
IPO	−0.70	−0.76	−0.82	−0.62
B	−0.56	−0.68	−0.72	
J	−0.52	−0.68	−0.71	
B/J		0.62	0.63	
Γ/BoneJ	0.54			0.54
Min_ε		0.68	0.73	

*The abbreviations of the microscopic measurements are listed in **Table 1**.*

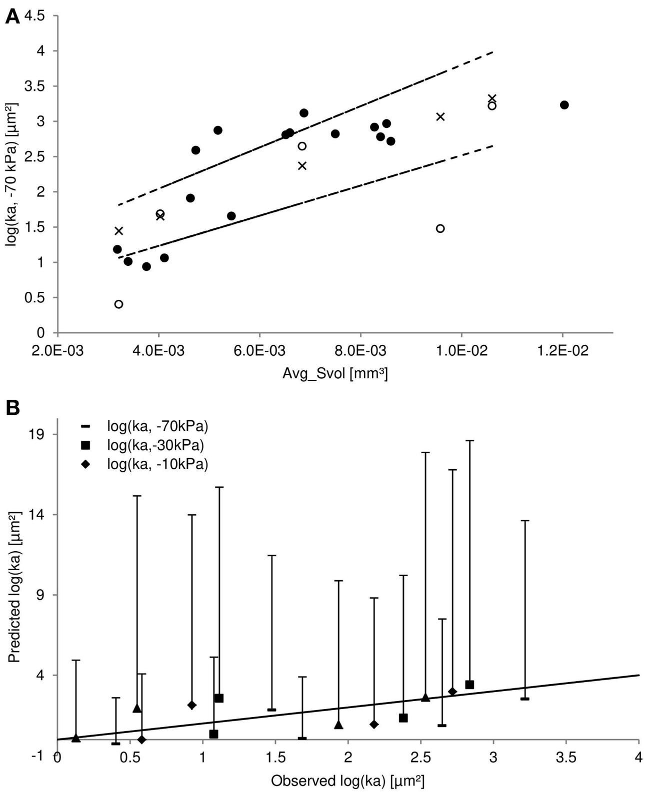

FIGURE 5 | (A) Logarithmic air permeability measured at a water matric potential of −70 kPa (ka) vs. the average pore volume of the smallest pores (Avg_Svol). Black and white circles represent the observations from the calibration and validation data sets, respectively. Crosses represent the predicted validation data points and the dotted lines the 25 and 75% regression model quantiles. **(B)** The predicted logarithmic air permeability from the average pore volume of the smallest pores vs. the observed logarithmic air permeability. Error bars represent the 75% regression model quantiles.

badly predicted data points out of five. The combination of Avg_Svol and average pore volume of all pores (Avg_Vol) performed slightly better in some cases, and slightly worse in others. **Figure 5B** shows the predicted log(ka) from Avg_Svol vs. the observed log(ka) values. Although the RRMSE were acceptable, the regression model distributions (the error bars represent the 75% regression models quantiles) were high which induce large uncertainty. That combination of two explaining variables was, in all cases, the best regression model of two explaining variables. Other important explaining variables were the average coordination number (Avg_Z), the proportion of isolated porosity (IPO), the average pore volume of the biggest pores (Avg_Bvol) and the combination of μCT_PO and Large_PO.

With soil air diffusivity, soil air permeability is one of the main processes governing the exchange of gases with the atmosphere, including therefore soil aeration. Through our experimentations, we aimed at unraveling the main physical drivers of air fluxes through the soil. We have previously observed that subdividing the pore volume averages into three categories (all of the pores, the biggest, and smallest) was not informative; in this study, we have shown the opposite. Avg_Svol was the average volume of the pores having a volume between 4×10^5 and $\pm 8 \times 10^7$ μm^3, in contrast to other cited studies; those pores were visible because of our high resolution (43 μm). Eventually, we suggested that Avg_Svol worked as a limiting factor.

CONCLUSION

X-ray microtomography, among other visualization techniques, has brought new insight into the study and the understanding of soil function. The challenge, however, is the representativeness of the studied soil samples (Vogel et al., 2010) and, to that purpose, the analysis of the same soil samples at two scales has become more prevalent. The resulting next challenge is the resolution at which the soil samples should be studied. To our knowledge, very few studies dealt with equivalent voxel size (43^3 μm^3) and, we did not find any micro-macro correlations such as the ones we observed.

Starting with the comparison of the calculated visible porosity for all pores and for those of at least 1,000 voxels in volume, it appeared that the difference was rather small but positively correlated to indicators of the pore network complexity. The uncommon relationships we observed might be due to the higher resolution we worked with and the resulting finer details of the pore network structure. For example, the calculated fractal dimension and degree of anisotropy are both global indicators of the pore network complexity and both were positively correlated to the saturated hydraulic conductivity, although with some limitations. The global connectivity showed interesting results although highly dependent on the decomposition software used to extract the pore size distribution. Identifying the key parameters that convey the complexity of the pore network is a motivating goal to reach. Pore network modeling has already proven useful (e.g., Vogel and Roth, 1998, or more recently, Köhne et al., 2011), and those three indicators are values that could be used for the generation of a phenomenological model.

Furthermore, we have reported various positive correlations between the air permeability measured at several water matric potentials and microscopic measurements. The average volume of the smallest pores (as small as $\pm 4 \times 10^5$ μm^3) showed the best link with air permeability. Due to our high resolution, we observed a higher number of pores than in other studies and consequently more isolated pores. The Euler number based on the connected space was expected to correlate well with air permeability, but this was not the case. Other measures that provide similar types of information (total pore length, total number of branches, and junctions) proved equally unsatisfactory. In fact, a pertinent link was the positive relationship between the average pore volume of the biggest pores and that of the smallest ones, suggesting dependence between pores of different volumes.

We also reported that the soil water retention curve was better predicted near saturation with the pore size distribution extracted from the X-ray μCT data. Indicators can be derived from the SWRC to characterize soil quality or extrapolate microorganism development (Rabot et al., 2018); its accurate description is therefore a prerequisite. The degree of saturation is also important in the modeling of microbial growth, the dissolution of O_2, the soil respiration, the NO and N_2O production. These processes are affected by the so-called water filled pore space, by soil oxygen content and by soil temperature, which all vary with the volumetric water content (Smith et al., 2003). Blagodatsky and Smith (2012) concluded that the microbial growth models (and we add to this statement: "among others") including "an explicit description of microbial growth, i.e., growth rate and efficiency, humidification ratios and their relationship with N availability, need to be coupled with well-developed soil transport models." The fluid transport predictions for a continuous range of water contents and from discrete measurements are possible through models that are, today, mostly not physically-based. From the pore space structures analyzed, we aimed at contributing to a better understanding of the potential influences of the pore network topology on the physical hydrodynamic properties of soil. Strong unequivocal conclusions could not be drawn because of the limited number of repetitions; image processing and analysis are time-consuming and will be increase with increasing resolution. The comparisons to others studies, as discussed multiple times, depends on many factors and we, therefore, strongly urge the open access to gray scale X-ray μCT images.

DATA AVAILABILITY

Grayscale images and soil physical properties data are available upon request (contact the corresponding author).

AUTHOR CONTRIBUTIONS

SS conceived and designed the research, acquired and analyzed the X-ray images, analyzed and interpreted the data, and wrote the manuscript. EB provided the general X-ray μCT images processing scheme. EP implemented the 3D morphological quantification's code in Avizo. SS, EB, EP, AL, and AD edited the manuscript.

FUNDING

This work was funded through a Ph.D. grant awarded to SS (FRIA, FNRS, Brussels, Belgium) and a FNRS grant awarded to EP (R.FNRS.3363–T.1094.14).

ACKNOWLEDGMENTS

The authors acknowledge the support of the National Fund for Scientific Research (Brussels, Belgium). We also thank Professor Yves Brostaux for his advices on statistical analysis and EP for its availability and expertise. The reviewers are also thanked for their constructive comments.

SUPPLEMENTARY MATERIAL

The Supplementary Material for this article can be found online at: https://www.frontiersin.org/articles/10.3389/fenvs.2018.00020/full#supplementary-material

REFERENCES

Anderson, S. H. (2014). Tomography-measured macropore parameters to estimate hydraulic properties of porous media. *Procedia Comput. Sci.* 36, 649–654. doi: 10.1016/j.procs.2014.09.069

Ball, B. C., and Schjønning, P. (2002). "Air permeability,"in *Methods of Soil Analysis, Part 1*, ed. J. H. Dane and G. C Topp (Madison, WI: Soil Science Society of America), 1141–1158.

Baveye, P. C., and Laba, M. (2015). Moving away from the geostatistical lamppost: why, where, and how does the spatial heterogeneity of soils matter? *Ecol. Model.* 298, 24–38. doi: 10.1016/j.ecolmodel.2014.03.018

Baveye, P. C., Pot, V., and Garnier, P. (2017). Accounting for sub-resolution pores in models of water and solute transport in soils based on computed tomography images: are we there yet? *J. Hydrol.* 555, 253–256. doi: 10.1016/j.jhydrol.2017.10.021

Beckers, E., Plougonven, E., Gigot, N., Léonard, A., Roisin, C., Brostaux, Y., et al. (2014a). Coupling X-ray microtomography and macroscopic soil measurements: a method to enhance near saturation functions? *Hydrol. Earth Syst. Sci.* 18, 1805–1817. doi: 10.5194/hess-18-1805-2014

Beckers, E., Plougonven, E., Roisin, C., Hapca, S., Léonard, A., and Degr,é, A. (2014b). X-ray microtomography: a porosity-based thresholding method to improve soil pore network characterization? *Geoderma* 219–220, 145–154. doi: 10.1016/j.geoderma.2014.01.004

Blagodatsky, S., and Smith, P. (2012). Soil physics meets soil biology: towards better mechanistic prediction of greenhouse gas emissions from soil. *Soil Biol. Biochem.* 47, 78–92. doi: 10.1016/j.soilbio.2011.12.015

Corey, A. T. (1986). "Air permeability," in *Methods of Soil Analysis. Part I. 2nd Edn,* ed A. Klute (Madison, WI: Agronomy Monograph 9, American Society of Agronomy, Inc.; Soil Science Society of America, Inc.,), 1121–1136.

Cousin, I., Levitz, P., and Bruand, A. (1996). Three-dimensional analysis of a loamy-clay soil using pore and solid chord distributions. *Eur. J. Soil Sci.* 47, 439–452. doi: 10.1111/j.1365-2389.1996.tb01844.x

Crestana, S., Mascarenhas, S., and Pozzi-Mucelli, R. S. (1985). Static and dynamic three-dimensional studies of water in soil using computed tomographic scanning. *Soil Sci.* 140, 326–332. doi: 10.1097/00010694-198511000-00002

Dal Ferro, N., Charrier, P., and Morari, F. (2013). Dual-scale micro-CT assessment of soil structure in a long-term fertilization experiment. *Geoderma* 204–205, 84–93. doi: 10.1016/j.geoderma.2013.04.012

Dal Ferro, N., Sartori, L., Simonetti, G., Berti, A., and Morari, F. (2014). Soil macro- and microstructure as affected by different tillage systems and their effects on maize root growth. *Soil Til. Res.* 140, 55–65. doi: 10.1016/j.still.2014.02.003

Dal Ferro, N., Strozzi, A. G., Duwig, C., Delmas, P., Charrier, P., and Morari, F. (2015). Application of smoothed particle hydrodynamics (SPH) and pore morphologic model to predict saturated water conductivity from X-ray CT imaging in a silty loam Cambisol. *Geoderma* 255–256, 27–34. doi: 10.1016/j.geoderma.2015.04.019

DIN ISO 11274 (2012). *Soil Quality–Determination of the Water Retention Characteristics–Laboratory Methods (ISO 11274:1998 + Cor. 1:2009) English Translation of DIN ISO 11274, 2012-04.* Deutsches Institut für Normung, Berlin.

Doube, M., Klosowski, M. M., and Arganda-Carreras, I., et al. (2010). Bone-J: free and extensible bone image analysis in ImageJ. *Bone* 47, 1076–1079. doi: 10.1016/j.bone.2010.08.023

Durner, W. (1994). Hydraulic conductivity estimation for soils with heterogeneous pore structure. *Water Resour. Res.* 30, 211–223. doi: 10.1029/93WR02676

Elliot, T. R., Reynolds, W. D., and Heck, R. J. (2010). Use of existing pore models and X-ray computed tomography to predict saturated soil hydraulic conductivity. *Geoderma* 156, 133–142. doi: 10.1016/j.geoderma.2010.02.010

Falconer, E. R., Houston, A. N., Otten, W., and Baveye, P. C. (2012). Emergent behavior of soil fungal dynamics: influence of soil architecture and water distribution. *Soil Sci.* 177, 111–119. doi: 10.1097/SS.0b013e318241133a

Garbout, A., Munkholm, L. J., and Hansen, S. B. (2013). Tillage effects on topsoil structural quality assessed using X-ray CT, soil cores and visual soil evaluation. *Soil Til. Res.* 128, 104–109. doi: 10.1016/j.still.2012.11.003

Grevers, M. C. J., De Jong, E., and St Arnaud, R. J. (1989). The characterization of soil macroporosity with CT scanning. *Can. J. Soil Sci.* 69, 629–637. doi: 10.4141/cjss89-062

Gutiérrez Castorena, E. V., Gutiérrez Castorena, M. D. C., Vargas, T. G., Bontemps, L. C., Martinez, J. D., Mendez, E. S., et al. (2016). Micromapping of microbial hotspots and biofilms from different crops using image mosaics of soil thin sections. *Geoderma* 279, 11–21. doi: 10.1016/j.geoderma.2016.05.017

Harrigan, T. P., and Mann, R. W. (1984). Characterization of microstructural anisotropy in orthotropic materials using a 2nd rank tensor. *J. Mater. Sci.* 19, 761–767. doi: 10.1007/BF00540446

Houston, A. N., Otten, W., Falconer, R., Monga, O., Baveye, P. C., and Hapca, S. M. (2017). Quantification of the pore size distribution of soils: assessment of existing software using tomographic and synthetic 3D images. *Geoderma* 299, 73–82. doi: 10.1016/j.geoderma.2017.03.025

Houston, A. N., Schmidt, S., Tarquis, A. M., Otten, W., Baveye, P. C., and Hapca, S. (2013). Effect of scanning and image reconstruction settings in X-ray computed microtomography on quality and segmentation of 3D soil images. *Geoderma* 207–208, 154–165. doi: 10.1016/j.geoderma.2013.05.017

Hunt, A. G., Ewing, R. P., and Horton, R. (2013). What's wrong with soil physics? *Soil Sci. Soc. Am. J.* 77, 1877–1887. doi: 10.2136/sssaj2013.01.0020

Jarvis, N., Larsbo, M., and Koestel, J. (2017). Connectivity and percolation of structural pore networks in a cultivated silt loam soil quantified by X-ray tomography. *Geoderma* 287, 71–79. doi: 10.1016/j.geoderma.2016.06.026

Jeffreys, H. (1961). *Theory of Probability.* Oxford, UK: Oxford University Press.

Katuwal, S., Moldrup, P., Lamandé, M.,Tuller, M., and de Jonge, L. W. (2015a). Effect of CT number derived matrix density on preferential flow and transport in a macroporous agricultural soil. *Vadose Zone J.* 14, 1–13. doi: 10.2136/v15.01.0002

Katuwal, S., Norgaard, T., Moldrup, P., Lamandé, M., Wildenschild, D., and de Jonge, L. W. (2015b). Linking air and water transport in intact soils to macropore characteristics inferred from X-ray computed tomography. *Geoderma* 237–238, 9–20. doi: 10.1016/j.geoderma.2014.08.006

Kim, H., Anderson, S. H., Motavalli, P. P., and Gantzer, C. J. (2010). Compaction effects on soil macropore geometry and related parameters for an arable field. *Geoderma* 160, 244–251. doi: 10.1016/j.geoderma.2010.09.030

Koestel, J., and Larsbo, M. (2014). Imaging and quantification of preferential solute transport in soil macropores. *Water Resour. Res.* 50, 4357–4378. doi: 10.1002/2014WR015351

Köhne, J. M., Schlüter, S., and Vogel, H.-J. (2011). Predicting solute transport in structured soil using pore network models. *Vadose Zone J.* 10, 1082–1096. doi: 10.2136/vzj2010.0158

Kravchenko, A. N., and Guber, A. K. (2017). Soil pores and their contributions to soil carbon processes. *Geoderma* 287, 31–39. doi: 10.1016/j.geoderma.2016.06.027

Kravchenko, A. N., Wang, A. N. W., Smucker, A. J. M., and Rivers, M. L. (2011). Long-term differences in tillage and land use affect intra-aggregate pore heterogeneity. *Soil Sci. Soc. Am. J.* 75, 1658–1666. doi: 10.2136/sssaj2011.0096

Lamandé, M., Wildenschild, D., Berisso, F. E., Garbout, A., Marsh, M., Moldrup, P., et al. (2013). X-ray CT and laboratory measurements on glacial till subsoil cores: assessment of inherent and compaction-affected soil structure characteristics. *Soil Sci.* 178, 359–368. doi: 10.1097/SS.0b013e3182a79e1a

Larsbo, M., Koestel, J., and Jarvis, N. (2014). Relations between macropore network characteristics and the degree of preferential solute transport. *Hydrol. Earth Syst. Sci.* 18, 5255–5269. doi: 10.5194/hess-18-5255-2014

Legland, D., Arganda-Carreras, I., and Andrey, P. (2016). MorphoLibJ: integrated library and plugins for mathematical morpholofy with ImageJ. *Bioinformatics* 32, 3532–3534. doi: 10.1093/bioinformatics/btw413

Liang, F., Paulo, R., Molina, G., Clyde, M. A., and Berger, J. O. (2008). Mixtures of g-priors for Bayesian variable selection. *J. Am. Stat. Assoc.* 103, 410–423. doi: 10.1198/016214507000001337

Loll, P., Moldrup, P., Schjønning, P., and Riley, H. (1999). Predicting saturated hydraulic conductivity from air permeability: application in stochastic water infiltration modeling. *Water Resour. Res.* 35, 2387–2400. doi: 10.1029/1999WR900137

Luo, L., Lin, H., and Halleck, P. (2008). Quantifying soil structure and preferential flow in intact soil using X-ray computed tomography. *Soil Sci. Soc. Am. J.* 72, 1058–1069. doi: 10.2136/sssaj2007.0179

Luo, L., Lin, H., and Schmidt, J. (2010). Quantitative relationships between soil macropore characteristics and preferential flow and transport. *Soil Sci. Soc. Am. J.* 74, 1929–1937. doi: 10.2136/sssaj2010.0062

Marin, J.-M., and Robert, C. P. (2007). *Bayesian Core. A Pratical Approach to Computational Bayesian Statistics*. New York, NY: Springer.

McKenzie, N., Coughlan, K., and Cresswell, H. (2002). *Soil Physical Measurement and Interpretation for Land Evaluation*. Collingwood: CSIRO Publishing.

Moldrup, P., Yoshikawa, S., Olesen, T., Komatsu, T., and Rolston, D. E. (2003). Air permeability in undisturbed volcanic ash soils: predictive model test and soil structure finderprint. *Soil Sci. Soc. Am. J.* 67, 32–40. doi: 10.2136/sssaj2003.3200

Monga, O., Garnier, P., Pot, V., Coucheney, E., Nunan, N., Otten, W., et al. (2014). Simulating microbial degradation of organic matter in a simple porous system using the 3-D diffusion-based model MOSAIC. *Biogeosciences* 11, 2201–2209. doi: 10.5194/bg-11-2201-2014

Morey, R. D., and Rouder, J. N. (2015). *BayesFactor: Computation of Bayes Factors for Common Designs.* R package version 0.9.12-2. Available online at: https://CRAN.R-project.org/package=BayesFactor

Mossadeghi-Björklund, M., Arvidsson, J., Keller, T., Koestel, J., Lamandé, M., Larsbo, M., et al. (2016). Effects of subsoil compaction on hydraulic properties and preferential flow in a Swedish clay soil. *Soil Til. Res.* 156, 91–98. doi: 10.1016/j.still.2015.09.013

Naveed, M., Moldrup, P., Arthur, E., Wildenschild, D., Eden, M., Lamandé, M., et al. (2012). Revealing soil structure and functional macroporosity along a clay gradient using X-ray computed tomography. *Soil Sci. Soc. Am. J.* 77, 403–411. doi: 10.2136/sssaj2012.0134

Naveed, M., Moldrup, P., Schaap, M. G., Tuller, M., Kulkarni,R., Vogel, H.-J., et al. (2016). Prediction of biopore- and matrix-dominated flow from X-ray CT-derived macropore networkds characteristics. *Hydrol. Earth. Syst. Sci.* 20, 4017–4030. doi: 10.5194/hess-20-4017-2016

Nuijten, M. B., Wetzels, R., Matzke, D., Dolan, C. V., and Wagenmakers, E.-J. (2015). *BayesMed: Default Bayesian Hypothesis Tests for Correlation, Partial Correlation, and Mediation.* R package version 1.0.1. Available online at: http://CRAN.R-project.org/package=BayesMed

Olson, M. S., Tillman, F. D. Jr., Choi, J.-W., and Smith, J. A. (2001). Comparison of three techniques to measure unsaturated-zone air permeability at Picatinny Arsenal, N. J. *J. Contam. Hydrol.* 53, 1–19. doi: 10.1016/S0169-7722(01)00135-8

Or, D., Smets, B. F., Wraith, J. M., Deschene, A., and Friedman, S. P. (2007). Physical constraint affecting bacterial habittats and activity in unsaturated porous media – a review. *Adv. Wat. Res.* 30, 1505–1527. doi: 10.1016/j.advwatres.2006.05.025

Otsu, N. (1979). A threshold selection method from gray-level histograms. *IEEE Trans. Syst. Man Cybern.* 9, 62–66. doi: 10.1109/TSMC.1979.4310076

Pachepsky, Y. A., Giménez, D., Crawford, J. W., and Rawls, W. J. (2000). "Conventional and fractal geometry in soil science," in *Developments in Soil Science,* eds Y. A. Pachepsky, J. W. Crawford and W. J. Rawls (Elsevier), 7–18.

Paradelo, M., Katuwal, S., Moldrup, P., Norgaard, T., Herath, L., and de Jonge, L. W. (2016). X-ray CT-derived characteristics explain varying air, water, and solute transport properties across a loamy field. *Vadose Zone J.* 192, 194–202. doi: 10.2136/vzj2015.07.0104

Parvin, N., Beckers, E., Plougonven, E., Léonard, A., and Degré, A. (2017). Dynamic of soil drying close to saturation: what can we learn from a comparison between X-ray computed microtomography and the evaporation method? *Geoderma* 302, 66–75. doi: 10.1016/j.geoderma.2017.04.027

Peng, S., Marone, F., and Dultz, S. (2014). Resolution effect in X-ray microcomputed tomography imaging and small pore's contribution to permeability for a Berea sandstone. *J. Hydrol.* 510, 403–411. doi: 10.1016/j.jhydrol.2013.12.028

Perret, J. S., Prasher, S. O., and Kacimov, A. R. (2003). Mass fractal dimension of soil macropores using computed tomography: from the box-counting to the cube-counting algorithm. *Eur. J. Soil Sci.* 54, 569–579. doi: 10.1046/j.1365-2389.2003.00546.x

Perret, J. S., Prasher, S. O., Kantzas, A., and Langford, C. (1999). Three-dimensional quantification of macropore networks in undisturbed soil cores. *Soil Sci. Soc. Am. J.* 63, 1530–1543. doi: 10.2136/sssaj1999.6361530x

Plougonven, E. (2009). *Link between the Microstructure of Porous Materials and their Permeability*. Ph.D. thesis, Université Sciences et Technologies, Bordeaux.

Pöhlitz, J., Rücknagel, J., Koblenz, B., Schlüter, S., Vogel, H.-J., and Christen, O. (2018). Computed tomography and soil physical measurements of compaction behavior under strip tillage, mulch tillage and no tillage. *Soil Til. Res.* 175, 205–2016. doi: 10.1016/j.still.2017.09.007

Pot, V., Peth, S., Monga, O., Vogel, L. E., Genty, A., Garnier, P., et al. (2015). Three-dimensional distribution of water and air in soil pores: comparison of two-phase two-relaxation-times lattice-Boltzmann and morphological model outputs with synchrotron X-ray computed tomography data. *Adv. Water Res.* 87, 87–102. doi: 10.1016/j.advwatres.2015.08.006

Raats, P. A. C., Zhang, Z. F., Ward, A. L., and Gee, G. W. (2004). The relative connectivity-tortuosity tensor for conduction of water in anisotropic unsaturated soils. *Vadose Zone J.* 3, 1471–1478. doi: 10.2136/vzj2004.1471

Rab, M. A., Haling, R. E., Aarons, S. R., Hannah, M., Young, I. M., and Gibson, D. (2014). Evaluation of X-ray computed tomography for quantifying macroporosity of loamy pasture soils. *Geoderma* 213, 460–470 doi: 10.1016/j.geoderma.2013.08.037

Rabot, E., Wiesmeier, M., Schlüter, S., and Vogel, H.-J. (2018). Soil structure as an indicator of soil functions: a review. *Geoderma* 314, 122–137. doi: 10.1016/j.geoderma.2017.11.009

Rachman, A., Anderson, S. H., and Gantzer, C. J. (2005). Computed-Tomographic measurement of soil macroporosity parameters as affected by stiff-stemmed grass hedges. *Soil Sci. Soc. Am. J.* 69, 1609–1616. doi: 10.2136/sssaj2004.0312

R Core Team (2015). *R: A Language and Environment for Statistical Computing*. Vienna: R Foundation for Statistical Computing.

Renard, P., and Allard, D. (2013). Connectivity metrics for subsurface flow and transport. *Adv. Wat. Res.* 51, 168–196. doi: 10.1016/j.advwatres.2011.12.001

Richards, L. A. (1948). Porous plate apparatus for measuring moisture retention and transmission by soils. *Soil Sci.* 66, 105–110. doi: 10.1097/00010694-194808000-00003

Roose, T., Keyes, S. D., Daly, K. R., Carminati, A., Otten, W., Vetterlein, D., et al. (2016). Challenges in imaging and predictive modeling of rhizosphere processes. *Plant Soil.* 407, 9–38. doi: 10.1007/s11104-016-2872-7

Rowell, D. L. (1994). *Soil Science: Methods and Application*. Harlow, UK: Longman Group Limited, Longman Scientific & Technical.

Sammartino, S., Lissy, A.-S., Bogner, C., Van Den Bogeart, R., Capowiez, Y., et al. (2015). Identifying the functional macropore network related to preferential flow in structured soils. *Vadose Zone J.* 14, 1–16. doi: 10.2136/vzj2015.05.0070

Sandin, M., Koestel, J., Jarvis, N., and Larsbo, M. (2017). Post-tillage evolution of structural pore space and saturated and near-saturated hydraulic conductivity in a clay loam soil. *Soil Til. Res.* 165, 161–168. doi: 10.1016/j.still.2016.08.004

Schaap, M. G., Porter, M. L., Christensen, B. S. B., and Wildenschild, D. (2007). Comparison of pressure-saturation characteristics derived from computed tomography and lattice Boltzmann simulations. *Water Resour. Res.* 43:W12S06. doi: 10.1029/2006WR005730

Schmid, B., Schindelin, J., Cardona, A., Longhair, M., and Heisenberg, M. (2010). A high-level 3D visualization API for Java and ImageJ. *BMC Bioinformatics* 11:274. doi: 10.1186/1471-2105-11-274

Schneider, C. A., Rasband, W. S., and Eliceiri, K. W. (2012). NIH Image to ImageJ: 25 years of image analysis. *Nat. Methods* 9, 671–675. doi: 10.1038/nmeth.2089

Shah, S. M., Gray, F., Crawshaw, J. P., and Boek, E. S. (2016). Micro-computed tomography pore-scale study of flow in porous media: effect of voxel resolution. *Adv. Wat. Res.* 95, 276–287. doi: 10.1016/j.advwatres.2015.07.012

Smet, S., Plougonven, E., Léonard, A., Degré, A., and Beckers, E. (2017). X-ray Micro-CT: how soil pore space description can be altered by image processing. *Vadose Zone J.* 17:160049. doi: 10.2136/vzj2016.06.0049

Smith, K. A., Ball, T., Conen, F., Dobbie, K. E., Massheder, J., and Rey, A. (2003). Exchange of greenhouse gases between soil and atmosphere: interactions of soil physical factors and biological processes. *Eur. J. Soil Sci.* 54, 779–791. doi: 10.1046/j.1351-0754.2003.0567.x

Taina, I. A., Heck, R. J., and Elliot, T. R. (2008). Application of X-ray computed tomography to soil science: a literature review. *Can. J. Soil Sci.* 88, 1–20. doi: 10.4141/CJSS06027

Tarplee, M., and Corps, N. (2008). *Skyscan 1072 desktop X-ray microtomograph. sample scanning reconstruction, analysis and visualisation (2D and 3D) Protocols*. Guidelines, notes, selected references and F.A.Qs.

Tracy, S. R., Daly, K. R., Sturrock, C. J., Crout, N. M. J., Mooney, S. J., and Roose, T. (2015). Three-dimensional quantification of soil hydraulic properties using X-ray computed tomography and image-based modeling. *Water Resour. Res.* 51, 1006–1022. doi: 10.1002/2014WR016020

Udawatta, R. P., and Anderson, S. H. (2008). CT-measured pore characteristics of surface and subsurface soils influenced by agroforestry and grass buffers. *Geoderma* 145, 381–389. doi: 10.1016/j.geoderma.2008.04.004

Ursino, N., Roth, K., Gimmi, T., and Flühler, H. (2000). Upscaling of anisotropy in unsaturated Miller-similar porous media. *Water Resour. Res.* 36, 421–430. doi: 10.1029/1999WR900320

van Genuchten, M. T. (1980). A closed-form equation for prediction the hydraulic conductivity of unsaturated soils. *Soil Sci. Soc. Am. J.* 44, 892–898. doi: 10.2136/sssaj1980.03615995004400050002x

Vogel, H.-J. (2000). A numerical experiment on pore size, pore connectivity, water retention, permeability, and solute transport using network models. *Eur. J. Soil Sci.* 51, 99–105. doi: 10.1046/j.1365-2389.2000.00275.x

Vogel, H.-J., and Roth, K. (1998). A new approach for determining effective soil hydraulic functions. *Eur. J. Soil Sci.* 49, 547–556. doi: 10.1046/j.1365-2389.1998.4940547.x

Vogel, H.-J., Tölke, J., Schulz, V. P., Krafczyk, M., and Roth, K. (2005). Comparison of a lattice-boltzmann model, a full-morphology model, and a pore network model for determining capillary pressure–saturation relationships. *Vadose Zone J.* 4, 380–388. doi: 10.2136/vzj2004.0114

Vogel, L. E., Makowski, D., Garnier, P., Vieublé-Gonod, L., Coquet, Y., Raynaud, X., et al. (2015). Modeling the effect of soil meso- and macropores topology on the biodegradation of a soluble carbon substrate. *Adv. Water Res.* 83, 123–136. doi: 10.1016/j.advwatres.2015.05.020

Vogel, H.-J., Weller, U., and Schlüter, S. (2010). Quantification of soil structure based on Minkowski functions. *Comput. Geosci.* 36, 1236–1245. doi: 10.1016/j.cageo.2010.03.007

Wagenmakers, E.-J., Verhagen, J., and Ly, A. (2016). How to quantify the evidence for the absence of correlation. *Behav. Res.* 48, 412–426. doi: 10.3758/s13428-015-0593-0

Wetzels, R., and Wagenmakers, E.-J. (2012). A default Bayesian hypothesis test for correlations and partial correlations. *Psychon. Bull. Rev.* 19, 1057–1064. doi: 10.3758/s13423-012-0295-x

Wildenschild, D., and Sheppard, A. P. (2013). X-ray imaging and analysis techniques for quantifying pore-scale structure and processes in subsurface porous medium systems. *Adv. Water Res.* 51, 217–246. doi: 10.1016/j.advwatres.2012.07.018

Young, I. M., Blanchart, E.,Chenu, C., Dangerfield, M., Fragoso, C., Grimaldi, M., et al. (1998). The interaction of soil biota and soil structure under global change. *Global Change Biol.* 4, 703–712. doi: 10.1046/j.1365-2486.1998.00194.x

Zhang, Z. F. (2014). Relationship between anisotropy in soil hydraulic conductivity and saturation. *Vadose Zone J.* 13:vzj2013.09.0172. doi: 10.2136/vzj2013.09.0172

Conflict of Interest Statement: The authors declare that the research was conducted in the absence of any commercial or financial relationships that could be construed as a potential conflict of interest.